

High Frequency Combustion Instabilities
of LO_x/CH₄ Spray Flames in Rocket
Engine Combustion Chambers

THESIS

By

M. Sliphorst, M.Sc.

The research carried out in this PhD-thesis is part of the European research project on high frequency combustion instabilities, REST. Which is a cooperation between universities and research institutes in Germany and France.

Keywords: Combustion, combustion instabilities, HF-instabilities, acoustics, eigenmodes, spray combustion, resonant combustion, resonance, Rayleigh criterion, response factor.

Copyright © 2011 M. Sliphorst
All rights reserved.

Printed by Ridderprint BV, Ridderkerk, the Netherlands

ISBN 978-90-5335-384-4

This thesis is also available online at: repository.tudelft.nl

*Front cover: False color photograph of LOx/CH₄ spray flame chemiluminescence taken by author. Schematic of combustor with secondary nozzle, and 1T-mode.
Back cover: Spectrogram analysis of dynamic pressure in cylindrical combustor, schematic of used combustor, modal analysis of cylindrical combustor.*

High Frequency Combustion Instabilities of LOx/CH₄ Spray Flames in Rocket Engine Combustion Chambers

PROEFSCHRIFT

ter verkrijging van de graad van doctor
aan de Technische Universiteit Delft,
op gezag van de Rector Magnificus prof.ir. K.C.A.M. Luyben,
voorzitter van het College voor Promoties
in het openbaar te verdedigen op dinsdag 22 maart 2011 om 12:30 uur

door

Mark SLIPHORST

Ingenieur Luchtvaart- en Ruimtevaarttechniek
geboren te Amsterdam.

Dit proefschrift is goed gekeurd door de promotor:

Prof.dr. D.J.E.M. Roekaerts

Samenstelling promotiecommissie:

Rector Magnificus voorzitter

Prof.dr. D.J.E.M. Roekaerts Technische Universiteit Delft, promotor

Prof.dr.ir. B.J. Boersma Technische Universiteit Delft

Prof.dr.ir. H.E.A. van den Akker Technische Universiteit Delft

Prof.dr.ir. T.H. van der Meer Universiteit Twente

Prof.dr.-ing. S. Schlechtriem Technische Universität Stuttgart, Germany

Dr.rer.nat. M. Oswald DLR Lampoldshausen, Germany

Dr. G. Searby IRPHE-CNRS Marseille, France

*„Earth is the cradle of humanity,
...but one cannot live in a cradle forever“*

-- Unknown

Preface

The thesis before you represents more or less five years of work. During this time I operated a test facility with cryogenic fluids and highly explosive gases, as well as developed many tools for data analysis. I say more or less because there have been some setbacks such as serious physical illness and lengthy hardware issues that caused the project to take longer than anticipated.

Surely, I could not have done the research alone. I'd like to thank Dirk Roekaerts for his confidence when I came to see him over 5 years ago with the research proposal and the request to supervise the thesis at Delft University of Technology. And of course for his time and assistance, but especially his understanding for the trouble I ran into. Also, I'd like to thank Michael Oswald firstly for giving me the opportunity at DLR to start the doctoral research, but also for his supervision and constructive criticism throughout the project. A special thanks goes to Markus Dengler, our technician, for activating the test bench at 6 in the morning so that I could run the experiments in a timely fashion, as well as his efforts to implement test bench configuration changes. But above all, I'd like to gratefully thank Bernhard Knapp for his endless help and support running the actual experiments and the many, many scientific discussions elaborating the new results I found.

I want to thank my parents and brothers as well for their support and confidence that I'd pull through. Also, Christine who, with love and understanding, helped me through the more difficult times, deserves a grateful 'thank you'.

Sitting here, looking back over the past 5 years, I realize that not only many things happened professionally, but also in private life. Not all positive either, those involved know what I mean, and swallowing was not always easy, and at a certain point I was ready to emergency exit, but I guess all events in a way contributed to the foundation that allowed and even motivated me to finish the thesis and start looking forward. Good things are *always* looming at the horizon...

Lampoldshausen, December 2010

Summary

Ever since the early stages of space transportation in the 1940's, and the related liquid propellant rocket engine development, combustion instability has been a major issue. High frequency combustion instability (HFCI) is the interaction between combustion and the acoustic field in the combustion chamber. It destroys the thermal boundary layer wall increasing heat transfer and could lead to compromised performance, and ultimately to destruction of the engine and mission loss. In order to sustain a combustion instability, the energy of combustion must be released in phase with the acoustic oscillation. Any combustion chamber process could be responsible for the energy transfer between combustion and acoustics, and is sensitive to either the acoustic pressure or velocity. Whether the coupling mechanism is pressure or velocity driven, and what process is predominantly responsible, has been the main issue in handling HFCI. Several theories have been developed but none were successful in predicting the occurrence of HFCI. In the last years, diagnostic means have dramatically improved as well as become less costly. Pressure transducers and high speed optical diagnostics of today allow high quality analyses that can specifically target individual processes to investigate their role in sustaining HFCI.

The main objective of this thesis is to take a few steps toward a better physical understanding of HFCI by experimentally investigating the interaction between flame and acoustic field in a combustor specifically designed for this research. To reach this goal, first a test series is carried out to characterize the combustion chamber by finding correlations between operating conditions and relevant acoustic parameters. Next, an second test series is performed where an externally forced acoustic field is imposed. This allows quantifying the effects of external forcing explicitly. Large amounts of data have been generated by means of pressure sensors, and high speed optical diagnostics of spray and flame phenomenology. With these data, well-defined spatially and temporally resolved pressure and corresponding velocity fields of the first acoustic eigenmode were found with a high degree of consistency. Also, the behavior of the spray was quantified and a spatially and temporally resolved map of the flame intensity could be derived.

The theoretically predicted existence of a rotating tangential eigenmode was experimentally confirmed in the test series without external forcing. The characteristics of such a rotating mode can consistently be determined with a high temporal resolution. Correlations of high quality were found between the energy contained by the pressure oscillation of the first eigenmode and the Weber number as well as the injection velocity ratio. The intact core length of the spray correlated with the momentum flux ratio similarly to what can be found in literature. The flame spreading angle was observed to decrease with both Weber number and momentum flux ratio, which is physically consistent. The spatial structure of the flame

intensity fluctuations was stochastic in nature, and no clear conclusion was obtained with respect to what coupling mechanism is at play.

External forcing increased the energy of the pressure oscillation of the first eigenmode by three orders of magnitude. The acoustic field is fixed in space when external forcing is applied, and the nodal line of the first eigenmode oriented itself perpendicular to the axis of external forcing. The position of the external forcing with respect to the spray axis strongly correlated with the energy of the oscillation. Perpendicular forcing (nodal line parallel to spray axis), yielded high energy, and parallel forcing (nodal line perpendicular to spray axis), yielded low energy. External forcing was found to amplify the correlation between flame spreading angle and injection conditions. But external forcing did not have any influence on the liquid core length. It was derived from these two results, that possible candidates for driving an instability are reduced to vaporization(rate) and mixing. The spatial structure of the fluctuating part of the intensity field was strongest for perpendicular and weakest for parallel forcing. These results were consistent with velocity coupling, with the flame responding to the velocity vector field.

An elaborate analysis has been carried out comparing the spatially resolved acoustic fields with the flame intensity field. The location where the intensity of the flame is the highest could only be partially explained with velocity coupling. For perpendicular forcing, it was clearly velocity coupling, but for parallel forcing the distribution of the extreme values of the intensity oscillations required considering pressure coupling as a possible candidate as well. This is substantiated by the analysis of the phase-field. The spatial structure of the phase-field with perpendicular forcing was consistent with velocity coupling, but with parallel forcing, the phase-field could only be explained with pressure coupling. A convective motion due to velocity, which moves gas parallel to the combustion zone, could not possibly be responsible for the structure observed. A response factor, which is a measure for how strong the flame responds to an acoustic perturbation, was calculated for perpendicular forcing of the flame. Assuming velocity coupling, the spatially resolved response factor was found to be positive in the entire combustion chamber with extreme values in the combustion zone. A further step was taken by calculating the time delay between the perturbation by the coupling mechanism and the response of the flame. In the combustion zone, the time delay during resonance was found to be about 50 μs , which is the same order of magnitude as the typical time scale of the mixing process.

Both velocity and pressure driven coupling mechanisms occurred, depending on the origin of the perturbation. Velocity coupling seems to be effective by amplifying the mixing process, where pressure coupling is effective through the vaporization process (typical timescale 1 ms). The geometry dependent eigenfrequencies therefore determine which process has the appropriate time scale for the respective coupling mechanism to be effective.

The research yielded tools that are able to determine the temporally resolved acoustic and flame intensity fields, as well as a spatially (and temporally) resolved response factor. The results can be implemented in models for simulating HFCI.

Samenvatting

Vanaf het begin van de ruimtevaart in de jaren '40, en de daarbij horende ontwikkeling van raket motoren met vloeibare stuwstoffen, waren verbrandingsinstabiliteiten een groot probleem. Een hoog frequente verbrandingsinstabiliteit (HFVI) is de interactie tussen verbranding en het akoestische veld in de verbrandingskamer. Het vaagt de thermische grenslaag weg waardoor de warmteoverdracht toeneemt en mogelijk de prestatie afneemt, en zelfs de motor uit elkaar kan scheuren en de missie verloren gaat. Om een verbrandingsinstabiliteit te handhaven, moet de energie van de verbranding in fase met de akoestische oscillatie worden vrijgegeven. Elk proces in de verbrandingskamer zou verantwoordelijk kunnen zijn voor de energieoverdracht tussen verbranding en akoestiek, en is gevoelig voor of akoestische druk, of akoestische snelheid. Of het koppelingsmechanisme door druk of snelheid gedreven wordt, en welk proces hoofdzakelijk verantwoordelijk is, is het belangrijkste thema in het hanteren van HFVI. Verscheidene theorieën werden er ontwikkeld, maar geen enkele was tot nog toe succesvol bij het voorspellen van HFVI. De laatste paar jaren zijn de diagnostische mogelijkheden sterk verbeterd en minder duur geworden. De huidige druksensoren en hoge snelheid optische diagnostiek maken hoogkwalitatieve analyses mogelijk, die de individuele processen in het vizier nemen om hun rol bij het handhaven van HFVI te onderzoeken.

Het belangrijkste doel van dit onderzoek is een paar stappen te zetten naar een beter fysisch begrip van HFVI door de interactie tussen vlam en akoestisch veld experimenteel te onderzoeken in een speciaal voor dit onderzoek ontworpen verbrandingskamer. Om dit doel te bereiken wordt eerst een testserie uitgevoerd om de kamer te karakteriseren door correlaties tussen operationele condities en relevante akoestische parameters te vinden. Daarna wordt een tweede testserie doorgevoerd waarbij een extern geëxciteerd akoestisch veld wordt opgelegd. Dit maakt het mogelijk om de effecten van externe excitatie te kwantificeren. Een grote hoeveelheid data werd gegenereerd met druksensoren en hogesnelheidsopnamen van spray en vlam fenomenologie. Met deze data werden goed gedefinieerde, in ruimte en tijd opgeloste, velden voor druk en daarbij horende snelheid van de eerste akoestische eigenmode gevonden, met hoge mate van consistentie. Daarbij werd het gedrag van de spray gekwantificeerd en kon een in tijd opgeloste kaart van de vlamintensiteit gedefinieerd worden.

De in de theorie voorspelde roterende tangentiële eigenmode werd experimenteel bevestigd in de testserie zonder externe excitatie. De karakteristieken van een roterende mode kan consistent worden bepaald met hoge tijdsresolutie. Correlaties van hoge kwaliteit werden gevonden tussen de energie van de druk oscillatie van de eerste eigenmode en zowel het Weber getal alsook de verhouding tussen inspuitingsnelheden. De kernlengte van de spray correleerde met de verhouding van inpulsstromen zoals in de literatuur. Er werd waargenomen dat de spreidings-

hoek van de vlam neemt af met zowel Weber getal alsook met de verhouding van impulsstromen, en dat is fysisch consistent. De ruimtelijke structuur van de oscillaties van de vlamintensiteit had een stochastisch karakter, en er kon geen duidelijke conclusie getrokken worden betreffende welk koppelingsmechanisme actief is.

Door externe excitatie nam de energie van de drukoscillatie drie orden van grootte toe. Het akoestische veld ligt ruimtelijk vast als externe excitatie toegepast wordt, en de knopenlijn van de eerste eigenmode richt zichzelf loodrecht op de excitatie as. De positie van externe excitatie ten opzichte van de spray as correleert sterk met de energie van de oscillatie. Loodrechte excitatie (knopenlijn parallel aan de spray as) geeft hoge energie, en parallelle excitatie (knopenlijn loodrecht op de spray as) geeft lage energie. Het werd waargenomen dat externe excitatie de correlatie tussen vlam spreidingshoek en injectie condities versterkt. Van dit resultaat werd afgeleid, dat van de mogelijke kandidaten om een instabiliteit aan te drijven alleen verdampen en mengen overblijven. De ruimtelijke structuur van het oscillerende deel van het intensiteitsveld is het sterkst voor loodrechte en het zwakst voor parallelle excitatie. Deze resultaten waren consistent met snelheidskoppeling, waarbij de vlam reageert op het snelheidsvector veld.

Een uitvoerige analyse is uitgevoerd om de ruimtelijk opgeloste akoestische velden met het vlamintensiteitsveld te vergelijken. De locatie waar de intensiteit van de vlam het hoogst is kon alleen gedeeltelijk door snelheidskoppeling worden verklaard. Bij loodrechte excitatie was uit duidelijk snelheidskoppeling, maar bij parallelle excitatie was het noodzakelijk door de ruimtelijke verdeling van de hoge waarden van de intensiteitsoscillaties om ook drukkoppeling als mogelijk kandidaat te overwegen. Dit werd bevestigd door de analyse van het faseveld. De ruimtelijke verdeling van het faseveld bij loodrechte excitatie was consistent met snelheidskoppeling, maar bij parallelle excitatie kon het faseveld alleen met drukkoppeling worden verklaard. De convectieve beweging veroorzaakt door de snelheid, die het gas parallel aan de verbrandingszone beweegt, kan onmogelijk verantwoordelijk zijn voor de waargenomen ruimtelijke structuur. Een responsfactor, wat een maat is voor hoe sterk een vlam reageert op een akoestische storing, werd berekend voor loodrechte excitatie. Onder de aanname van snelheidskoppeling, de ruimtelijk opgeloste responsfactor was groter dan nul in de hele verbrandingskamer met grote waarden in de verbrandingszone. Een volgende stap was om de vertragingstijd tussen de storing door het koppelingsmechanisme en het antwoord van de vlam te berekenen. In de verbrandingszone bleek de tijdsvertraging tijdens resonantie ongeveer $50 \mu\text{s}$, te bedragen, wat in de zelfde orde van grootte ligt als de typische tijdsschaal van het mengproces.

Beide, snelheid en druk gedreven, koppelingsmechanismen kwamen voor, afhankelijk van de positie van de storing. Snelheidskoppeling is effectief via versterking van het mengproces, en drukkoppeling is effectief via het verdampingsproces (typische tijdsschaal 1 ms). De geometrie afhankelijke eigenfrequenties bepalen dus welk proces de gepaste tijdsschaal heeft waarmee het betreffende koppelingsmechanisme effectief is.

Dit onderzoek heeft een stuk gereedschap geleverd waarmee het mogelijk is de in de tijd opgeloste akoestische en vlamintensiteitsvelden te bepalen, alsook een ruimtelijk (en in de tijd) opgeloste responsfactor. Deze resultaten kunnen worden gebruikt in modellen om HFVI te simuleren.

Nomenclature

Latin symbols

A	Amplitude of pressure	[bar]
a	Speed of sound	[m/s]
c^*	Characteristic velocity	[m/s]
D	Diameter	[m]
E	Acoustic energy per volume	[kg/m/s ²]
f	Frequency	[Hz]
J	Momentum flux ratio	[-]
J_n	Bessel function of the first kind	[-]
L	Length	[-]
l, m, n	Mode number	[-]
M, N	Amplitude of pressure	[bar]
\dot{m}	Mass flow rate	[g/s]
N	(Local) Response factor	[-]
p	Pressure	[bar]
p_{off}	Offset parameter in fit function	[bar]
\dot{q}	Heat release per unit volume	[kg/m/s ³]
R	Radius	[m]
R_F	Global response factor	[-]
R_{OF}	Mixture ratio	[-]
R_v	Velocity ratio	[-]
r	Cylindrical coordinate, radius	[-]
T	Temperature	[K]
T	Period of harmonic oscillation	[s]
t	Time	[s]
\vec{u}	Velocity vector	[m/s]
v	Velocity	[m/s]
V	Propellant injection velocity	[m/s]
We	Weber number	[-]
x, y, z	Cartesian coordinates	[-]
z	Cylindrical coordinate, axial position	[-]

Greek symbols

α_{nm}	(m+1) th root of the derivative of the Bessel function	[-]
Γ	Line width	[1/s]
γ	Ratio of specific heats	[-]
δ	Constant of integration	[-]
θ	Cylindrical coordinate, azimuth angle	[-]
θ	Angle	[rad], [°]
ϕ	Phase angle	[rad], [°]

φ	Orientation nodal line relative to positive x-axis	[rad], [°]
$\dot{\varphi}$	Angular velocity	[rad/s]
π	Tangential wave, parallel to cavity	[-]
ρ	Density	[kg/m ³]
σ	Surface tension	[kg/s ²]
σ	Tangential wave, perpendicular to cavity	[-]
τ	Time	[s]
τ	Time lag (delay time)	[s]
λ	Eigenvalue	[-]
ξ	Distortion parameter in fit function	[°]
ω	Circular frequency	[rad/s]
ω_0	Natural frequency of damped system	[rad/s]
ω_n	Natural frequency of undamped system	[rad/s]

Indices

0	At resonance
'	Fluctuation
∞	Free stream
C	Combustion chamber
f	Fuel
l, m, n	Mode number
max	Maximum
min	Minimum
ox	Oxidizer
p	Pressure
rms	Root mean squared
std	Standard deviation
t	Throat
V, v	Velocity

Operators

∇	Gradient
Δ	Laplace operator = ∇^2
Σ	Sum

Acronyms

CH ₄	Gaseous methane
CRC	Common Research Chamber
H ₂	Gaseous hydrogen
LH ₂	Liquid hydrogen
LOx	Liquid oxygen
NPSD	Normalized PSD
PSD	Power spectral density

Contents

PREFACE	i
SUMMARY	iii
SAMENVATTING	v
NOMENCLATURE	vii
1 INTRODUCTION	1
1.1 BACKGROUND OF APPLICATIONS	2
1.1.1 <i>Launchers</i>	2
1.1.2 <i>Liquid propellant rocket engines</i>	4
1.2 COMBUSTION CHAMBER PROCESSES	5
1.2.1 <i>Atomization and spray formation</i>	5
1.2.2 <i>Vaporization and mixing</i>	7
1.2.3 <i>Combustion</i>	7
1.3 COMBUSTION INSTABILITIES.....	8
1.3.1 <i>Classification of combustion instabilities</i>	8
1.4 HF-INSTABILITY	9
1.4.1 <i>Driving mechanisms</i>	10
1.4.2 <i>Coupling mechanisms</i>	11
1.4.3 <i>HF-instability control</i>	11
1.5 OVERVIEW OF PREVIOUS RESEARCH	13
1.5.1 <i>Early stages</i>	13
1.5.2 <i>Follow up in the 1980s</i>	16
1.5.3 <i>Recent developments</i>	17
1.6 OBJECTIVES AND STRUCTURE	19
1.6.1 <i>Objectives</i>	19
1.6.2 <i>Structure</i>	20
2 BACKGROUND	21
2.1 THEORY.....	21
2.1.1 <i>Three-dimensional wave equation</i>	23
2.2 NUMERICAL SIMULATION	26
2.2.1 <i>CRC without cavity</i>	27
2.2.2 <i>CRC with cavity</i>	29

2.3	VELOCITY ASSOCIATED WITH PRESSURE WAVE	29
2.4	ROTATING WAVE	31
2.4.1	<i>Limit cases of the rotating wave</i>	31
2.4.2	<i>Characteristics of the rotating wave</i>	32
2.5	INTERACTION BETWEEN ACOUSTICS AND COMBUSTION	36
2.5.1	<i>Rayleigh Criterion</i>	37
2.5.2	<i>Crococo's (n-τ)-model</i>	39
2.5.3	<i>Response factor</i>	39
2.6	DAMPING	42
2.7	COLD FLOW ACOUSTICS IN THE CRC.....	45
2.7.1	<i>Frequency spectrum</i>	45
2.7.2	<i>Effect of the resonator</i>	45
2.7.3	<i>Ramp excitation</i>	47
2.8	OPERATING PARAMETERS.....	48
2.8.1	<i>Control parameters</i>	48
2.8.2	<i>Injection parameters</i>	49
3	APPROACH	51
3.1	EXPERIMENTAL SET-UP	51
3.1.1	<i>Test facility</i>	51
3.1.2	<i>Combustion chamber</i>	53
3.1.3	<i>Essential modules</i>	54
3.2	DATA ACQUISITION	56
3.2.1	<i>Static sensors</i>	56
3.2.2	<i>Dynamic sensors</i>	57
3.2.3	<i>Optical diagnostics</i>	57
3.3	TEST PROGRAM	58
3.3.1	<i>First test campaign, without external excitation</i>	58
3.3.2	<i>Second test campaign, with external excitation</i>	60
4	DATA REDUCTION AND ERROR MANAGEMENT	63
4.1	DATA REDUCTION	63
4.1.1	<i>Operating parameters</i>	63
4.1.2	<i>Dynamic pressure</i>	65
4.1.3	<i>Spray and flame optical diagnostics</i>	68
4.2	ERROR MANAGEMENT	73
4.2.1	<i>Error estimation</i>	73
4.2.2	<i>Error propagation</i>	75
5	EXPERIMENTAL RESULTS: DYNAMIC PRESSURE	79
5.1	CRC WITHOUT EXTERNAL EXCITATION	79
5.1.1	<i>Noise</i>	80
5.1.2	<i>Frequency shifts</i>	82

5.1.3	<i>Energy content</i>	84
5.1.4	<i>Damping</i>	86
5.2	CRC WITH EXTERNAL EXCITATION.....	88
5.2.1	<i>Introduction</i>	89
5.2.2	<i>Energy content</i>	91
5.3	PRESSURE FIELD.....	93
5.3.1	<i>CRC without external excitation</i>	94
5.3.2	<i>CRC with external excitation</i>	102
6	EXPERIMENTAL RESULTS: OPTICAL DIAGNOSTICS	107
6.1	SPRAY PHENOMENOLOGY	108
6.1.1	<i>Intact Core Length</i>	108
6.2	FLAME PHENOMENOLOGY	110
6.3	INTENSITY FLUCTUATIONS	114
6.3.1	<i>Global analysis, large window method</i>	114
6.3.2	<i>Local analysis, small window method</i>	116
7	EXPERIMENTAL RESULTS: INTERACTION AND COMBUSTION RESPONSE	125
7.1	INTERACTION OF ACOUSTIC FIELD AND COMBUSTION.....	126
7.1.1	<i>Relation of acoustic field and intensity field, without external excitation</i>	126
7.1.2	<i>Relation of acoustic field and intensity field with external excitation</i>	128
7.2	COMBUSTION RESPONSE.....	137
7.2.1	<i>Phase relation between acoustic pressure and flame intensity, without external excitation</i>	137
7.2.2	<i>Phase relation between acoustic pressure and flame intensity, with external excitation</i>	138
7.2.3	<i>Phase relation between acoustic velocity and flame intensity, with external excitation</i>	141
7.2.4	<i>Response factor</i>	143
7.2.5	<i>Time delay</i>	148
8	CONCLUDING REMARKS	153
8.1	REVIEW OF RESULTS	153
8.2	INTERPRETATION	157
8.3	PERSPECTIVES	158
8.3.1	<i>Follow-up test campaigns</i>	158
8.3.2	<i>General recommendations</i>	161
APPENDICES	163	
A.	CHEMICAL MECHANISM OXIDATION OF METHANE	165
B.	GAIN PROFILE HIGH SPEED CAMERA.....	167
C.	BESSEL FUNCTIONS	169
D.	NUMERICAL SIMULATIONS.....	171

<i>D.1 CRC without secondary nozzle</i>	171
<i>D.2 CRC with secondary nozzle</i>	172
BIBLIOGRAPHY	177
CURRICULUM VITAE	191

1 Introduction

Ever since the early stages of space transportation in the 1940's, and the related liquid propellant rocket engine combustion chamber development, combustion instability has been a major issue. An issue that even today, in spite of all efforts yielding patch solutions to control or avoid instabilities for specific engines, has not been quite understood. These high frequency (HF) instabilities are caused by the coupling of combustion and an acoustic eigenmode of the combustion chamber. And when it occurs, the thermal boundary layer is destroyed which therefore cannot protect the wall from the hot gas anymore, causing an elevated heat flux and an increased risk to not only compromise the engine's performance, but lose the entire mission. Due to their hazardous effect on rocket engine performance, or even destructive effect on the engine itself, HF-instabilities are considered one of the most dangerous phenomena in rocket combustors.

In the past 70 years, much experience has been gathered, (see for example [59] and [159]) and the basic mechanisms for the coupling between combustion and acoustics have been identified. The search for a fundamental solution preventing HF-combustion instabilities has nevertheless been unsuccessful. Even though rockets are launched on a regular basis, the solutions in their thrust chambers are highly empirical in nature. And stability is mostly achieved by passive damping elements, such as baffles or absorbers.

The research presented here is carried out at DLR Lampoldshausen, Germany, in the framework of a cooperation between German (DLR, Astrium and TU Munich) and French institutes (CNRS, ONERA, CNES and SNECMA) on high frequency combustion instabilities [21].

Since space transport has become an essential aspect of life, and the demands on rocket propulsion will become even steeper in the future as they already are, it is of utmost importance that the little understanding with respect to high frequency combustion instabilities that exists today is expanded to ensure a successful further development of rocket combustion chambers. Also because the financial consequences of a case of combustion instability during flight are immense due to loss of the mission as well as the additional allocation of resources of the research programs in solving combustion instability behavior of an engine that was already flight qualified.

1.1 Background of applications

The space industry is booming, and only because the market demands it. There's high demand for more, better and safer means to transport satellites into orbit or interplanetary trajectories for research, observation, telecommunication, navigation, etc. But lately the issue of manned travel to for example Mars was raised again as well. To comply, the launch vehicle's capabilities must be improved. And, surely, to do so, the engines propelling the launchers beyond the Earth's atmosphere need to be developed.

1.1.1 Launchers

Current launchers such as Ariane 5 (Figure 1.1), must be further developed to increase payload capacity in the near future. Besides enhancing the main engine's (Vulcain2 for Ariane 5, Figure 1.2) performance, replacing the solid booster rockets with liquid propellant boosters is under consideration in the European rocket engine community, especially with respect to the fuel of choice [15], [16], [55], [74], [90], [108]. Methane tends to be preferred over kerosene because of better cooling and soot forming characteristics.



Figure 1.1: Ariane 5 launcher [4]

In addition, since HF-instabilities strongly depend on the internal geometry (see Chapter 2 for a theoretical discussion) of the combustor, and the booster engines will be much bigger than the main engine of the rocket (Thrust Vulcain2: 1.35 MN, Booster: 7 MN), the problem of combustion instabilities will become bigger as well. In this light, it is evident that the research here presented, and carried out with methane and liquid oxygen, is an important step in developing a fundamental understanding for combustion instabilities.

Generally, there exist three types of rocket engines, shown in Figure 1.3. But only for one of them, combustion instability is a ‘common’ issue. Even though the combustion instabilities that were witnessed in Ares [73] and to a lesser extent in Ariane 5 booster rockets are of structural harmonic rather than acoustic nature, the relatively small pressure amplitudes caused, due to the large size of the engine, high thrust variations which in the case of Ares would have resulted in oscillatory acceleration levels unacceptable for astronauts. The gas column on the other hand that exists in a solid rocket can, on the other hand, sustain instability which justifies the modeling work by for example Flandro [47]. But because the entire rocket basically forms the combustion chamber of which the internal geometry continuously changes during burn down, hence having continuously changing acoustic characteristics, they are relatively safe with respect to acoustic instabilities. The same is more or less valid for hybrid rockets. They have a liquid oxidizer, but still a solid fuel grain, hence the safe instability character of the solid rocket is still present. In combustion chambers of liquid propellant rocket engines on the other hand, there are many processes taking place in the combustion chamber that in one way or another could couple with the due to the geometry relatively constant acoustic properties and cause instability.

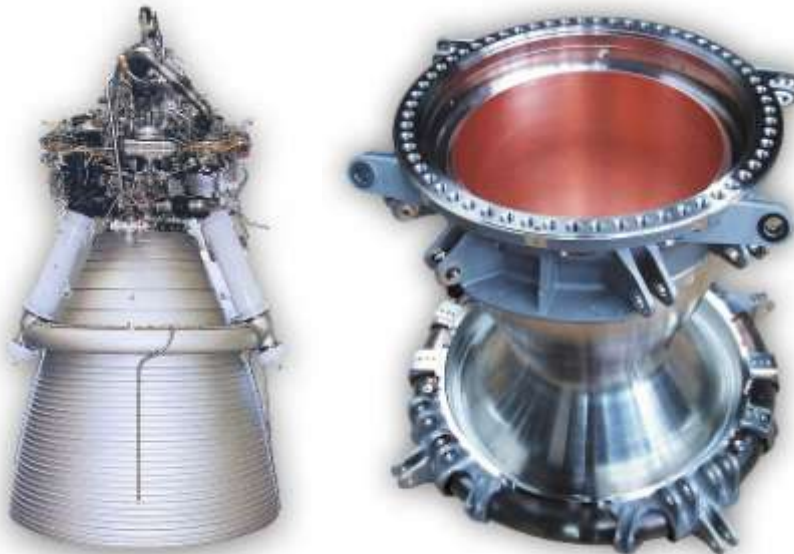


Figure 1.2: Vulcain2 main engine of Ariane 5 (left: complete rocket engine with nozzle extension, right: combustion chamber) [42]

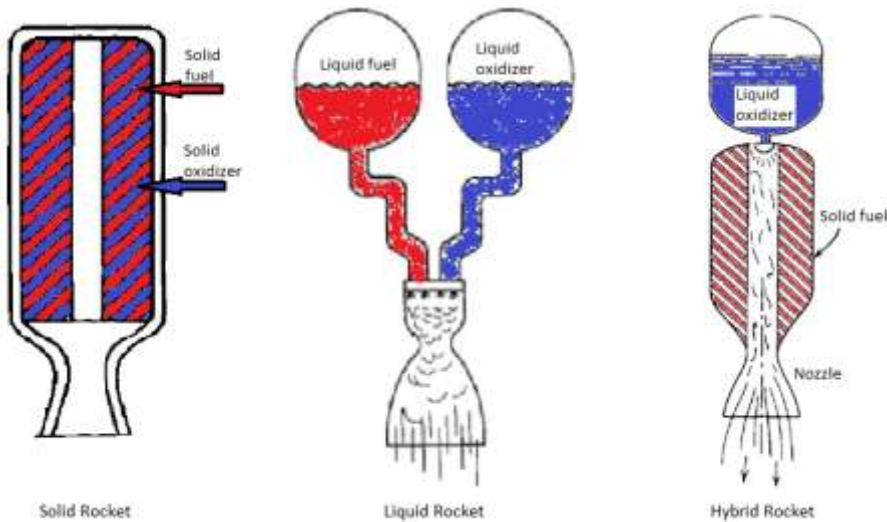


Figure 1.3: Types of rocket engines (edited from [148])

1.1.2 Liquid propellant rocket engines

Many high thrust liquid propellant rocket engines (LPRE) are bi-propellant engines. Mostly using liquid oxygen (LOx) as the oxidizer and in many cases liquid hydrogen (H_2) as fuel (Space Shuttle Main Engine, Ariane 5 main stage Vulcain 1 and 2, Ariane 5 new upper stage Vinci), because of the high performance capabilities of this propellant combination. The propellants are injected through a number of coaxial elements, with LOx usually flowing through the center post. Since shear coaxial injector elements are superiorly effective in mixing two propellants with large density difference, these are usually implemented for the liquid oxygen and hydrogen or methane (CH_4) propellant combinations. Other possible injectors are impinging injectors, which are more often used for two liquid propellants with similar densities, or swirl coaxial injectors [130] in which one of the two propellants is given an angular velocity. But even for a shear coaxial injector there exist several variations in geometry, all having an influence on combustion characteristics and (in)stability [59], [74]. The most common variations of a shear coaxial injector are shown in Figure 1.4. The injector on the left is a straightforward shear coaxial injector, the middle has a tapered LOx post, and the injector on the right has a recessed LOx post. Combinations thereof and variations of the fuel annulus are also possible. The flow direction in Figure 1.4 is from top to bottom.

1.2 Combustion chamber processes

The injection process, even though essential, is only the first in a series of processes that lead to combustion of the propellants. The injector's geometry plays a dominant role in the injection velocities of the propellants, which in turn control the aerodynamic forces that first break up and consecutively atomize the liquid oxygen jet to form a spray of small droplets. After spray formation, the small droplets will start to vaporize, and the oxygen gas will then mix with the fuel to a combustible mixture to allow the chemical reaction to take place. In Figure 1.5, a schematic representation is shown of all the processes that lead up to combustion.

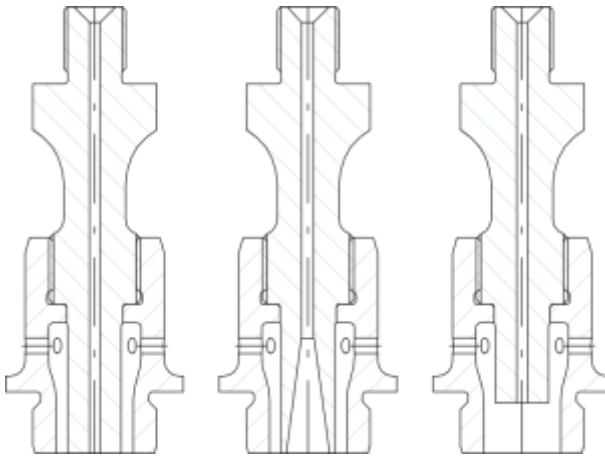


Figure 1.4: Coaxial injector variations

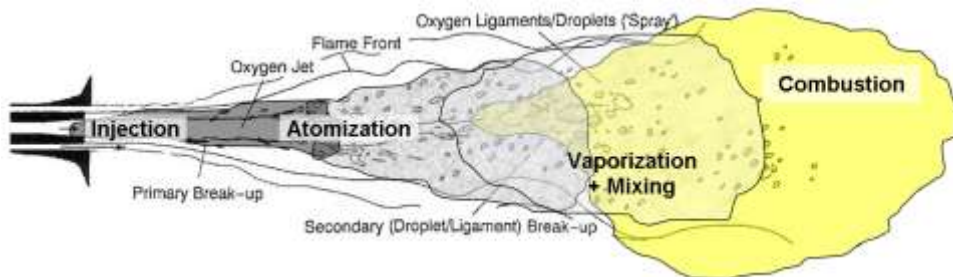


Figure 1.5: Schematic sequence of processes leading to combustion (edited from [95])

1.2.1 Atomization and spray formation

Atomization is the process following injection. It can be divided into two main sub-processes. Primary breakup is controlled by the velocity difference between the liquid core and the annular jet. Aerodynamic shear forces, due to the velocity

difference, cause the liquid jet to become unstable, and start tearing off large segments of liquid. These so-called ligaments are then subject not only to aerodynamic forces, but internal hydrodynamic forces in the liquid play a larger role as well. The combination of these forces results in the secondary breakup of the ligaments to form the droplets in the fully developed spray.

Much research has been carried out in order to understand and model the sub-processes of atomization, or ‘molecularization’ as Harrje and Reardon [59] express it. They estimate the average number of molecules per droplet in a fully developed spray to be as large as 10^{15} . Branam [13], for example, briefly describes how injection characteristics affect the coaxial jet and thus the atomization process.

Lasheras and Hopfinger [84] discuss the physical mechanisms involved in the primary breakup (near-field) of the jet, as well as a statistical description of the far-field distribution of the fully developed spray. Primary breakup specifically was investigated by Raynal [121], Villermaux [152] and Lasheras [85]. The concept of liquid core length is also mentioned in [84] as well as in [35], [85], [152], [158]. The liquid core length denotes the stable length of the jet. It is the length beyond which the jet does not form an intact body anymore but consists of large independent ligaments of liquid, see Figure 1.6 (L denotes the intact core length). Its relevance will become clear in section 6.1 where the experimental results of the current research are discussed.

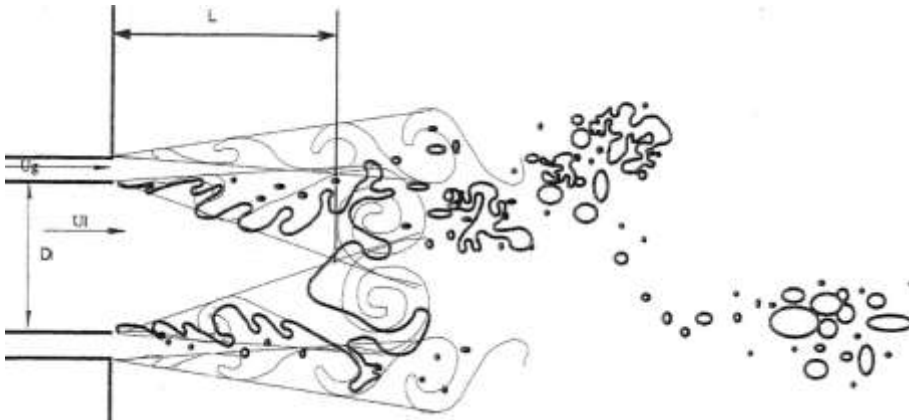


Figure 1.6: Jet break-up [84]

Rehab [123], Villermaux [152] and Marmottant [91] give very detailed discussions from an experimental point of view of all steps from primary breakup via ligament dynamics and secondary breakup to droplet formation and droplet size in the fully developed spray. One could use such experimental findings to verify a numerical model to describe a liquid spray [75]. A combined computational and experimental report was given in [72], where droplet sizes in the liquid spray predicted by the model are compared to the actually measured droplets.

Due to its physical characteristics, in most rocket engines liquid oxygen is injected under super-critical conditions (critical pressure ~ 50 bar), which shows the relevance of the work done by for example Davis and Chehroudi [35]. They show that behavior of the jet under oscillatory conditions is very different for sub- and super-critical injection.

Not only spray characteristics themselves, also the effect of acoustics and acoustic perturbations on the liquid spray and vice versa are subject to dedicated investigations [35], [51], [52], [69], [88].

1.2.2 Vaporization and mixing

Directly after injection, the liquid starts to vaporize, but not until the small droplets are formed, vaporization becomes the dominant process. A liquid can vaporize by either boiling (liquid heating to boiling point, driven by temperature difference) or evaporation (to achieve thermodynamic equilibrium with its surroundings, driven by concentration of species). These processes are to be considered an integrated process because they occur simultaneously and dependently. For example, if a droplet is small, it will heat up quicker but will therefore also shift the equilibrium of the droplet such that evaporation accelerates. A large droplet can evaporate quicker due to its large surface, which in turn accelerates the heating of the droplet. Sirignano [139] argues that droplet heating and vaporization are in the order of 1 ms, which is the same order of magnitude as an acoustic oscillation. Which is substantiated by the discussion on characteristic time scales by Benedictis [11].

Evaporation can be accelerated when the surroundings impose a convective motion that ‘blows’ the just evaporated liquid away from the droplet to cause a deviation from the thermodynamic equilibrium which in turn causes more liquid to evaporate to restore this equilibrium. After vaporization, the propellants can start to mix. The mixing process is, of course, also enhanced when the convective motion carries newly formed gas into the mixing zone.

When a mixture develops where a chemical reaction can be sustained, the local chemical reaction will then combine with the other regions to build a flame. Dedicated research for mixing of coaxial sprays can be found for both with chemical reaction and without chemical reaction (inert gases) in for example [151] and [147] respectively.

1.2.3 Combustion

If, at any location, in the combustion chamber the propellants are sufficiently mixed (and in some cases a required temperature threshold is reached) they will chemically react. If enough mixing takes place due to injection/atomization and mass flow is sustained, enough reactions will take place to build a flame. The ignition process in rocket combustors is far from trivial, hence the many dedicated works on ignition, see for example [56] and [34]. The combustion flame will anchor at the LOx post, and those locations where mixing is complete will form the reaction zone, or flame front. The volume of the combustion chamber will contain a heterogeneous mixture of liquid propellants, mixed but un-burnt gases and hot combustion products. With this heterogeneity obviously comes a non-uniform distribution of temperature (hence speed of sound), pressure and other properties.

1.3 Combustion instabilities

The stochastically occurring pressure variations do not pose a problem. It is when the variations start to occur systematically, sustained by an energy release caused by the coupling of combustion with any other part of the system, it becomes a hazard. Usually, thrust chambers are designed for high efficiency and minimized for losses, but it is exactly those characteristics that help sustain an oscillation.

Combustion is not a stationary process. It depends on injection, atomization, vaporization and mixing. Some of these processes are more stochastic than others, thus combustion is, at least partially, a stochastic process as well. As long as the stochastic pressure variations do not exceed 5% of the mean chamber pressure, combustion is considered 'smooth' [148]. Even when the variations are larger than 5%, but still have a stochastic distribution, combustion is only considered 'rough'. A sample of smooth and rough combustion is illustrated in Figure 1.7. But when the pressure fluctuations are over 5% and show a significant periodicity, due to interaction with feed system, engine structure, or acoustic modes of the combustion chamber, it is called combustion instability.

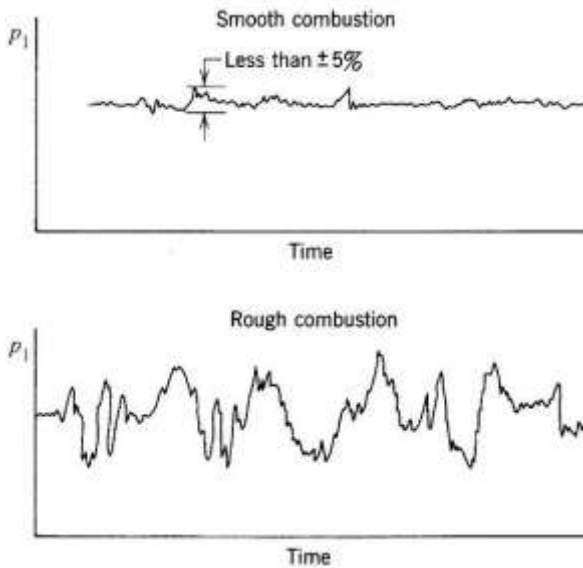


Figure 1.7: Chamber pressure trace of smooth (upper) and rough (lower) combustion [148]

1.3.1 Classification of combustion instabilities

Three classes of combustion instabilities were identified [25], [59]. At relatively low frequencies (LF), in the range of up to a few 100 Hz, the LF-instability, or 'chugging' or 'howling' could have several causes. One possibility is a coupling of com-

bustion with the injector, where the injector “acts as a diaphragm and oscillates in an oil-can mode” [59], causing fluctuations in the propellant injection.

Instability at very low frequency (a few Hz), or “pogo-instability”, is ultimately caused by thrust variations that are transferred through the propellant column in the tank to cause pump inlet pressure variations, which are amplified by the pump’s function to amplify the pressure, which in turn are responsible for propellant flow rate variations. But since combustion is perturbed so slowly it can be considered quasi-steady, it is usually not considered combustion instability.

Intermediate frequency (IF) instability occurs at frequencies of several 100 to 1000 Hz, and is also sometimes referred to as ‘buzzing’. This type can also have several causes. One is the entropy wave caused by cyclic mixture ratio variation.

The last class of combustion instabilities is HF-instability, or (thermo-)acoustic instability, resonant combustion or “screeching”, and generally lie above 1000 Hz. HF-instability is caused by the excitation, usually by the combustion process, of an acoustic eigenmode of the combustion chamber. Due to the energies involved, this type of instability can have catastrophic consequences.

LF and IF-instability can easily be avoided in designing the engine and launch vehicle. Simple analytical tools can be applied when structurally designing the launch vehicle system to include damping measures to avoid LF. Also, in the structural design of the engine itself, elements of the feed system can be combined such that no coupling can occur. Avoiding HF-instability is not so trivial, as experience over the past 60-70 years proves. An historical overview of the experiences gathered by the community is given in section 1.5.

1.4 HF-instability

High frequency combustion instability, or thermo-acoustic instability, is caused by an interaction between combustion and the acoustic field. The acoustic field is defined by the geometry of the volume wherein it manifests itself, in this case the combustion chamber. The wall, injector head and nozzle throat can all be considered acoustic boundaries. Even though an acoustic coupling between combustion chamber and injector volume was reported in one occasion [71], this is very rare and this type of injection coupling is not considered the driving force behind the instability.

Acoustic eigenmodes have a very distinct shape and specific frequency, all depends on the geometry and the momentary speed of sound. In general, eigenmodes in liquid rocket engines can have two fundamentally different characters, defining three types of modes. Longitudinal modes show much analogy with the propagating wave in a musical instrument. A pressure wave moves up and down in the column of air within the instrument, whereas in a combustion chamber, the pressure wave moves along the chamber axis, see Figure 1.8a. Transverse modes move within a plane perpendicular to the chamber axis. These modes can be divided into two sub-types, radial and tangential modes. Radial modes show strong similarity with the waves seen when throwing a rock in a pond. The ripples run from the center outward, which is illustrated in Figure 1.8b. A tangential mode is a standing wave and even though it is a two dimensional wave,

shows some analogy with a (1-D) pulled guitar string. The amplitude swings back and forth across the symmetry (nodal-) line (zero amplitude). For the first mode, the guitar string, being 1-D, has one point where the amplitude is zero, and around which the rest of the string fluctuates. Tangential modes have been witnessed as being fixed in orientation, or with a rotating axis, such that the amplitude moves along the circular combustion chamber wall, but keeping the geometry of a standing tangential wave. The two variations of the tangential mode are illustrated in Figure 1.8c and Figure 1.8d. The third type is a combination of longitudinal and transversal modes, resulting in a complex three dimensional wave.

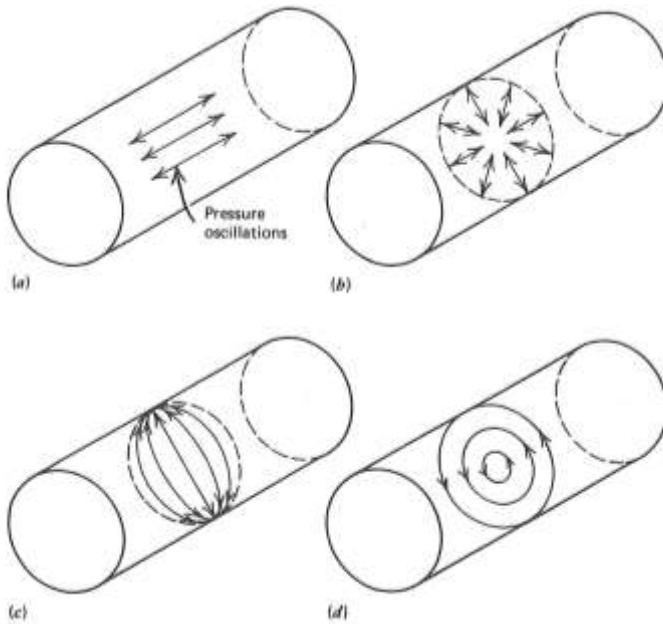


Figure 1.8: Fundamental characters of eigenmodes in a cylindrical volume. (a) Longitudinal mode, (b) Radial mode, (c) Standing tangential mode, (d) Rotating tangential mode [166]

1.4.1 Driving mechanisms

Whereas LF instabilities are more often than not coupled with and caused by the injection system, and are therefore driven by periodic variations in mass input to the system, HF instabilities are driven by heat release from combustion, and the coupling thereof with the acoustic system. By the end of the 19th century, Lord Rayleigh [119], [120] confirmed that an acoustic instability is driven by periodically adding (or subtracting) heat to the system at that point in the cycle where the acoustic pressure is maximum (or minimum).

The excellent theoretical discussion of Sirignano [139] (or Benedictis [11]) on characteristic times of the individual processes in the combustion chamber and their candidacy to drive combustion instabilities may shine some light on the situation. Sirignano first argues that there are three types of possible driving mechan-

isms. The first type is a rate controlling process. Such as process' characteristic time is of the same order of magnitude as the period of the oscillation. In this case, the process can strongly respond to acoustic oscillations, either pressure or velocity. Important boundary condition to actually drive instability, is that the phase must be correct and the amplitude sufficient to overcome other losses. The second and third type both are indirect mechanisms that control the combustion distribution, and can be considered one and the same because they occur simultaneously. It is a process that controls the characteristic time of a rate controlling process, such as atomization. The characteristic time of atomization ($<100 \mu\text{s}$ [139]) is roughly an order of magnitude smaller than the period of oscillation ($\sim 1 \text{ ms}$), but the acoustic variations affect the droplet size distribution, which in turn influences a rate controlling process' characteristic time. The variations of droplet size distribution cause variations in combustion distribution, hence local response affecting an interaction with particular eigenmodes. Sirignano [139] then goes through all processes from liquid injection via atomization and vaporization to mixing and even chemical kinetics. He considers only vaporization to be a potential candidate for the driving force behind self-sustained combustion instability.

1.4.2 Coupling mechanisms

In case of an HF-instability, the question then remains through which mechanism an acoustic oscillation modulates the energy (heat) release rate. All efforts in research, theoretically and experimentally, have not produced a conclusive account with respect to whether coupling happens through acoustic pressure or velocity. Considering the many processes propellants have to undergo before combustion can take place, it is not so trivial. Chemical reaction rate, injection rate and vaporization for example are sensitive to pressure variations, whereas vaporization rate, atomization and mixing have a stronger sensitivity to velocity perturbations.

Many researchers have come up with as many theories with respect to coupling mechanisms. Usually with little evidence, and maybe even lack of statistics, but all it really proves, is that coupling mechanisms and especially the processes dominantly involved are inadequately understood. In 1964, Reardon and Crocco [122] claim that velocity coupling should not be neglected, even though Crocco's time lag theory [24], [26], [27] finds its roots in the idea of pressure coupling. Both ideas' existence is justified because neither mechanism was conclusively verified which is substantiated by the parallel research of Wieber in 1960 [157] identifying velocity coupling as the responsible mechanism. More recently, Knapp et al. [80], [82], and Oswald et al. [106] were convinced the responsible mechanism was pressure related. But Richecoeur [124] seems to have a preference for velocity coupling. The results with respect to coupling mechanisms that were found in this thesis will be elaborated in Chapter 7.

1.4.3 HF-instability control

High frequency combustion instability, especially due to tangential modes, is one of the most dangerous phenomena in rocket engines. Fundamentally, there are

two possible solutions to the problem. The first is to control where energy is released to avoid coupling with an acoustic wave. This is relatively difficult in a rocket engine without compromising the engine's functionality. There are many parameters to consider without even knowing which parameters are responsible for coupling in the first place.

The second possibility is damping of possible modes. One way to increase damping is with absorbers. These are quarter-wave resonators and are acoustically connected to the combustion chamber in radial direction, such that the acoustic characteristics are modified such that eigenmodes are highly damped. These absorbers must be tuned to a specific frequency to be effective in damping the chamber eigenmode. Here lies the problem of designing absorbers. Due to the inhomogeneity in the combustion chamber, the eigenfrequencies will also continuously shift. An absorber will be rendered useless when the eigenfrequency is shifted away from the frequency to which the absorber was tuned. In addition, the presence of a quarter-wave cavity could also shift the eigenfrequencies [107], making tuning problematic.

Despite the efforts of the past, no solution to the problem applicable for all engines has been found. Every single engine type was individually tested and modified through a tedious trial and error procedure to find a fixer-upper for that specific engine. Without finding any systematic means for keeping HF-instability under control. A number of patch solutions were found such as baffles, injector modifications, acoustic absorbers, ignition sequence altering, etc. But none of these solutions could convince because they are not universally applicable and they require trying and modifying for every new engine design.

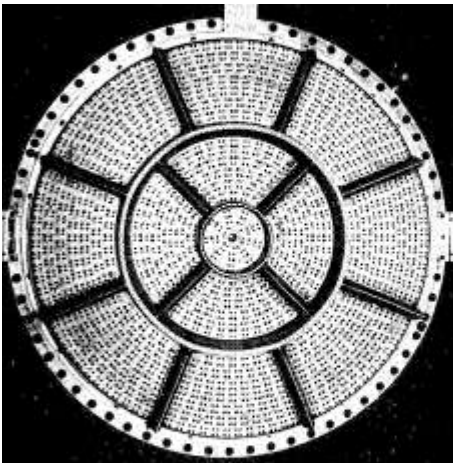


Figure 1.9: F-1 engine injector-baffle configuration [104]

The best example to illustrate the tediousness of such a process to control combustion instability is the design and qualification of the Saturn V engine, the F-1 engine. Oefelein [104] gives an excellent overview of Project First, which was initiated to solve the instabilities problem of the F-1 engine. Over 2000 tests were performed in 4 years time in the mid 1960s, testing 14 injection and 15 baffle patterns. The injector-baffle configuration of the F-1 engine that was flight qualified is shown in Figure 1.9.

1.5 Overview of previous research

This section gives a brief historical overview of gathered experiences, results and findings, with respect to the relevant aspects involved in high frequency combustion instabilities. The time period in which research with respect to combustion instabilities was conducted can be sub-divided into three parts. The first period was in the beginning of the space age, and was driven by the moon/Apollo program, and mainly took place in the US. During the second period, in the 1980s, Europe started to become an important player in space propulsion, and encountered the high frequency combustion instability problem as well. Of course, the Russians had their own development programs with their own instabilities issues. These programs ran parallel to the research programs in the west and were only published as late as the late '80s and '90s. The Russian approach and research programs are described in length by Natanzon [100] and Dranovsky [38]. During the third stage, the instability issue is attacked both experimentally and numerically. Due to incredible increase in computational resources as well as large improvements in data acquisition methods, it is now possible to investigate interaction between acoustic perturbations and combustion chamber processes individually.

1.5.1 Early stages

Almost all research done in the early stages were carried out by or under contract for NASA. Especially in the 1960s, parallel to the development of the F-1 engine [104], Saturn V program, a lot of effort was allocated to gather understanding of the HF-instabilities problem.

Because the diagnostic equipment, such as pressure transducers or even optical access, was not affordably available, the first attempts to explain the observed phenomena were theoretical in nature. Crocco [24], [26], [27] developed and refined over time the well known 'sensitive time-lag theory'. It was first derived for longitudinal modes, and later also for transversal instabilities. The theory was verified [27] to be able to predict longitudinal instabilities relatively accurately. The time-lag model (briefly explained in section 2.5.2) does not incorporate the physics of all processes taking place in the combustion chamber, and with the currently available diagnostic means, allowing the investigation of some individual processes, the theory has become obsolete [139], or its applicability at least compromised [31].

In 1957, Mickelsen [98] investigated how in theory pressure oscillations affect mixing of fuel and oxidizer. He claims that a peak to peak oscillation as large as the mean chamber pressure can cause a reduction of the mixing wake behind a droplet by as much as 60%. This implies that mixing is dramatically improved.

The majority of the research was nonetheless done experimentally, where many researchers seem to have had their focus on the interaction between vaporization and acoustics. Heidmann [62], [63] discovered that during the presence of spinning mode instability, the oxygen jet length decreased, and that the length varied periodically with the oscillation. The effect of acoustic oscillations on fuel droplets was investigated by Wieber and Mickelsen [157]. They claim that these oscillations

greatly increase the vaporization rate which in turn could explain the higher combustion efficiency during resonant combustion. In 1966, Heidmann and Feiler [64] found out that even the smallest tangential velocity variations that incur for any reason, could have strong amplifying or damping effects on the energy release in phase with the oscillation. He also argues that this could be a possible measure to prevent instabilities. Heidmann and Wieber [67], [68] describe a way to quantify the response of vaporization to a pressure oscillation by means of a response factor. Their response factor is determined for an entire cycle and is positive for positive interaction, and negative for negative interaction. They determined the frequency response for several effects and combined these effects into one frequency factor, a transformed frequency. The relation is shown in Figure 1.10. The response factor approach is pursued further in [61], [65], [66]. A response factor will be discussed in more detail in section 2.5.3 and 7.2.4.

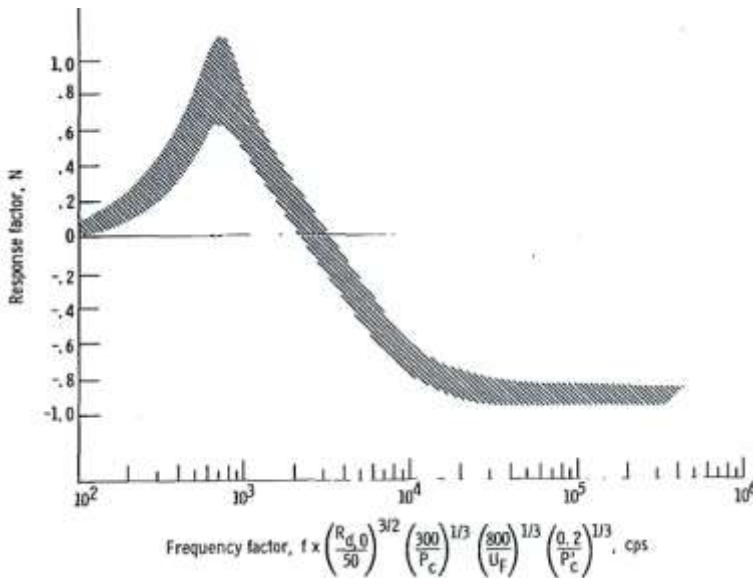


Figure 1.10: Response factor vs. frequency factor [66]

In 1967, Feiler and Heidmann [46] investigated whether there exists a coupling between pressure oscillations in the combustion chamber and the fuel (hydrogen) feed line. It was concluded that the out-of-phase coupling found was substantial enough to consider important in the instability research for hydrogen systems. The coupling became stronger for higher hydrogen density (or lower temperature at constant pressure). This research was practically a spin-off of the work by Wanheinen et al. [156]. He examined the effects of injection velocities of the propellants on resonant combustion, using a single coaxial injector, and found that operation was stable above a hydrogen-oxygen injection velocity ratio of 6.5, and unstable below 6.5, irrespective of hydrogen temperature. The research with their engine was continued and Conrad [23] published some more general, but fundamental, conclusions. The hydrogen temperature could be reduced to as low as 33 K before combustion became unstable. Stability was also strongly affected by variations in contraction ratio, controlling chamber pressure or mass flow. A

larger contraction ratio improved the stability limits. The hydrogen temperature below which combustion becomes unstable (transition temperature) was used the following years by several researchers to quantify an engine's stability margin.

In a further continuation of this research, Wanheinen et al. [154] investigated different parameters' effect on the transition temperature. Mass flow variations to control chamber pressure had no effect. Increasing oxygen temperature (or decreasing density) as well as the oxygen jet diameter increased the transition temperature (deteriorating stability margin). He also manufactured an empirical parameter consisting of several operating variables, which yielded a constant value as stability limit, see Figure 1.11.

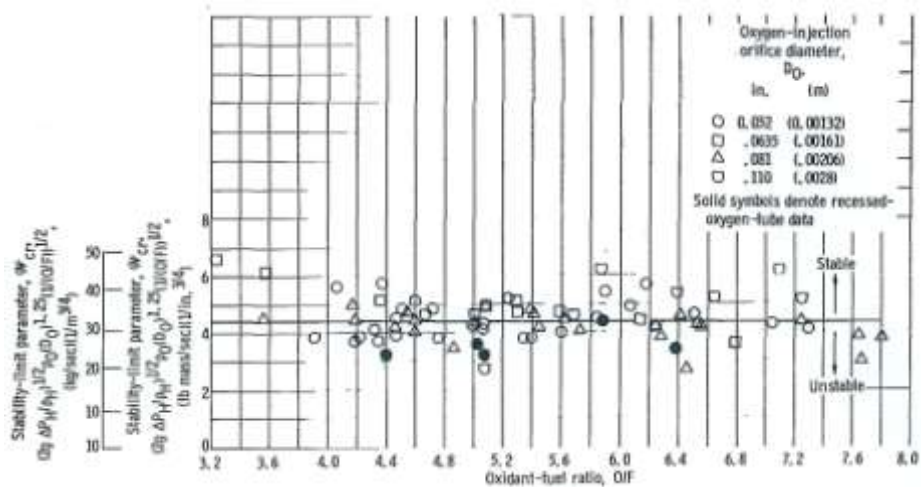


Figure 1.11: Stability parameter Wanheinen [154]

This stability-limit parameter covered all trends mentioned but was, obviously, only valid for the investigated injector-engine combination. In turn, Salmi et al. [131] varied the number of injector elements and determined that an increase in thrust per element positively influenced the transition temperature at which instabilities could be induced. The effect of the injector element distribution was then investigated by again Wanhainen [155]. An increase in distance between the outer elements and the wall destabilizes combustion, independent from the chamber diameter. Neither the number of elements nor the spacing between the elements had an influence on stability.

Rupe and Jaivin [129] investigated the mass flow distribution and resonant combustion on heat flux. Apparently heat flux shows a strong correlation to the mass flux through the injector, substantiated by calculated temperature distributions from an analogue model. But they also concluded that this type of method is inadequate until boundary layer flow phenomena are well understood and can be predicted. Clayton and his colleagues [19], [20] investigated the severity of rotating waves. He came to the conclusion that this type of instability is more dangerous than the standing wave type because, as he theorizes, the detonation like wave is driven due to its propagation along the wall, implying the movement is its own

driving mechanism. But he still considers a large number of processes to be not fully understood, amongst which the size distribution, shattering effects, and transient heating of the droplets.

Theoretical studies of non-linear and three dimensional combustion instabilities were published by Sirignano [138] and Zinn [165]. Both authors based their approach on the sensitive time-lag model [24]. Sirignano [138] focused on longitudinal waves and one of his important results was that unstable combustion is only possible if the characteristic time of combustion is negligible compared to or in the same order of magnitude as the period of oscillation. Zinn's work [165] had more affinity with transversal modes and he discovered that increasing the mean flow Mach number shifts the unstable region which he associates with pure transversal modes. The new unstable regions appearing correspond to mixed modes.

In 1972, Harrje and Reardon [59] published a comprehensive review of all the work done up to date. It was considered an all-knowing document that would provide all future developments an answer to combustion instabilities. Research programs regarding combustion instabilities in liquid propellant rocket engines more or less shifted to the background, also due to a lack of funding [60]. It was not until 1980, due to the self-destruction of an Ariane rocket and a new heavy launcher program in the US [159], when combustion instabilities regained full attention of the research community.

1.5.2 Follow up in the 1980s

In the 1980s, Rockwell/Rocketdyne (Jensen et al. [74]), under NASA contract, carried out a very extensive experimental test program to verify whether hydrocarbons, especially methane, could be stability rated similarly as hydrogen was in the 60s and early 70s, using the same techniques such as temperature ramping and bomb tests. With a 40,000 lb thrust combustor, they were successful in finding a stability threshold as a function of fuel temperature and other relevant parameters to allow the comparison with hydrogen. Their most important conclusions are summarized here. They found that the temperature ramping technique is a valid method, even though it excited higher order modes instead of the searched for first tangential mode (as for hydrogen). Also, the ramping does not uniquely characterize that combustor for stability because all spontaneous as well as bomb triggered instabilities were preceded by some unexplained activity at a lower frequency. Higher mixture ratios as well as higher fuel injection velocities improved the stability margin. Practically every unstable test showed a coupling between combustion chamber pressure fluctuations and injector elements (LOx post and or fuel annulus). In relation, Priem [116] (presented at 25th JANNAF combustion meeting by Breisacher) and Breisacher [14] show a model that describes feed system coupling for both methane and oxygen. The most important conclusions are summarized here. Increasing LOx velocity increases stability in general. LOx-coupled oscillations can be counteracted by decreasing methane velocity, and to stabilize CH₄-coupled oscillations, its velocity should be increased. Varying the atomization distance can, depending on operating conditions, stabilize or destabilize combustion.

Philippart and Moser [112] analyzed three analytical tools predicting stability limits of two different engines. All three models are designed to make n - τ plots, based on the sensitive time lag model of Crocco [24]. The analytical predictions were compared to a hot fire test of each engine, and all came up with comparable results in good agreement with the experimental data. They concluded that the distribution of resonator cavities and combustion distribution were predominant factors in determining stability.

1.5.3 Recent developments

Even though the analytical models available do a fairly decent job in predicting stability limits, they do not incorporate actual physics of the individual processes taking place in the combustion chamber. Since these processes are individually significant, in for example controlling combustion distribution, in a way these types of time-lag models prohibit predicting stability before an engine is actually built and tested. In other, related, fields, predicting stability is not as difficult. In burners (furnaces) or gas-turbines, there generally is no liquid propellant, it may be non-premixed gas [76], [83], but many researchers, such as Candel [17], DeZilwa [164], Schuller [134], [135], [136], Ducruix [39], [40], Bernier [12], Zähringer [163] or Lee [87] very often occupy themselves with premixed and/or laminar combustion. For these types of combustion regularly transfer functions, basically describing the response of the flame to an acoustic perturbation, can be defined. This shows the necessity to understand the individual processes in more detail before for example a transfer function, that takes into account injection, atomization, vaporization and mixing, can be defined for acoustic perturbations in a rocket combustor.

During the 1990s much work has been done in Russia at for example the Moscow State Aviation Institute. Bazarov investigated the influence of injector dynamics on combustion (in)stability [6], [7], [8], [9] due to its self-pulsating and phase-shifting characteristics. He found that controlled modification of fuel injector dynamics can be used as a means of diagnostics by observing the effects on combustion chamber stability [6]. He concludes that the self-pulsating behavior of the injector must be avoided at all cost, even though this pulsating may increase atomization quality and mixture homogeneity [8].

In 1995 Yang and Anderson (Penn State University) were editors of a very extensive work [159] covering all possible aspects of combustion instabilities in liquid rocket engines, with contributions from leading researchers in the field, such as Culick [32] from CalTech (California Institute of Technology). It contains a comprehensive summary of the experience gathered in the previous 50 years and a chapter by Sirignano [139] from UCLA (University of California Los Angeles) who gives an excellent theoretical discussion on characteristic times of the individual processes in the combustion chamber.

Even though so much work has been done on liquid propellant rocket engine combustors, and many discoveries were made, it is still unknown what exactly triggers combustion instability. This is an important reason why recently the focus has shifted towards searching for instability mechanisms by actively imposing a forced acoustic oscillation. It is done in cold flow to study for example

atomization under oscillatory conditions. Or, more frequently, forced excitation is applied on combustion where the main target is to investigate instability, but even if instability is not triggered it allows investigating how oscillatory conditions affect for example vaporization or heat release.

Currently, the leading research institutes affiliated with high frequency combustion instabilities are DLR in Germany, CNRS in France, Anderson's group at Purdue University [2], [114], [140], Penn State University (PSU), United States Air Force and NASA in the United States, NAL in Japan, and of course a few others. Marshall et al. [92], [93] from PSU report the development of a rectangular chamber, and a test program carried out with LOx-CH₄ propellant combination targeting different means of inducing instabilities, including different possible injector element positions, see Figure 1.12. The experimental work is supposed to allow validation of the concurrent numerical efforts.

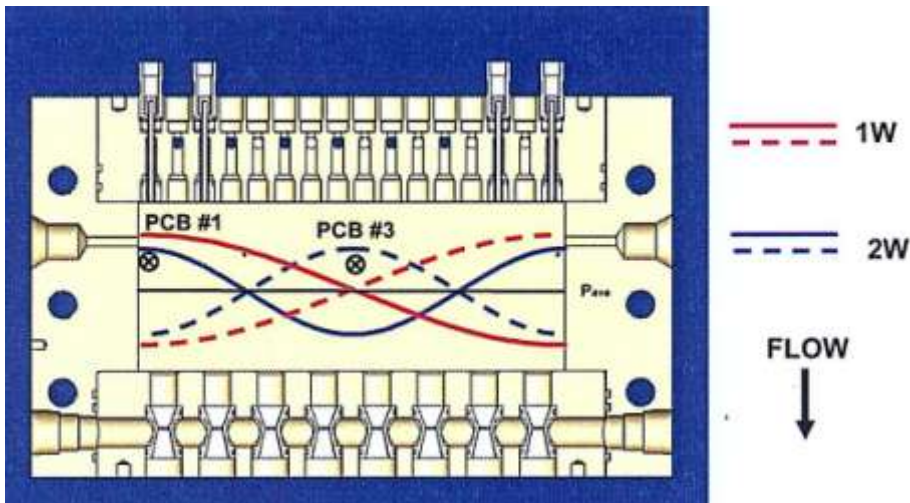


Figure 1.12: Rectangular combustor of PSU for instability research [93]

Tamura et al. [149], in a NAL-DLR cooperation, investigated, also with LOx-CH₄, stability characteristics and state that, even though the combustor is stable within the prospected test range, the induced tangential mode's amplitude increases for larger fuel to oxygen injection velocity ratios, which matches the findings of Wanhainen et al. in 1966 [156].

At ONERA, the MASCOTTE test facility is operated [57], [153]. Richecoeur et al. report on interaction between transverse acoustics and a LOx-CH₄ spray flame [126], [127]. The qualitative comparison in the first publication between numerical modeling and experiment show little discrepancies in their results for a reduced intact core length as well as improved mixing due to acoustic modulation. The second publication shows that combustion becomes sensitive to external modulation at low gas injection velocities which is in agreement with Wanhainen et al. [156]. Mery et al. [97] describe the development of VHAM, Very High Amplitude Modulator. It is a combustion chamber for LOx/CH₄ with two main nozzles that can be opened and closed periodically and in phase opposition, to modulate

100% of the mass flow. They want to generate extremely high amplitude oscillations in order to investigate the interaction between combustion and transverse acoustic modes. In a follow up report [96], Mery claims that the high acoustic amplitudes are reached and that with respect to the velocity fields the experiment shows good agreement with numerical simulation. Much of the numerical simulation work at ONERA is being done by Nicole [102], [103]. In 2009, Richecoeur et al. [125] reported on how temperature fluctuations, for example due to the inhomogeneity of the combustion zone, cause the eigenfrequency to fluctuate around a mean value. In a power spectral density analysis this fluctuation of the eigenfrequency would present itself as an increase in the line width, as if dissipation were enhanced.

Dissipation plays, obviously, an important role in damping instabilities or preventing them altogether. Oschwald et al. [107] in a DLR-CNRS cooperation quantify the significance of an acoustic absorber and the effects of its acoustic coupling to a combustion chamber on eigenfrequencies and mode symmetry under cold and hot flow conditions.

1.6 Objectives and structure

1.6.1 Objectives

In the past, much experience was collected on LOx/LH₂ combustion instabilities, but also on LOx/RP1 (Rocket Propellant 1, modified kerosene) in the US [104] and LOx/kerosene in Russia/Soviet Union, and hypergolic propellants in again Russia/Soviet Union as well as in Europe on multiple occasions with the Ariane 1-4 main engine Viking [58], [145], and the third stage of Ariane 4, the HM7B engine [113]. More recently much work has been done to resolve the anomaly encountered in Aestus, the second stage of Ariane 5 [5], [41], [86], [77], [117], [133], [147]. Due to the present developments in the space industry, methane has become an important candidate to replace the solid rocket boosters and other applications for several reasons. Therefore, LOx/CH₄ combustion must be free of uncontrolled, spontaneous combustion instabilities and to achieve this the problem must be at least somewhat understood for effective countermeasures to be designed. The research performed in this thesis targets to take the first few steps in developing a physical understanding of the interaction between acoustics and LOx/CH₄ combustion. The findings in this thesis will then function as some of the necessary building blocks to develop a theory describing high frequency combustion instabilities in general. It will do so by quantifying influences of acoustic oscillations on spray and flame phenomenology, and, on this basis, bringing more clarity in which coupling and driving mechanisms and which combustion chamber processes play dominating roles in sustaining acoustic instabilities. The relations between control parameters, operating conditions, and experimentally determined quantities should give the general direction in which follow-up research should go in order to solve the problem of self-sustained high frequency combustion instabilities on a fundamental level.

1.6.2 Structure

This section briefly discusses the structure of the thesis. A general background including some brief mathematical derivations is given in Chapter 2. All relevant topics to the problem of acoustic combustion instabilities will be discussed. The applied approach in this thesis is described in Chapter 3. It illustrates the experimental set-up used and discusses the designed test program. During the experimental phase, a large amount of measurements are taken. In order to learn anything from them, the data are processed and reduced to useful and presentable information. This process of data reduction as well as the related topic of measurement uncertainty and error propagation is discussed in Chapter 4. Chapter 5, 6 and 7 then respectively present the obtained results and correlations for dynamic pressure, spray and flame phenomenology, and a combined, more sophisticated, analysis of the combustion response to acoustic perturbations. In the last Chapter (8), the conclusions from the research carried out, and recommendations for follow-up research, are summarized.

In some chapters image sequences are applied to illustrate the temporal dependence of the results. When such an image sequence is shown or in other cases where it might be illustrative, a video is available on the enclosed CD (referenced in the text), which can more clearly demonstrate the dynamic behavior shown by the images.

2 Background

2.1 Theory

Under the assumption of isentropic flow (no dissipation losses due to viscosity) the equations for conservation of mass (continuity equation) and momentum are given in (2-1) and (2-2) respectively. These equations can be found in any academic gas dynamics or acoustics textbook, for example Zucrow and Hoffman [166].

$$\frac{\partial \rho}{\partial t} + \bar{\nabla} \cdot (\rho \bar{u}) = 0 \quad (2-1)$$

$$\rho \frac{D\bar{u}}{Dt} + \bar{\nabla} p = 0 \quad (2-2)$$

where

$$\frac{D}{Dt} = \frac{\partial}{\partial t} + \bar{u} \cdot \bar{\nabla}$$

To continue, a relation for the speed of sound a is necessary. Assuming small thermodynamic perturbations or quasi-equilibrium, any thermodynamic variable can be expressed as a function of any other two (independent) thermodynamic variables. Commonly used is pressure p as a function of entropy and density: $p = p(s, \rho)$. In differential notation, the relation expresses dp as a linear combination of ds and $d\rho$, and can be found, including the relevant thermodynamic coefficients, in any thermodynamics or acoustics textbook such as [128]. The resulting differential equation is given in (2-3)

$$d\rho = \frac{1}{a^2} dp - \frac{\rho\beta T}{c_p} ds \quad (2-3)$$

Specific heat at constant pressure c_p , coefficient of thermal expansion β and speed of sound a are given by

$$c_p = T \left(\frac{\partial s}{\partial T} \right)_p \quad (2-4)$$

$$\beta = \rho \left(\frac{\partial(1/\rho)}{\partial T} \right)_p \quad (2-5)$$

$$a = \left(\frac{\partial p}{\partial \rho} \right)_s \quad (2-6)$$

For an ideal gas, equations (2-4) to (2-6) reduce to (with the universal gas constant $R = 287 \frac{\text{J}}{\text{kgK}}$ and ratio of specific heats $\gamma = 1.4$)

$$c_p = \frac{\gamma R}{\gamma - 1} \quad (2-7)$$

$$\beta = \frac{1}{T} \quad (2-8)$$

$$a = \sqrt{\gamma R T} \quad (2-9)$$

In combination with the isentropic flow condition ($Ds/Dt = 0$), the entropy disappears and (2-3) reduces to the sought relation for the speed of sound, given in (2-10).

$$\frac{Dp}{Dt} - a^2 \frac{D\rho}{Dt} = 0 \quad (2-10)$$

In linear acoustics it is now assumed that the acoustic perturbations can be described as follows.

$$\rho = \rho_\infty + \rho' \quad (2-11)$$

$$p = p_\infty + p' \quad (2-12)$$

$$\vec{u} = \vec{u}_\infty + \vec{u}' \quad (2-13)$$

$$a = a_\infty + a' \quad (2-14)$$

Where $\vec{u}_\infty = 0$ and p' , ρ' and a' are perturbations much smaller than the corresponding free stream values, p_∞ , ρ_∞ and a_∞ . Combining equation (2-1) and (2-10) are yields

$$\frac{Dp}{Dt} + \rho a_\infty^2 \vec{\nabla} \cdot \vec{u} = 0 \quad (2-15)$$

Now substituting equations (2-11) – (2-14) for the linearized perturbations into equation (2-15), the following system of equations for the propagation of an acoustic perturbation is found.

$$\frac{\partial p'}{\partial t} + \rho_\infty a_\infty^2 \vec{\nabla} \cdot \vec{u} = 0 \quad (2-16)$$

$$\rho_\infty \frac{\partial \vec{u}'}{\partial t} + \vec{\nabla} p' = \vec{0} \quad (2-17)$$

Equation (2-17) can be broken down into 3 equations, one for each dimension of space. One may assume that the second derivatives of pressure and velocity are continuous, so one can differentiate (2-16) with respect to time, and (2-17) with respect to space. Combining and eliminating the partial derivatives of the velocity with respect to time and space yields the three-dimensional wave equation. For a shorter notation, the primes and ∞ as an indicator for a perturbation and free stream respectively are dropped, and the Laplacian is written as Δ .

$$\frac{\partial^2 p}{\partial t^2} - a^2 \Delta p = 0 \quad (2-18)$$

2.1.1 Three-dimensional wave equation

Since equation (2-18) is linear, any solution may be superimposed on another. Also, the three-dimensional wave equation is valid for any orthogonal (for example Cartesian, cylindrical or spherical) coordinate system. It can be written in the relevant coordinate system by expressing the Laplace operator Δ in the corresponding coordinates. Here, considering a combustor commonly has a circular cylindrical geometry, it is useful to write the wave equation in cylindrical coordinates.

$$\frac{\partial^2 p}{\partial t^2} - a^2 \left(\frac{\partial^2 p}{\partial r^2} + \frac{1}{r} \frac{\partial p}{\partial r} + \frac{1}{r^2} \frac{\partial^2 p}{\partial \theta^2} + \frac{\partial^2 p}{\partial z^2} \right) = 0 \quad (2-19)$$

Assuming the boundary conditions describe a cylinder with solid walls, equation (2-19) can be solved analytically by a standard procedure, the method of separation of variables. One assumes the solution, to be the product of four independent complex-valued functions of the relevant variables, r , θ , z , and t , given in equation (2-20).

$$p(r, \theta, z, t) = R(r)\Theta(\theta)Z(z)T(t) \quad (2-20)$$

A cylindrical combustor has simple boundary conditions for the three-dimensional wave equation.

- At every cylinder wall, the velocity of the gas in normal direction to the wall is equal to zero.
- The solution must be n -periodic in θ with a period 2π .

And, to represent a physical solution:

- The function must be finite for all values of r , θ , z and t .

Substituting (2-20) into (2-19), one finds a system of 4 ordinary differential equations. After applying the boundary conditions on the relevant individual equations, some of the constants will be eliminated. The differential equations (2-21) and the corresponding simplified solutions (2-22) for a cylindrical cavity are given in Table 2.1. An elaborate derivation of these equations and the complex-valued constants in (2-22) can be found in gas dynamics or acoustics texts like Zucrow and Hoffman [166].

Table 2.1: System of ordinary differential equations and corresponding solutions describing the propagation of a perturbation in a cylindrical cavity.

System of differential equations	Solutions to the system
$T'' + \lambda^2 a^2 T = 0$	$T(t) = \tilde{A}e^{i\omega t} + \tilde{B}e^{-i\omega t}$
$Z'' + \lambda^2 a^2 Z = 0$	$Z(z) = \tilde{C}e^{\left(\frac{i\xi z}{L}\right)} + \tilde{D}e^{\left(-\frac{i\xi z}{L}\right)}$
$\Theta'' + \lambda^2 a^2 \Theta = 0$	$\Theta(\theta) = \tilde{E}e^{i\nu\theta} + \tilde{F}e^{-i\nu\theta}$
$r^2 R'' + rR' + (\sigma^2 r^2 - \gamma^2)R = 0$	$R(r) = \tilde{G}J_n\left(\alpha_{nm}\frac{r}{R}\right)$
Relationship between constants	Relationship between constants
$\lambda^2 = \phi^2 + \sigma^2$	$\begin{aligned} \lambda &= \omega/a \\ \sigma &= \alpha/R \\ \phi &= \xi/L \end{aligned} \quad \frac{\omega^2}{a^2} = \frac{\alpha^2}{R^2} + \frac{\xi^2}{L^2}$

Substituting the solutions of (2-22) into the wave equation gives the general form of the solution of the wave equation. If one then considers that pressure is a physical property, and therefore must be a real quantity, one must now ignore the imaginary part of the solutions in (2-22). This yields the following real-valued relation for the acoustic pressure distribution in a cylindrical cavity.

$$p(r, \theta, z, t) = \sum_{l,m,n} \left[J_n \left(\alpha_{nm} \frac{r}{R} \right) \cos \left(l\pi \frac{z}{L} \right) \right]. \quad (2-23)$$

$$[A \cos(n\theta) \cos(\omega t) + B \cos(n\theta) \sin(\omega t) + C \sin(n\theta) \cos(\omega t) + D \sin(n\theta) \sin(\omega t)]$$

with

- J_n = Bessel function of the first kind, of order n
- α_{nm} = $(m+1)^{\text{th}}$ root of the derivative of J_n : $\partial J_n(\alpha_{nm})/\partial r = 0$
- l, m, n = Mode number ($l, m, n = 0, 1, 2, \dots$)
- r, θ, z = coordinates in cylindrical coordinate system
- ω = angular frequency
- t = time

The (eigen)mode numbers are a consequence of the boundary conditions and yield an infinite number of solutions, mode number l because of the periodicity of cosine and mode number n and m due to the characteristics of the derivative of the Bessel function, which has an infinite number of roots. The Bessel function is described in more detail in Appendix C. The actual values of the roots of the derivative of the Bessel function, α_{nm} , can easily be numerically determined and are given in the next section, in Table 2.2. Because the wave equation is linear, any combination of solutions is itself a solution, hence the summation over all acoustic eigenmodes in equation (2-23).

Equation (2-23) can also be written in a more convenient form by applying the trigonometric identities that can be found in any academic mathematics textbook, such as [1], and is given in (2-37).

$$p(r, \theta, z, t) = \sum_{l,m,n} \left[J_n \left(\alpha_{nm} \frac{r}{R} \right) \cos \left(l\pi \frac{z}{L} \right) \right]. \quad (2-24)$$

$$[M \cos(n\theta + \omega t - \delta_1) + N \cos(n\theta - \omega t - \delta_2)]$$

The solution consists of three parts

- The longitudinal (L-)mode's spatial distribution is given by $\cos(l\pi z/L)$.
- The radial (R-)mode's spatial distribution is described by the Bessel function and its dependence on r/R .
- The tangential (T-)mode is described by two propagating waves that move in opposite direction, with arbitrary constant amplitudes M and N .

The radial mode ($l, n = 0$) is made up by a constant amplitude, depending on r , and a fluctuation described by the two propagating waves that only depend on time. The tangential mode ($l = 0, n \neq 0$) has an additional dependence on the angular position θ . The constant phase angles δ_1 and δ_2 define the orientation of a particular mode at time $t = 0$, and can be chosen freely. They will be set to 0 in the further discussion. The mode numbers l, m, n denote the type of mode and its order. For the third tangential mode (3T), for example, $l = m = 0$ and $n = 3$, and for the second radial mode (2R), $l = n = 0$, and $m = 2$. The modes and their corresponding mode numbers are listed in Table 2.2.

2.2 Numerical simulation

The wave equation (2-18) is valid for any geometry, and was simplified for a circular cylinder in section 2.1.1. The experiment at the DLR institute (Common Research Chamber, CRC) was designed to allow externally exciting the combustion by means of a secondary nozzle in radial direction and a siren wheel, see section 3.1.3. Such a piece of hardware modifies the geometry of the CRC such that it destroys the symmetry and it cannot be considered a circular cylinder anymore. For arbitrary geometries, such as the CRC with secondary nozzle, the wave equation (2-18) can only be solved numerically. In order to find the pressure field, refuge is sought in numerical partial differential equations solvers, like FlexPDE [48] or MatLAB® [94]. To be solved by numerical solvers, equation (2-18) is converted to an eigenvalue problem. It is therefore assumed that the pressure harmonically depends on time:

$$p(r, \theta, z, t) = p_0(r, \theta, z) \sin(\omega t) \quad (2-25)$$

In (2-25), $p_0(x, y, z)$ is a function of spatial position and its distribution is different for every eigenmode. Developing the second derivative with respect to time of (2-25) yields

$$\frac{\partial^2 p}{\partial t^2} = -p_0(r, \theta, z) \omega^2 \sin(\omega t) \quad (2-26)$$

Inserting (2-25) and (2-26) in the wave equation (2-18) then gives

$$-p_0(r, \theta, z) \omega^2 \sin(\omega t) - a^2 \Delta [p_0(r, \theta, z) \sin(\omega t)] \quad (2-27)$$

The Laplace operator, Δ , is a function of space only, thus collecting variables and rewriting results in

$$\Delta p + \lambda p = 0 \quad (2-28)$$

Where λ is the squared ratio of angular frequency and speed of sound

$$\lambda = \frac{\omega^2}{a^2} \quad (2-29)$$

and represents the eigenvalues of the problem, with corresponding eigenmodes. The eigenfrequencies f can now be found by substituting the identity $\omega = 2\pi f$.

$$f = \sqrt{\lambda} \frac{a}{2\pi} \quad (2-30)$$

In the following, first the numerical results are compared with the analytical results for the CRC without cavities. After which the numerical approach is applied for the CRC with secondary nozzle.

2.2.1 CRC without cavity

The eigenmodes of the CRC without a cavity are analytically derived in section 2.1.1, note equation (2-24). The eigenfrequencies can be calculated through their definitions.

Longitudinal mode: $f_l = l \frac{a}{2L}$

Transversal mode: $f_{nm} = \frac{\alpha_{nm} a}{2\pi R}$

In case of a combined longitudinal and transversal mode, the frequency can be found through (2-31).

$$f_{lnm}^2 = f_l^2 + f_{nm}^2 \quad (2-31)$$

In Table 2.2, the calculated frequencies are given for a number of modes for air at ambient temperature, with the speed of sound $a = 340 \text{ m/s}$. It is obvious, that due to the combustion chamber design (length L much smaller than the radius R), also see section 3.1, the longitudinal modes are pushed to higher frequencies.

Table 2.2: Eigenmode characteristics - eigenfrequencies and mode numbers

Eigenmode	l	m	n	α_{nm}	f_{lnm}
1T	0	0	1	1.841	996
2T	0	0	2	3.054	1653
1R	0	1	0	3.832	2073
3T	0	0	3	4.201	2273
4T	0	0	4	5.318	2878
1R1T	0	1	1	5.331	2885
5T	0	0	5	6.416	3472
1R2T	0	1	2	6.706	3629
2R	0	2	0	7.016	3796
6T	0	0	6	7.501	4059
1L	1	0	0	-	4250
1R3T	0	1	3	8.014	4337
2R1T	0	2	1	8.536	4619

In Figure 2.1, the first 6 solutions to (2-28) are shown for the same conditions mentioned before (a larger number is discussed in Appendix D.1). In Figure 2.1, it can be seen that the first eigenvalue is double-valued. That means, that for that eigenvalue there exist 2 independent solutions. These solutions manifest themselves as two perpendicular orientations of the pressure field, but at the identical frequency. This happens to be the case for all tangential modes. The radial modes on the other hand are all single-valued.

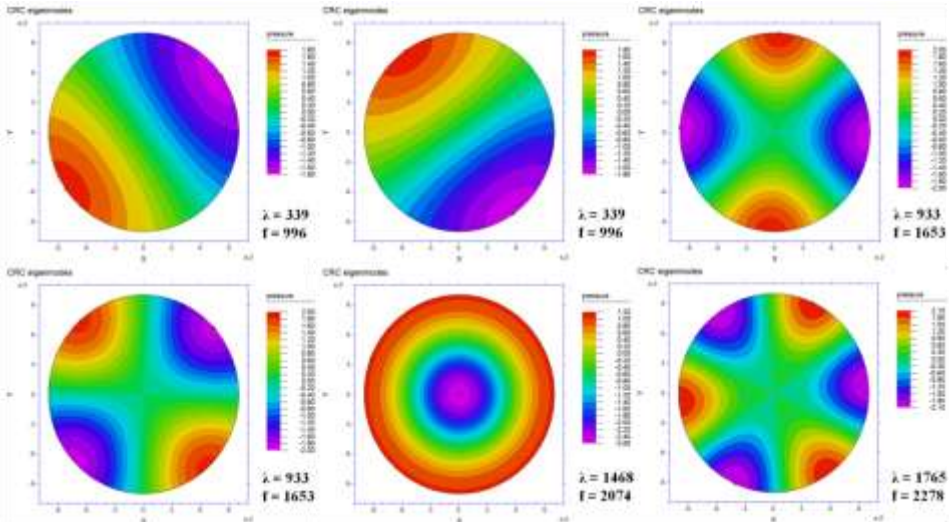


Figure 2.1: Numerical simulation for CRC without cavity, first 6 solutions

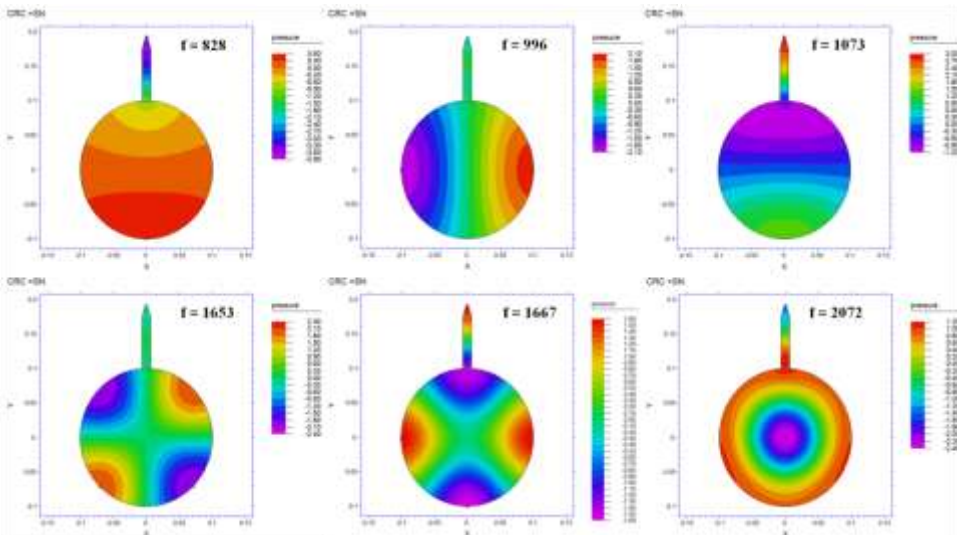


Figure 2.2: Numerical simulation for CRC with cavity, first 6 solutions

2.2.2 CRC with cavity

The numerical simulation proved to be accurate for the CRC without cavity. Therefore the same numerical tools will be applied with confidence for the CRC with cavity, where an analytical solution does not exist. In Figure 2.2, the first 6 solutions are given for again the same conditions, and for the current geometry of the CRC with cavity. The effect of a resonator is more elaborately discussed in Appendix D.2.

When now again the first two modes are investigated, the effect of the cavity becomes clear. The first eigenvalue is not double-valued anymore, but, instead, became two different eigenvalues. One is significantly lower than the original value, the other is virtually unchanged. In order to distinguish between the two solutions, a convention is introduced here. The first (lowered) solution is called $NT\sigma$, and the unchanged $NT\pi$. Where N denotes the number of the mode, so the third tangential mode will have the pair of solutions $3T\sigma$ and $3T\pi$. The $T\sigma$ mode will orient itself such that the nodal line is perpendicular to the axis of the cavity which is the symmetry line of the geometry. When mirrored in this symmetry line, the $T\sigma$ mode remains unchanged. The $T\pi$ mode will orient itself such that when mirrored in the symmetry line (secondary nozzle's axis), its sign changes. The angle over which the $T\pi$ mode is rotated with respect to the $T\sigma$ mode, depends on the mode number N , and is given by $N/90^\circ$.

2.3 Velocity associated with pressure wave

The previous sections discuss the pressure field and its development with time, because it is derived from the wave equation (2-18). Because at this stage it is still unclear which coupling mechanism is responsible for the interaction between acoustics and combustion, the equation describing the velocity field is briefly derived as well. Rewriting the linearized momentum equation (2-17) yields

$$\frac{\partial \bar{u}'}{\partial t} = -\frac{1}{\rho} \nabla p' \quad (2-32)$$

To find the velocity, this equation must be integrated over time. The geometry of the pressure field does not have a temporal component, only the amplitude of the fluctuation depends on time and is described by an harmonic function. So, the pressure is written as

$$p'(r, \theta, z, t) = p_0(r, \theta, z) \cos(\omega t) \quad (2-33)$$

Substituting and integrating over time then yields

$$\int \frac{\partial \vec{u}'}{\partial t} dt = -\frac{1}{\rho} \nabla p_0 \int \cos(\omega t) dt \quad (2-34)$$

$$\vec{u}'(r, \theta, z, t) = -\frac{1}{\rho} \nabla p_0 \frac{1}{\omega} \sin(\omega t) \quad (2-35)$$

The constant of integration in (2-35) vanishes because it was assumed that the time average of the fluctuating part of the velocity \vec{u}' is zero. If on the right hand side of (2-35) a constant would appear, this would then exactly be an offset from zero around which \vec{u}' fluctuates. Also, the density of the hot gas in the combustion chamber is assumed constant, which, of course, is only an approximation and the incurred error is assumed marginal. Nevertheless, it must be respected that in some cases it may cause non negligible error. But, as the density is only a scaling factor to the pressure gradient, the results based on the resulting velocity field and the respective conclusions, have to be taken with caution quantitatively. But it can be expected that they are qualitatively correct.

Note that the temporal dependence of \vec{u}' is 90 degrees phase shifted compared to p' (2-33). One can re-substitute (2-33) and apply the common notation j for the 90 degree phase shift. To further simplify the notation, the primes denoting fluctuation are dropped here as well.

$$\vec{u}(r, \theta, z, t) = -\frac{j}{\rho \omega} \nabla p(r, \theta, z, t) \quad (2-36)$$

So, the velocity field (2-36) is found by computing pressure gradient in the combustion chamber and changing its sign, dividing it by an average density and the circular frequency of the respective eigenmode and imposing a 90 degree phase shift. The velocity field for the 1T-mode in the CRC without secondary nozzle is illustrated in Figure 2.3.

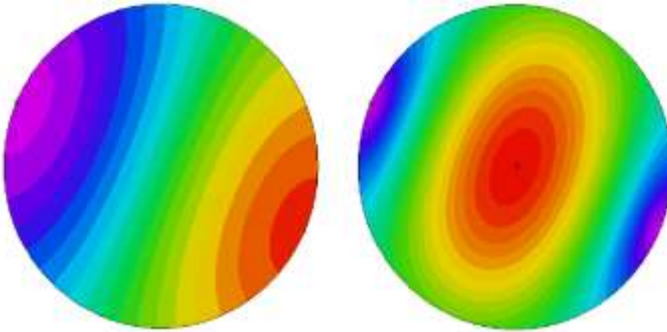


Figure 2.3: Pressure field (left) and corresponding velocity field (right) of the 1T-mode

2.4 Rotating wave

The analytical solution of the wave equation for the CRC without secondary nozzle, repeated in (2-37) for convenience, has some interesting characteristics which are elaborated in this section.

$$p(r, \theta, z, t) = \sum_{l,m,n} \left[J_n \left(\alpha_{nm} \frac{r}{R} \right) \cos \left(l\pi \frac{z}{L} \right) \right] \cdot [M \cos(n\theta + \omega t - \delta_1) + N \cos(n\theta - \omega t - \delta_2)] \quad (2-37)$$

In the current study, the focus lies on transversal modes and the first tangential mode (1T) in particular. Thus, setting m and l equal to 0, and n equal to 1 in (2-37), one finds for the acoustic pressure field of the first tangential mode in a cylindrical combustor.

$$p(r, \theta, t) = J_1 \left(\alpha_{10} \frac{r}{R} \right) [M \cos(n\theta + \omega t) + N \cos(n\theta - \omega t)] \quad (2-38)$$

2.4.1 Limit cases of the rotating wave

In order to clearly discuss rotating modes, it is necessary to make a distinction between propagating waves and standing waves, and point out the essential differences between them. If in (2-38), M and N are equal, the two propagating waves give, through superposition, and using the relevant trigonometric identity, a standing wave, see (2-39).

$$p(r, \theta, t) = 2J_1 \left(\alpha_{10} \frac{r}{R} \right) M \cos(\theta) \cos(\omega t) \quad (2-39)$$

This becomes clear when looking at (2-39) more closely. The entire term left from $\cos(\omega t)$ describes how the amplitude depends on both r and θ . The position dependent amplitude is multiplied by $\cos(\omega t)$ which denotes the time dependence. So, apparently the amplitude of the fluctuation at a certain position does not vary with time anymore, which shows that it is indeed a standing wave. Characteristically, the phase of any signal showing a standing wave only depends on the position relative to the nodal line and not on r or θ . So, for the CRC, the pressure signals will either be in phase or in anti phase, as is illustrated in Figure 2.4.

If in (2-38) either M or N is equal to 0, only one propagating wave remains. So, assuming $N = 0$, this results in a clockwise propagating wave and the acoustic pressure field is described by (2-40).

$$p(r, \theta, t) = J_1 \left(\alpha_{10} \frac{r}{R} \right) M \cos(\theta + \omega t) \quad (2-40)$$

A synthetic signal for the CRC is shown in Figure 2.5. The pressure field of (2-40) is rotating with angular frequency ω , hence the constant amplitude for all sensors. The phase between the signals is obviously exactly equal to the angle between the sensor positions.

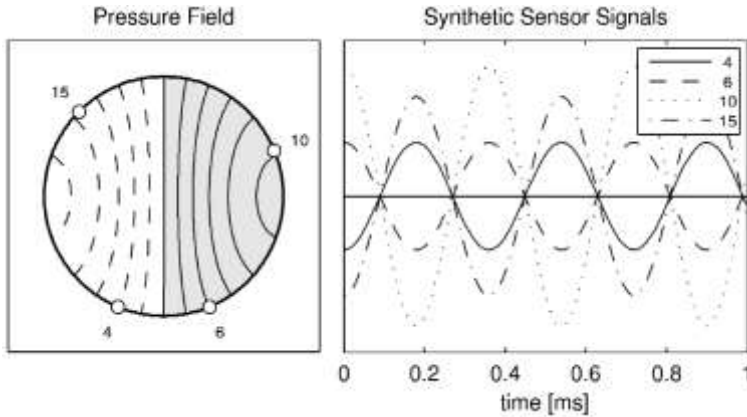


Figure 2.4: Acoustic pressure field of a standing wave

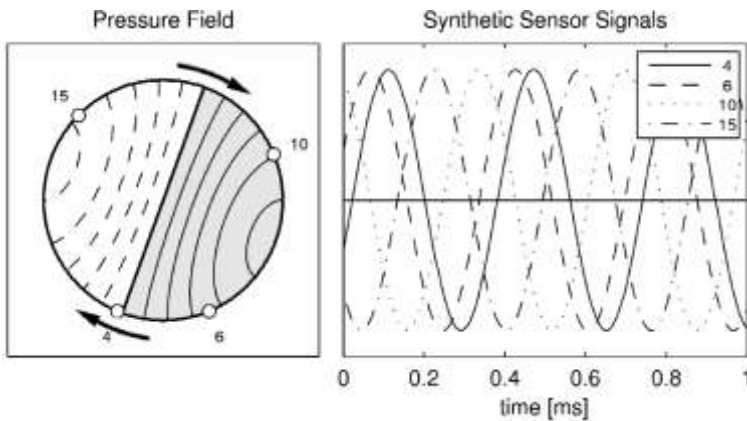


Figure 2.5: Acoustic pressure field of a rotating wave

2.4.2 Characteristics of the rotating wave

Generally, M and N are neither equal to each other, nor equal to 0. Thus, experimental signals will show both phase shifts not necessarily equal to the angle between the sensors and variable amplitude. These characteristics will now be shown analytically. A discussion of the experimental identification can be found in section 5.3.1. Since, experimentally, only the wall pressure can be measured, only the wall pressure distribution is of interest, so, in (2-38), $r = R$. Note that the pressure distribution at the wall also uniquely defines the acoustic pressure field in the entire volume. Again setting the phase angles δ_1 and δ_2 to zero without

losing generality, and only looking at the acoustic pressure distribution for the 1T mode ($l = m = 0$), (2-37) becomes

$$p(\theta, t) = J_1(\alpha_{10})[M \cos(\theta + \omega t) + N \cos(\theta - \omega t)] \quad (2-41)$$

An example of such a general distribution for arbitrary values of M and N is shown in Figure 2.6. This wave is a combination of a propagating wave (with constant angular velocity) and a standing wave, resulting in an acoustic field with non-constant angular velocity, constantly changing amplitudes and phase relations between signals.

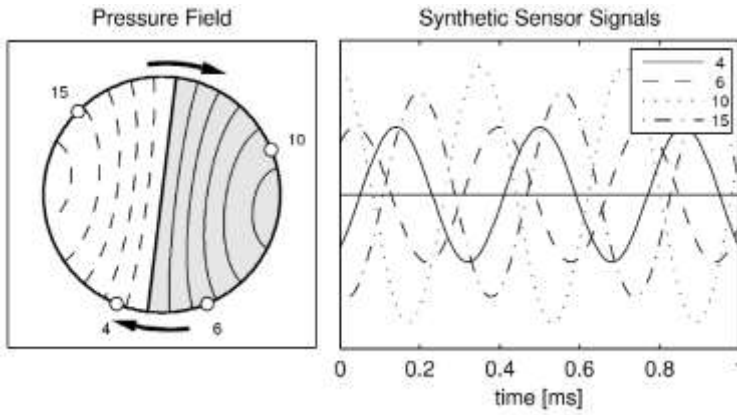


Figure 2.6: Acoustic pressure field of arbitrary wave

In (2-41) $J_1(\alpha_{10})$ is a constant which scales the amplitudes of the cosines. It can be analytically shown that the wall pressure distribution has the shape of a sine. So, it is assumed that the wall pressure distribution for the 1T mode is described by (2-42), which has exactly one period along the circumference, has amplitude A and phase φ , both of which are functions of time.

$$p(\theta, t) = A \sin(\theta - \varphi) \quad (2-42)$$

To find A and φ , (2-41) and (2-42) are set equal and solved. Using trigonometric identities for sums and equating the coefficients of the resulting system of equations, one finds for A

$$A = J_1(\alpha_{10})\sqrt{M^2 + N^2 + 2MN \cos(2\omega t)} \quad (2-43)$$

Equating (2-41) and (2-42) yields two possible solutions for the amplitude A at the wall, positive and negative. Both are equivalent solutions because the negative solution gives the identical sine function as the positive, with a phase shift of

half a period. Therefore the convention is here introduced that the amplitude is always positive. When a standing wave is considered a special case of a rotating wave (i.e. $M = N$) then this convention is consistent even for the standing wave. Knowing A , it allows a relation between the phase angle and M and N , as well as the angular frequency and time.

$$\varphi = -\arcsin\left(\frac{(M + N)\cos(\omega t)}{\sqrt{M^2 + N^2 + 2MN\cos(2\omega t)}}\right) \quad (2-44)$$

The phase angle defines the orientation of the acoustic pressure field in the combustion chamber. As such, it can also be interpreted as a rotation angle of the dynamic pressure field. This is illustrated in Figure 2.7, where φ is the distance from $\theta = 0$ to where the θ -axis is intersected by the sine function with positive tangent, which is also where the pressure fluctuation is zero. By definition, the angle is measured counterclockwise (CCW) from the positive x-axis. Therefore, φ can also be interpreted as the angle between x-axis and the nodal line of the acoustic pressure field, which is also illustrated in Figure 2.7.

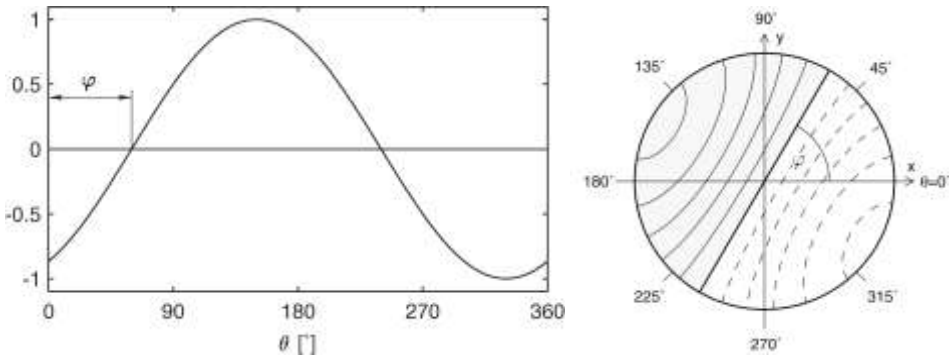


Figure 2.7: Phase angle definition (left) and interpretation of phase angle as rotation angle (right)

Since the angle of the pressure field as a function of time is known, it is possible to determine the angular velocity by taking the time derivative of (2-44).

$$\dot{\varphi} = \frac{\omega(M + N)(M - N)}{(M - N)^2 + 4MN\cos^2(\omega t)} \quad (2-45)$$

The actual values of M and N are irrelevant in the current analysis, so the behavior of the phase angle, and angular velocity is shown for different values for N/M rather than independent values for N and M . Arcsin is only defined for phase angles between $-\pi/2$ and $\pi/2$. This means time between $t = 0$ and $t = 1/2f$, with f the 1T-frequency, or a half period. In Figure 2.8 the temporal evolution of the phase angle during a half period is illustrated. A similar result was discussed by Harrje and Reardon [59] for propagating waves moving in opposite direction in a pipe.

For small values of N/M , which means $M \gg N$, the phase angle increases almost linearly, which in turn means that the angular velocity is almost constant. If N/M approaches 1, which means M is almost equal to N (standing wave) the angle does not change much at all until t approaches $1/4f$. Here the angle increases very rapidly until its rate of growth decreases again to almost zero after the transition. This consequently means the angular velocity is very small at first, becomes very high around $t = 1/4f$, after which the velocity decreases again.

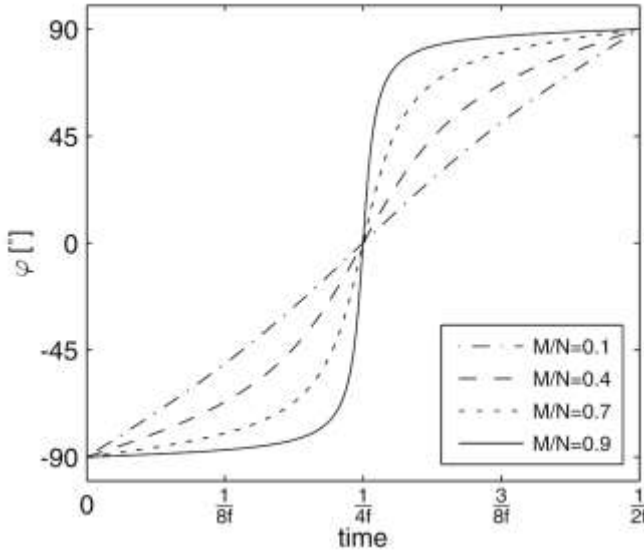


Figure 2.8: Evolution of the phase angle during a half period

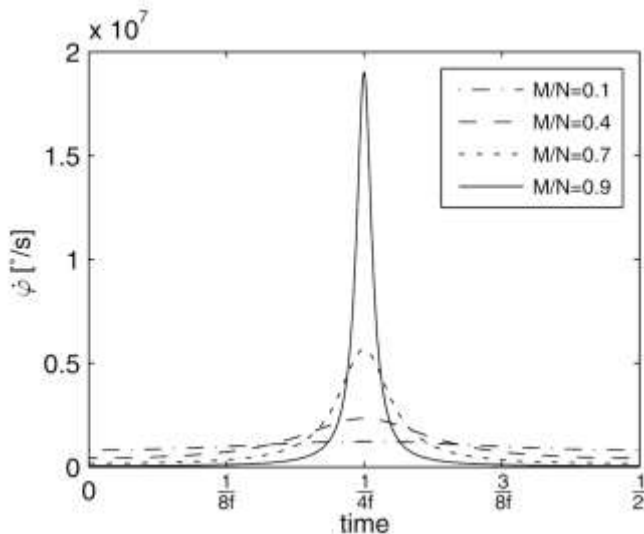


Figure 2.9: Evolution of the angular velocity during a half period

In Figure 2.9 the angular velocity from (2-45) is plotted against time. As could be derived from Figure 2.8, the angular velocity is almost constant when N/M approaches 0. When N/M approaches 1, the angular velocity is lower than for $N/M = 0$ around $t = 0$, but approaches infinity at $t = 1/4f$. Of course, when integrating these curves, they will all yield the same result, since they all have the same angular frequency.

From (2-45) it is also possible to express the maximum and minimum angular velocity during one period as a function of M and N . Obviously, the maximum velocity occurs when $\cos^2(\omega t) = 0$, whereas the minimum velocity occurs when $\cos^2(\omega t) = 1$. Substituting into (2-45) yields for the extreme velocities

$$|\dot{\phi}_{max}| = \omega \left| \frac{(M+N)}{(M-N)} \right| \quad \text{and} \quad |\dot{\phi}_{min}| = \omega \left| \frac{(M-N)}{(M+N)} \right|$$

Note that if N or M equals 0, $|\dot{\phi}_{max}| = |\dot{\phi}_{min}| = \omega$. This means that the angular velocity is constant throughout a complete rotation, a pure propagating wave. If $N = M$, $|\dot{\phi}_{max}| = \infty$ and $|\dot{\phi}_{min}| = 0$. Looking at the relation for the angle (2-44) and taking the relevant trigonometric identities into account one finds for the angle at $N = M$.

$$\varphi = -\frac{\pi}{2} \text{sgn}[\cos(\omega t)] \quad (2-46)$$

This implies that the angle of the acoustic pressure field of the standing wave ($N = M$) instantaneously jumps from 0 to $\pi/2$ when cosine changes its sign, at $t = 1/4f$, and does so with infinite velocity. During any other time, the angle is constant and the angular velocity equal to 0. This proves that the standing wave can be interpreted as a limit case of the general rotating wave.

2.5 Interaction between acoustics and combustion

Combustion instabilities in rocket engine combustion chambers occur when an exchange of energy takes place between the combustion processes and the acoustic field. This interaction will always result in combustion instability when this interaction amplifies itself. During such a so-called self-sustained combustion instability, the acoustic field is enhancing the heat release of combustion, which in turn yields an enhanced energy transfer into the acoustic field, causing the amplitude of the modulated fluctuation to increase exponentially. The system becomes unstable. If the exponential behavior is tempered by sufficiently high energy dissipation (a non-linear process), the increase will evolve towards a limit cycle [30], [160] wherein the losses equal the amplification.

2.5.1 Rayleigh Criterion

The feed-back loop just described is illustrated in Figure 2.10, which also includes many combustion chamber processes that could be responsible for coupling.

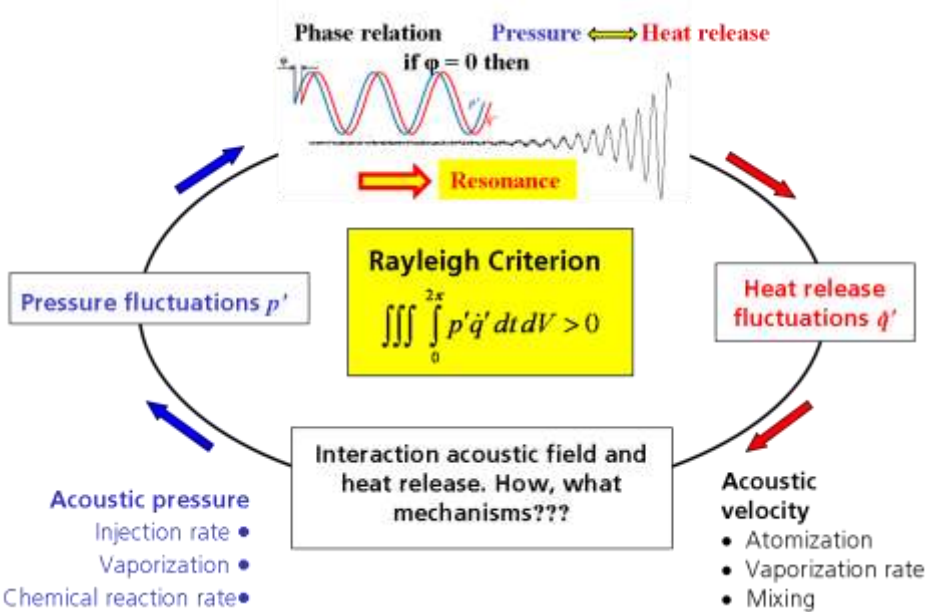


Figure 2.10: Feed-back loop between combustion and acoustic field

The principle of the interaction between heat release (here: combustion) and acoustic field was first formulated by Sir Lord Rayleigh [119], [120]. He postulated:

“If heat be periodically communicated to, and abstracted from, a mass of air vibrating (for example) in a cylinder bounded by a piston, the effect produced will depend upon the phase of the vibration at which the transfer of heat takes place. If heat be given to the air at the moment of greatest condensation, or be taken from it at the moment of greatest rarefaction, the vibration is encouraged. On the other hand, if heat be given at the moment of greatest rarefaction, or abstracted at the moment of greatest condensation, the vibration is discouraged.”

Therefore, to excite an acoustic instability, heat must be added to a gas at the moment of greatest compression, and subtracted at the moment of deepest depression. This was later captured in mathematical form, equation (2-47), which became known as the Rayleigh criterion.

$$\iiint_V \int_T p' \dot{q}' dt dV > 0 \quad (2-47)$$

In this formulation p' and \dot{q}' denote the oscillations of pressure and rate of heat release respectively. The product of p' and \dot{q}' are integrated over one period of acoustic oscillation and when this yields a value larger than zero, a self-sustained instability can occur. For harmonic oscillations this integral can only be larger than zero if, and only if, the absolute value of the phase difference between the oscillations of pressure and heat release is less than 90 degrees. This condition must be true regardless whether the coupling mechanism is pressure or velocity driven. The criterion only states that heat release must be in phase with the acoustic pressure. In a combustion chamber, the combustion processes are the source of the energy added to the acoustic field. When the mentioned phase relation is respected, the acoustic oscillations are amplified by combustion. If not, the oscillations are damped.

The criterion is not sufficient because it neglects any other causes for damping, such as all 'natural' causes for energy loss, such as turbulence, sound damping/absorption, radiation, friction, etc. This means that not only must the phase relation be respected, it is also necessary to transfer more energy into the acoustic system than is dissipated by natural causes, to sustain a heat driven instability.

A more in-depth discussion regarding the Rayleigh criterion can be found in Putnam [118]. A very thorough discussion and an analytical derivation of a more generalized form of the Rayleigh criterion are given by Culick [32]. Cheuret [18], as well, provides a decent theoretical derivation. Due to its relevance, a short summary of the derivation that can be found in [18] is given here.

In his derivation of the wave equation, Cheuret takes into account the equation of state, and the energy equation with a source term including conservation of species. Carrying out the derivation, this will yield the wave equation with a source term by heat release, given in (2-48), which basically describes the interaction between heat release and pressure fluctuation.

$$\frac{\partial^2 p'}{\partial t^2} - a_\infty^2 \Delta p' = (\gamma - 1) \frac{\partial^2 \dot{q}'}{\partial t^2} \quad (2-48)$$

In (2-48) the primes denote a fluctuation. Combining (2-48) with the linearized momentum equation (2-17) and performing a few algebraic operations and transforming to an integral equation, one finds equation (2-49).

$$\int_V E_{\tau_a} dV + \int_A \vec{F} \cdot \vec{n} dS = \int_V \int_T p' \dot{q}' dt dV \quad (2-49)$$

Where the first term on the left denotes the acoustic energy over one period of fluctuation per unit volume, and the second term is the average energy flux during one period of oscillation. One can recognize on the right hand side the same integral as in the Reynolds criterion. If the average energy flux is zero, then (2-49) yields the Reynolds criterion (2-47).

In a rocket engine combustion chamber, heat release takes place during the chemical reaction between an oxidizer and a fuel, here between liquid oxygen (LOx) and gaseous methane (CH₄). This chemical reaction is the last step in a

series of processes that simultaneously take place in a combustor. All processes (injection, atomization, evaporation, mixing and chemical reaction) are in some particular way influenced by an acoustic excitation. An acoustic wave is defined by two physical parameters, pressure and velocity. Any of the stated processes can therefore be affected by either of these quantities. The influence of pressure fluctuations tends to be stronger on injection rate, evaporation rate and reaction rate, whereas atomization, evaporation and mixing are more influenced by velocity. It is an open question whether pressure coupling or velocity coupling is the dominant mechanism influencing heat release or initiating combustion instabilities. It is a difficult question because the many processes influencing heat release cannot be investigated individually in realistic operating conditions.

2.5.2 Crocco's (n- τ)-model

In the 1950s, when combustion instabilities were first encountered in liquid rocket engines, Crocco [24], [25], [26] in great detail developed a model for this mechanism based on a time lag, the (n- τ)-model. Essentially, this model assumes that there exists a finite time between the propellants entering the combustion chamber, and the reaction to release their chemical energy. Since combustion of a droplet does not always take place at the same location, but can occur throughout the entire combustion chamber, in reality the lag is not constant. In [18] a straightforward derivation, based on this (n- τ)-model, is given for the rate of growth of a fluctuation, depending on the coupling mechanism. Culick [32] argues that because no physical processes are considered in the formulation of the (n- τ)-model, even though it was successfully used in correlating data from extensive test programs in the 1960s, as for example shown in [59], the sensitive time lag concept must be used with caution. The time lag model is quickly losing relevance as time passes, especially in the last few years due to the strong increase in computing power for sophisticated simulations or technological advancements that for example allow optical access into combustors. With these new developments available, it is now possible to directly analyze whether there is a coupling through pressure or velocity, or even both, by correlating pressure signals and flame intensity (assumed to be proportional to heat release), see Chapter 7.

2.5.3 Response factor

The Rayleigh criterion is not the only factor playing a role in quantifying how strongly an acoustic oscillation is amplified by the fluctuating heat release. The amount of damping is an important factor as well. Damping depends not only on geometry, but also on the type of propellants and any other characteristics that cause turbulence or control when and where energy is released. Different geometry causes different turbulence characteristics and it therefore plays an important role in where and how much energy is dissipated. The type of propellants determines how fast the individual combustion chamber processes take place, which in turn controls where heat is predominantly released and therefore has a decisive role in whether coupling can occur or not. In order to include the effects of damping, and create a number to compare different cases of combustion instabilities, the Rayleigh criterion is normalized by what can be seen as the vo-

lume integral of the energy of the pressure oscillation during one acoustic period. This so-called Response Factor was first defined by Heidmann and Wieber [66] under the assumption that heat release fluctuations were related to the pressure fluctuations. They initially defined it as the amplitude ratio of vaporization rate and acoustic pressure oscillation taking into account the phase relation between the two quantities [67]. Later, the response factor was presented in the more general form based on the Rayleigh criterion [66], and is given in equation (2-50).

$$N = \frac{\int_V \int_T p'(V, t) \dot{q}'(V, t) dt dV}{\int_V \int_T [p'(V, t)]^2 dt dV} \quad (2-50)$$

In this equation, the primes denote the normalized dynamic pressure and dynamic heat release as defined in (2-51), where the barred quantities denote an average (the chamber pressure is used as the average pressure).

$$p' = \frac{p - \bar{p}}{\bar{p}}, \quad \dot{q}' = \frac{\dot{q} - \bar{\dot{q}}}{\bar{\dot{q}}} \quad (2-51)$$

Assuming that the pressure and heat release fluctuations harmonically depend on time, they can be described by (2-52) and (2-53), where ϕ is the phase shift between heat release and pressure fluctuations.

$$p'(t) = p'_{max} \sin(\omega t) \quad (2-52)$$

$$\dot{q}'(t) = \dot{q}'_{max} \sin(\omega t + \phi) \quad (2-53)$$

Substituting (2-52) and (2-53) into the relation for the response factor (2-50), and applying trigonometric identities, yields

$$N = \frac{\dot{q}'_{max}}{p'_{max}} \cos \phi \quad (2-54)$$

To find the response factor, knowledge about the heat release is necessary. When looking at a kinetic system of reactions for combusting LOx and CH₄, for example by Hughes [69] (see Appendix A), one finds several reactions producing OH-radicals. These are among the most reactive combustion products available due to a free electron. Freshly formed OH is in an energetically elevated state (OH*), having a very short lifetime. The OH* returns to the electronic ground state by emitting light at a specific wavelength (around 308 nm). This wavelength is too far into the ultra violet part of the spectrum for the human eye to observe, but with a UV-filter mounted on a high speed camera (Photron Ultima APX I², [109]), it is possible to detect this spontaneous chemiluminescence of the OH-radicals. It can be detected where at least part of the chemical reaction takes place, hence, where the propellants release their chemical energy in the form of heat. It is as-

sumed that the intensity of the emitted light is a measure for how much energy is released. So, instead of the heat release directly, the intensity of the chemiluminescence is analyzed. The intensity signal is a fluctuation around a mean, but analogue to equation (2-53) only the fluctuation is of interest. So, after normalizing the intensity fluctuation with the mean intensity one finds

$$I'(t) = I'_{max} \sin(\omega t + \phi) \quad (2-55)$$

Where $I' = \frac{I - \bar{I}}{\bar{I}}$

Taking I' as a measure for the heat release \dot{q}' , the response factor becomes

$$N_p = \frac{I'_{max}}{p'_{max}} \cos \phi_p \quad (2-56)$$

In (2-56) the subscript p was introduced to denote that this response factor is calculated under the assumption of a pressure driven coupling mechanism. The phase was given the subscript p as well to clarify that it denotes the phase between heat release and acoustic pressure, see also [143]. An analogous derivation can be done for a velocity related response factor. The velocity fluctuations are defined as the velocity perturbation (mean flow velocity is equal to zero), associated with the pressure gradient (2-36), normalized with the average speed of sound.

$$v' = \frac{|\bar{u}|}{a} \quad (2-57)$$

The velocity related response factor [142], [143] is given in (2-58), where the subscript v denotes that the response factor is velocity related.

$$N_v = \frac{I'_{max}}{v'_{max}} \cos \phi_p \quad (2-58)$$

The velocity related response factor has added value with respect to the pressure related response factor because the spatial structure of the velocity field is significantly different compared to that of the pressure field. With (2-56) the pressure related response factor can be determined by simultaneously measuring the fluctuations of pressure and intensity. At the same time, with (2-58), the velocity related response factor can be determined by deriving the velocity fluctuations from the pressure measurements.

Intuitively one would claim that when the pressure response factor is high while the velocity response factor is low, the coupling mechanism is pressure driven and when the velocity response factor is high while the pressure response factor is low, the coupling mechanism is velocity driven. The experimental results in Chapter 7 will show that matters are not as simple and straightforward as that.

2.6 Damping

As was mentioned before, the coupling mechanism must transfer more energy into the acoustic field as is lost through natural damping for the Rayleigh criterion to hold, and, hence, make a combustion instability possible. In that respect, quantifying of the combustion chamber's damping characteristics in relation to for example operating and/or injector conditions might yield important results. To do so, a damped harmonic oscillator is considered and the reasonable assumption is made that the natural dissipation of energy is linear. The equation of motion for the acoustic pressure can be found in any acoustics or vibration textbook such as [128] and is given in (2-59)

$$\frac{d^2 p}{dt^2} - \frac{2}{\tau} \frac{dp}{dt} + \omega_n^2 \Delta p = 0 \quad (2-59)$$

In this equation τ denotes the characteristic time of natural decay and ω_n is the resonance (natural) frequency of the undamped system. The solution to this equation, the chamber's response to an impulse is given by (2-60).

$$p(t) = p_0 \Gamma (e^{i\omega_0 t} + e^{-i\omega_0 t}) \text{ for } t > 0 \quad (2-60)$$

$$\Gamma = \frac{1}{\tau}$$

$$\omega_0^2 = \omega_n^2 - \Gamma^2$$

Now, under the assumption that the time derivative of the pressure is zero (fast transients have already decayed, hence $dp/dt \approx 0$) and a constant of integration is equal to $p_0 \Gamma$, the Fourier transform of the impulse response yields the following response in the frequency spectrum.

$$R(\omega) = \int_{-\infty}^{\infty} p(t) e^{i\omega_0 t} dt \quad (2-61)$$

$$R(\omega) = p_0 \left[\frac{\Gamma}{\Gamma + i(\omega - \omega_0)} + \frac{\Gamma}{\Gamma + i(\omega + \omega_0)} \right] \quad (2-62)$$

The spectral power is given by

$$S(\omega) = R(\omega) \cdot R^*(\omega) \quad (2-63)$$

with R^* the complex conjugate of R .

If $\Gamma \ll \omega_0$ (the decay time is much larger than one acoustic period at resonance frequency), then S simplifies to

$$S(\omega) = p_0^2 \left[\frac{\Gamma^2}{\Gamma^2 + (\omega - \omega_0)^2} + \frac{\Gamma^2}{\Gamma^2 + (\omega + \omega_0)^2} \right] \quad (2-64)$$

The two terms in brackets are two Lorentzian curves. Because negative frequencies are physically impossible, for ω near ω_0 , the first term will be the largest contribution, so S reduces to

$$S(\omega) = p_0^2 \left[\frac{\Gamma^2}{\Gamma^2 + (\omega - \omega_0)^2} \right] \quad (2-65)$$

The width of a Lorentzian curve at half its maximum is by definition equal to $2\Gamma \equiv 2/\tau$. The acoustic energy density of the oscillation in dependence on time is proportional to the acoustic pressure squared

$$E(t) \propto p_0^2 e^{-2\Gamma t} \quad (2-66)$$

The energy density rate of change is then given by

$$\frac{1}{E} \frac{dE}{dt} = 2\Gamma \equiv \sigma \quad (2-67)$$

Figure 2.11 and Figure 2.12 illustrate how a damped acoustic oscillation is related to a Lorentz profile.

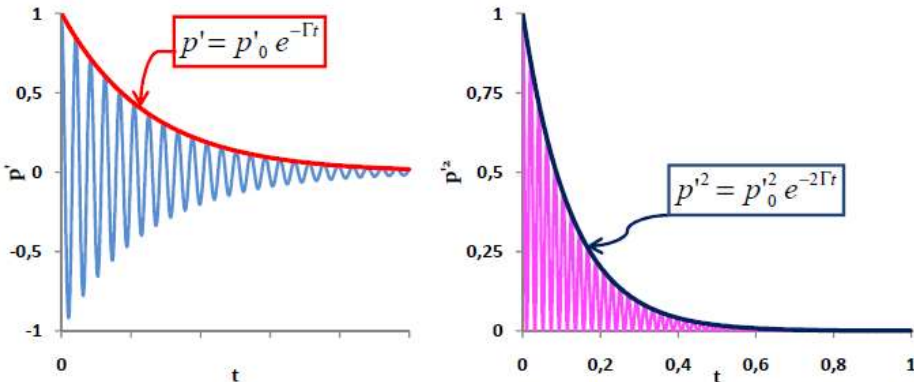


Figure 2.11: Temporal development damped acoustic oscillation (left: pressure, right: energy)

This derivation shows the importance of determining the energy of an acoustic oscillation, rather than its amplitude, to learn about the damping. In Figure 2.13 several normalized Lorentz profiles are shown (where x is used for the frequency).

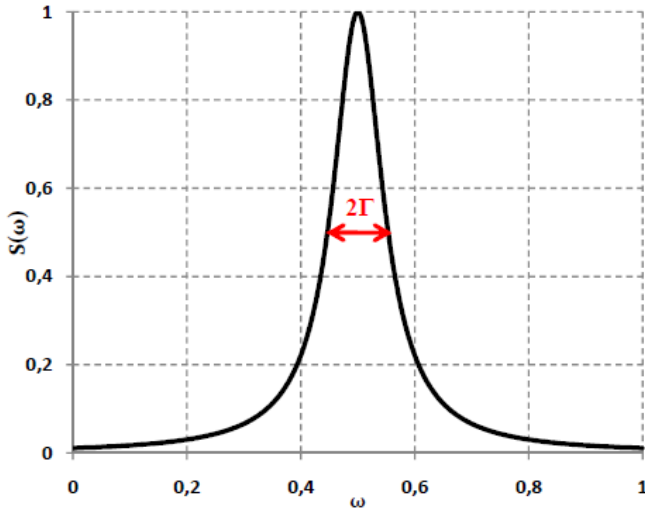


Figure 2.12: Lorentzian line profile

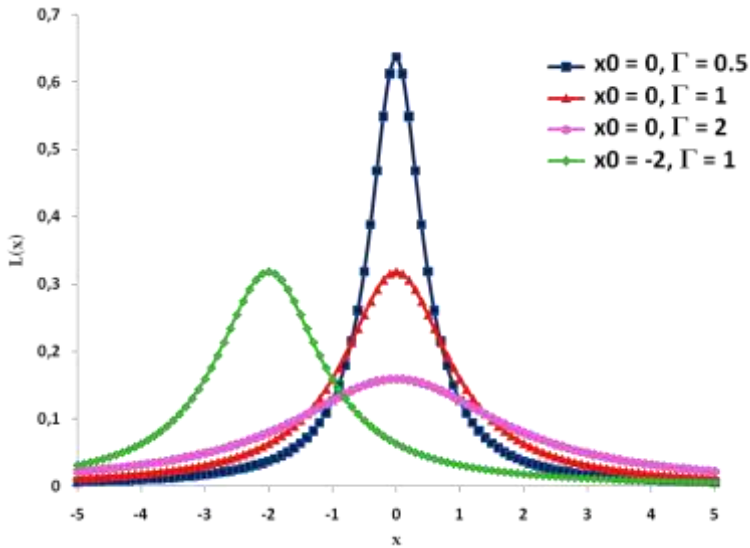


Figure 2.13: Normalized Lorentz profile

They are normalized such that their integral, or the area A underneath the curve, is equal to $A = \pi H \Gamma \equiv 1$. H is the height of the curve. The normalized Lorentz profile is described by (f_0 is the center frequency)

$$L(f) = \frac{1}{\pi} \frac{\Gamma}{(f - f_0)^2 + \Gamma^2} \quad (2-68)$$

If (2-68) is multiplied by $\frac{\pi H \Gamma}{A} \equiv 1$, the relation describing a Lorentz profile becomes

$$L(f) = \frac{H}{A} \frac{\Gamma^2}{(f - f_0)^2 + \Gamma^2} \quad (2-69)$$

In (2-69) one recognizes the same form for a Lorentzian curve as in (2-65), and where in (2-65) the square of the acoustic pressure, p_0 , shows up, there is the scaling factor H/A in (2-69). The energy of the oscillation (p_0^2) can easily be calculated from the pressure measurements. Even though the pressure signal is discrete, it allows for a relatively straightforward fitting procedure (see section 4.1.2) to find the Lorentz profile. Knowing the characteristics of the Lorentz profile, one knows the full width at half maximum (FWHM), hence the damping.

2.7 Cold flow acoustics in the CRC

2.7.1 Frequency spectrum

At the DLR-institute multiple series of cold acoustics tests in ambient conditions have been executed and reported by Farago [44]. The results are also used for calibration and verification whether the numerical eigenvalue calculations are accurate. In Figure 2.14, the frequency spectrum of the CRC during a cold acoustics test is shown. The calculated eigenfrequencies of the CRC were presented in Table 2.2, and are briefly summarized in Table 2.3. Comparing the calculated (Table 2.3) and measured (Figure 2.14) frequencies, one must conclude the agreement is excellent.

Table 2.3: Summary eigenfrequencies of the CRC under 'cold' conditions

Eigenmode	α_{nm}	f_{lnm}
1T	1.841	996
2T	3.054	1653
1R	3.832	2074
3T	4.201	2278
1L	-	4250

2.7.2 Effect of the resonator

Adding a resonator, or cavity, to the CRC destroys the cylindrical symmetry. Farago [44] reports that, if properly tuned, the secondary nozzle functions as a quarter wave resonator or an effective damping device for the respective eigenmode to which it is tuned. But without tuning the resonator still causes the double valued eigenmodes to be split up in two independent modes. One with lower frequency (how much lower depends on resonator geometry and is discussed in more detail in Appendix D.2) than the original mode, and the second with a frequency that is virtually unchanged.

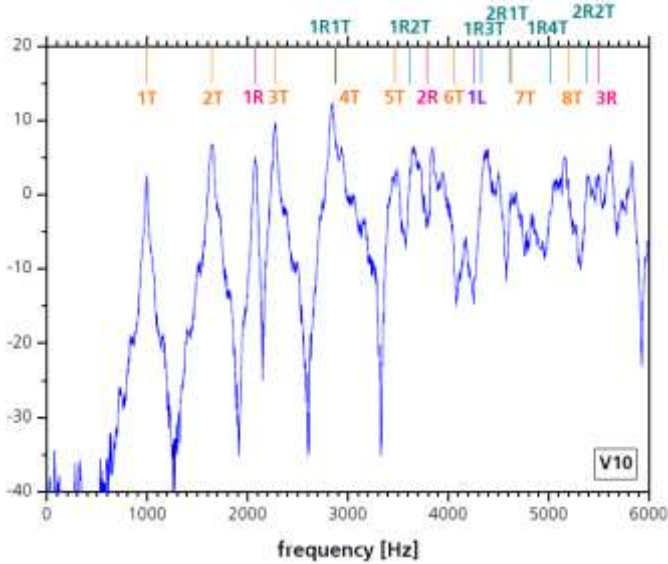


Figure 2.14: Frequency spectrum of the CRC under 'cold' conditions [44]

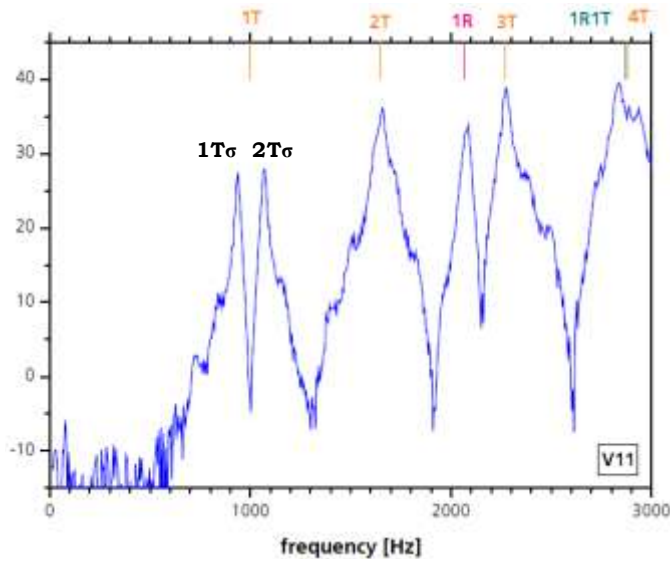


Figure 2.15: Frequency spectrum of the CRC with resonator under 'cold' conditions [44]

When examining the frequency spectrum of the CRC with a resonator tuned to the first tangential mode (Figure 2.15), surely two peaks show up, one at lower and one at slightly higher frequency than the eigenmode of the CRC without cavity (compare Figure 2.14). This is because also the second tangential mode was a double valued eigenmode, which, due to the resonator, is also split up in two independent modes. This frequency of the $2T\sigma$ mode is so much lower that it

approaches the unchanged $1T\pi$ mode. The $1T\pi$ mode itself cannot be seen in the spectrum because in the cold experiment, the loudspeaker was mounted 180 degrees relative to the cavity, placing it in an anti-node, unable to excite the $1T\pi$ mode.

2.7.3 Ramp excitation

To excite combustion, a siren wheel is applied to modulate the flame by opening and closing the secondary nozzle at a set frequency (see section 3.1.3). A similar configuration was used to quantify the effect of the ramp steepness of the excitation in cold flow conditions. In cold flow tests with either nitrogen or helium, the pressurized CRC with secondary nozzle was excited with a linearly increasing frequency [82]. A steep ramp implies a shorter excitation time at a specific frequency, hence less energy input per frequency interval. The duration of excitation T_{ex} is calculated as the division of an assumed line width of the $1T$ -mode, Γ_{1T} , of 100 Hz, and siren wheel's acceleration a_{SW} (ramp speed).

$$T_{ex} = \frac{\Gamma_{1T}}{a_{SW}} = \frac{100}{a_{SW}} \quad (2-70)$$

A ramp speed of 200 Hz/s for example yields an excitation duration of 500 ms. The amplitude of the pressure fluctuation caused by the excitation is plotted against the ramp speed in Figure 2.16. It shows that when a frequency interval experiences longer duration excitation (shallow ramp), it yields higher amplitude pressure fluctuations.

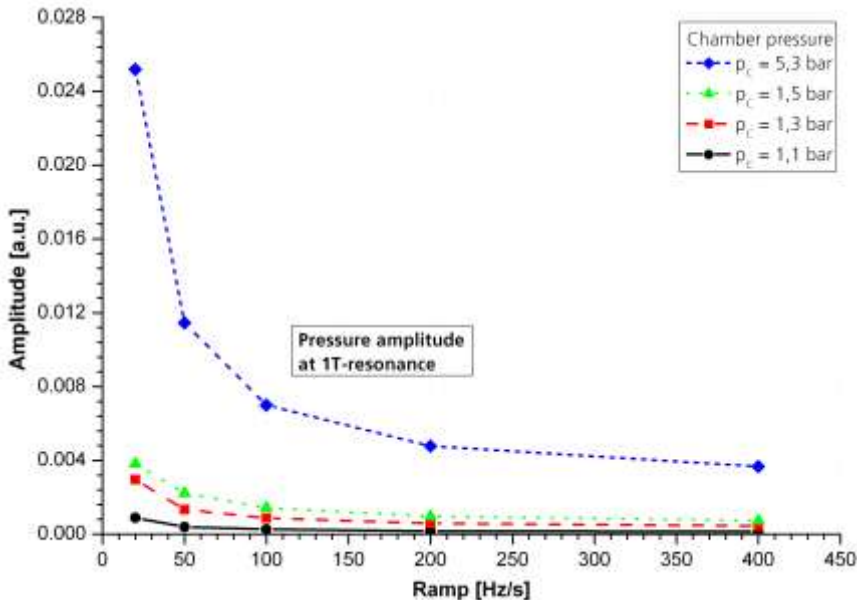


Figure 2.16: Effect of excitation ramp on pressure fluctuation amplitude [82]

2.8 Operating parameters

There is a large number of parameters that play a role in liquid propellant rocket engine research. This section briefly introduces the most important parameters describing the operating conditions and the context in which they are generally used.

2.8.1 Control parameters

To define operating points in the test program (see section 3.3), three control parameters, chamber pressure, mass flow rate and mixture ratio, are used.

The chamber pressure, p_{CRC} , is directly measured in the combustion chamber and compared to the predicted pressure to verify whether the operating pressure was met. The pressure is uniquely defined when the mass flow rate (\dot{m} in grams per second) of both propellants and the nozzle throat area is known, and the theoretical value can be compared with the measurement. The mass flow rate is also directly measured in the test facility and is used to calculate the theoretical (predicted) chamber pressure. When both mass flow rates for fuel and oxidizer are known, the exact mixture ratio can be calculated which is defined as

$$R_{OF} = \frac{\dot{m}_o}{\dot{m}_f} \quad (2-71)$$

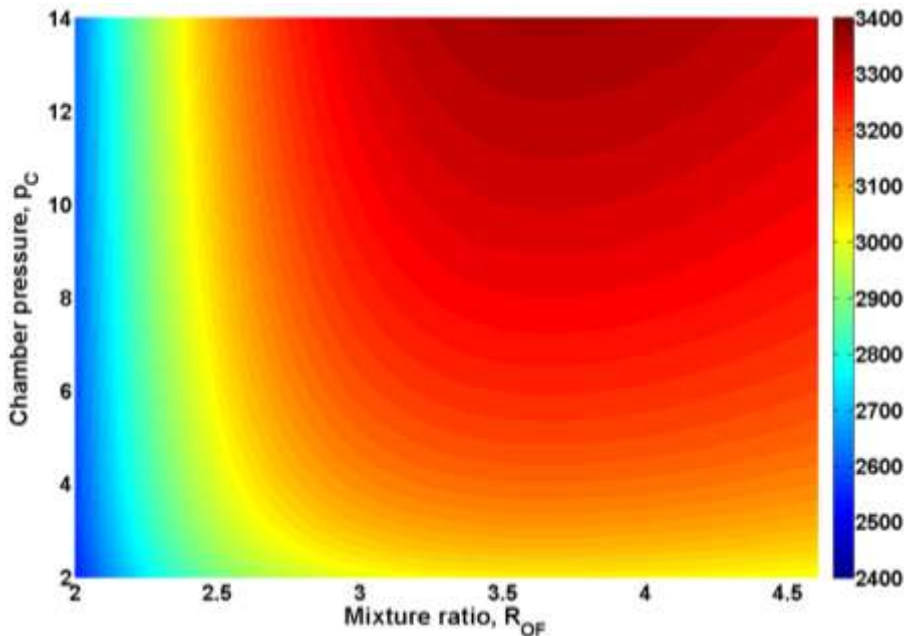


Figure 2.17: Adiabatic flame temperature $T[K]$ as a function of R_{OF} and p_c

The mixture ratio is an important control parameter to define and compare operating conditions as well, because it says something about how much fuel is injected in relation to the amount of fuel necessary to completely use all injected oxygen, which in turn strongly influences the adiabatic flame temperature and homogeneity of the propellant distribution in the chamber. The relation between mixture ratio, combustion chamber pressure and adiabatic flame temperature is illustrated in Figure 2.17.

2.8.2 Injection parameters

Besides the operating parameters, the injector parameters play an important role in liquid propellant rocket engines as well. They are used to compare different injector geometries and the corresponding spray properties.

Injection velocity ratio

The mass flow rates are used, through the continuity equation, to calculate the injection velocity (2-72), which in turn, when calculated for both oxidizer and fuel, is inserted in the relation for the (injection-) velocity ratio. The velocity ratio is usually used to compare injectors.

$$V = \frac{\dot{m}}{\rho A} \quad (2-72)$$

With ρ the density of the fluid and A the respective injector exit area.

$$R_V = \frac{V_f}{V_{ox}} \quad (2-73)$$

Weber number

Since many processes take place in the combustion chamber, many dimensionless quantities have been defined for comparison between injectors and combustion chambers. Experience has shown [18], [37], [158] that the Weber number can be correlated to acoustic fluctuations in the combustion chamber. The Weber number (2-74) for co-axial injectors describes the ratio of shear forces due to the gaseous annular jet flowing past the liquid core and the surface tension of the liquid jet. Droplet size strongly correlates negatively with the Weber number [72], so large Weber numbers cause small droplets.

$$We = \frac{\rho_{ox}(V_f^2 - V_{ox}^2)D_{ox}}{\sigma} \quad (2-74)$$

Where D_{ox} is the diameter of the LOx-post at injector exit, and σ is the surface tension of LOx.

Momentum flux ratio

Another parameter involved in atomization of liquid jets is the momentum flux ratio (2-75). This ratio is determined by dividing the momentum flux of the fuel jet over momentum flux of the oxidizer jet. This dimensionless quantity is quite often associated with jet core length [84], [85], or with how fast the jet is broken into ligaments (primary breakup).

$$J = \frac{\rho_f V_f^2}{\rho_{ox} V_{ox}^2} \quad (2-75)$$

3 Approach

Generally, in the past, extensive experimental work has been done providing many solutions for the rocket engine under investigation at the time. These solutions, as they were found for a single engine, cannot be applied directly to other engines because all these types of patch solutions depend on injector and combustion chamber geometry, propellant combination and operating and injection conditions. So, every new engine is required to undergo such an extensive experimental research process to qualify it for actual flight.

Due to the lack of representative data, modeling high frequency combustion instabilities is difficult. The engines that experienced instabilities and provided the data that is available usually have no possibility for optical access due to the cooling channels in the wall. In addition, they have a large number of injectors which makes analysis of the interaction between injector and acoustics even more difficult. But most importantly, those engines are not equipped with enough sensory equipment to resolve any process in the combustion chamber well enough for validating models and simulations.

These observations explain why a different approach is taken at the combustion instabilities department at DLR. A test facility specifically designed to investigate combustion instabilities should provide the empirical numbers that any modeling of today needs, as well as produce qualified datasets with good instrumentation and diagnostics to validate computational models. With the combustion chamber described in section 3.1.2 many parameters can be varied to form correlations between the variables describing instabilities characteristics.

Considering that at this facility the propellant combination hydrogen and liquid oxygen has been under investigation for a while (see for example [80], [81], [82]) and the research cooperation REST foresaw methane as a fuel from the beginning of the program [21], the propellant combination gaseous methane and liquid oxygen were used for this work.

3.1 *Experimental Set-up*

3.1.1 Test facility

To allow for high frequency combustion instabilities research, a dedicated test facility was built at DLR Lampoldshausen. Today, this test bed makes it possible to provide a research combustion chamber with several different sets of propellants at a large range of operational parameters. The test bench can run with

different fuels, such as hydrogen (H_2), cryogenically cooled if necessary, methane (CH_4) and even ethanol (C_2H_5O). As the oxidizer, oxygen is usually applied in liquid form. It is liquefied by keeping the oxygen container in a reservoir with liquid nitrogen (at 77K). Inert gases such as helium and nitrogen are used for pressurizing the propellants or purging the feed lines before and between tests. Figure 3.1 shows the test bench before cool down. The left hand side of Figure 3.1 shows the combustion chamber and excitation system and all the necessary equipment for executing tests successfully.



Figure 3.1: Test facility for HF-instabilities research, supply system (right) and CRC (left)



Figure 3.2: Test facility for HF-instabilities research after cool down

secondary nozzle, but also all kinds of sensory equipment, where sensors for pressure and temperature are the most essential ones.

Also, the CRC allows for optical access through small and large windows. The position of two small windows (diameter is 60 mm) can be chosen at several positions (see for example the small circles in the front view of the CRC (left image) in Figure 3.4). The large window provides a view of the entire combustion chamber (diameter is 200 mm). The material is a special type of quartz glass that can withstand the typical high pressure and temperature that occur during operation of the CRC for a large number of tests, typically a few hundred.

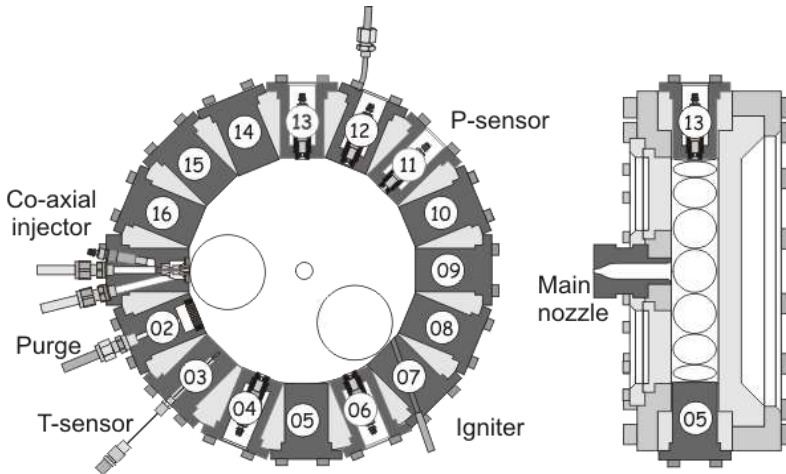


Figure 3.4: Schematic of the combustion chamber (CRC)

3.1.3 Essential modules

Injector module

The co-axial injector is a crucial part of the experiment. Through this element, liquid oxygen (LOx) and gaseous methane (CH_4) are injected into the combustion chamber. To investigate the influence of injector conditions on stability, several injector geometries, such as recessed and/or tapered LOx-posts (see Figure 1.4), have been applied. Also, in both propellant lines of the injector module dynamic pressure sensors are located.

In the first two test campaigns (see section 3.3), a tapered shear coaxial injector was used. In a shear coaxial injector, the liquid jet is broken up by the much faster flowing gas jet. Due to the relative velocity, the gas tears off ligaments of liquid. This principle is illustrated in Figure 3.5. From experience [18], [37] was known that higher pressure amplitudes could be achieved at higher Weber numbers (defined in section 2.8.2), which can be reached with high relative velocity of the gas stream with respect to the liquid jet. So, in order to increase the range of Weber numbers in the test campaigns it was decided to use a tapered LOx-post. The operating range of this injector in the CRC then played an important role in designing the test program (see section 3.3).

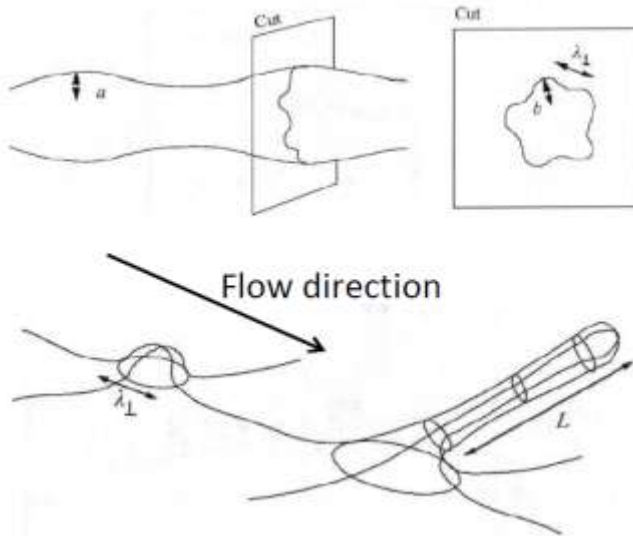


Figure 3.5: Principle of breakup of the liquid jet in shear coaxial injector [91]

Sensor module

These modules allow the measurement of pressure or temperature at any of the free positions along the combustion chamber wall

Secondary nozzle

This second nozzle is very important in the combustion instabilities investigations and is mounted in radial direction onto the combustion chamber, at one of the free positions. In Figure 3.1 it is mounted to position 12. With a siren wheel the secondary nozzle exit can be opened and closed continuously. This generates pressure waves with a pre-set frequency that couple with the combustion chamber's acoustic field. Three secondary nozzles are available. Each of the secondary nozzles matches one of the three main nozzles in a sense that the throat area ratio of secondary to main nozzle is 10%.

External excitation system, siren wheel

The siren wheel [28], [29] is a steel disk with 60 teeth, see Figure 3.6, which, through rotation, closes the secondary nozzle at well defined time intervals. As previously mentioned, acoustic waves are generated by opening and closing the secondary nozzle periodically with the siren wheel. So, when a higher than ambient pressure is maintained in the combustion chamber and during the siren wheel's rotation one of the teeth blocks the secondary nozzle exit to prevent the gas from escaping, the pressure will build up in the combustion chamber. And when, by further rotation of the disk, the secondary nozzle opens again, the gas is released, and the pressure falls.

The siren wheel is driven by an electromotor whose rpm can be freely chosen up to 6000, which corresponds to 100 rounds per second. Given the 60 teeth on the wheel, that yields a frequency range of up to 6000 Hz for the external excitation. This is more than sufficient to excite the modes of interest directly.

When the rpm is modified, for example linearly increased, during a test, it is possible to find the spectrum of the combustion chamber's response to the external excitation and it also allows for exactly locating the eigenfrequencies.

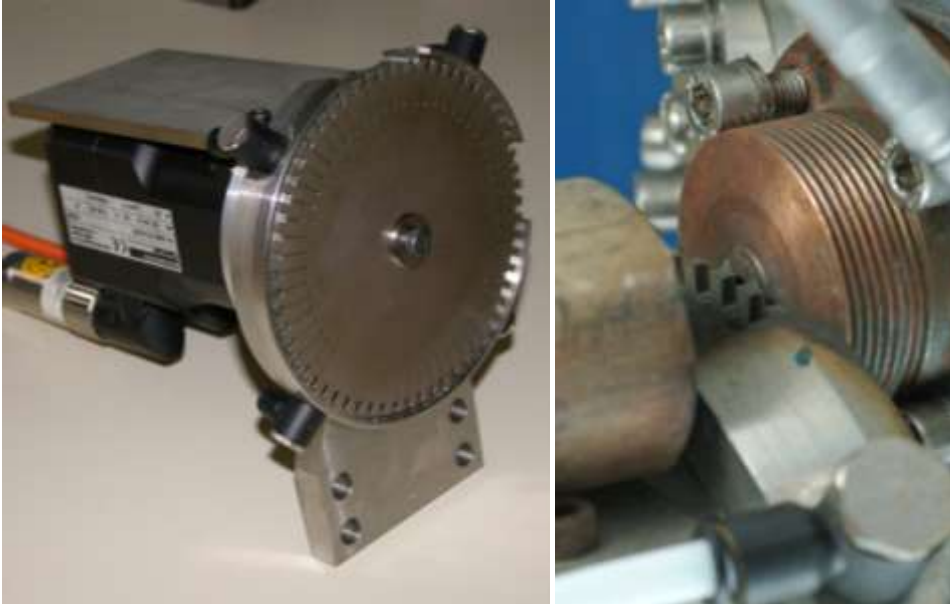


Figure 3.6: Excitation system and siren wheel (left), mounted exciter wheel (right)

3.2 Data acquisition

3.2.1 Static sensors

All static sensors have data acquisition rates of 1000 Hz (Lucas Shaevitz sensors [3]) for pressure and thermocouples (Type K and N) from TC Ltd [150] for temperature). This allows for a good temporal resolution of the effects up to millisecond timescale. These static sensors are essential for tracking the control parameters during a test. Operating parameters such as mass flow rate and chamber pressure are also tracked with static sensors to verify whether the targeted operating conditions were actually met. The measured signals are consequently used to calculate other operating conditions such as Weber number We and momentum flux ratio J . The mass flow rate is measured with a Coriolis sensor [43]. This sensor has a specifically designed shape to force the fluid to flow through bends within the sensor housing and generate out of plane accelerations. The deviations caused by these accelerations are calibrated to the mass flow rate of the fluid. Relevant hot gas and propellant properties needed for those calculations are determined with the CEA combustion code from NASA [54] and the thermo-physical properties from Younglove [161], [162] respectively.

3.2.2 Dynamic sensors

To capture the dynamic fluctuations of the chamber pressure, Kistler dynamic pressure transducers with matching charge amplifiers are applied [78], [79]. These sensors are capable of acquisition rates up to 100 kHz. A signal recorded with a higher acquisition rate obviously has more information, hence is more accurate. On the other hand, the datasets tend to become very large, and a balance had to be found between ease to handle the data, the information contained and the information required. A few considerations were taken into account. The first few eigenmodes should be visible in the data, the Nyquist limit had to be respected, and to perform a fast fourier transform (FFT), the sampling rate should be a power of 2, or close to it. The first few eigenmodes have a frequency in the order of magnitude of 5 kHz. Hence, an acquisition rate of 32 kHz ($2^n = 32768$, for $n = 15$) was chosen for the first test series. After analyzing this test series, it was decided to increase the acquisition rate to 65 kHz ($2^n = 65536$, for $n = 16$) for the second test campaign with external excitation, because the computation time was very low and the (filtered) discrete signal more closely agreed with a sinusoidal continuous signal.

3.2.3 Optical diagnostics

Optical access of the combustion chamber allows for measuring spray and flame characteristics during combustion. The high speed digital cameras used for optical diagnostics of the spray and OH-intensity can only be set to certain frequencies in combination with specific image resolutions. So, here it is important to consider whether spatial resolution is more important or that the focus should lie more on temporal resolution. After experience taught that the high speed recordings for experiments without external excitation do not show any clear signal, it was decided to decrease the acquisition rate to allow for a higher spatial resolution. For the second campaign, on the other hand, the temporal resolution was more important.

Spray

To collect spray images, two small windows on opposing sides of the combustion chamber suffice to carry out a backlighting procedure. Due to the high density of the liquid spray, the light coming from a strong lamp on one side of the chamber is redirected creating a shadow, which is captured by the camera on the other side. For the spray images a Photron Ultima 1024 PCI [111] was used, at a rate of 12500 frames per second and a resolution of 256x256 pixels per image.

OH-intensity

For combustion instabilities research it is interesting to know where the chemical reaction takes place, which is where the heat is released into the system. During combustion of oxygen and methane, several chemical reactions take place, see Appendix A for a chemical mechanism for the oxidation of CH_4 . Several of these reactions create the very reactive OH-radicals and this predominantly occurs in the flame front. In this reaction zone most heat is released. OH-radicals tend to react fairly quickly, even though at such high temperatures as in the combustion chamber ($\sim 3500\text{K}$) the equilibrium concentration of OH is significant and recom-

bination might be slowed. When OH-radicals are formed they appear in an energetically excited state which decays by emission of light. This effect of light emission due to a chemical reaction is called chemiluminescence. The light emitted by OH-radicals has a wavelength of around 307 nm.

By placing an interference filter for this wavelength and a UV-objective on the intensified high speed camera, only the chemiluminescence of the OH-radicals is recorded. The camera used was a Photron APX I² [109], [110]. When the temporal resolution was important, a rate of 12500 frames per second and a resolution of 256x256 pixels per image were used. When the focus was on spatial rather than temporal resolution, a rate of 6000 frames/s and a resolution of 512x512 pixels per image were used. All high speed images are stored as grey value images of 16 bit, so every pixel has a value between 0 ... $2^{16}-1$ (= 0 ... 65535), where 0 and 65535 represent the colors black and white respectively. The set-up of the high speed cameras around the combustion chamber is illustrated in Figure 3.7.

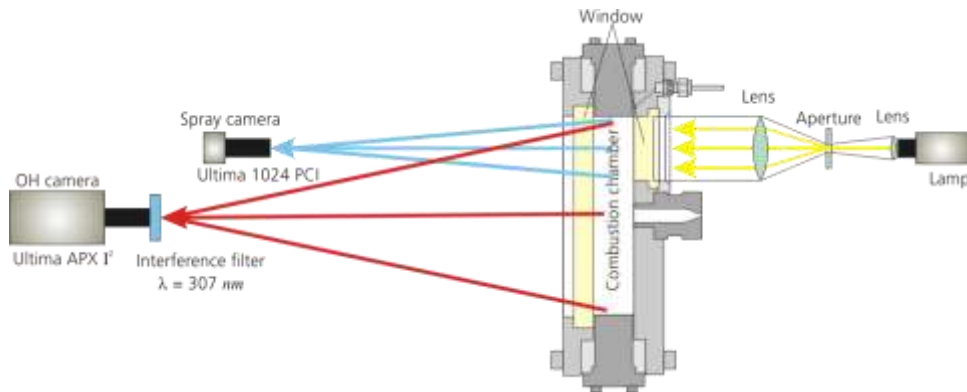


Figure 3.7: Optical diagnostics set-up

3.3 Test program

The setup of the test program shows the general approach that was applied for the thesis. The operating conditions and control parameters are varied and the range of values explored to define the test program. The reasoning behind the test program and the goals of the specific test campaigns are discussed in detail in the following sections.

3.3.1 First test campaign, without external excitation

Combustion is the engineer's expression for the collection of a number of processes taking place in the combustion chamber, such as atomization, vaporization, mixing and the chemical reaction between the CH₄ and O₂. When this project started, it was unknown which of these various processes were, and if so, to what extent, responsible for the phenomenon of high frequency combustion instabilities. So, when this specific project with CH₄/LOx as propellant combina-

tion started, the most important principle for designing the approach was to run the experiments such that a foundation of basic understanding and a broad reference frame was developed first, before looking at other (external) influences. The main goal of the first test campaign was to extensively investigate the combustion chamber and its behavior to develop a basic understanding of the processes in the combustion chamber and maybe find correlations between for example injector conditions and energy contained in an eigenmode. The test matrix for the first test campaign is shown in Table 3.1, and a more intuitive representation of the control parameters is given in Table 3.2.

Table 3.1: Test matrix of the first two test campaigns with LOx/CH₄ (values in italics are omitted in 2nd campaign)

Variable	Value / Range
Chamber pressure, p_c [bar]	2 – 10
Mixture Ratio, R_{OF} , (Equivalence Ratio)	2.3, 3.4, 4.0 (0.6, 0.85, 1.0)
Total mass flow rate, \dot{m} [g/s]	4.4, 7.4, 9.0, 15.0, 18.7
Main nozzle throat diameter, D_t [mm]	5.0, 7.2, 10.2
Velocity Ratio, R_v [-]	20 – 125
Momentum Flux Ratio, J [-]	2 – 25
Weber number, We [-]	400 – 12000

Table 3.2: Test matrix of control parameters of the 1st test campaign with LOx/CH₄

		Throat diameter main nozzle								
		5 mm			7.2 mm			10.2 mm		
R_{OF}		2.3	3.4	4.0	2.3	3.4	4.0	2.3	3.4	4.0
Total mass flow rate	4.4	$p_c=4.4$	4.1	4.0						
	7.4	7.4	7.0	6.8	3.6	3.4	3.3			
	9.0	9.0	8.5	8.3	4.4	4.1	4.0	2.1	2.0	1.9
	15.0				7.3	7.0	6.8	3.6	3.4	3.3
	18.7				9.0	8.5	8.3	4.4	4.1	4.0

In this campaign the three driving variables of rocket engine combustion chamber operation, the chamber pressure, the total mass flow and the mixture ratio, are varied throughout the entire operational domain of the CRC to allow for an as large as possible spread of conditions at which the CRC is investigated. Globally, the chamber pressure is varied by keeping all other variables constant and varying the main nozzle diameter. The matrix has three main columns which distinguish these main nozzle diameters. Where, obviously, for a single main nozzle, the chamber pressure is varied by varying the mass flow rate. The rows signify different mass flows, which were selected again based on the maximizing the operational spread of operational parameters, in this case the chamber pressure.

The three columns that show up for every main nozzle belong to the mixture ratios at which the tests are executed. The mixture ratios are chosen based on significant points in the combustion chamber characteristic. The first mixture ratio maximizes the characteristic velocity, which is a representation of chamber performance. The second maximizes the temperature of the combustion gas. The third is the stoichiometric mixture ratio, at which methane and oxygen are completely converted to combustion products. The actual points were defined by asking the question, 'What mass flow yields the maximum pressure allowed by the design limits of the CRC (9 bar relative pressure) assuming the smallest nozzle?' This provided the starting point of 9 g/s mass flow, at a mixture ratio of 2.3 and a chamber pressure of 9 bar. Consequently, keeping the mass flow constant, all other operational points in the third row were defined. To find the effect of mass flow variation, two mass flows were defined which yielded the same chamber pressure but with different nozzle diameters. This defined the first row, at 4.4 g/s and the fifth row at 18.7 g/s. The second and fourth rows (of constant mass flow) were selected to achieve better statistics. Note that these two rows in themselves also cover the variation of chamber pressure and mass flow. As a visual aid, in Table 3.2 settings with identical chamber pressures are given the same color. The mentioned range in mass flow and chamber pressure, combined with the three main nozzles yield a large range for the parameters describing injection conditions, Weber number and momentum flux ratio, which is also listed in Table 3.1. Experience from the past [37] teaches that the frequency spectrum of the dynamic pressure shows the eigenmodes when combustion is not externally excited. The high speed recordings of the OH-intensity of the flame without external excitation, on the other hand, do not. So, to further define combustion in the CRC, the focus of the high speed imaging was on spatial resolution to characterize flame and spray phenomenology without external excitation, rather than temporal resolution which would only allow searching the intensity signal for eigenmodes that the signal did not have without insight in local phenomena.

3.3.2 Second test campaign, with external excitation

After the first campaign characterized the combustion chamber, and determined the influences of the three variables investigated, the next step would be to apply external excitation. The main goal of this second campaign is to develop an understanding of the effect of external excitation on the combustion chamber processes. External excitation of combustion takes place through a secondary nozzle mounted to the CRC in radial direction, see section 3.1.3. Four positions for the secondary nozzle were selected, see Figure 3.8.

Position 5 and 13 have an angle of 90° and 270° with respect to the injector which should basically have the same effect but are included both to see if there are other effects in play. These positions force the nodal line, in case of the first tangential (1T) mode, to be roughly in the same plane as the LOx-jet, which is shown in Figure 3.9. This allows for an investigation towards a possible effect of high velocity fluctuations in the combustion area due to the acoustic field. Position 9 is directly opposite from the injector and forces a pressure anti node to be directly in front of the injector which allows for determining if the local high pressure fluctuations have an influence on combustion. Position 11 puts a combination of medium pressure and velocity fluctuations in the combustion zone and

allows for a more thorough comparison between excitation at 90° or 180° with respect to the injector. To keep the relative effect of the external excitation equal for all three main nozzles, the area ratio of the secondary nozzle exit to the main nozzle exit was taken constant at 10%. In that way the secondary gas volume flowing through the secondary nozzle with respect to the main volume is always constant.

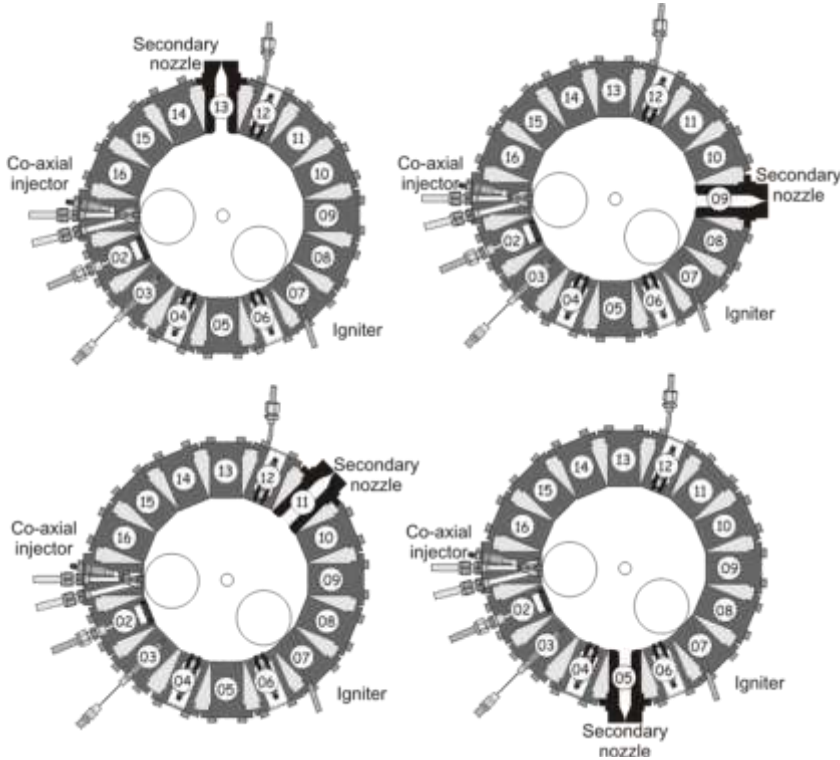


Figure 3.8: Angular positions of the secondary nozzle

Considering that downloading the high speed recordings takes two hours for 4 seconds of images, and therefore a possible reduction of the number of experiments would be welcome, the general effects of the three operating variables on the amplitude of the pressure fluctuations are known (this was the main focus of the first campaign), it is not necessary to repeat all operating points of the first campaign here with external excitation. The operating points omitted in the second campaign are written in *italics* in Table 3.1. In Table 3.3, the executed operating points executed in the second campaign are shown. So, comparing to the test matrix of the first campaign in Table 3.2, the intermediate mixture ratio, and two intermediate mass flow rates were skipped. Considering that the focus of the second campaign is on the effects of external excitation, surely the selected points still allow for determining the effects of these driving variables, but with less effort. The effect of excitation, especially the position of the secondary nozzle, is investigated by executing every operating condition in Table 3.3 once for each of the four angular positions defined in Figure 3.8.

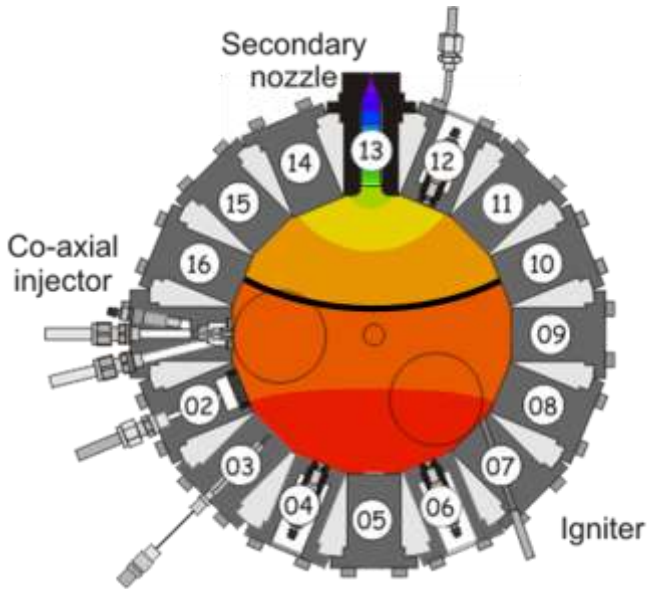


Figure 3.9: First tangential mode in CRC with SN at position 13

The focus of the optical diagnostics shifted from spatial resolution to temporal resolution (see section 3.2.3 on optical diagnostics) because now it is necessary to resolve the first eigenmode to see whether the flame (and spray) responds to the external excitation at all and, if so, whether pressure or velocity fluctuations have an influence on the flame's intensity.

Table 3.3: Test matrix of control parameters of the 2nd test campaign with LOx/CH₄

		Throat diameter main nozzle								
		5 mm			7.2 mm			10.2 mm		
RoF		2.3	3.4	4.0	2.3	3.4	4.0	2.3	3.4	4.0
Total mass flow rate	4.4	p _c =4.4		4.0						
	7.4									
	9.0	9.0		8.3	4.4		4.0	2.1		1.9
	15.0									
	18.7				9.0		8.3	4.4		4.0

4 Data Reduction and Error Management

4.1 Data Reduction

This chapter briefly discusses the procedures carried out after data acquisition. Generally, the raw data is first prepared for processing. This pre-processing consists of reading and sorting data such that the main analysis can be done systematically and automatically, without further user interaction. The main analysis routines do all the calculations necessary for analysis and prepare the results for post-processing. Post-processing is done manually, and consists of either directly interpreting the results, or cross-correlating different results. In any case, post-processing yields the conclusions with respect to the results and experiment.

4.1.1 Operating parameters

The data sets containing the operating parameters (see section 2.8), such as static pressure and temperature, do not undergo excessive pre-processing. A time interval is defined such that therein only 'stationary' combustion takes place, so ignition and the transient start-up phase are excluded from the analysis. The calculations mainly consist of determining all operating conditions, such as pressure drops over valves and injector, chamber pressure, and all variables describing injector conditions (all described in section 2.8.2), such as Weber number,

We, momentum flux ratio, J , and velocity ratio, R_v . The measured values of quantities determining operating conditions show very small fluctuations due to combustion noise. Therefore, all quantities are averaged over the time interval wherein combustion is considered stationary, and are then used in post-processing for correlating results. Usually, here, the transient start-up phase is assumed to be completed 3 seconds after ignition. So, to be safe, the stationary time interval is defined between 4 and 10 seconds, after which the test is terminated. An example of operating parameters is given in Figure 4.1. Shown is the chamber pressure, mass flow, and injector pressure. The time interval used to calculate the averages for this specific case was between 4 and 10 seconds.

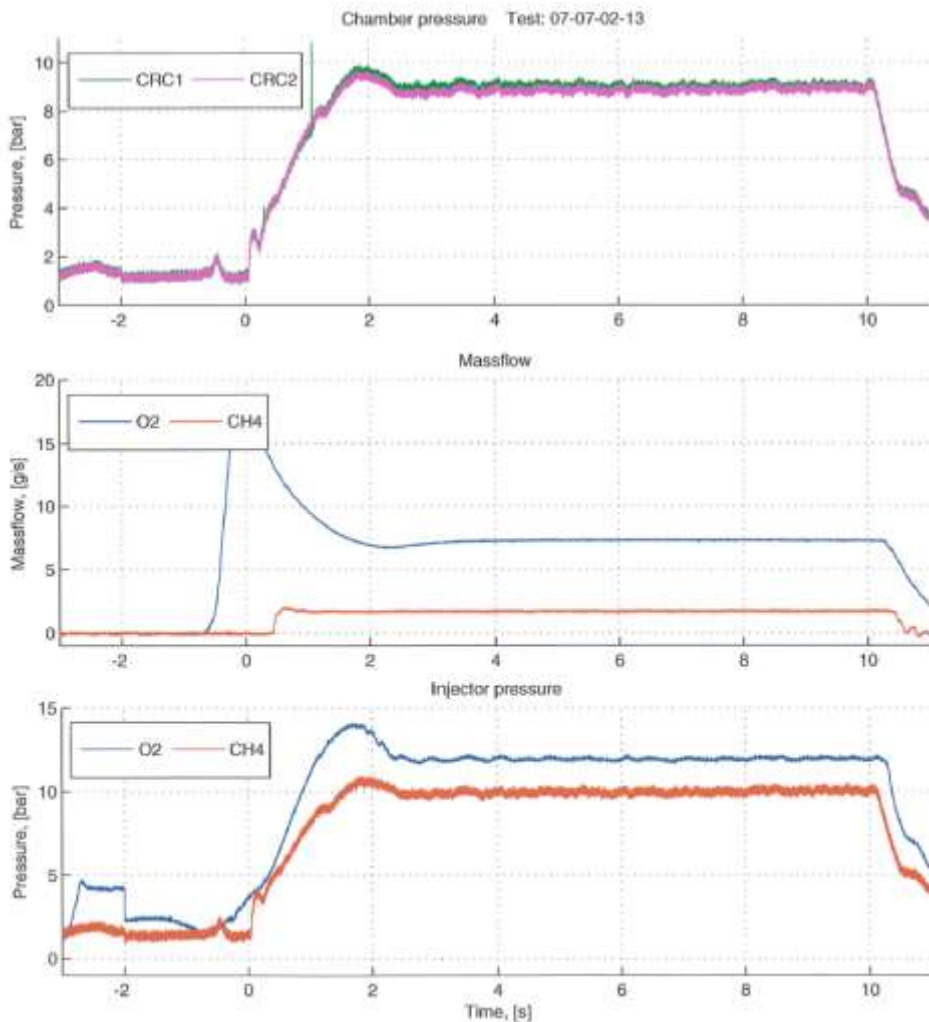


Figure 4.1: Traces of operating parameters

4.1.2 Dynamic pressure

As opposed to the operating parameters, the raw dynamic pressure signals need to undergo a number of operations before any relevant information can be extracted. The raw signal contains all possible acoustic eigenmodes which, by superposition, contribute to the combustion noise. Before the data set is reduced further beyond the aforementioned time interval, a sort of average pressure fluctuation is calculated over this time interval by means of the root mean squared (see equation (4-1)) of the dynamic pressure.

$$p'_{rms} = \sqrt{\frac{\sum_{i=0}^N (p'_i)^2}{N}} \quad (4-1)$$

Subsequently, the signal is Fourier transformed to identify the individual eigenmodes. Experience [59] teaches that the first tangential (1T-) mode is the most dangerous, thus, after the Fourier transformation, the signal is band pass filtered around the found 1T-frequency.

Filtering

Filtering usually generates a phase shift between the raw signal and the filtered signal that is not constant and depends on frequency. Due to the different types of analyses carried out on the dynamic pressure signal, it is necessary to make a distinction here. When the noise of an individual mode is analyzed, for which the phase information is basically irrelevant, the filter procedure is a straightforward one-way Chebyshev (type 2) [146] filtering. If the signals are used to derive the pressure distribution along the wall and the pressure field in the entire combustion chamber for comparison with the intensity field (see Chapter 7), where the phase information is an essential aspect of the signal, the filtering then consists of a two-way filter. This procedure basically applies a Butterworth band pass filter once in forward and once in backward direction to guarantee a zero-phase shift with respect to the unfiltered signal.

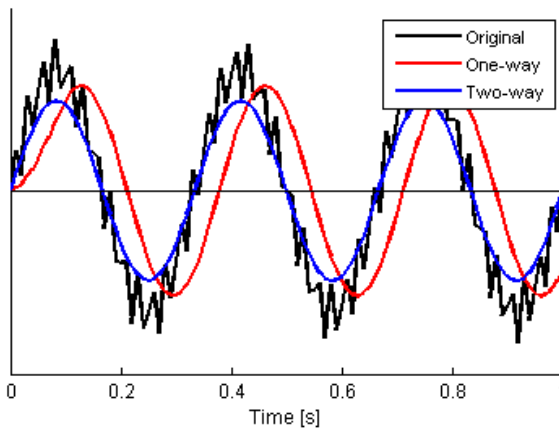


Figure 4.2: Comparison raw (synthetic) signal, one-way filtered and two-way filtered signal

This procedure is elaborated in detail and mathematically proved in [146]. The effect of the two-way filtering is illustrated in Figure 4.2, which shows the raw signal, the one-way filtered signal and the two-way filtered signal.

Energy, PSD

Since the severity of a pressure fluctuation depends on the energy of the fluctuation, rather than its amplitude, it was decided to analyze the energy of the eigenmode. A power spectral density analysis can be defined as Fourier transformation of the auto-correlation function $R(\tau)$ and determines how the power, or energy, is distributed in the frequency spectrum (auto spectral density), see equation (4-2). More information on PSD or the auto-correlation function can be found in digital signal processing literature, like [10], [105], [146].

$$PSD(f) = \int_{-\infty}^{\infty} R(\tau) e^{-2i\pi f\tau} d\tau \quad (4-2)$$

A maybe more intuitive definition is found when writing the spectral density as the product of the Fourier transform $X(f)$ of the discrete signal $x(t)$ and its complex conjugate. This relation is called the Wiener-Khinchin relation [10], wherein T is the interval over which the signal is Fourier transformed.

$$PSD(f) = \frac{2}{T} [X^*(f) \cdot X(f)] = \frac{2}{T} |X(f)|^2 \quad (4-3)$$

$$X(f) = \int_0^T x(t) e^{-2i\pi ft} dt$$

Fourier transforming a pressure signal (measured in [bar]) yields the frequency spectrum of the pressure signal with the unit [bar/Hz]. When determining the PSD according to equation (4-3) by squaring the frequency spectrum and dividing through the length of the time interval, one finds for the PSD the unit [bar²/Hz]. By integrating the PSD over a frequency interval, centered on the 1T-frequency, the ‘energy’ of the eigenmode is found with unit [bar²]. The result is used as a qualitative indication how for different operating conditions, the energy of the 1T-mode changes.

Damping, linewidth

For the previously discussed analysis on energy contents of the fluctuation (PSD) it does not matter whether the signal is ‘stationary’ or that the tests are executed with external excitation. For the latter case, the signal cannot be considered to be stationary, making it impossible to use the Fourier transformed signal as source of information on the spectral characteristics (PSD). The damping can therefore only be analyzed for those tests without external excitation, or at least for time intervals where excitation is absent.

The PSD is then cut around the 1T-frequency, equal to the interval used to calculate the energy, and it is to this distribution that a Lorentz profile (see section 2.6) is curve fitted by means of a procedure that applies a robust non-linear least-squares method with a Levenberg-Marquardt algorithm. The procedure

yields all relevant data describing the Lorentz profile, including the line width which measures the damping.

Pressure field

Every eigenmode has its own pressure distribution. The pressure field in the combustion chamber is uniquely defined (assuming a constant speed of sound in the combustion chamber) by the wall pressure distribution, which is derived from the dynamic pressure sensors, located around the circumference of the combustion chamber. A description of how the pressure field is derived from the wall pressure measurements can be found in section 5.3. As previously expressed, the phase is in this case an essential piece of information because the relations of the signals to each other are what define the pressure field. The signals are therefore two-way filtered to guarantee a zero phase-shift. To find the wall pressure distribution, there is distinguished between geometries with or without secondary nozzle. It is fair to assume the pressure field resembles that of a standing wave for the geometry with secondary nozzle, see section 2.2.2. If the secondary nozzle is not present, the CRC is close enough to a perfect cylindrical combustor for spinning modes to occur. From the theoretical analysis of the spinning mode (section 2.4) it was known that the rotational velocity of the nodal line could be so high (Figure 2.9) that the data acquisition rate would be too low to temporally resolve the rotation of the pressure field well. After the pressure field is established, for both with and without external excitation, it will be compared to the flame intensity field with respect to the phase shift between them. For this reason, the pressure signals (as well as the flame intensity signals) are resampled at 200 kHz or higher (80-84 points per period of oscillation) before determining the temporal development of the pressure field. With this kind of resampling, the rotating mode very close to a standing mode can be temporally resolved, and the maximum error in the phase between pressure and intensity is decreased to 2.5 degrees.

Velocity field

The pressure field is then used as input to determine the acoustic velocity field. The gradient of the pressure field is computed and accordingly scaled to find the velocity, according to equation (4-4) as derived in section 2.3.

$$\vec{u}(x, y, z, t) = -\frac{j}{\rho\omega} \nabla p(x, y, z, t) \quad (4-4)$$

Only under the assumption that the dynamic pressure fluctuation is described by a harmonic function this relation is valid. In any other case, one would have to numerically integrate the pressure to find the velocity. The pressure gradient is readily determined and scaled according to equation (4-4). To account for the phase shift j , the discrete signal is shifted over the appropriate time interval. The number of measurement points depend on the temporal resolution of the signal, 200 kHz in this case. Typically 80-84 measurements per period, hence 20-21 per 90 degrees, yielding an error less than 2.5 degrees. If the pressure were to be integrated numerically, obviously the phase shift would occur automatically.

4.1.3 Spray and flame optical diagnostics

High speed digital cameras are used to investigate spray and flame phenomenology. The image sequences generally consist of grayscale images. The images are read and processed in accordance to the required analysis. In order to analyze the information in the images, binarization is, for both spray and OH-intensity, required. When binarizing an image, the foreground that contains the relevant information is separated from the background. In order to binarize an image, a threshold has to be found which specifies what gray level indicates the boundary between foreground and background. The binarizing then consists of segmenting the image, or changing the gray image into a black and white image, with the threshold as the separator. A good segmentation is essential to accurately interpret the information in the image. There exist a number of types (classes) of thresholding, each having different methods or technique. A extensive discussion on thresholding techniques is given by Sezgin [137]. Multiple thresholding techniques have been investigated, but unfortunately it proved to not be possible to find one method that works well on both types of images.

Spray

The analysis of the spray image sequences is fairly straightforward. After binarization, the length of the liquid core (intact core length, ICL) is determined. The thresholding technique applied for the spray images is a spatial class method called Random Sets [49]. Essentially, this method binarizes the images at every gray level and maps the distances of all pixels to the pixels of the opposite color. A global average distance is then found over all thresholds, and the threshold with an individual average closest to the global average is selected. The method is illustrated in Figure 4.3. It shows an original grayscale image and its binarized counterpart.

Flame phenomenology

The OH-intensity images are analyzed for flame characteristics such as flame spreading angle and, if relevant, lift-off distance. To do so, the images have to be binarized as well. For the OH-intensity, an entropy class technique based on Renyi's entropy is used, which was proposed by Sahoo [130]. The entropy class is based on information theory, which states that the information carried by an image is determined by its entropy. An image's entropy is generally described by the gray level probability distribution (4-5).

$$H = - \sum_{g=0}^L p(g) \ln[p(g)] \quad (4-5)$$

In this equation, $p(g)$ is the probability distribution of gray levels and describes the relative appearance of every gray level in the image and looks like a normalized histogram. The entropy of the image is defined as the sum of the entropies of every gray level, where different authors might derive marginally different equations.

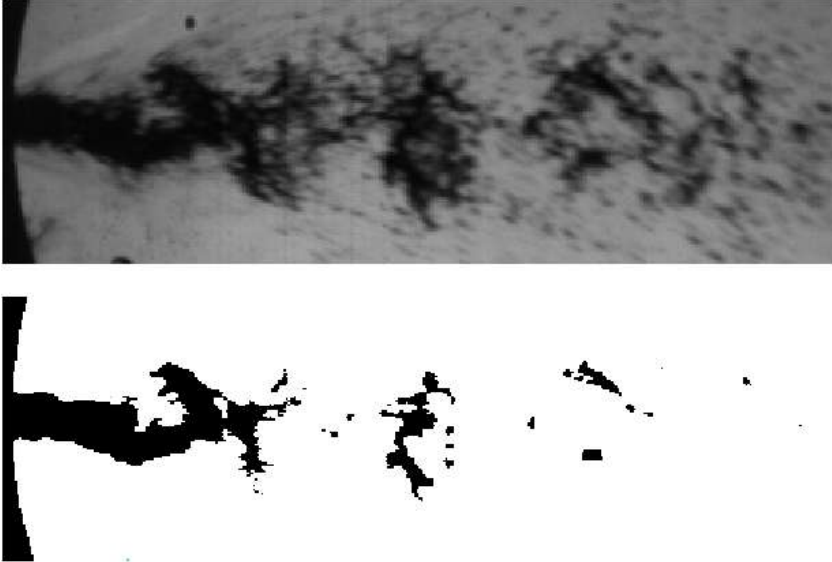


Figure 4.3: Spatial class “Random Sets” binarization method, raw image (top) and binarized image (bottom)

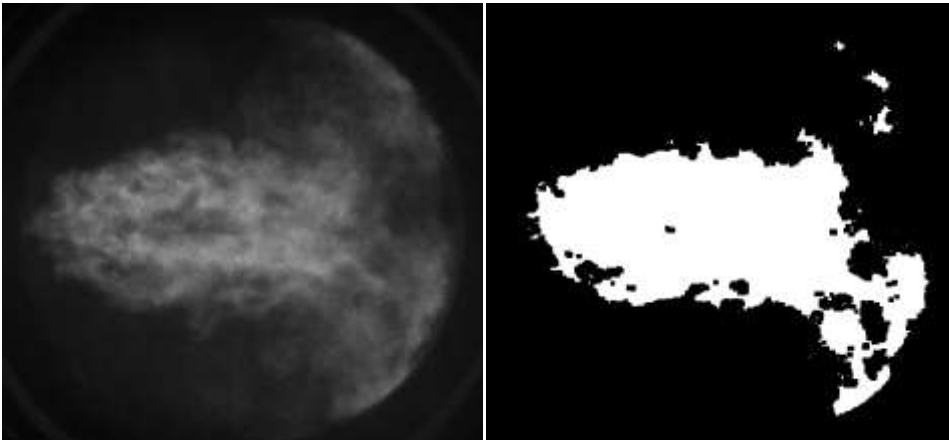


Figure 4.4: Entropy class “Renyi’s entropy method”, raw image (left) and binarized image (right)

The method described by Sahoo [130] compares an original image to the binarized image and the entropy in this case is a function of the probability distributions of both images. The calculated entropy is considered the distance between the two images. This method essentially seeks to represent the data as consistently as possible for the entire image. By minimizing the entropy, the distance between the original and the binarized image is also minimized. The threshold selected is the gray level that minimizes the cross entropy. In Figure 4.4, this method is illustrated. Figure 4.4 shows both the original and the binarized image.

The flame spreading angle is determined by two straight lines capturing the flame. In the binarized image, the flame front is assumed to be described by the boundary between the black and white areas in Figure 4.4. For every point along this boundary, a straight line is defined connecting this point to the beginning of the flame (the left-most point of the white area in Figure 4.4). The angle this line makes with the horizontal axis, through the beginning of the flame, is then calculated. This then gives two sets of angles describing the flame front, both above and below the horizontal axis (two flame half angles). These sets are then averaged to find the upper and lower half angles which combined make up the flame spreading angle.

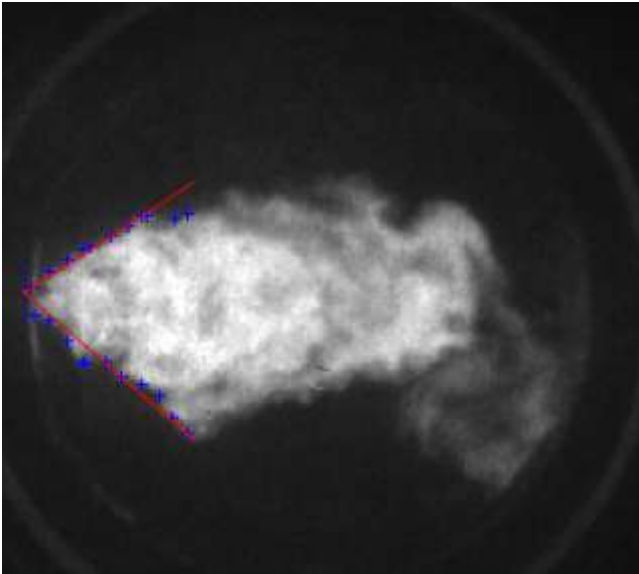


Figure 4.5: Flame angle

Obviously, the calculated flame spreading angle depends on how much of the flame is taken into account. In general, the image shows the entire combustion chamber and flame, but the flame only over the first 20% of its length qualitatively shows a clear spreading angle. Therefore, the analysis to determine the flame spreading angle is done based on this first 20% of its length. This procedure is illustrated in Figure 4.5. The blue crosses depict the flame front, the red lines the averaged angles for both halves of the flame.

This way, it is also possible to analyze whether the flame is moving in its entirety or that its axis is fixed, and whether the flame's behavior is symmetric above and below its axis or not.

OH-intensity

The investigation of the OH-intensity high speed recordings focuses, of course, on the intensity of the flame. More specifically, the variations of the intensity with time are the most important because it is assumed to be a measure of how the heat release fluctuates, and it is this fluctuation that can be correlated to the pressure fluctuations to find the Response Factor (see section 2.5.3). Before any

calculation is done, the images are all normalized to correct for camera settings, such as electronic gain or camera aperture width. The electronic gain setting, electronically amplifies the signal before displaying and storing it. Aperture width controls whether more or less photons (OH-emission) hit the photovoltaic plate (CCD). It is necessary to change both settings for different operating points, because the OH-intensity is not equally well visible for all operating points with identical settings. But in changing these settings the actual intensity is falsified. In order to compare the data quantitatively, it is required that the data are normalized. The number of photons that pass through the aperture is linearly dependent on its area. The aperture can therefore easily be corrected for by normalizing for its area. The correction factor for the electronic gain is provided by the manufacturer, and shown in Appendix B. It must be noted that measuring the OH-intensity is performed with a line-of-sight measurement. This can cause marginal errors that cannot be corrected through for example an Abel inversion, because the flame is not rotationally or axi-symmetric. The probable effect is an amplification of the difference between high and low OH-intensity and its fluctuations, and hence only quantitative in nature. The consequences for physical interpretation are therefore negligible.

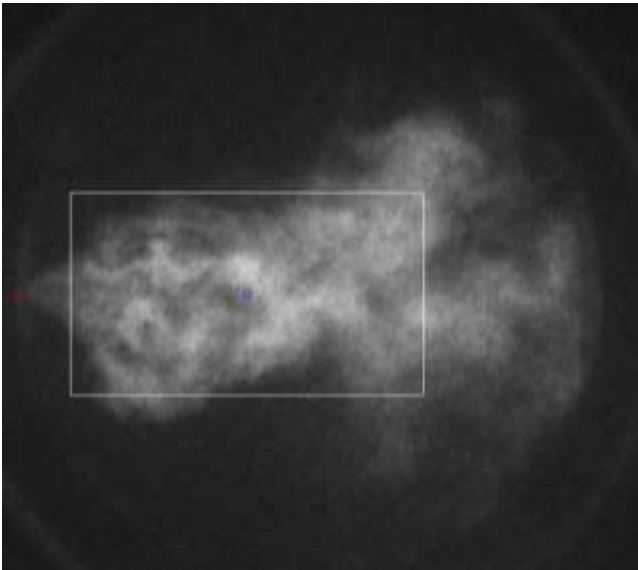


Figure 4.6: Large window for global intensity fluctuation analysis

The flame intensity can be analyzed in two different ways, respectively providing global and local fluctuations, depending on the goal of the analysis. So, to analyze this behavior and determine the global intensity variations, a window that covers the largest part of the flame in most cases is laid over an image, and the flame's intensity is analyzed within this window. This first method of intensity analysis, for global intensity fluctuations, is illustrated in Figure 4.6. In the last few years [80], [81], [82], one possible interpretation of velocity coupling has been that it would be irrelevant for the droplets in the combustion zone from which side they are excited. So, with external excitation from 90° (see section 3.3, Fig-

ure 3.8) the acoustic wave would travel from top to bottom and vice versa, and there would be no difference for the droplets to be hit from above or below by the acoustic wave. Hence, following this reasoning, if there is velocity coupling, the response of the flame should be the same at any location and occur twice during one oscillation, because the wave travels up and down during one acoustic period and causes the same result in both directions. Hence, the response should be at double the excitation frequency, and the response should be visible in the entire flame.

The second method is to analyze the local intensity variations. In order to do so, a grid of small windows of 1x1cm is laid over the image, see Figure 4.7. This reduction of spatial resolution is done to prevent an immensely time consuming calculation for analyzing every pixel. Every single one of these windows (292) is then analyzed.

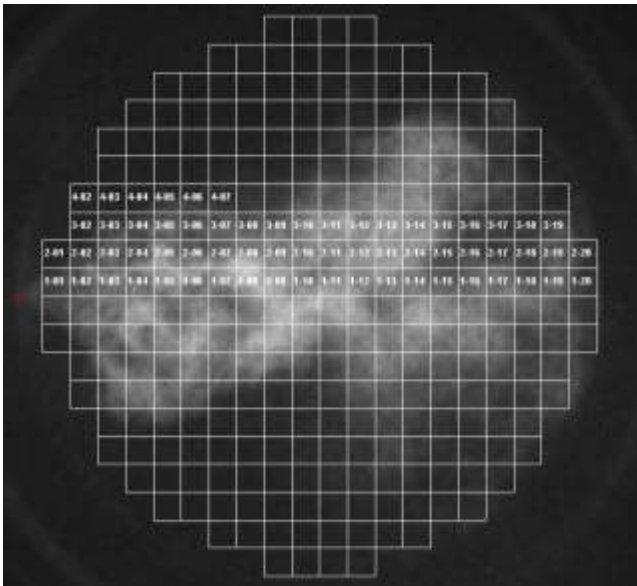


Figure 4.7: Grid of windows for local intensity fluctuation analysis

The intensity fluctuations are calculated as follows. The entire sequence of images is used to define an image with temporally averaged intensity. All images in the sequence are summed and divided through the number of images. Of this time-averaged image, no matter whether local or global intensity is investigated, an average intensity, $I_{avg,i}$, is calculated for every window by only taking into account those pixels within the window. So, this average intensity for every window is a time-averaged and locally space-averaged value, described in (4-6) with N the number of images and i denoting the individual windows.

$$I_{avg,i} = \frac{\sum_{i=1}^N I_i}{N} \quad (4-6)$$

Then, for all images, a spatially averaged intensity, $I_{win,i}$, is determined for every window in the image. To find the intensity fluctuation per window, the time-averaged intensity, $I_{avg,i}$, is then subtracted from the time dependent local space-averaged window intensity, $I_{win,i}$.

$$I_{fluc,i} = I_{win,i} - I_{avg,i} \quad (4-7)$$

So, every window yields one signal, with a length equal to the number of images. In order to allow direct comparison between image sequences (or tests) and the individual windows between each other, it is required to normalize the acquired intensity signals. This is done by dividing the intensity fluctuations (4-7) through the space averaged (window) intensity

$$I_{norm} = \frac{I_{fluc,i}}{I_{win,i}} \quad (4-8)$$

This way, the normalized intensity fluctuations (4-8) are in relation to their local (window) space-average, and therefore the individual windows can be quantitatively and qualitatively compared to one another.

The energy of the intensity fluctuations is computed exactly as was described for the dynamic pressure fluctuations. A PSD is determined, and cut around the center frequency before discretely integrated over the cut interval. In case the intensity signals are directly compared to the pressure signals, the intensity signal is filtered first. The filtering procedure is identically the same two-way filter procedure as for the dynamic pressure to guarantee a zero phase shift between the filtered and unfiltered signal.

4.2 Error Management

4.2.1 Error estimation

In the process of measuring physical quantities, processing data and analyzing results, it is a certainty that errors (experimental, computational or of other nature) will be made. This section discusses the relevant errors of the measuring chain and the possible errors of the data processing procedures.

Types of errors

Two different types of hardware related errors are relevant in this case. Systematic errors are generally caused by hardware malfunctioning, or wrong calibration of the sensory equipment. This kind of error usually is a deviation from the actual value, so a deviation to either larger or smaller values. This can be avoided, or at least minimized, by checking the hardware and repeating calibrating the equipment at specific time intervals. These checks and repeated calibration of the

sensors are carried out at DLR according to clear protocols and these types of errors are therefore considered negligible.

Statistical errors describe the scatter that measurements of the same quantity under identical conditions show. All sensors produce statistical errors, and can usually be fairly accurately quantified by executing such a measurement repeatedly. Most manufacturers have determined these types of errors and state them on the relevant data sheets as a percentage of either measurement value or measurement range. For the relevant sensors, used in the measurement chain of the CRC, the quantified statistical errors are summarized in Table 4.1.

The high speed digital cameras register the number of photons. The number of photons, even if not recorded accurately, is for the spray dynamics recordings practically irrelevant, the contrast will still be such that the spray dynamics can be analyzed accurately. The dominant errors are introduced by the image processing algorithm.

Table 4.1: Statistical errors of sensory equipment CRC

Quantity		Measurement uncertainty
Static pressure	∣ CRC	52.5 mbar
	∣ Injector/tank	75 mbar
Dynamic pressure		3.6 mbar
Mass flow rate	∣ Methane	0.50%
	∣ LOx	0.10%
Temperature [K]	∣ CRC	0.40%
	∣ Cryogenic (LOx)	1.50%
High speed camera	∣ Spray boundary	<4 pixel
	∣ OH contour	<4 pixel

An electronically amplified camera is used for recording flame emission. The electronic gain of the camera will introduce more and more losses over time, see the gain profile of the camera for Begin of Life and End of Life in Appendix B. The time frame over which the camera was used allows assuming the gain profile to be constant (no losses), and no additional inaccuracies (errors) are introduced. Plus that these losses would be cancelled out in the qualitative analyses for intensity fluctuations as discussed in Chapter 6.

Only the quantitative analyses of for example intact core length (spray images) or flame angle (flame emission images) would suffer from errors introduced in the data acquisition. In these analyses a thresholding technique is applied (see section 4.1.3) to convert the images to black and white (binarized) images for further analysis. Errors possibly made during the acquisition cause the threshold to shift not more than a few percent. Experience with manually selecting a threshold teaches that shifting the threshold by up to 20 percent, only causes the black to white boundary in the binarized image to shift up to 5 pixels. The 20% shift is far beyond what the automated thresholding procedure yields and even the inexperienced eye would find the binarized image obtained with such a threshold an unrealistic representation of the real image. So, the entire chain of acquisition and processing of high speed images will not contain errors larger than 4 pixels.

The error of the dynamic pressure largely depends on the measurement range of the amplifier. The measurement range of the amplifier was set to ± 1 bar, whereas

the amplitudes without external excitation turned out to be in the order of 30 mbar. In order to quantify the error made by the sensors, the dynamic pressure was measured in a pressurized CRC (at 10 bar) without combustion for a duration of ten seconds, with a large number of dynamic pressure sensors. The pressure traces recorded are basically the statistical noise (or error) produced by the measurement chain, including the amplifiers. These 'measured errors' had a root mean squared (rms) that varied from 0.5 to 3.6 mbar, thus the measurement uncertainty for the dynamic pressure measurements is 3.6 mbar. Since the found rms values are different for all sensors, these rms values are allocated to the corresponding sensors in the dynamic pressure analysis (Chapter 5). In that analysis, only the noise in the frequency band of the 1T-mode is of interest, and therefore the rms values of the filtered signals are more relevant. The rms values of the filtered signals of the individual sensors have been evaluated and lie between 0.02 and 0.14 mbar.

4.2.2 Error propagation

The measured physical quantities are used to calculate other quantities in order to for example verify the operating conditions. These indirectly measured quantities contain a measurement uncertainty. This measurement uncertainty is made up of all the errors that can occur during data acquisition and processing until the final (indirect) quantity has been determined. The behavior of the measurement uncertainty is described by the Gaussian error propagation law, given in equation (4-9), and can be found in any textbook dealing with mathematical statistics and error estimation/propagation.

$$\Delta U = \sqrt{\left(\frac{\partial U}{\partial x}\right)^2 \Delta x^2 + \left(\frac{\partial U}{\partial y}\right)^2 \Delta y^2 + \left(\frac{\partial U}{\partial z}\right)^2 \Delta z^2} \quad (4-9)$$

In this relation is U the indirectly measured quantity, as a function of x, y and z, and Δx , Δy and Δz are the maximum measurement uncertainties of the respective variables which in the case of directly measured quantities are given by the manufacturer.

If U depends on the product of a number of measured quantities,

$$U = x^n \cdot y^m \cdot z^l \quad (4-10)$$

relation (4-9) can be rewritten as follows.

$$\frac{\Delta U}{U} = \sqrt{n^2 \left(\frac{\Delta x}{x}\right)^2 + m^2 \left(\frac{\Delta y}{y}\right)^2 + l^2 \left(\frac{\Delta z}{z}\right)^2} \quad (4-11)$$

As an example, let U be the density, and determine the measurement uncertainty of the density as indirect quantity, depending on pressure and temperature through the universal gas law, given in (4-12).

$$\rho = \frac{p}{RT} \quad (4-12)$$

The measurement uncertainty for the density is then

$$\frac{\Delta\rho}{\rho} = \sqrt{\left(\frac{\Delta T}{T}\right)^2 + \left(\frac{\Delta p}{p}\right)^2} \quad (4-13)$$

For methane, the measurement uncertainty for temperature is 0.4% of the measurement value. And for the pressure the uncertainty is 0.15% of the measurement range, which comes to about 53 mbar in the injector exit. Assuming 2 bar combustion chamber pressure the relative uncertainty $\Delta p/p$ comes to about 0.03%. Substituting in (4-13), this amounts to 0.4% for the relative measurement uncertainty for the density.

For liquid oxygen, there is no simple relation between the density and the pressure and temperature, but the relation can be found in tables such as [161]. With use of these tables, it is estimated that a liquid oxygen temperature error of 5 degrees in the operating range of the test facility (between 75 and 90 K) would cause an error in the density in the order of 2%. The maximum error in the oxygen temperature given by the manufacturer [150] is about 1.5%, which is only about 1.25 degrees. Linearly interpolating ($2\% * 1.25/5$) then yields a measurement uncertainty in the oxygen density of less than 0.5%.

For both fluids, there is an additional error made in measuring the temperature in the injector. The temperature is not measured at the injector exit, but somewhat upstream. For liquid oxygen, the error made is in the same order of magnitude as the sensor error, but for methane the error may be in the order of 10 or even 15 degrees [37], which amounts to a few percent. So, in order to take these errors into account, the density error uncertainty for oxygen is set to 1% (instead of 0.5%) and for methane the cumulative uncertainty comes to 5% (instead of 0.4%).

One can use the measurement uncertainty of the indirectly measured quantity again to find other operating parameters as well. The injection velocity (4-14) for example depends on direct and indirect variables.

$$V_f = \frac{\dot{m}_f}{\rho A} \quad (4-14)$$

So the uncertainty in the injection velocity of methane is calculated as follows

$$\frac{\Delta V_f}{V_f} = \sqrt{\left(\frac{\Delta\rho}{\rho}\right)^2 + \left(\frac{\Delta\dot{m}_f}{\dot{m}_f}\right)^2} \quad (4-15)$$

The mass flow rate is measured directly and the uncertainty given by the sensor manufacturer is 0.5%. The uncertainty of the density was calculated previously

and amounts to 0.4%. That yields an uncertainty for the methane injection velocity of up to 0.64%. This process can be repeated for all relevant parameters, and the determined measurement uncertainties for a number of operating parameters are summarized in Table 4.2.

As can be learned from Table 4.2, the errors of operating parameters in the entire chain from measurement to data processing are not negligible, but acceptable. In most cases, the measurement uncertainties will therefore not be included as for example error bars in the figures on experimental results in Chapters 5, 6 and 7. The uncertainty due to the image processing procedures is acceptable as well, and will therefore also only be included as error bars on some occasions to clarify the scatter patterns as well as to make it easier to interpret the results from the optical diagnostics in Chapter 6.

Table 4.2: Measurement uncertainty of selected operating parameters due to error propagation

Quantity		Measurement uncertainty
Density injector exit	• Methane	5.0%
	• LOx	1.0%
Mixture ratio		0.51%
Injection velocity	• Methane	5.0%
	• LOx	1.0%
Velocity ratio		5.1%
Momentum flux ratio		11%
Weber number	• Low velocity range	2.7%
	• High velocity range	10%
High speed camera	• Core Length	< 8% (~1 L/D)
	• Flame angle	< 7% (~ 2°)

5 Experimental results: Dynamic Pressure

In section 3.3 the order and logic of the test program was discussed and each different test campaign explained. All campaigns yielded specific results which have been collected and integrated here. In this chapter, the results brought forth by the analyses of the dynamic pressure are presented and a differentiation has been made between tests with and without external excitation, sections 5.1 and 5.2 respectively. A separate section (5.3) is dedicated to the derivation and analysis of the pressure field in the CRC under all possible conditions.

5.1 CRC without external excitation

Figure 5.1 shows a typical spectrogram of a hot flow test without external excitation. The first 4 eigenmodes can be clearly seen, and such spectrograms can be used to manually identify the modes for further analysis, or, in case of anomalies, the identification of time intervals where the ‘stationary’ combustion deviates from its average. To learn more about the signal than where the eigenmodes are, the dynamic pressure sensor signals are investigated in more detail by looking at the noise.

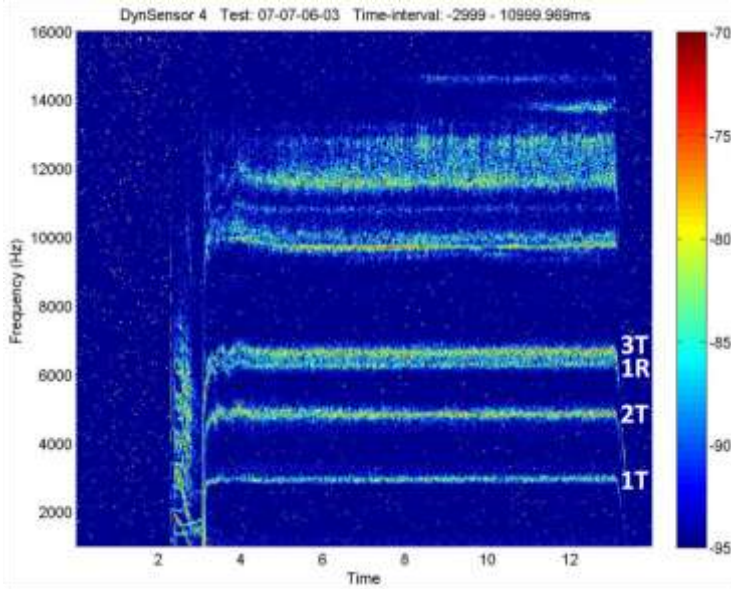


Figure 5.1: Typical spectrogram of a hot run without external excitation

5.1.1 Noise

Past experience (for example [59]) shows that the first tangential mode is the most dangerous and that useful correlations might be found in analyzing specifically the 1T-mode. In order to not overlook any possible information the pressure signal might contain, the raw, unfiltered, dynamic pressure, in the ‘stationary’ time interval (see section 4.1 on data reduction), is analyzed as a whole. Combustion noise of the tests without external excitation clearly displays several eigenmodes. This is illustrated in Figure 5.2, showing an example of an FFT of one of these tests.

To compare noise levels of all tests without excitation, the mean pressure fluctuation is determined by calculating the root mean squared (rms) of the pressure signal (5-1).

$$p'_{rms} = \sqrt{\frac{\sum_{i=0}^N (p'_i)^2}{N}} \quad (5-1)$$

The result is shown in Figure 5.3. In this figure, p'_{rms} is correlated with the Weber number (repeated in equation (5-2) for convenience). The Weber number negatively correlates with droplet size as for example Ibrahim [72] shows, so when the Weber number is high, the droplets are small.

$$We = \frac{\rho_{ox}(V_f^2 - V_{ox}^2)D_{ox}}{\sigma} \quad (5-2)$$

Thus, for the same injected propellant volume, a higher Weber number means a more homogeneous spatial distribution of propellant. And this homogeneity could have an influence on how efficient coupling between combustion and the acoustic field is. Obviously, from Figure 5.3, the general combustion noise does not correlate with the Weber number (or with any other significant quantity such as momentum flux ratio J ; not shown), and this method was therefore omitted for the remainder of the test program.

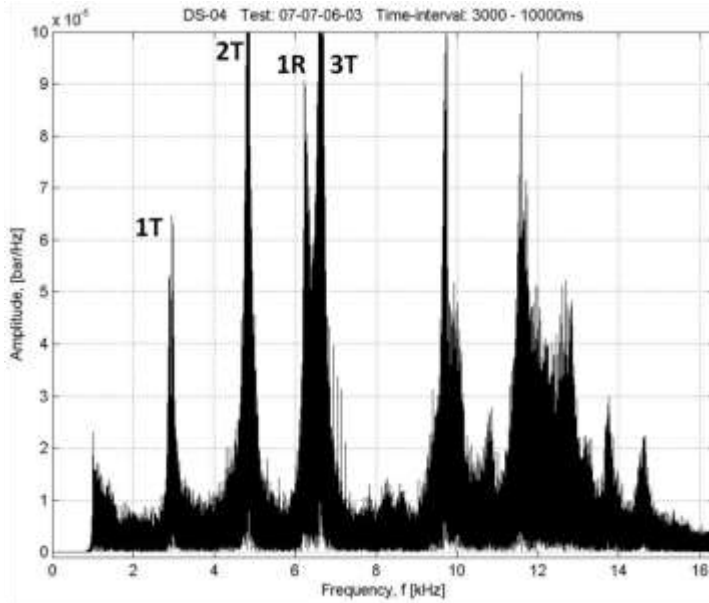


Figure 5.2: Typical FFT of a hot run without external excitation

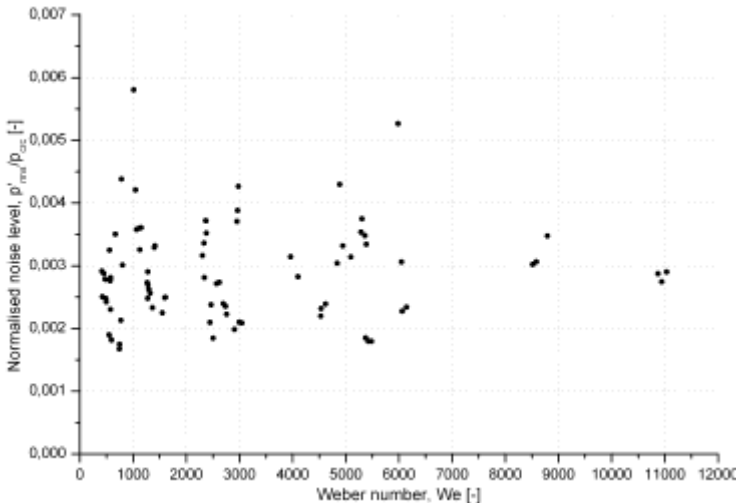


Figure 5.3: Correlation of combustion noise and the Weber number

5.1.2 Frequency shifts

During the same test campaign (without excitation), it was discovered that the distribution of the eigenmodes not always coincided with the theoretically predicted frequency distribution (see section 2.2) [144]. Theory prescribes a well defined distance between the different eigenfrequencies by means of a_{nm} . An FFT analysis of an exemplary test is shown (in black) in Figure 5.4.

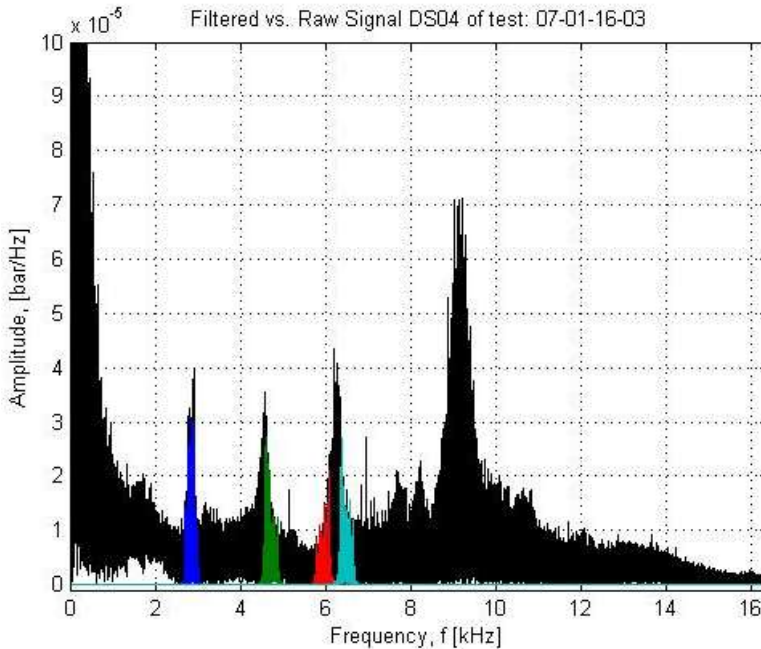


Figure 5.4: FFT spectrum with calculated and measured frequency peaks

The frequency of the first eigenmode was in Figure 5.4 manually chosen to agree with the peak in the experiment (blue), and the theoretical frequencies of the next 3 eigenmodes are drawn in green, red and cyan respectively. Since the speed of sound is a factor in calculating the eigenfrequency, the influence of local variations of the speed of sound (temperature, density) might explain this behavior. And it is a fairly realistic assumption that temperature and density are not uniform throughout the combustion chamber, hence gradients in speed of sound are also realistic.

A numerical simulation was carried out with an imposed non-constant distribution of the speed of sound, see Figure 5.5. The highest speed of sound is selected for the immediate area around the spray (yellow region), coinciding with the combustion zone, and the lowest for the remaining volume (blue region). The numerical results are summarized in Table 5.1. The important result of this analysis is that when the ratio of the speeds of sound, a_1/a_2 , is larger, the frequency of the tangential modes generally decreases and the distance between the tangential modes becomes smaller. A second effect is that the frequency of the radial modes increases and the distance between the radial modes becomes larger.

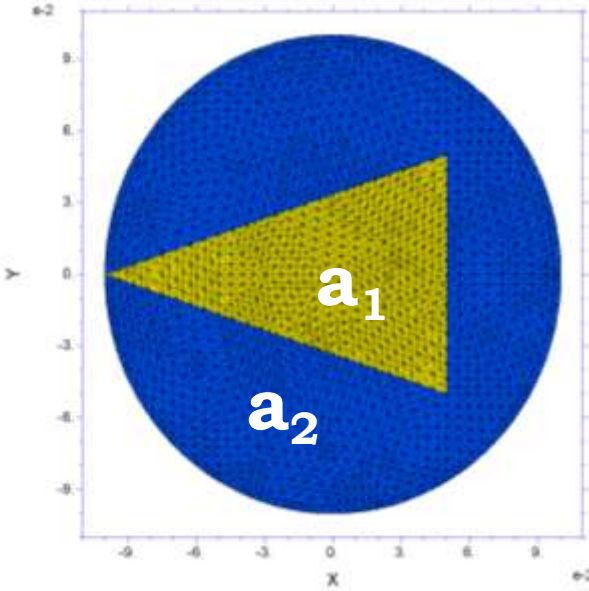


Figure 5.5: Regions with imposed non-constant distribution of the speed of sound

Table 5.1: Influence of a non-constant distribution of the speed of sound on the eigenfrequency distribution

$a_1 = 1100$	1T	2T	1R	3T
$a_2 = 1100$				
f_r	3223	5347	6708	7355
Ratio, f/f_{1T}	1	1.66	2.08	2.28
$a_1 = 1200$	1T	2T	1R	3T
$a_2 = 1069$				
f_r	3152	5224	6931	7165
f_{1T}	3185	5237		7192
Ratio, f/f_{1T}	1	1.65	2.19	2.27
$a_1 = 1300$	1T	2T	1R	3T
$a_2 = 1037$				
f_r	3071	5087	7068	6963
f_{1T}	3129	5109		7003
Ratio, f/f_{1T}	1	1.64	2.28	2.25
Experiment	1T	2T	1R	3T
Ratio, f/f_{1T}	1	1.57	2.6*	2.18

* Likely candidate for 1R. With the distribution in Figure 5.4, 1R could have even overtaken the 4T mode, which lies in this vicinity as well.

This can cause, when the ratio a_1/a_2 is large enough, that the shifts of the first radial mode to a higher frequency and the third tangential (3T) mode to a lower frequency are so big that the first radial mode overtakes the third tangential mode, so that the 3T mode (normally the fourth mode) becomes the third mode. These effects are summarized by the ratio of the frequencies with respect to the

1T frequency. For the tangential modes the frequency ratio becomes smaller for increasing a_1/a_2 , whereas the frequency ratio increases for the radial modes. Following this argumentation, the effect shown by Figure 5.4 can now be explained. The 2T mode is lower than calculated, caused by a ratio a_1/a_2 significantly larger than unity. This gradient also caused the 3T mode (theoretical frequency in cyan) to shift to a lower frequency, whereas the 1R mode (theoretical frequency in red) is shifted to a higher frequency. The two modes possibly ended up having a similar frequency which could explain why only 1 peak shows up in the FFT analysis where theoretically 2 peaks should lie closely next to each other (red and cyan).

In addition, the simulated distribution of the speed of sound has a similar effect as a secondary nozzle. The circular symmetry of the chamber is destroyed and the double valued tangential modes split up and their orientation fixed parallel and perpendicular to the remaining symmetry axis, as was discussed in section 2.2. The difference between the two parts of a split mode is too small to distinguish in an FFT analysis, but does grow for an increasing a_1/a_2 .

5.1.3 Energy content

Because combustion instabilities become more dangerous with increasing energy content of the pressure fluctuations, instead of combustion noise the energy of first eigenmode (1T) is calculated. To do so, the power spectral density (PSD [bar²/Hz]) is determined, which is elaborated in section 4.1 on data reduction. In the frequency domain, the PSD is then integrated over the resonance interval to determine the total energy (in [bar²]) of the 1T-mode. In order to be able to compare all tests, the total energy is normalized by (5-3) to find NPSD, which is a dimensionless quantity.

$$NPSD = \frac{1}{p_{CRC}} \sqrt{\int_{f_1}^{f_2} PSD df} \quad (5-3)$$

The calculated NPSD for all tests without external excitation is correlated with the Weber number in Figure 5.6. Operating points with identical mass flow rate have been plotted with the same color and symbol. It is obvious that a few operating points (circled in corresponding color) lie far outside the correlation described by the majority of the points. It has been pointed out in literature (Cheuret [18]) that this type of behavior could be caused by the flame not being attached to the injector. And also Moore [99] shows that lifted coaxial LOx/CH₄ diffusion flames are not uncommon. Such a lifted flame would be much more sensitive to pressure fluctuations than an anchored flame, and would therefore show higher energies in the 1T mode. Results with respect to flame phenomenology will be discussed in Chapter 6.

Every operating point was executed three times to guarantee reproducibility. This is true for all points along the correlation as well as the circled outliers. All equal colored points that form a set of 3 (or sometimes just 2) are one and the same operating point. That implies that the outliers are reproducible as well, which could support the theory that these are operating conditions at which the flame could not attach to the injector.

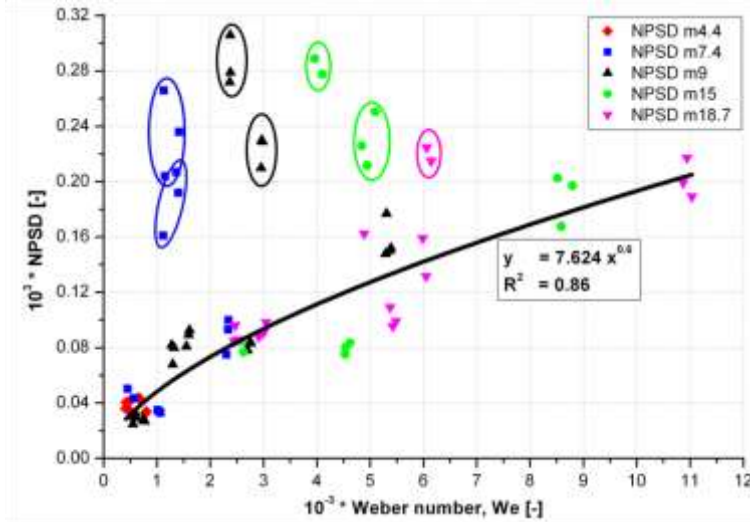


Figure 5.6: Correlation of energy content of 1T-mode with the Weber number for hot runs without external excitation

When ignoring the circled operating points, one finds a very good correlation, where the energy of the 1T-mode shows a power dependence on the Weber number. A higher Weber number means smaller droplets, hence a more homogeneous distribution of propellants. That means that when the droplets are small, the combustion processes transfer more energy into the acoustic field. Reformulated this implies that for higher Weber numbers, the interaction between the combustion chamber and acoustic field is stronger.

The same collection of operating points is plotted, in Figure 5.7, against the velocity ratio, R_V , which is defined as the injection velocity of CH₄ divided by the injection velocity of LOx (5-4).

$$R_V = \frac{V_f}{V_{ox}} \quad (5-4)$$

This quantity is a measure for the relative velocity of CH₄. The physical effect of this ratio is similar to that of the momentum flux ratio (introduced in section 2.8.2, repeated in (5-5)) because it depends on, besides the density of the propellants, the square of the velocity ratio.

$$J = \frac{\rho_f}{\rho_{ox}} \left(\frac{V_f}{V_{ox}} \right)^2 \quad (5-5)$$

If this value is higher, the spray break up length is shorter [158], and the droplets are more evenly distributed into a larger volume of the combustion chamber, resulting in a more homogeneous combustion. When ignoring the same points as in the relation for the Weber number, Figure 5.6, one finds, for every operating point with the same mass flow, a strong linear correlation (through the origin)

between the energy content of the 1T-mode and the velocity ratio. Also in Figure 5.7, it is not difficult to see that the circled points lie far outside the correlation that the other points follow. And, without exception, the correlations are of high quality ($R^2 > 0.85$). Physically this means that the previously mentioned more homogeneous combustion allows a stronger interaction between the burning CH_4/LOx -spray and the acoustic field. A similar distribution of operating points was found for the relation between NPSD and momentum flux ratio J , but the scatter made it impossible to define a clean correlation as for the velocity ratio and is therefore omitted.

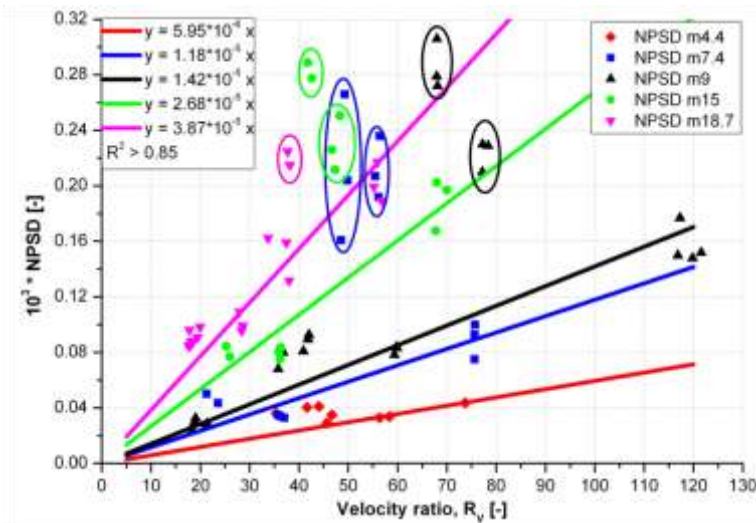


Figure 5.7: Correlation of energy content of 1T-mode with injection velocity ratio for hot runs without external excitation

5.1.4 Damping

In a combustion chamber, several processes influence the energy content of the turbulent flow. Both energy addition and dissipation take place simultaneously. These processes include, but are definitely not limited to, viscous interaction of the hot gas with the wall, geometric imperfections causing additional turbulence on top of the turbulence caused by the combustion itself, radial and angular acceleration which are more dominantly present in the CRC, due to its geometry, than in conventional combustion chambers, and so on. The energy these processes require, is taken from the total energy available and in doing so, they reduce the potential of the interaction to become unstable. This natural damping, surely, is for a rocket engine in operation a good thing. The damping can be analyzed by again investigating the energy of the fluctuation. More specifically, the characteristics of the energy density of the fluctuation (PSD) are used to quantify the damping, see section 4.1. These characteristics are found by fitting a Lorentz profile, $L(f)$, (5-6) to the PSD around the 1T-frequency. The linewidth Γ in this relation, represents the damping.

$$L(f) = \frac{1}{\pi} \frac{\Gamma}{(f - f_0)^2 + \Gamma^2} \quad (5-6)$$

Of course, for any physical meaning to be awarded to the shape of a PSD and conclude anything with respect to damping, the signal of which the PSD was taken must be ‘stationary’. With or without external excitation, combustion in the CRC experiments is considered stationary 3-4 seconds after ignition.

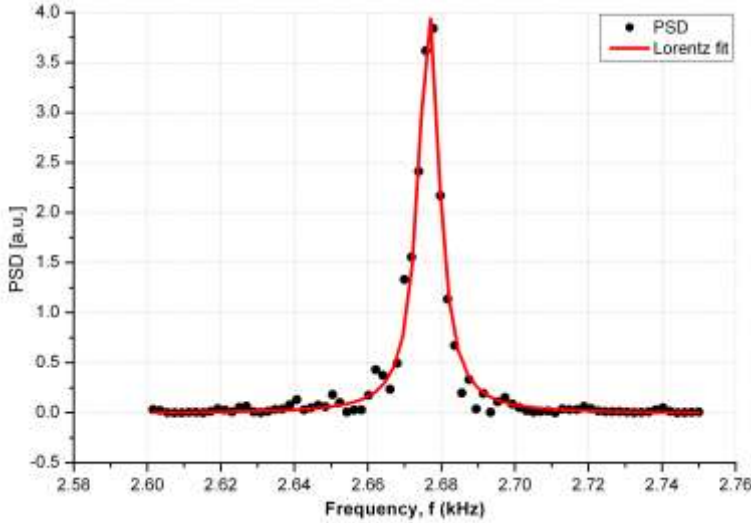


Figure 5.8: Lorentz profile fitted to PSD

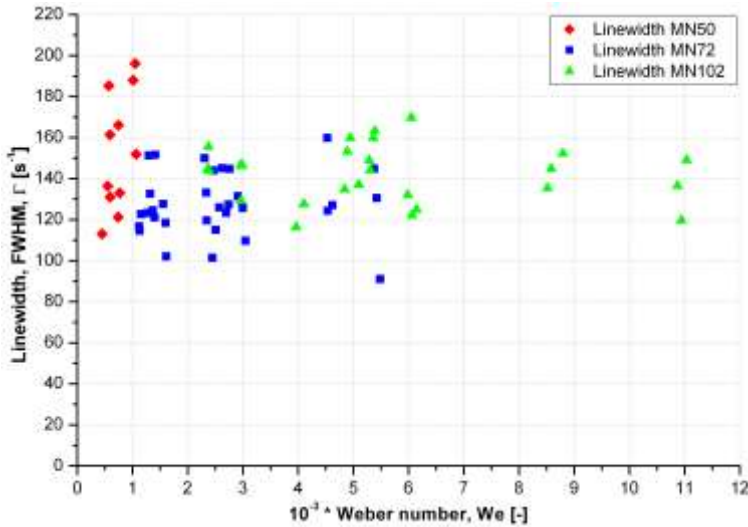


Figure 5.9: Relation of line width of the 1T-mode with the Weber number for hot runs without external excitation

But the excitation causes the pressure signal to be unstationary, because the frequency of the excitation changes with time (see section 2.7.3, ramping). Strictly speaking, one could analyze such a short time interval that the frequency increase of the excitation is negligible with respect to the line width and as such the signal can be considered quasi-stationary. But, based on the obtained results, this approach was not further pursued. An example of a Lorentz fit is given in Figure 5.8. The fit quality, $R^2 > 0.9$, is representative for most signals.

The damping was determined for all applicable tests and correlated to several operating and injector conditions that could have an influence on damping. Unfortunately no correlations have been found. Figure 5.9 and Figure 5.10 show the relations of the damping of the first tangential (1T) mode with the Weber number, and with the momentum flux ratio.

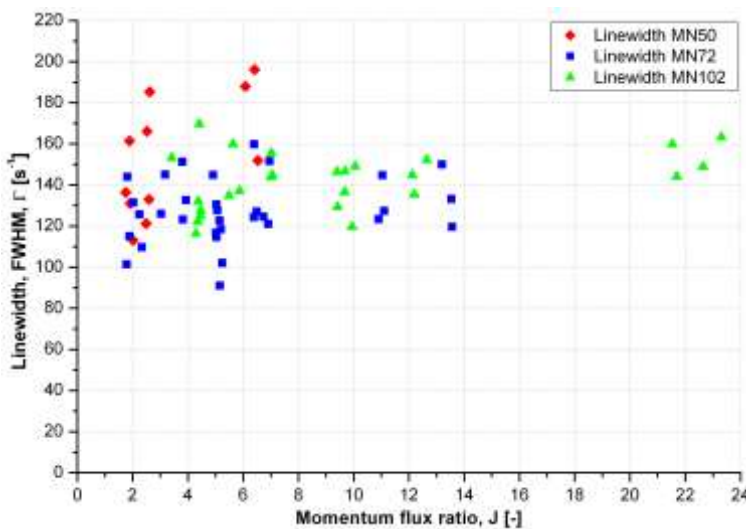


Figure 5.10: Relation of line width of the 1T-mode with the momentum flux ratio for hot runs without external excitation

5.2 CRC with external excitation

External excitation was applied to increase the amplitudes of the dynamic pressure. The main focus of the test series was to develop some understanding of what influence the external excitation had on the combustion chamber processes, especially in comparison with the results from the tests without external excitation. For this reason, many operating points that were executed without excitation were repeated with external excitation, see section 3.3. All operating points were executed with 4 angular positions of the secondary nozzle in order to fix the nodal line of the pressure field at different orientations and investigate the effects of this relative orientation.

5.2.1 Introduction

The excitation gradient (ramp steepness, [Hz/s]) has a strong influence on the amplitude of the pressure fluctuations, as was discussed section 2.7.3 (illustrated Figure 2.16). High amplitudes are of interest because it improves the signal to be analyzed, which in turn increases the possibility of finding a correlation with operating or injector conditions. The duration of excitation, therefore, was chosen to be as long as possible, but avoiding the risk of not capturing the entire line width. It was decided to increase the excitation frequency during 5 seconds with 80 Hz/s, covering 400 Hz. The resonance frequency was targeted to be in the middle of the ramp, considering 100 Hz on each side as the domain of resonance where combustion starts to respond to the excitation but is not at full resonance yet. And another 100 Hz on each side allows taking into account uncertainty due to the possibility that the eigenfrequency shifted to a lower or higher frequency as a result of temperature differences due to for example the inhomogeneous propellant distribution in the chamber or even due to the variability (uncertainty, see section 4.2) of the operating conditions. For example, assuming an average temperature of 3000 K, an increase in temperature of 100 degrees, causes, through

$$a = \sqrt{\gamma RT} \quad (5-7)$$

an increase in the speed of sound of about 20 m/s. In turn, such an increase in the speed of sound yields a rise of the eigenfrequency of the first tangential mode ($\alpha_{10} = 1.841$), with equation (5-8) (first introduced in section 2.2.1)

$$f_{nm} = \frac{\alpha_{nm} a}{2\pi R} \quad (5-8)$$

of roughly 30 Hz. So, a change in temperature results in a change of frequency roughly equal to 30% of the magnitude of the change in temperature. So, the 100 Hz kept on either side of the assumed resonance domain is more than enough to account for possible temperature inhomogeneities in the combustion chamber. This method proved to be successful in always capturing the resonance domain in its entirety.

In Figure 5.11 an example is presented of a spectrogram and a corresponding dynamic pressure trace, with time (in ms) on the horizontal axis. A spectrogram procedure performs an FFT analysis for a very small time interval (hence quasi-stationary with respect to the input signal, therefore allowed) and does so for the entire time domain. The pronounced frequency is the external excitation which is seen to start at 2450 Hz and starts increasing at $t = 4s$ to 2950 Hz at $t = 9s$. In the pressure trace in the bottom part of Figure 5.11, it can also be seen that the intensity of the fluctuation starts increasing around $t = 4.8s$ (visible in the spectrogram as well), and reaches its maximum at $t = 5.8s$, after which it starts to decrease again.

Due to the nature of excitation, the generated pressure fluctuations in the secondary nozzle are not purely sine wave shaped. Hence, overtones are formed

which can be clearly seen in the spectrogram, Figure 5.11. The shape of the generated pressure wave depends on the opened (closed) area of the secondary nozzle (SN) exit.

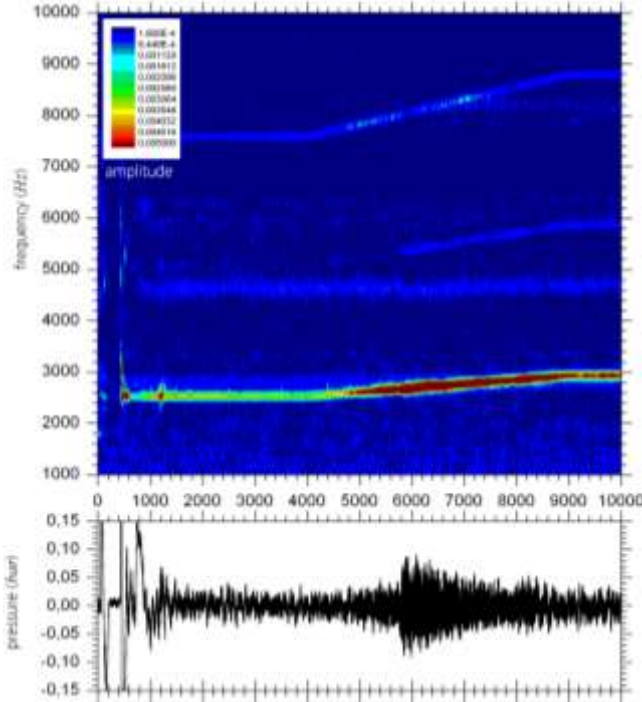


Figure 5.11: Typical spectrogram and corresponding pressure trace for a hot run with external excitation

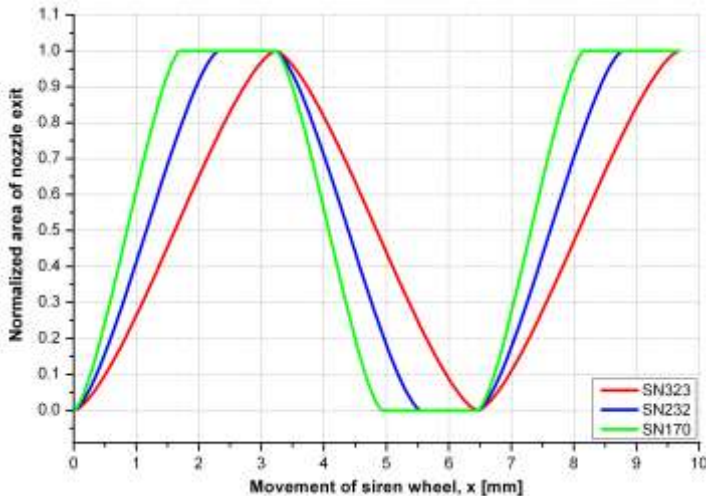


Figure 5.12: Excitation profile for 3 different secondary nozzle exit diameters

The development of the exit area for the three applied secondary nozzles is shown in Figure 5.12. Because for every SN the same siren wheel was used, with its teeth dimensioned such that the largest SN could be closed off completely, the smaller secondary nozzles show a less harmonic behavior for the exit area. For hot fire tests with smaller SN up to twelve overtones appear. To illustrate this, a PSD is shown in Figure 5.13. The excitation frequency is about 2430 Hz, and ten overtones (red arrows) are distinguishable [144].

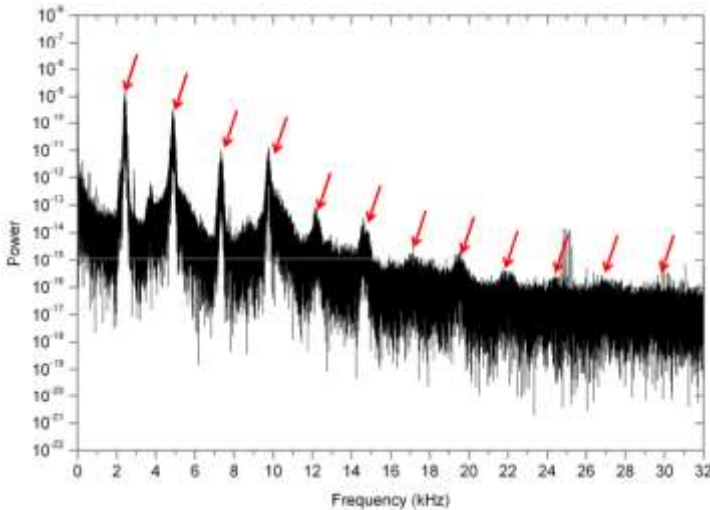


Figure 5.13: Power spectrum with overtones

5.2.2 Energy content

The NPSD has been calculated for the tests with external excitation in the same way as for the tests without external excitation. In Figure 5.14 is shown how the NPSD correlates with the Weber number, where again is distinguished between different mass flows by differentiating color. It should be noted that, compared to tests without excitation (Figure 5.6), the order of magnitude of the NPSD of the tests with excitation is 1000 times higher.

The behavior of the NPSD in relation to the Weber number is similar to the correlation for tests without external excitation, but unfortunately, the scatter is too large to fit a decent correlation and is therefore omitted. The range of NPSD for a small range of Weber numbers is remarkable, and it is unclear at this point what causes this spread. A possible explanation, as for the unexcited tests, would be that a lifted flame causes the large scatter but this could not be verified yet. Another, more likely, explanation is that, due to the procedure of taking apart the excitation system to change the position of excitation on a regular basis, the distance between the exciter wheel and the secondary nozzle exit was not constant for all tests. When the distance is larger, the SN cannot be closed off as effectively causing the modulation to be weaker, and vice versa. And it is reasonable to expect the scatter to be much smaller when a small number of tests are repeated with only one excitation position.

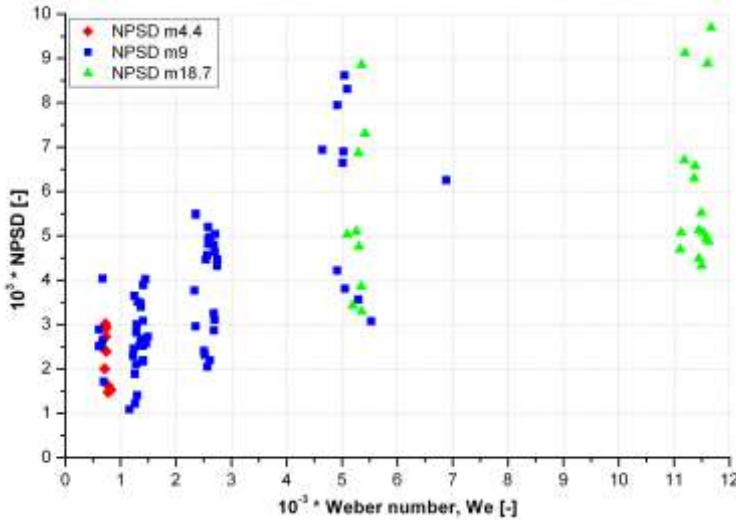


Figure 5.14: Correlation of energy content with the Weber number for hot runs with external excitation

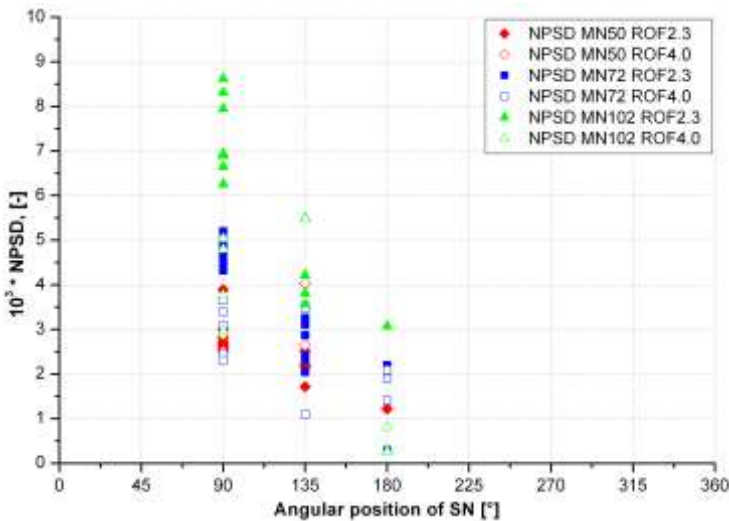


Figure 5.15: Correlation NPSD with angular position of the SN

The test campaign with external excitation consisted of executing every operating point with four different angular positions of the SN, see section 3.3.2. In Figure 5.15, the energy of the excited fluctuation, NPSD, is plotted against the excitation angle, where position 5 and 13 are both considered to make a 90° angle, position 9 makes a 180° angle, and position 11 a 135° angle [144].

It is obvious that the energy of the fluctuation shows a strong dependence on the angular position of the SN. The highest energy is reached for a 90° angle, and the lowest for 180° . The acoustic pressure field in the CRC with secondary nozzle is

again shown in Figure 5.16. Apparently when the nodal line of the pressure field lies closest to or in the combustion zone, the response is highest. This implies that the response is highest when the highest velocity fluctuations occur in the combustion zone, which in turn could mean that the dominant coupling mechanism to transfer energy from combustion to the acoustic field is velocity driven. Coupling mechanisms will be elaborately discussed in Chapter 7.

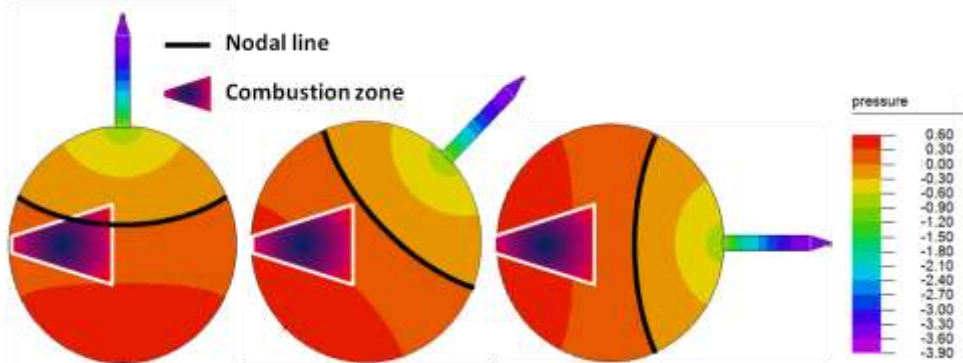


Figure 5.16: Acoustic field in the CRC with secondary nozzle (3 positions)

5.3 Pressure field

One of the important goals of this research is to find evidence of which processes in the combustion chamber are responsible for the coupling between combustion and acoustics to sustain combustion instability. In order to do so, through the Rayleigh criterion, repeated in (5-9) for convenience [118],

$$\iiint_V \int_T p'q'dt dV > 0 \quad (5-9)$$

it is necessary to compare the pressure fluctuations and the fluctuations of the heat release (OH-intensity, see Chapter 6) in great detail. Hence, the need arises to know the temporal behavior of the pressure field in the combustion chamber, or at least in those regions where heat release is significant. The results on reconstruction of the pressure field in the combustion chamber are discussed in this section. Chapter 7 is dedicated to the comparison between the pressure field and the OH-intensity field.

The experimental results with respect to the pressure field without external excitation will be shown in section 5.3.1. These results represent only 1 test. The analysis has been carried out for a large number of hot fire tests under many different operating conditions and for all cases results of similar quality were obtained. The results with respect to the pressure field with external excitation cover a series of tests and will be elaborately discussed in section 5.3.2.

5.3.1 CRC without external excitation

In the past fifty or so years, it was always assumed that the acoustic field takes the form of a standing wave (see [59] or [159]) or a spinning wave, as has been theorized by Clayton [19], [20] and again by Harrje and Reardon [59] in the 1960s and 1970s, or more recently by Litchford [89]. The spinning waves are considered to be the most dangerous. During discussions [37] spinning waves were thought to have a constant rotational velocity of the nodal line because no experiment reported on in literature was found to indicate otherwise. So, it was expected that the pressure field of the 1T-mode in the CRC would, just as the reported cases in literature, either appear as a standing wave or a spinning wave with constant rotational velocity of the nodal line. An elaborate discussion with respect to spinning modes was given by Sliphorst [141]. The standing wave and the spinning wave, as derived in section 2.4.1, in the CRC are given by equations (5-10) and (5-11) respectively.

$$p'(r, \theta, t) = 2J_1\left(\alpha_{10}\frac{r}{R}\right)M \cos(\theta) \cos(\omega t) \quad (5-10)$$

$$p'(r, \theta, t) = J_1\left(\alpha_{10}\frac{r}{R}\right)M \cos(\theta + \omega t) \quad (5-11)$$

There are two fundamental differences between the two. The first one is that for the standing wave, the temporal variation of p' measured by the sensors along the combustor wall are either in phase or in anti-phase, for all angular positions θ . For the spinning wave, the phase depends on the position of the sensor (θ). The second difference is that the amplitude of the standing wave depends on the angular position of the sensor. For θ equal to 90° or 270° the amplitude becomes zero, corresponding to the fixed nodal line of the standing wave. For the spinning wave there is, at any instant in time, an angle theta for which $\cos(\theta + \omega t) = 1$, which yields a maximum p' . The maximum propagates along the combustor wall with angular velocity ω , and all sensors will detect a signal with the same maximum amplitude, but with a phase shift corresponding to their mounting position θ .

Summarizing, if a standing wave presents itself in the CRC, the signals measured by the sensors distributed around the circumference of the combustor must be either in phase or in anti-phase with a nodal line fixed at one position. A spinning wave would show constant amplitudes for all signals, with a varying phase shift between the sensors.

In Figure 5.17 an exemplary sample of wall pressure measurements, two-way filtered (see section 4.1.2) at the 1T-frequency, is presented. It shows that neither the amplitudes are constant nor are the signals in phase or anti-phase. So, the experimental data did not show the signature of a standing or a spinning wave. In addition, the characteristics of the wave were observed to vary with time.

The analytical derivation of the pressure field for the CRC without cavities is given in section 2.1. The pre-processing and further preparation of the pressure data was elaborated in section 4.1.2. Here the actual determination of the pressure field will be briefly discussed.

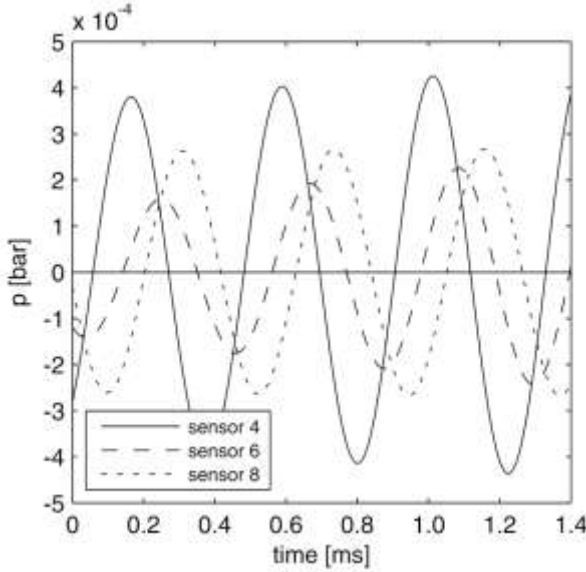


Figure 5.17: Typical set of several dynamic pressure traces measured at the combustion chamber wall

The pressure field in the entire combustion volume is fixed when the pressure distribution along the wall is known. So, in order to derive the pressure field in the combustor, it is required to first determine the wall pressure distribution, which is described by equation (2-42), and is repeated here for convenience.

$$p(\theta, t) = A \sin(\theta - \varphi) \quad (5-12)$$

The pressure distribution in dependence on θ is fitted to a few discrete measurements. An example is shown in Figure 5.18. The circles are a sample of dynamic pressures at one instant in time, to which equation (5-12) is fitted.

It was observed that sometimes the data showed an offset, which physically means that the fluctuation of the dynamic pressure is not symmetric around zero.

$$p(\theta, t) = A \sin(\theta - \varphi) + p_{off} \quad (5-13)$$

The values of the offset determined from the experimental data are generally small. Why the experimental data show such an offset is not yet understood. A possible solution is briefly discussed in section 4.1 on data reduction. The fitting procedure has been carried out with and without offset. The obtained results for the essential characteristics of the 1T-mode are practically identical.

Figure 5.18 shows the fit with and without offset. Because the agreement between the experimental data and equation (5-13) is very good and the fits ob-

tained with offset resulted in a smaller residual, it was decided to carry out the entire analysis with offset. The fit procedure was carried out with a least squares method with a trust-region algorithm (discussed in for example [22]) to minimize errors.

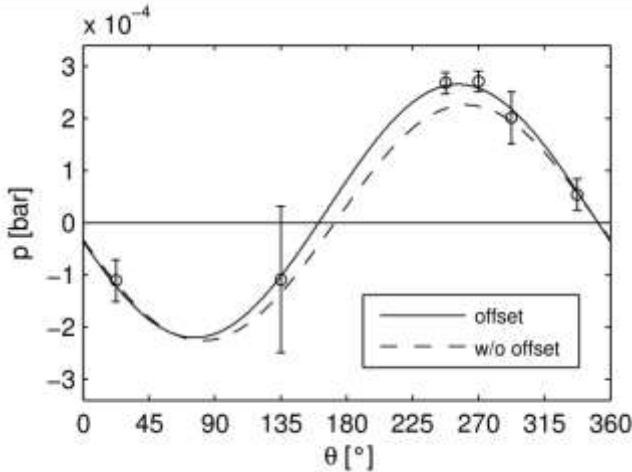


Figure 5.18: Fitted wall pressure distribution

After the wall pressure distribution has been determined, isobars in the interior are determined as in intermediate step. These isobars are sampled at discrete points to generate a grid that is the input for an interpolation using a Delaunay-Triangulation [36] with which the pressure at virtually any set of coordinates in the CRC can be determined. A more elaborate discussion on determination of the wall pressure distribution and the pressure field is given in [53].

With equation (5-14),

$$\varphi = -\arcsin\left(\frac{(M + N)\cos(\omega t)}{\sqrt{M^2 + N^2 + 2MN\cos(2\omega t)}}\right) \quad (5-14)$$

derived in section 2.4.2, the orientation of the nodal line of the 1T-mode is determined. Figure 5.19 shows the development of the orientation of the pressure field for the duration of one test, during stationary conditions. The direction of rotation of the nodal line apparently changes frequently, even though the nodal line prefers a specific direction.

The insert shows a zoom into 50 ms to illustrate the typical time scale of such a direction change. The typical time scale was found to be 8-10 ms, equivalent to 20-25 oscillations of the 1T-mode. Figure 5.20 shows a close-up of a small time interval that shows a direction change.

A direction change always happens according to the same sequence of events. A spinning wave with a rotating nodal line with constant rotational velocity changes its character slowly into a standing wave with fixed nodal line. The angle's rate of change is almost constant first and exhibits an increasingly stepwise character, exhibiting all features already seen in Figure 2.8 for the various ratios M/N.

When the angle's rate of change reaches zero, the direction of rotation is switched. After the direction change, the angle's rate of change slowly loses its stepwise character until it becomes constant again and the process starts over. In the data shown in Figure 5.20, a rotating wave with almost constant angular velocity develops into a standing wave in less than 8 milliseconds.

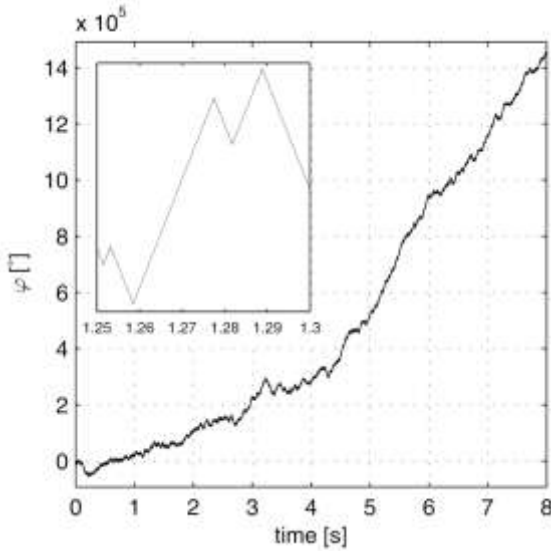


Figure 5.19: Temporal development of the orientation of the pressure field

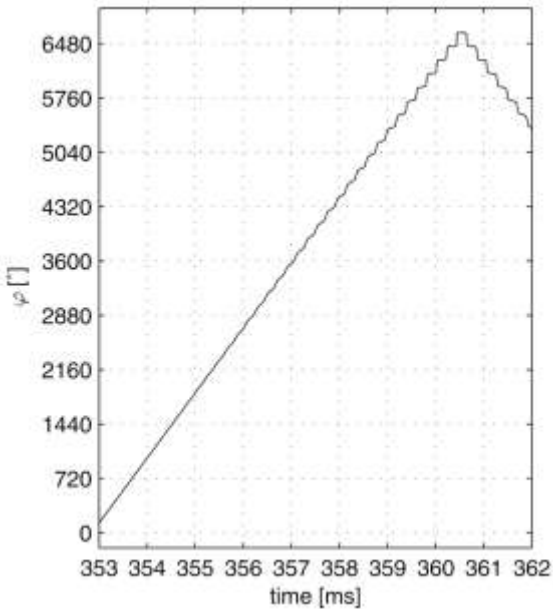


Figure 5.20: Change of direction of the pressure field's rotation

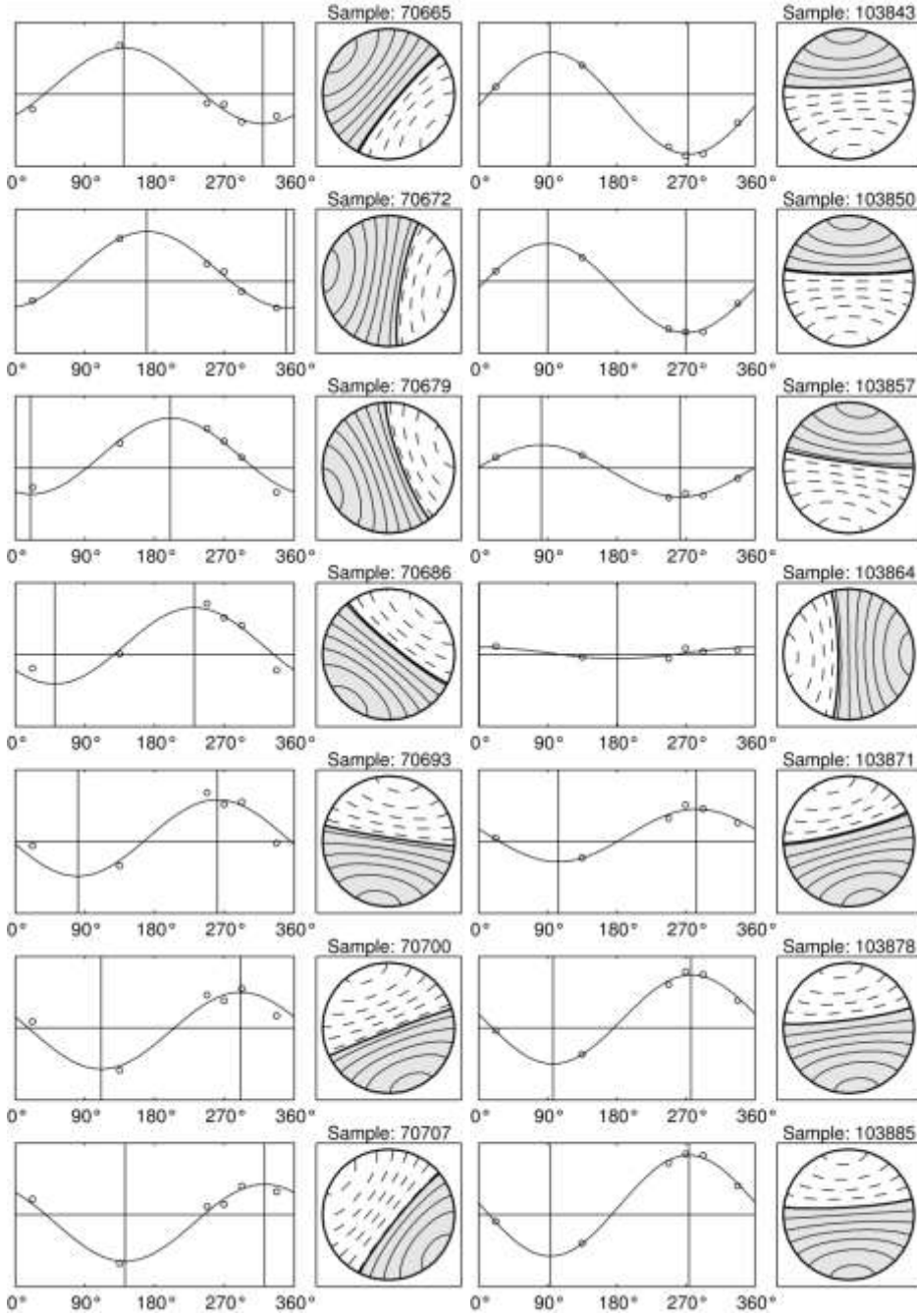


Figure 5.21: Rotating wave with constant angular velocity (left), and almost standing wave (right)

The different characters of the rotating wave that occur in the CRC are shown in the image sequences of Figure 5.21. The left sequence of Figure 5.21 (Video 1) shows a propagating wave with almost constant angular velocity. Note that the samples shown are equidistant and show a constant change of orientation. The right sequence of Figure 5.21 (Video 2) shows an almost standing wave with a very high rate of change of the orientation angle φ in the middle of the sequence. The robustness of the procedure that derives the pressure field from the wall pressure measurement has been verified by applying the procedure to a significantly distorted synthetic signal. Synthetic white noise with an rms value of 0.12 mbar in the 1T frequency range, which is almost 100% of the maximum measured error determined in section 4.2.1 on only 1 sensor, was superimposed to all sensors. The total signal of the sensors now consisted of a synthetic white noise and a synthetic sine wave with a same order of magnitude amplitude. This can be considered as the worst possible case simulation, and resulted in a relative error for the amplitude of $\Delta A/A = 13\%$ and an absolute error for the phase of $\Delta\varphi = 15^\circ$. Considering the occurrence of this size of measurement error is rare even for 1 sensor, it is virtually 0 to occur for all sensors at the same time. This means that the procedure is very robust and fairly insensitive to measurement errors.

Determination of the Spinning mode's character, M vs. N

The dependence of the amplitude A on the values of M and N (2-43) was derived in section 2.4.2, and is repeated here for convenience.

$$A = J_1(\alpha_{10})\sqrt{M^2 + N^2 + 2MN \cos(2\omega t)} \quad (5-15)$$

The coefficients M and N for the clockwise and counter-clockwise spinning waves respectively can easily be obtained by inverting equation (5-15). The maximum amplitude A_{\max} and minimum amplitude A_{\min} during one period are readily determined from the experimental data. An example of the temporal evolution of the amplitude is shown in Figure 5.22, where A_{\max} and A_{\min} are symbolized by circles and diamonds respectively.

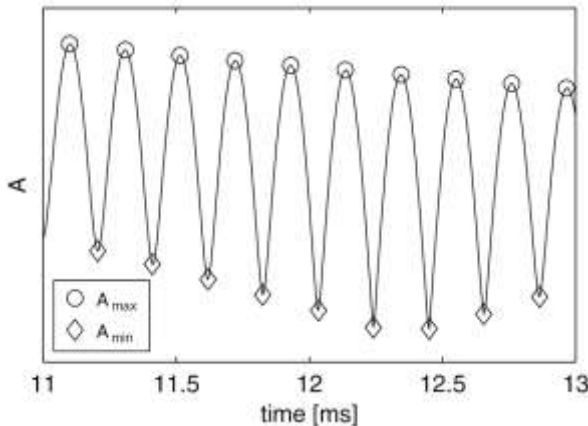


Figure 5.22: Temporal development of the oscillation's amplitude

When taking into account, in equation (5-15), that A_{max} and A_{min} occur for $\cos(\omega t) = \pm 1$ respectively, and following the convention that A , M and N are always positive numbers, the following equations for A_{max} and A_{min} are found.

$$A_{max} = J_1(\alpha_{10})(M + N) \quad (5-16)$$

$$A_{min} = J_1(\alpha_{10})|M - N| \quad (5-17)$$

Solving equation (5-16) and (5-17) for M and N yields

$$M = \frac{(A_{max} + A_{min})}{2J_1(\alpha_{10})} \quad (5-18)$$

$$N = \frac{(A_{max} - A_{min})}{2J_1(\alpha_{10})} \quad (5-19)$$

For a brief time interval, the evolution of $M(t)$, $N(t)$ and $\varphi(t)$ is shown in Figure 5.23. For $M > N$, φ is negative and the rotation is clockwise and for $M < N$, φ is positive, hence the rotation is counter-clockwise. If the two curves intersect ($M = N$), a standing wave occurs as well as a change of direction of rotation which can be seen from the development of φ .

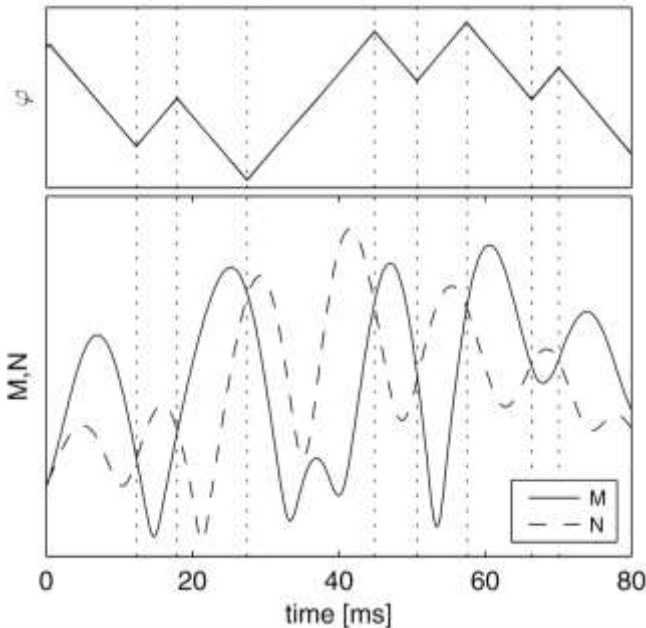


Figure 5.23: Temporal development of rotating mode's characteristics, M , N and φ

The evolution of the propagating wave seems to be a fairly arbitrary process. However, the propagating wave apparently does have a preferred orientation. Figure 5.24 presents a histogram showing the orientation φ of the nodal line that is evaluated at every instant in time. It is obvious that preferred orientation lies around 110° , measured from the injector in clockwise direction. It was assumed that the CRC was perfectly cylindrical, but it is, of course, not quite. There are a number of small volumes acoustically connected to the CRC at different modules along the wall, such as the injector, igniter, purging orifices and other volumes, see section 3.1. The result of a modal analysis (numerical solution of the eigenvalue problem, (2-28)) of the CRC including these small cavities is shown in Figure 5.25. The position of the nodal line of the numerical analysis coincides with the experimentally found preferred position.

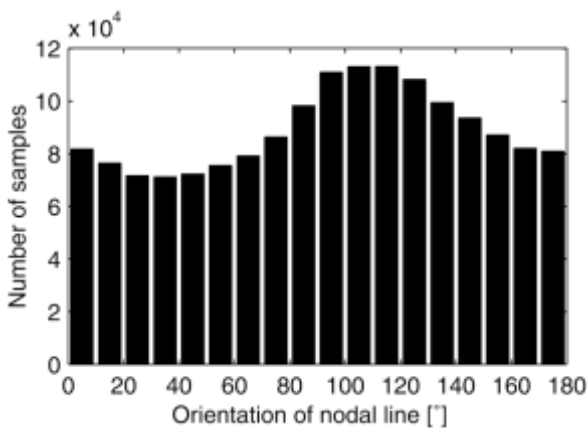


Figure 5.24: Histogram of rotating wave's position

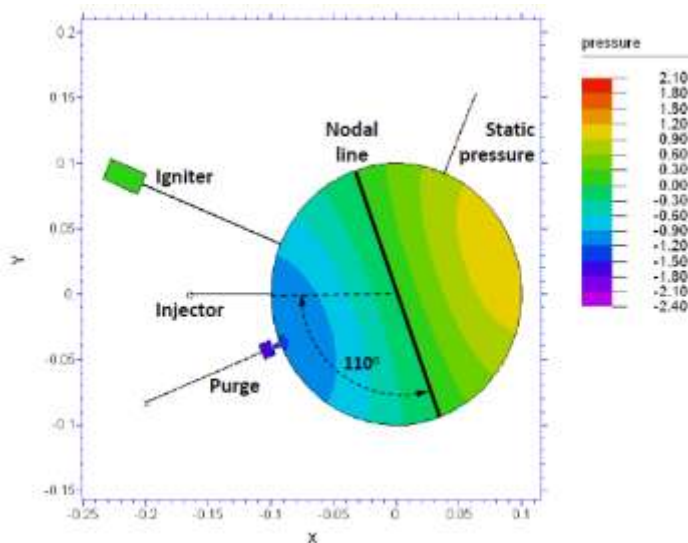


Figure 5.25: Modal analysis of CRC with additional cavities

Offset

The offset that was found is at times significantly large compared to the amplitude of the sine wave. Therefore it was studied more closely. In the aforementioned simulation of a synthetic sine wave with a superimposed high amplitude white noise signal, also the offset signal was analyzed. The rms value of the offset signal of the simulation was found to be of the same order of magnitude as the rms value of the experimental offset signal. Because theory disallows such an offset, it can be concluded that the white noise in the simulation (or measurement errors in the experiment) are the one and only cause for this offset. Therefore, fitting with the offset parameter covers, at least partially, for the measurement errors and fitting without the offset parameter would actually falsify the found results because in that way the measurement errors would be assumed to be part of the actual signal instead of being an error.

5.3.2 CRC with external excitation

The CRC with a secondary nozzle for external excitation obviously is not cylindrical. The geometry has been modified to such an extent, that the asymmetry does not allow spinning modes anymore. On one hand, this simplifies the analysis because only one (limit) case of all possible solutions of the pressure equation (the standing wave) needs be considered. And for this standing wave, the acoustic field, at least theoretically, does not vary with time.

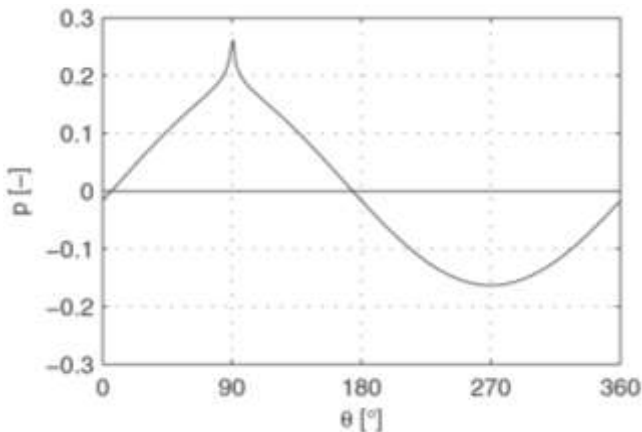


Figure 5.26: Numerical simulation of the instantaneous wall pressure distribution in the CRC with secondary nozzle

On the other hand, because the combustor's geometry is not rotationally symmetric anymore, it is no longer physically allowed to assume an analytical solution of the rotationally symmetric case for the wall pressure distribution, which complicates the analysis. The wall pressure distribution for a given test can be found compared to the result of a numerical simulation. In Figure 5.26, an example of a numerical simulation is presented. It can be seen that the pressure field no longer has a sinusoidal profile as the rotationally symmetric case. The secondary nozzle imposes its axis as symmetry axis of the acoustic field (here the SN is at

$\theta = 90^\circ$) and causes the angular position of where the pressure is zero to shift towards the position of the secondary nozzle. This means that the locations where the nodal line ($p = 0$) meets the wall, hence the nodal line itself is ‘pulled’ towards the secondary nozzle. A modal analysis yields an acoustic field which is scaled differently than the actual measurements, but the shape of the distribution is correct. Since the position of the secondary nozzle is known, the proper wall pressure distribution is then found by linearly scaling the numerical solution such that the amplitude of the discrete measurements are reproduced best. The basic three parameters, the amplitude A , an angle defining the orientation of the acoustic field φ and an offset p_{off} , are known from the determination of the wall pressure distribution without secondary nozzle (section 5.3.1). Since the CRC with secondary nozzle does not allow spinning modes, the parameter φ becomes obsolete and a different parameter was found to be necessary to improve results. This parameter ξ describes a distortion of the pressure field in comparison to the numerical solution where only the secondary nozzle is included as geometric deviation from the perfectly cylindrical geometry. Physically there is no argument to either way, since there is no reason to assume the combustor actually is perfectly cylindrical and therefore perfectly symmetrical (with respect to the secondary nozzle’s axis) or why the flow field would not impose additional (time-dependent) asymmetries causing the anti-node to shift.

It was found experimentally that the pressure anti-node on the opposite side as the secondary nozzle tends to move back and forth along the combustor’s wall. This behavior is captured with ξ , which denotes the angle over which the anti-node is shifted. The three fit parameters are illustrated in Figure 5.27. A number of tests have been analyzed both with and without ξ as a parameter, and it was found that other parameters, such as amplitude and offset, of the derived wall pressure distributions were only marginally different. Obviously, with ξ active, the pressure field in the interior is distorted somewhat as well, and the nodal line is rotated marginally, but also here the general characteristics do not change. Therefore it was decided for the fit of the wall pressure distribution to keep ξ an active parameter because it does decrease the error of the fit (the sum of the squared residuals was decreased).

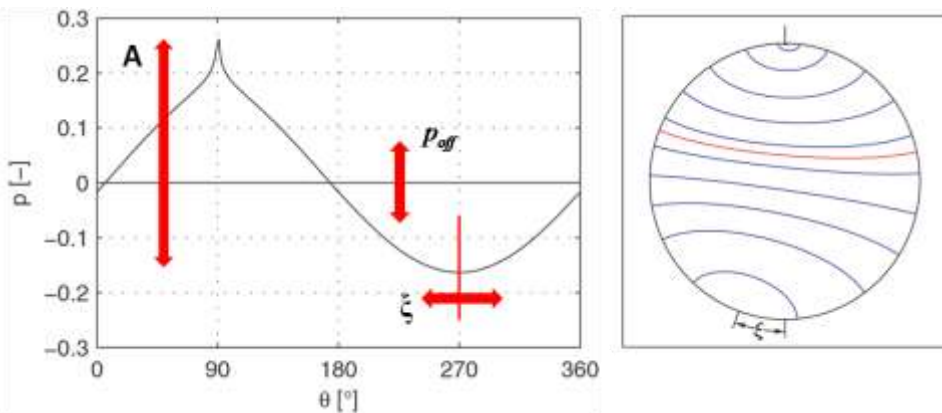


Figure 5.27: Fit parameters of the wall pressure distribution in the CRC with secondary nozzle [53]

Because the wall pressure distribution is not an analytical function, trust-region methods are inapplicable and the Downhill-Simplex method [101] is applied instead, which Press et al. [115] claim to be very robust at a price of slower convergence. The wall pressure distribution is then used in the same way as for the case without external excitation to interpolate the pressure field using a Delaunay-Triangulation [36], so first the isobars are defined and discretized as input for interpolation. The applied procedures are elaborately discussed in [53]. In Figure 5.28, an example of the fitted wall pressure distribution is shown. The secondary nozzle is again located at $\theta = 90^\circ$.

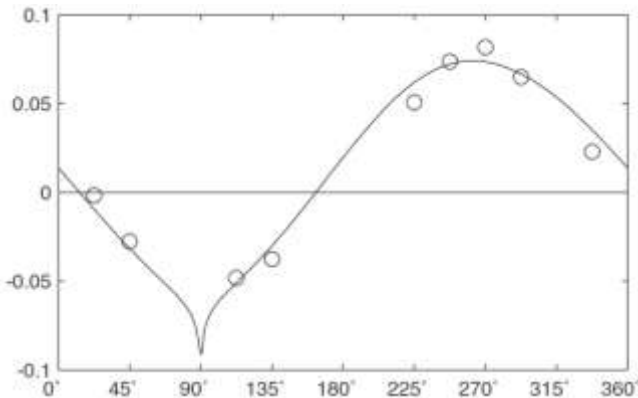


Figure 5.28: Typical fit of wall pressure distribution

The derived pressure field for the three positions of excitation is shown in Figure 5.29, Figure 5.30 and Figure 5.31. Three tests are presented here with identical operating conditions but with external excitation from three different angular positions. Note that the nodal line that faces the secondary nozzle is shifted and bent towards the secondary nozzle. More importantly, the scale of the figures is not the same. The amplitude of the pressure's anti-nodes decreases when the secondary nozzle is moved from 90° to 135° and to 180° (with respect to the injector, measured clockwise). This behavior substantiates the results found in section 5.2.2 where the energy contents of the fluctuations of all tests were compared as a function of angular position of the secondary nozzle. So, consequently, these results suggest velocity related processes as the responsible mechanism for combustion instability.

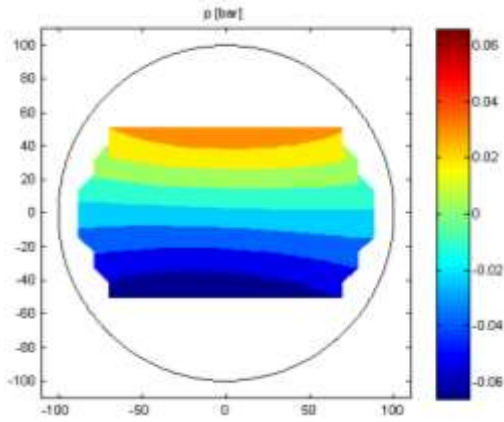


Figure 5.29: Typical pressure field for external excitation with $\theta = 90^\circ$

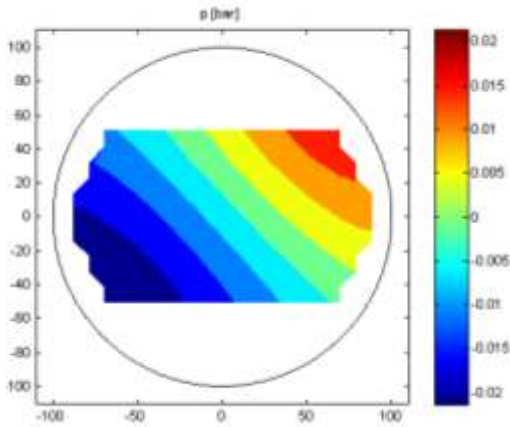


Figure 5.30: Typical pressure field for external excitation with $\theta = 135^\circ$

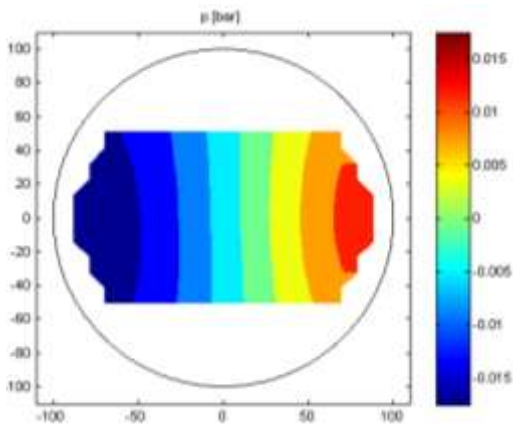


Figure 5.31: Typical pressure field for external excitation with $\theta = 180^\circ$

6 Experimental

Results: Optical

Diagnostics

This chapter treats the results of the analysis of the high speed image sequences. Spray and OH-intensity recordings are done with different acquisition rates due to hardware limitations. Since it was known from experience [37] that without external excitation, the recordings do not show any eigenmodes, focus lay upon spatial rather than temporal resolution. For tests with external excitation, the spatial resolution was traded for a better temporal resolution. The applied settings are shown in Table 6.1.

Table 6.1: Camera settings for individual test campaigns

	Temporal resolution	Spatial resolution
1 st campaign, w/o excitation	6,000 Hz	512x512 pixel
2 nd campaign, with excitation	12,500 Hz	256x256 pixel

To retrieve the information contained in the images, the images need to be binarized. As was discussed in section 4.1.3 on data reduction, a spatial class method called Random Sets [49] was applied for the spray images and an Entropy class method (Renyi's entropy [130]) was used for the OH-intensity images. The specifics and logic of binarization and the applied methods is also discussed in section 4.1.3. The results are presented in section 6.1 and 6.2 respectively for spray and flame phenomenology. Section 6.3 is then dedicated to the dynamic information content (fluctuations around the mean) of the OH-intensity images.

6.1 Spray Phenomenology

LOx-jet breakup could be an important factor in sustaining combustion instabilities. It could be that the ligaments are torn from the jet at a frequency to which coupling with the acoustic field is sensitive. In general, this is not considered likely because the characteristic time of jet breakup does not lie in the same order of magnitude as the eigenfrequencies, as for example Sirignano [139] describes. He argues that the time scale of jet atomization is an order of magnitude smaller than the acoustic oscillations (~ 0.1 - 1 ms). The order of magnitude of this time scale was confirmed by Benedictis [14]. Another possibility is that the droplets are released in an area where coupling between combustion and acoustic field is stronger.

6.1.1 Intact Core Length

From the spray recordings, it can be determined where jet breakup is terminated by analyzing the intact core length (ICL), or break-up length, of the spray. The ICL can be calculated in two ways. The first is the straightforward, axial (linear) length of the ICL, for which it basically is determined at what x-coordinate, with respect to the injector in the origin of the coordinate system, the ICL terminates. The second way determines the arc length of the liquid jet. The arc length is always longer than the axial length and is defined as the length of the center line of the jet. The center line is found as follows. First, at every axial position, the width (or height) of the spray was determined from the binarized (see section 4.1.3) image. Next, a point was defined at exactly half the width of the spray and a line

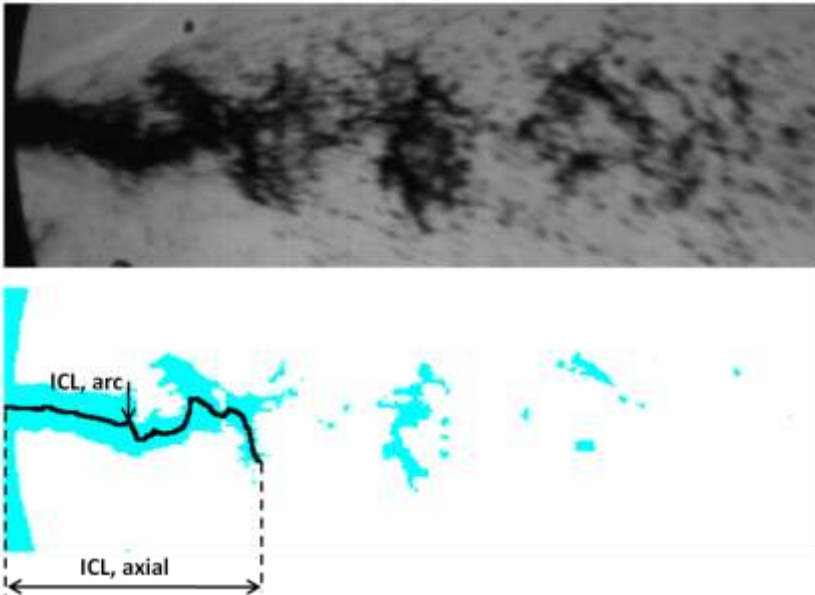


Figure 6.1: Definition of intact (liquid) core length (ICL)

connecting these points for all axial positions is defined as the center line, or the arc length of the jet. Both definitions are illustrated in Figure 6.1. In this way, some of the dynamic behavior is included in the analysis by taking into account the swinging sections of the jet which could become important when there's high jet-acoustics interaction. The difference in actual length between the two methods is illustrated in Figure 6.2. It shows the relation between the ICL and the momentum flux ratio. The data shown are generated by calculating the ICL for every image, and averaging over the number of images.

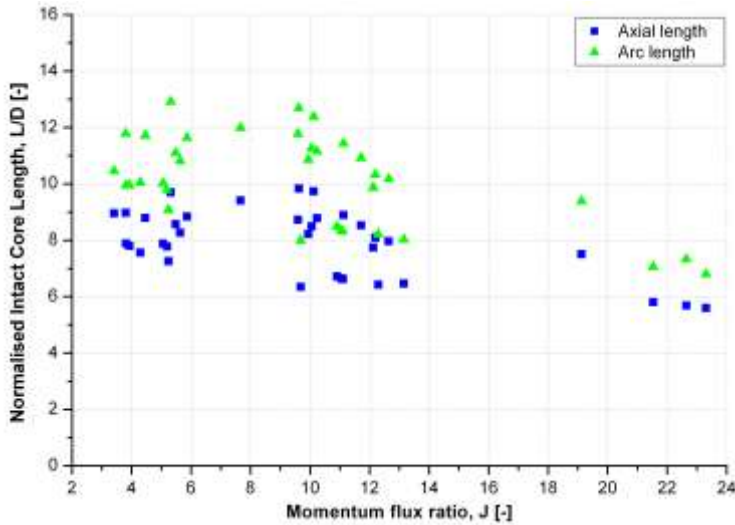


Figure 6.2: Relation between axial and arc intact core length and momentum flux ratio J

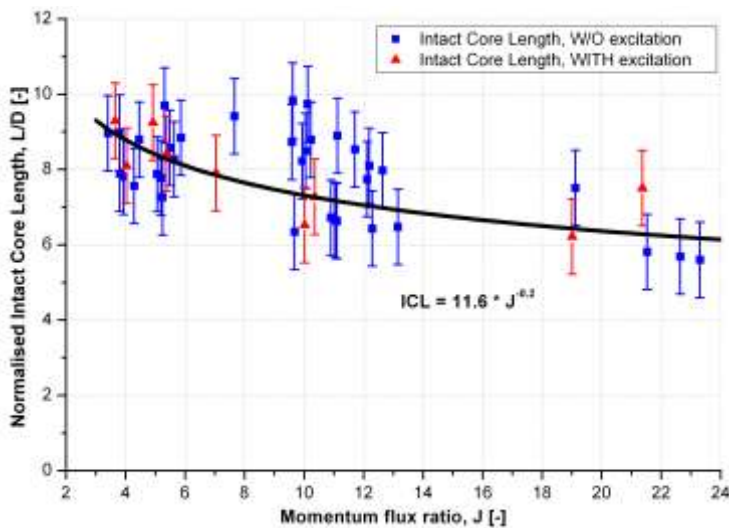


Figure 6.3: Correlation of the ICL with momentum flux ratio J

Because the general behavior of the arc length is very similar to that of the axial length, and is only linearly increased by about 30%, it will not be considered further in the following physical interpretation.

The correlation between the axial ICL and the momentum flux ratio is shown in Figure 6.3. In accordance to correlations found in literature [35], [158] a power dependence $\sim J^n$, with $n = -0.2$ was applied. The constant in this case (11.6) was only about half as large as was found by Davis (25) for subcritical atomization [35], but the correlation generally captures the trend shown by the measurements fairly well. The effect on the ICL of external excitation at 1T-frequency (typical amplitude at resonance: $p' = 150 - 200$ mbar) is also shown in Figure 6.3. Tests with excitation are shown in red and without excitation in blue. Even though the number of tests with external excitation is low, it is obvious that the points are well distributed throughout the scatter of the points without external excitation. Hence, in the CRC, external excitation hardly, if at all, influences the intact core length of the LOx-jet, which implies that jet breakup or primary atomization is not influenced. It is likely that the inertia of the LOx jet is too high to respond to acoustic waves.

6.2 Flame Phenomenology

Flame phenomenology could give insights in to where coupling between spray combustion and the acoustic field might occur. Specifically, the flame spreading angle describes the flame front, or boundary of the combustion zone, and therefore clearly shows the domain where combustion takes place. An exemplary set of images is shown in Figure 6.4. The flame spreading angle is defined as the the angle between boundaries of the spray (red lines in the binarized image), capturing the flame. It seems in the binary image, there exists a significant distance between the base of the flame and the injector. But when considering the original (average) image, the flame is connected, may it be with low intensity, to the injector. To find whether, and if so, how far, the flame is lifted off from the injector, a different type of analysis must be carried out. The images with the current spatial resolution do not allow such an analysis, and this type of analysis is left for follow-up research.

Combustion is only possible when the propellants have been properly mixed, and for this it is required that the propellants are distributed in the combustion chamber first. Therefore, the flame spreading angle has been correlated with the injector conditions that are related to the propellant distribution. The Weber number is inversely proportional to the (LOx-) droplet size, and momentum flux ratio measures the relative momentum of the gas jet compared to the LOx jet, hence the momentum with which the LOx droplets that are torn off are carried into the combustion chamber. It can be assumed that the higher this relative momentum is, the further the droplets are transported away from the jet.

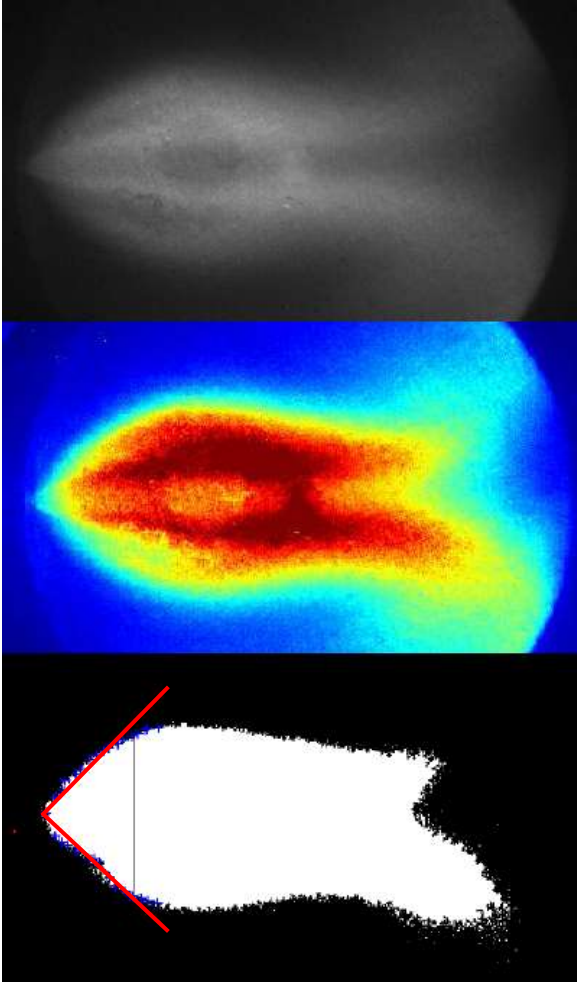


Figure 6.4: Exemplary set of the raw (averaged) OH-intensity (top), false color (middle), and binarized image (bottom)

Figure 6.5 and Figure 6.6 show a correlation between the flame spreading angle of tests without external excitation and the Weber number and the momentum flux ratio, respectively [144]. In these figures, only operating points with identical mass flows (9 g/s) are included. A distinction is made between main nozzles (MN), or, considering the constant mass flow, chamber pressures. For higher Weber numbers, the flame angle seems to decrease. Physically, this can be explained as follows. The droplets become smaller for higher Weber numbers, and therefore they evaporate more quickly. This implies that the droplets engage the chemical reaction faster, or in closer proximity to the spray, keeping the flame spreading angle smaller. Cuoco [33] observed an opposite effect, but without physical explanation. He does argue that lifted flames were often observed which would indicate the flames observed in the CRC are anchored, also the test cam-

paigns in the CRC were executed with a tapered injector, Cuoco had an injector without taper. A higher momentum flux ratio has a similar effect on the flame spreading angle as the Weber number. For higher momentum flux ratio, the droplets are carried into the combustion chamber further in the direction of injection, before combusting. The radial movement away from the LOx-jet is less influenced, which explains the smaller flame spreading angle.

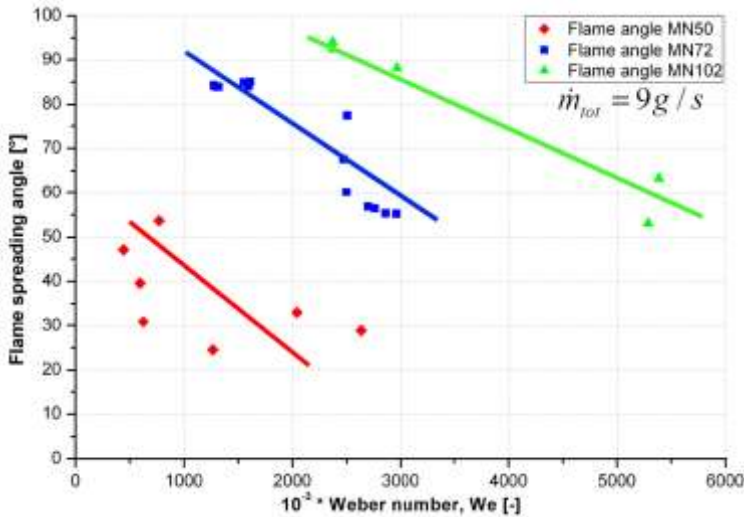


Figure 6.5: Correlation of the flame spreading angle and Weber number

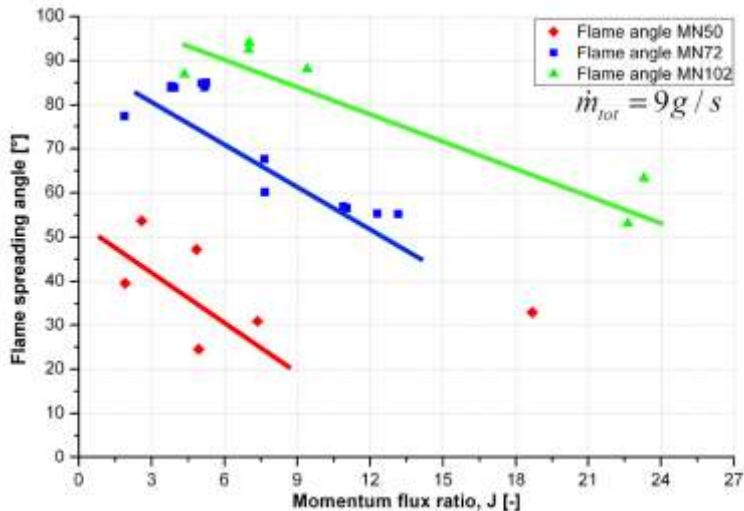


Figure 6.6: Correlation of the flame spreading angle and momentum flux ratio J

In Figure 6.7, the relation between the flame spreading angle and the mixture ratio, again for tests with constant mass flow, is shown. For increasing mixture

ratio (R_{OF}), the flame angle tends to increase as well. Which is physically consistent with the aforementioned relations between flame spreading angle and Weber number and momentum flux ratio, because both the Weber number and momentum flux ratio decrease for higher R_{OF} .

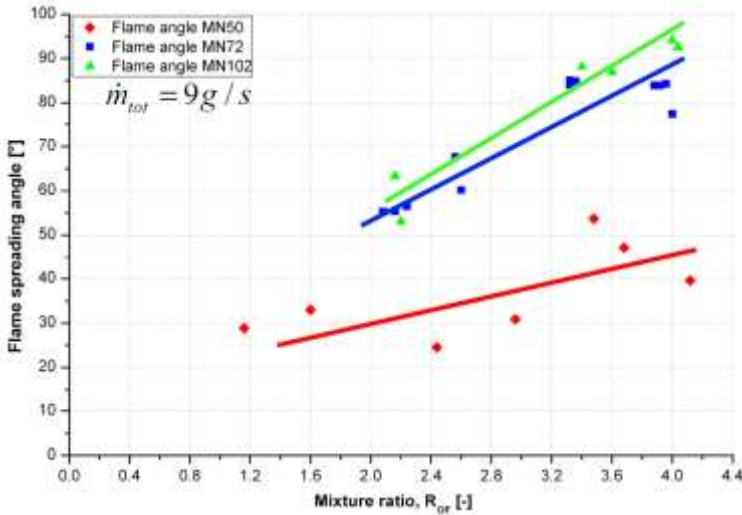


Figure 6.7: Correlation of the flame spreading angle and mixture ratio R_{OF}

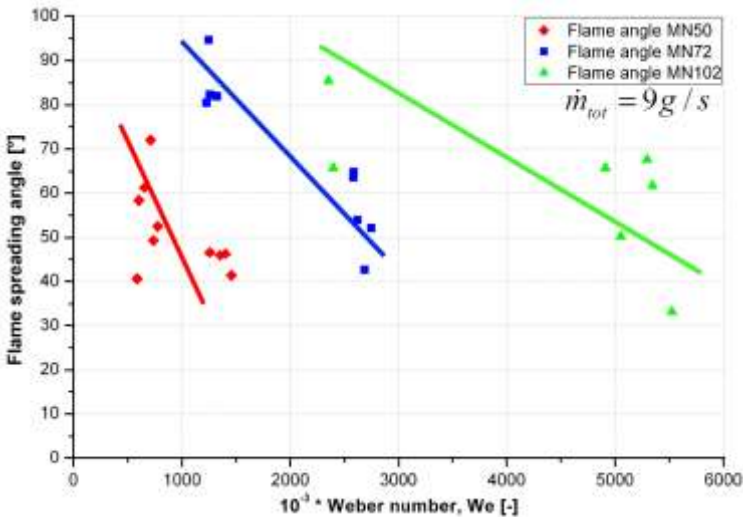


Figure 6.8: Correlation of the flame spreading angle and Weber number, with external excitation

In Figure 6.8 the flame spreading angle found for tests with external excitation is plotted against the Weber number. The correlation is similar as for without excitation, but the effect that the flame spreading angle becomes smaller for increas-

ing Weber number is enforced, compare Figure 6.5 and Figure 6.8. This implies that externally exciting the flame at the 1T-frequency causes the flame spreading angle to decrease. Physically that means the distance between the spray axis and the flame front is decreased due to external excitation, which in turn means that the transition from liquid jet to combustible gas mixture is taking place in a shorter distance, hence is accelerated.

In the spray analysis it was found that the ICL was not influenced by external excitation, hence the jet breakup was unchanged. Thus, the processes of injection and atomization are insensitive to external excitation and therefore are not likely to play a role in triggering combustion instabilities. Consequently, of all the processes leading up to combustion, the first two (injection and atomization) can be eliminated based on these experimental findings.

The next processes having a significant influence on where combustion takes place, and therefore controlling the flame angle, are vaporization and liquid heating. Vaporization is a pressure related process and the rate at which a droplet vaporizes depends on the relative velocity between the droplet and the surrounding gas. The gas passing by the droplet, takes away the newly formed gas, making room for more liquid to vaporize. This could explain the sensitivity to the external excitation, which forces an increased velocity field onto the combustion zone, increasing the velocity around the droplets, increasing the vaporization rate, accelerating the transition from liquid to combustible mixture, and therefore decreasing the flame spreading angle. This would agree with the elaborate theoretical discussion of Sirignano [139] on characteristic timescales of the individual combustion chamber processes. He basically identified vaporization (rate) as the only possible candidate for driving combustion instability because the characteristic timescale of only vaporization has the same order of magnitude as the acoustic oscillations.

The response of the combustion zone to acoustic oscillations, and the interaction between the imposed acoustic field and the intensity field will be elaborately discussed in Chapter 7.

6.3 Intensity fluctuations

6.3.1 Global analysis, large window method

The OH-, or flame intensity describes where combustion takes place, or heat is released. Experience shows that the flame intensity recorded during tests without external excitation do not show eigenfrequencies. This was verified by analyzing the frequency spectrum of the flame intensity of two tests, with similar operating point, but one with and the other without external excitation. The PSDs are shown in Figure 6.9 and Figure 6.10. As was described in section 4.1.3, two methods for intensity analysis were applied. For this purpose, the large window (see Figure 4.6) was used. Only Figure 6.10 shows a significant peak at the 1T-frequency. All peaks in Figure 6.9, as well as the peak in Figure 6.10 at 3.2 kHz are too sharp to be resonance peaks and have been proven to be camera settings related artifacts that cannot be avoided.

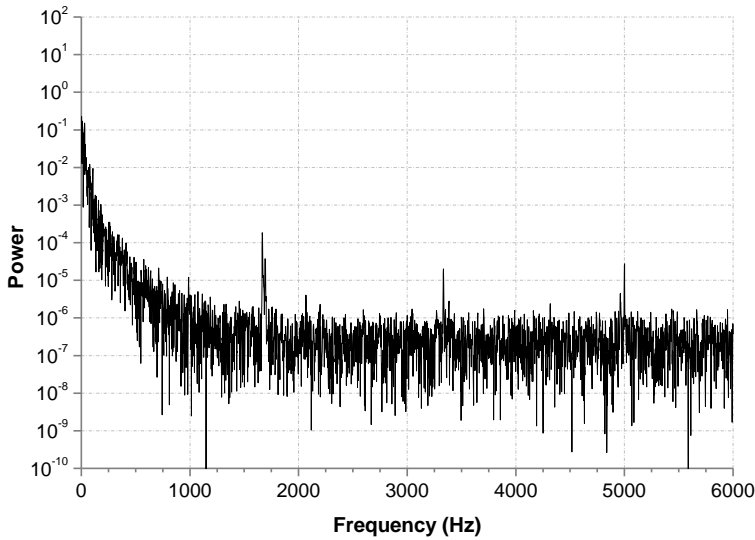


Figure 6.9: Sample PSD of flame intensity, without external excitation, $f_{1T} \approx 2525\text{Hz}$

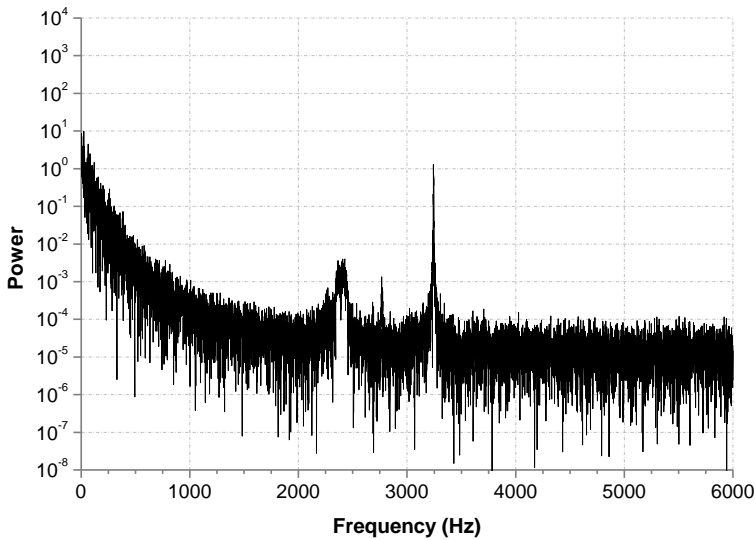


Figure 6.10: Sample PSD of flame intensity, with external excitation, $f_{1T} \approx 2375\text{Hz}$

2 ω Analysis

Knapp [80], [81], [82] assumed that for velocity coupling between combustion and the acoustic field, combustion responds to the magnitude of the velocity, hence should show a signal at double the excitation frequency (in this case at 1T-frequency). He argues that it is irrelevant whether the reacting molecules are excited by the velocity in upward or in downward direction (for $\theta = 90^\circ$) for them to respond to the velocity wave. This principle is illustrated in Figure 6.11, which

shows a wave of acoustic velocity (sine-wave), and the absolute value of the velocity. The magnitude of the velocity physically is a periodic signal with a frequency twice that of the velocity wave. Hence, if coupling were to occur through velocity, following this interpretation, combustion response should have a frequency twice the 1T-frequency.

The temporal structure of the global intensity (large window method) illustrated with the PSD in Figure 6.10, shows that there exists no response at double the 1T-frequency. Hence, it can be concluded that velocity coupling with the magnitude of the velocity does not occur.

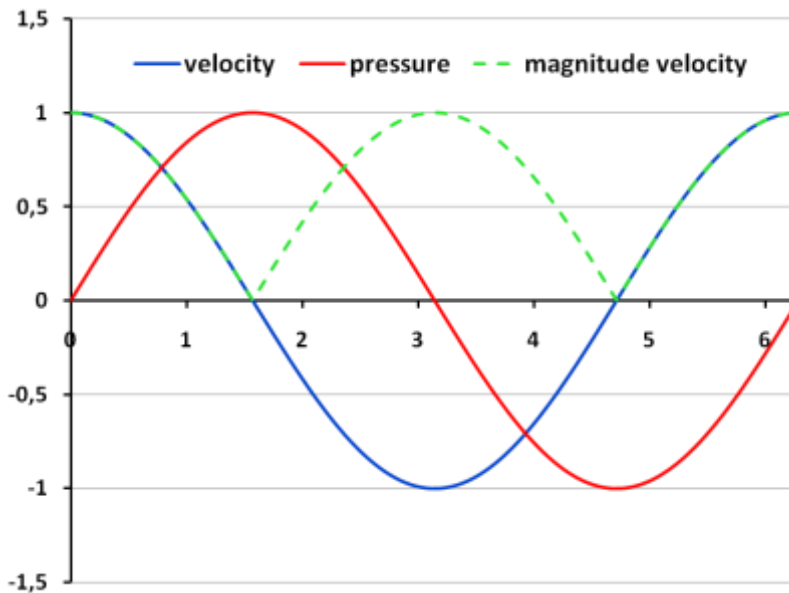


Figure 6.11: Relation between acoustic pressure and velocity

6.3.2 Local analysis, small window method

As an example of the behavior of the intensity throughout the flame, the variation of the local mean intensity of the flame analyzed with the small window method (see section 4.1.3, Figure 4.7) is shown in Figure 6.12 and Figure 6.13. They show the variation of the mean intensity in x- and y-direction respectively. The data is taken from a test, with external excitation with an angular position of the SN of 90° with respect to the injector axis. Figure 6.12 shows that the intensity directly next to the spray axis (black line) is at some coordinates lower than further away from the spray (blue and red lines). Surely, in the spray most volume is taken by the liquid jet, and therefore cannot combust to produce heat. This is substantiated by the distribution in y-direction, in Figure 6.13. Most sections show a sharp decrease around the middle coordinates, exactly where the liquid spray is.

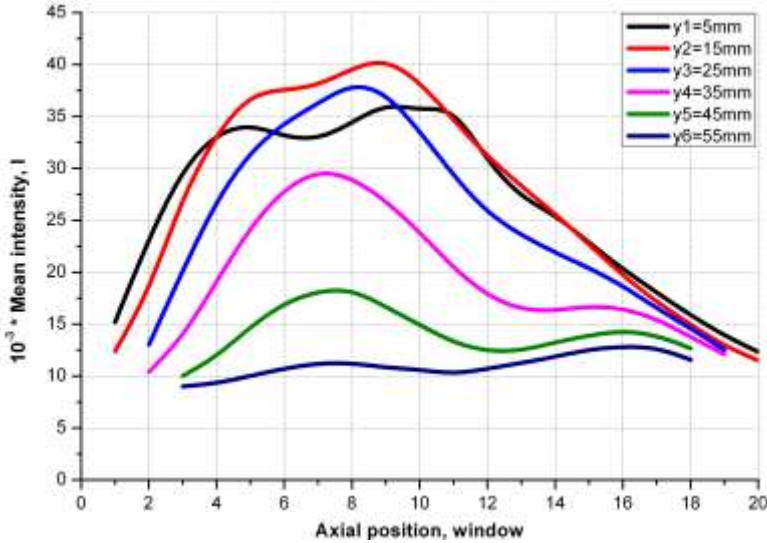


Figure 6.12: Variation of mean intensity in x -direction, at several y -values

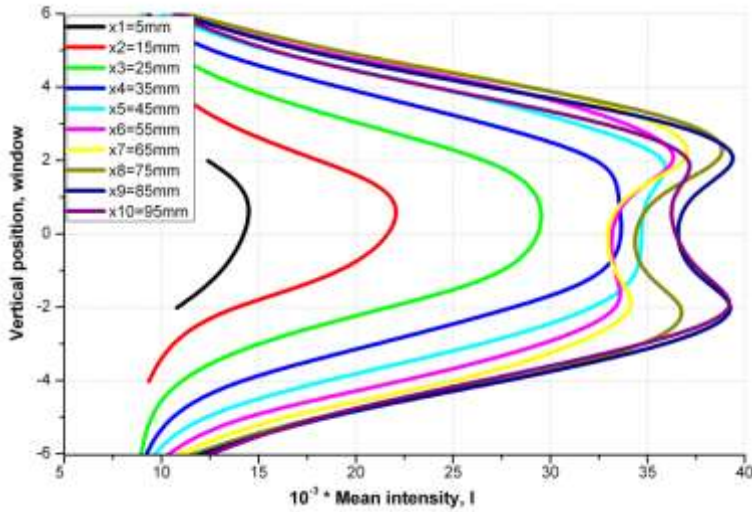


Figure 6.13: Variation of mean intensity in y -direction, at several x -values

Normalized intensity fluctuations

Since, in the first place, the intensity is measured to compute a response factor, see section 2.5.3, the spatial distribution of the normalized intensity fluctuations must be determined. The normalized intensity fluctuation (see section 4.1.3 on data reduction), I_{norm} , was defined as the measured intensity fluctuation divided by the mean intensity (4-8).

$$I_{norm} = \frac{(I - I_{mean})}{I_{mean}} = \frac{I'}{I_{mean}}$$

So, for every window a ‘measured’ intensity fluctuation is determined by averaging over the pixels in that particular window. This yields a set of time dependent intensity signals, for every window one signal. The mean is then determined for every window individually by time-averaging the signal. Finally, this local mean is subtracted from the local signal to yielding the local intensity fluctuation (I') per window, which is then divided by again the mean.

From here on normalized intensity fluctuation or intensity fluctuation will be used interchangeably. Generally, as for the dynamic pressure, the 1T-frequency is determined through an FFT procedure. And the I_{norm} signal is then filtered to clean up the signal.

So, for every window, this quantity is calculated, and inserted in the surface plot shown in Figure 6.14. The data is taken from a test with the secondary nozzle at 90° from the injector, measured clockwise, and the injector sits on the southwest side (SN at northwest side). Note that in this plot the maximum amplitudes of the fluctuations are shown, so the absolute value of the deviations from the mean. This plot clearly shows the concentration of reaction zone around the LOx-jet, which corresponds to the red concentration in the 2D false colors image of the same test shown in Figure 6.4.

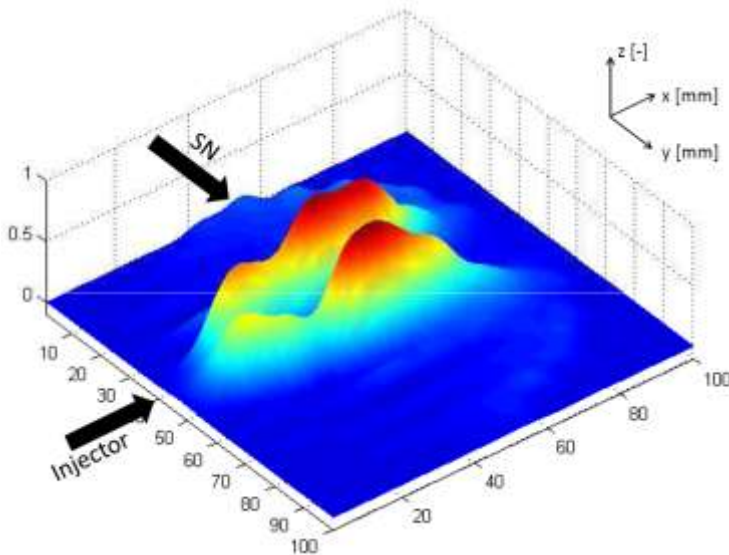


Figure 6.14: Surface plot of normalized intensity fluctuation

Additionally, the small window method was applied for an unexcited flame as well, to determine and compare the normalized intensity fluctuation distributions between tests with and without external excitation. Since an FFT does not show any resonance for the unexcited flame, the I_{norm} signal was band pass filtered around the 1T-frequency determined from the dynamic pressure signals of the same test. An example of such an intensity field for the same test without exter-

nal excitation, which was investigated with the large window method in the previous section, is shown in Figure 6.15. It does not show any structure whatsoever and a temporal dependence is also absent, which was also illustrated with the PSD shown in Figure 6.9.

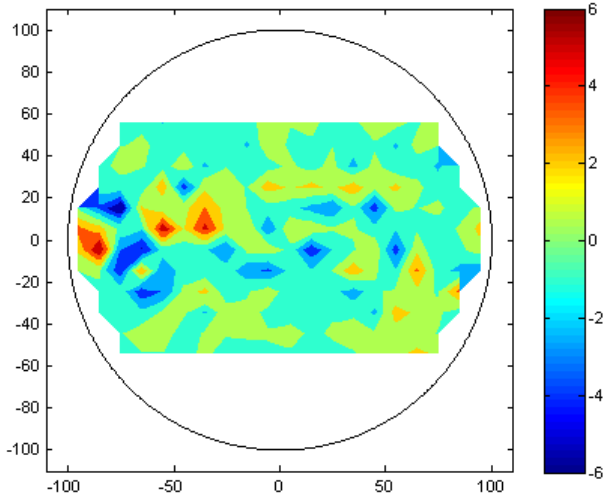


Figure 6.15: Sample of intensity field without external excitation

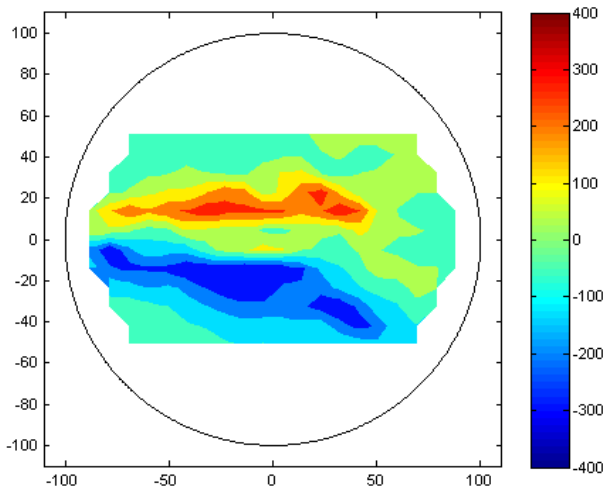


Figure 6.16: Sample of intensity field with external excitation ($\theta = 90^\circ$)

Figure 6.16 shows the intensity field of the test with external excitation with $\theta = 90^\circ$. This example obviously shows a very clear spatial structure, which is in accordance with the resonance peak previously shown in Figure 6.10. It clearly illustrates that the normalized intensity fluctuations possess a maximum in the upper section when a minimum exists in the lower section. The temporal structure will be shown in the next section.

Effect of angular position of the SN, with external excitation

In a similar way as for the analysis of the dynamic pressure, the energy of the intensity fluctuation was investigated to determine the effect the angular position of the secondary nozzle (SN). An approach as systematic as for the dynamic pressure fluctuations is not possible for the intensity fluctuations because only 1 high speed recording could be made of every combination of operating point and angular position of the SN. The energy of the fluctuation is analyzed by comparing the PSD of several tests with identical operating point but varying angular position of the SN (compare the NPSD analysis and discussion in section 5.1.3 for the dynamic pressure). The positions 5 and 13 (see section 3.1.2) are again both considered to make an angle relative to the injector axis of 90° . Position 9 and 11 make angles of 180° and 135° respectively.

The intensity fluctuations were analyzed with both the global (large window) and the local (small window) method. Because the global analysis yielded qualitatively the same results as the local analysis with respect to the effect of the angular position of the SN, it will not be further discussed. For the local analysis, two procedures were followed, which are illustrated in Figure 6.17. This figure shows the analysis grid (small window method) with a roughly estimated position of the nodal line (dashed lines) for three angular positions of the SN, green for $\theta = 90^\circ$, yellow for $\theta = 135^\circ$ and red for $\theta = 180^\circ$, and three circled small windows in corresponding colors.

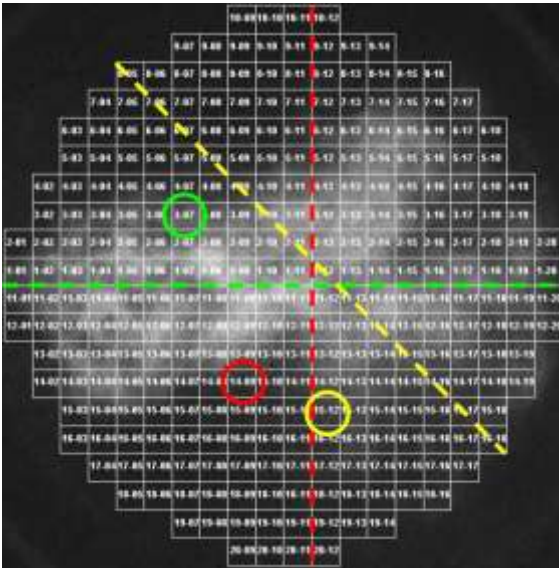


Figure 6.17: Illustration of two procedures for analysis local intensity fluctuations

The first method consisted of selecting these windows such that they have the same relative position to the nodal line of the acoustic field for all three angular positions of the SN. Of course, the selected windows represent different regions of the combustion zone, so, in the second procedure, only one window (circled in green) was analyzed for the three angular positions of the SN. Both procedures produced results that were qualitatively very similar. Therefore, only the results

of the second procedure are shown. The normalized PSD of the OH-intensity for a test with $\theta = 90^\circ$ is shown in Figure 6.18. For $\theta = 135^\circ$ and $\theta = 180^\circ$, the PSD is shown in Figure 6.19 and Figure 6.20 respectively. Comparing the three figures illustrates the effect of external excitation on the normalized intensity fluctuations. External excitation with $\theta = 90^\circ$ yields the highest response in the intensity fluctuations, and 180° yields the smallest response.

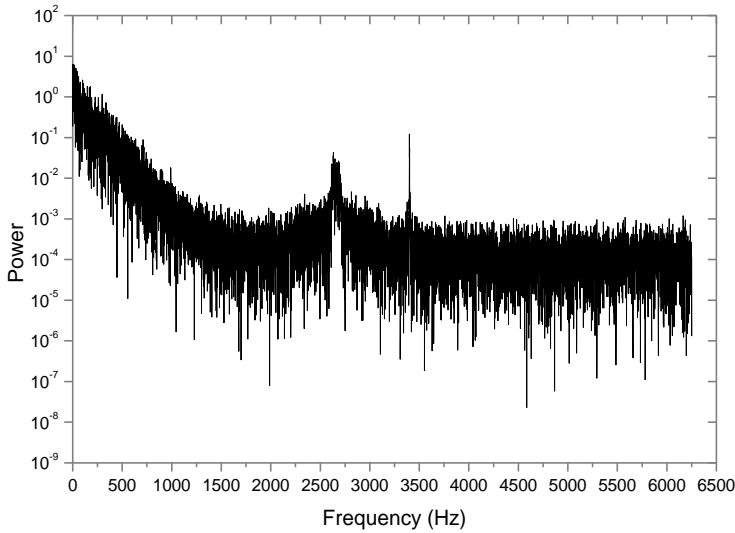


Figure 6.18: PSD of OH-intensity with angular position of the SN $\theta = 90^\circ$

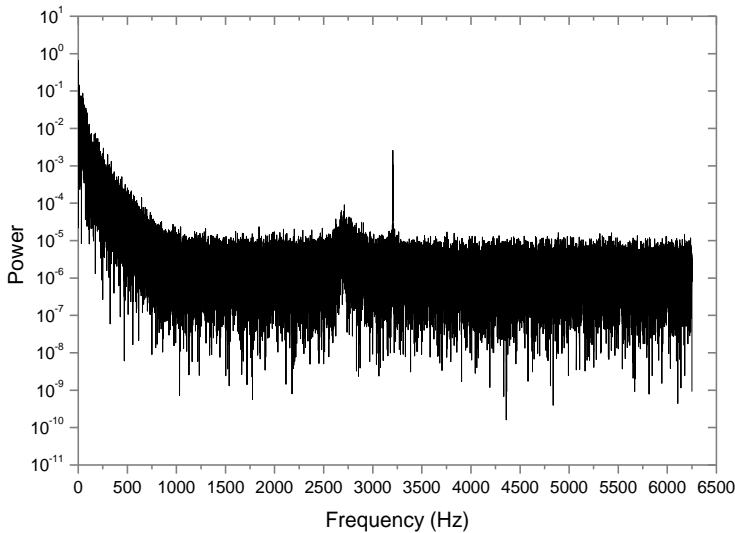


Figure 6.19: PSD of OH-intensity with angular position of the SN $\theta = 135^\circ$

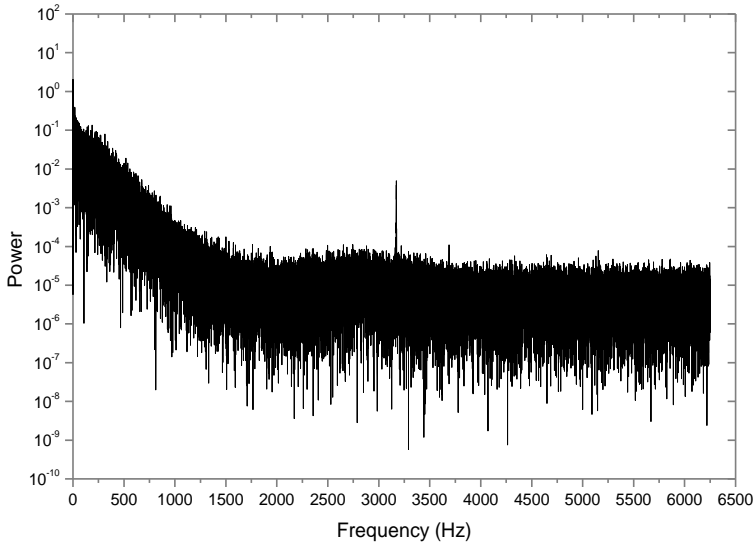


Figure 6.20: PSD of OH-intensity with angular position of the SN $\theta = 180^\circ$

This behavior is supported by the image sequences shown in Figure 6.21. These sequences show the temporal development of the intensity field for each of the three angular positions of the SN.

Also here, the 90° case exhibits the most pronounced temporal structure and the 180° case the least pronounced structure. The response of the flame to external excitation with an angular position of the SN of $\theta = 135^\circ$ again lies in the middle. The spatial structure is also illustrated in these figures. For an angular position of $\theta = 90^\circ$, the spatial structure possesses a very clear line of symmetry on the spray axis, perpendicular to the axis of the SN. For $\theta = 135^\circ$ and $\theta = 180^\circ$ the spatial structure becomes less pronounced, even though the symmetry line is still oriented facing the secondary nozzle. As for the temporal structure, the structure is strongest for $\theta = 90^\circ$, and weakest, if at all present, for $\theta = 180^\circ$.

In Figure 6.22, Figure 6.23 and Figure 6.24, the spatial distribution of the instantaneous intensity fluctuations at several subsequent moments in time is presented (and a continuous time evolution in the corresponding video), which is important in order to determine where in the combustion chamber the flame responds strongest with respect to the acoustic field. The highest fluctuations are illustrated in red and the lowest fluctuations in blue. In these figures, the absolute value of the fluctuations is shown. These figures, as well, show that a spatial structure is most pronounced for excitation from $\theta = 90^\circ$, and least to non-existent for $\theta = 180^\circ$. The spatial and temporal structures of the normalized intensity fluctuations in relation to the acoustic field are extensively discussed in Chapter 7.

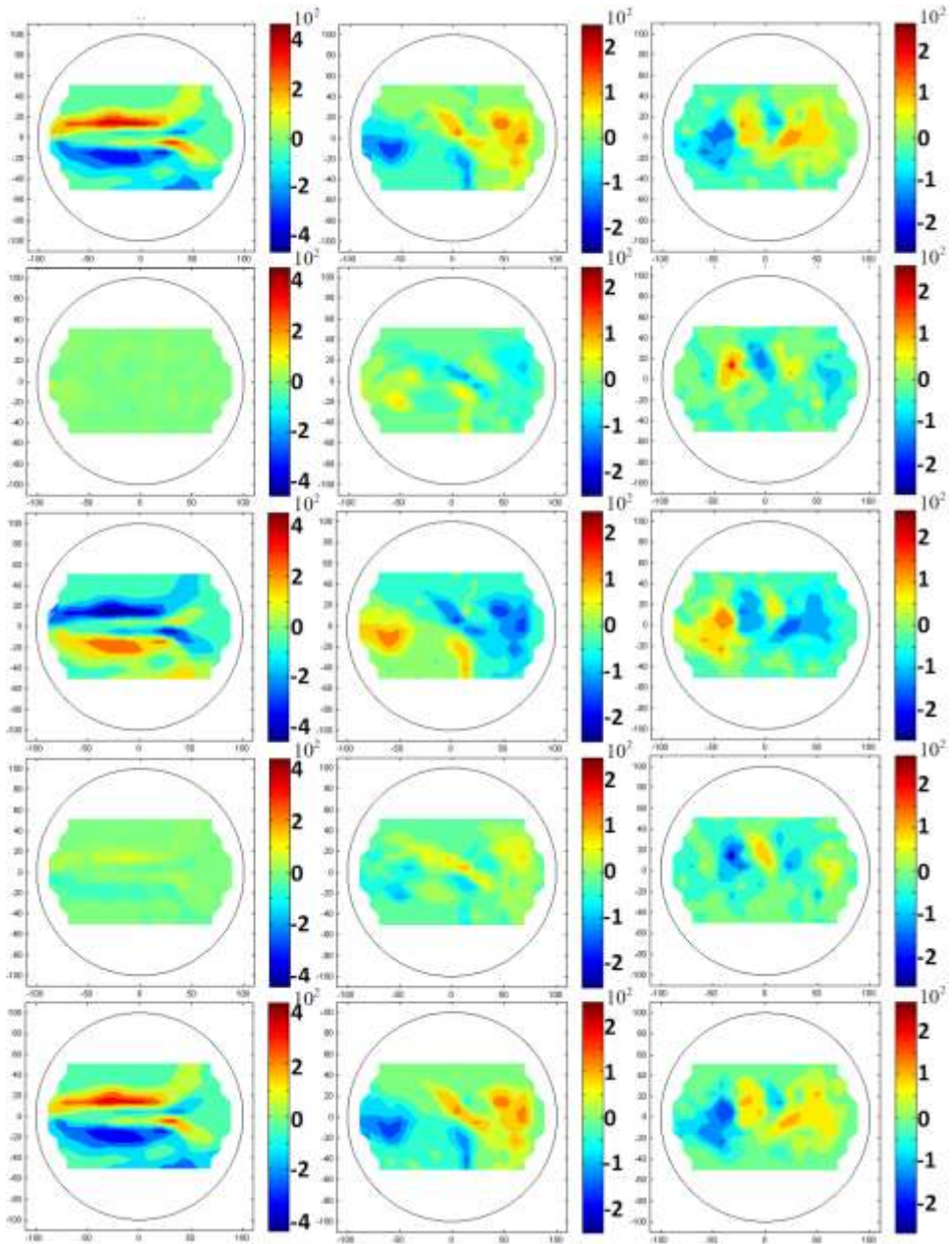


Figure 6.21: Temporal development intensity field for $\theta = 90^\circ$ (left), for $\theta = 135^\circ$ (middle), for $\theta = 180^\circ$ (right)

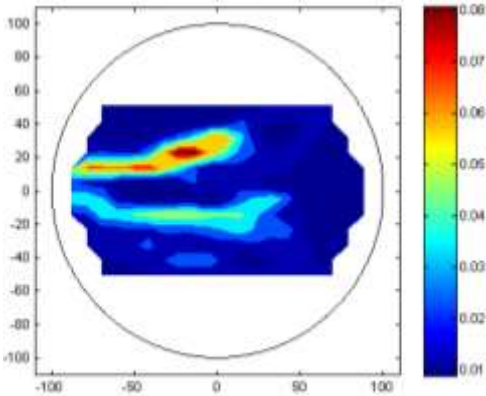


Figure 6.22: Spatial distribution of intensity fluctuations $\theta = 90^\circ$

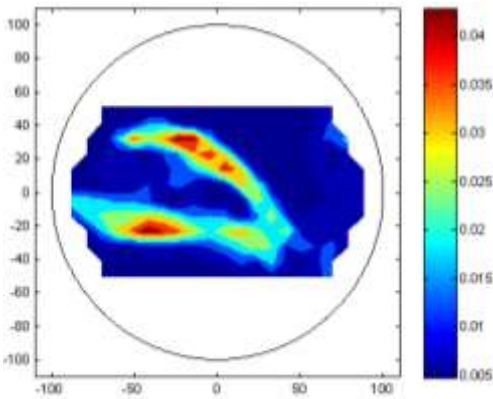


Figure 6.23: Spatial distribution of intensity fluctuations $\theta = 135^\circ$

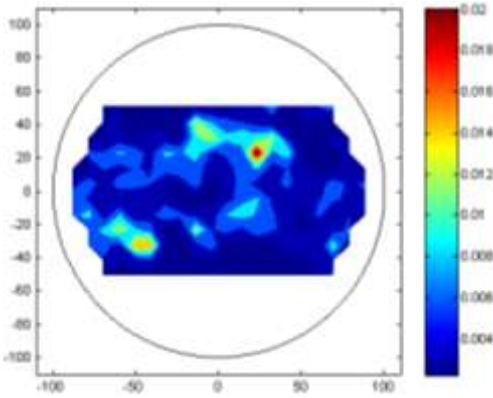


Figure 6.24: Spatial distribution of intensity fluctuations $\theta = 180^\circ$

7 Experimental

Results:

Interaction and

Combustion

Response

This chapter covers the analysis that compares the temporal evolution of the spatial structure of the acoustic field in the CRC with the temporal evolution of the flame intensity field's spatial structure. The first important aspect of this analysis is localizing the high amplitude intensity fluctuations in space in relation to the acoustic field in order to establish whether pressure or velocity coupling is more likely. This analysis is presented in section 7.1. The second important aspect is the calculation of the phase shift between the acoustic signal, which consists of either the dynamic pressure oscillations or the corresponding velocity

oscillations, and the intensity oscillations, in order to determine the combustion response. In section 7.2, the combustion response is elaborately discussed and is concluded with a quantification thereof by means of the response factor (including the temporal evolution of its spatial distribution in the CRC) and time delay. This analysis should also enlighten the discussion whether velocity coupling is ‘just’ more dominant than the pressure driven mechanism, or really the only one mechanism present.

7.1 Interaction of acoustic field and combustion

The acoustic field has two components, pressure and velocity. The dynamic pressure signal is measured with the pressure transducers mounted to the CRC wall. From these pressure signals, the complete wall pressure distribution is derived, and from the wall pressure distribution the entire dynamic pressure field in the combustion chamber is extrapolated. The velocity component of the acoustic field is directly coupled to the pressure component through equation (7-1), which was derived in section 2.3, and is calculated using the pressure field as input (see section 4.1 on data reduction).

$$\vec{u}(r, \theta, z, t) = -\frac{j}{\rho\omega} \nabla p(r, \theta, z, t) \quad (7-1)$$

As was shown in section 6.3.2, the intensity does not show significant spatial structure for tests without external excitation. It will nonetheless be briefly discussed here in comparison with the acoustic field in section 7.1.1. The significant spatial and temporal structures of the intensity field for tests with external excitation are then more elaborately discussed in section 7.1.2.

7.1.1 Relation of acoustic field and intensity field, without external excitation

The image sequence in Figure 7.1 shows the temporal evolution of the acoustic pressure and velocity field simultaneously with the intensity field of the flame emission in the left, middle and right columns respectively (Video 3). The time step between images is a quarter period, $\Delta t \approx 0.1$ ms. As mentioned, the intensity field’s spatial structure seems stochastic in nature. Looking more closely reveals that there indeed exists a minor temporal dependence. The spatial structure does not seem to change at all, but it does show a fluctuation, even though the amplitude is very low.

The arrows that display a velocity field in the figures following, denote the direction of the flow. For one image, they can be used as a quantitative measure for the velocity, but because the arrows are scaled for every time step individually, they cannot be compared with other instants in time.

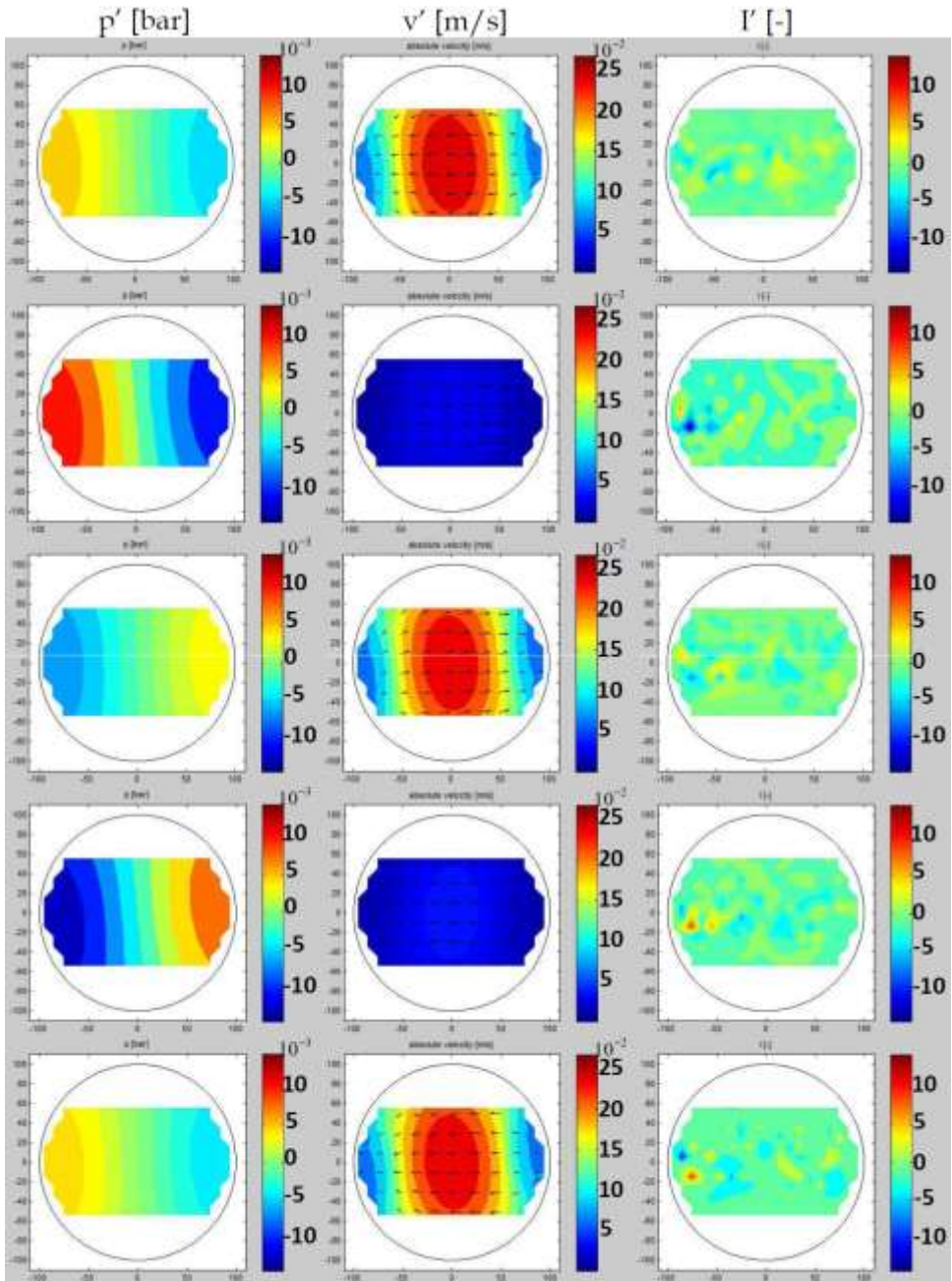


Figure 7.1: Temporal evolution of the acoustic field and the intensity field ($\Delta t \approx 0.1$ ms)

They more or less denote the relation of the local velocity to the rest of the velocity field. This explains why the magnitude of the velocity seems to not become zero at a pressure anti-node. This effect is amplified by the fact that it is very likely that the pressure anti-node lies between two measurements and had to be interpolated across, hence there will always be a pressure gradient, even when it's infinitesimally small, and therefore the arrows will 'flip' from one side to the other without becoming smaller when passing the pressure anti-node.

The 1T-mode without external excitation (see section 6.3) was investigated with respect to a correlation with the intensity oscillation's amplitude but none was found. From section 6.3 is also known that the frequency spectrum of the intensity fluctuation does not show any frequency accumulation (Figure 6.9) at the 1T-frequency that the acoustic pressure shows, which physically means there is no eigenfrequency in the intensity signal, or at least not more dominantly present as any other frequency, and the intensity fluctuation mainly consists of general noise. So, it must be concluded that the observed temporal dependence is visible only because of filtering of the signal.

7.1.2 Relation of acoustic field and intensity field with external excitation

In chapter 5 and 6 respectively, was shown that external excitation has a significant effect on the dynamic pressure fluctuations and flame characteristics. The energy content of the fluctuation correlates strongly with the angular position θ of the SN and is large for excitation perpendicular to the spray axis ($\theta = 90^\circ$) and small for excitation parallel to the spray axis ($\theta = 180^\circ$), see section 5.2.2. The flame angle experienced a decrease due to external excitation, confining combustion to a smaller space. All results indicate that the structure of the velocity field might play a bigger role than that of the pressure field. The temporal evolution of both acoustic pressure and velocity fields are compared with the intensity field in Figure 7.2, Figure 7.3 and Figure 7.4 (Video 4, Video 5 and Video 6) for external excitation from 90° , 135° and 180° respectively (injector on the left, and θ measured CW from the injector axis). Figure 7.2 to Figure 7.4 show 1 period of oscillation. These image sequences display the acoustic pressure oscillations in the left column, the velocity oscillations in the middle and the intensity oscillations on the right. The time step between the images in one series is about a quarter period, in this case $\Delta t \approx 0.1$ ms. Note that the scaling varies from one figure to the next.

The nodal line of the pressure field perpendicular to the SN-axis is shifted and bent towards the secondary nozzle, and at the same position the velocity has its anti-node. The intensity field as well shows a full period of fluctuation, but its symmetry line around which the intensity fluctuates is not as strongly affected by the position of excitation. It seems to not bend like the pressure nodal line, but merely rotate towards the secondary nozzle. The intensity field of a test without external excitation does not have a symmetry line at all and the spatial structure of the intensity of tests with external excitation shows a symmetry line most clearly for the angular position perpendicular to the spray axis, $\theta = 90^\circ$. For all three angular positions of the SN, the symmetry line of the intensity field does not coincide with the nodal line the pressure field.

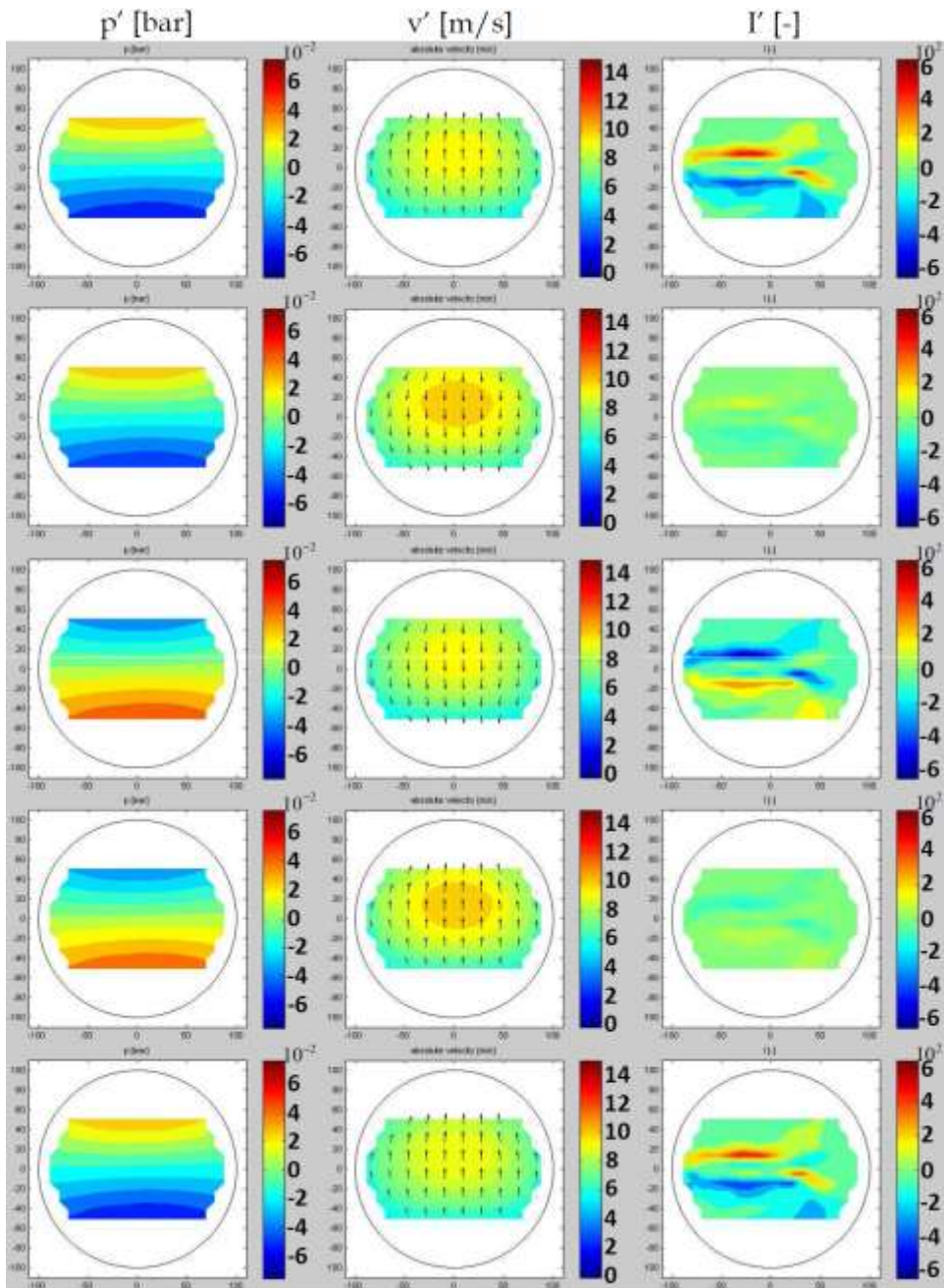


Figure 7.2: Acoustic field vs. Intensity field for $\theta = 90^\circ$ ($\Delta t \approx 0.1$ ms)

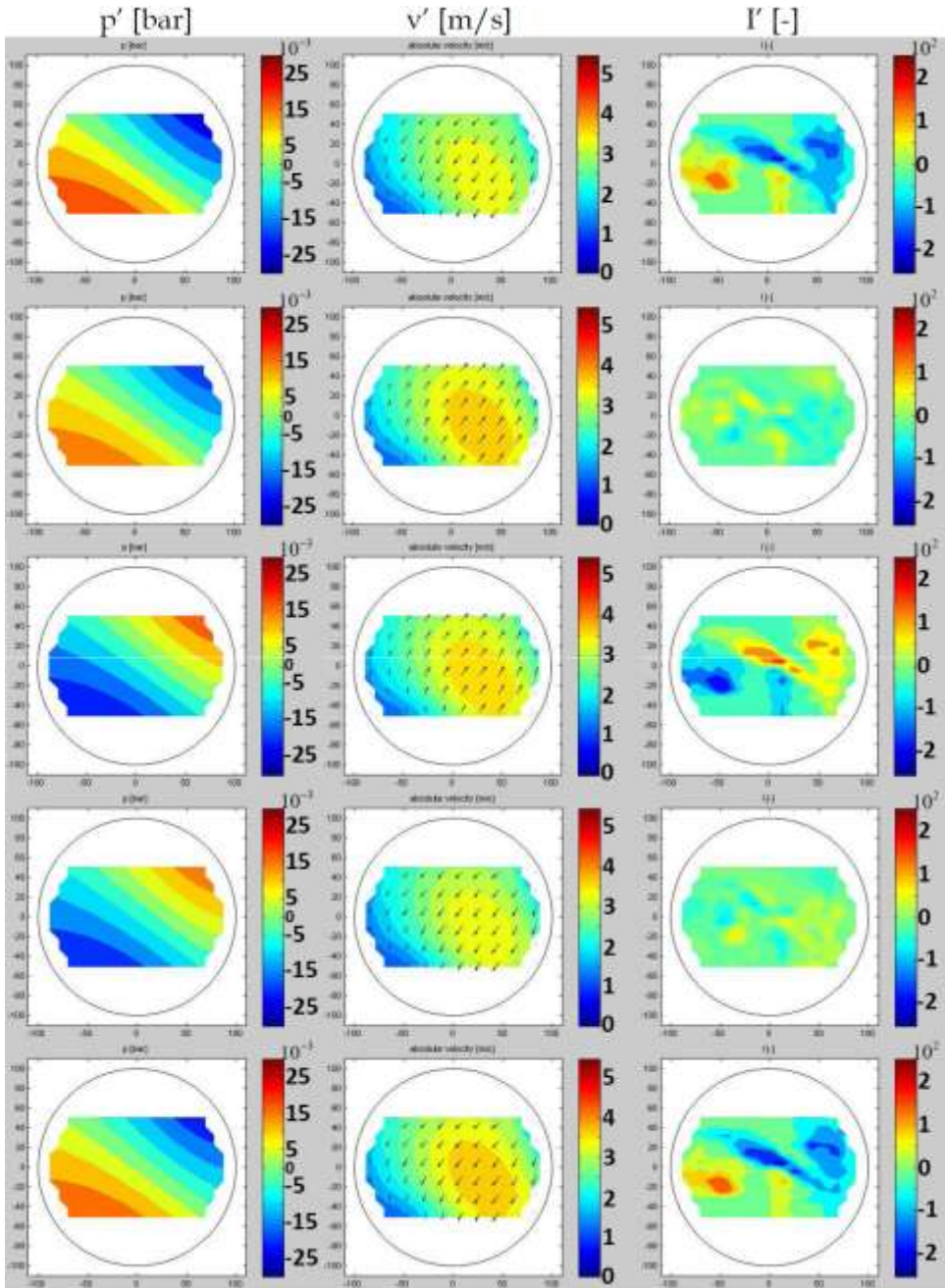


Figure 7.3: Acoustic field vs. Intensity field for $\theta = 135^\circ$ ($\Delta t \approx 0.1$ ms)

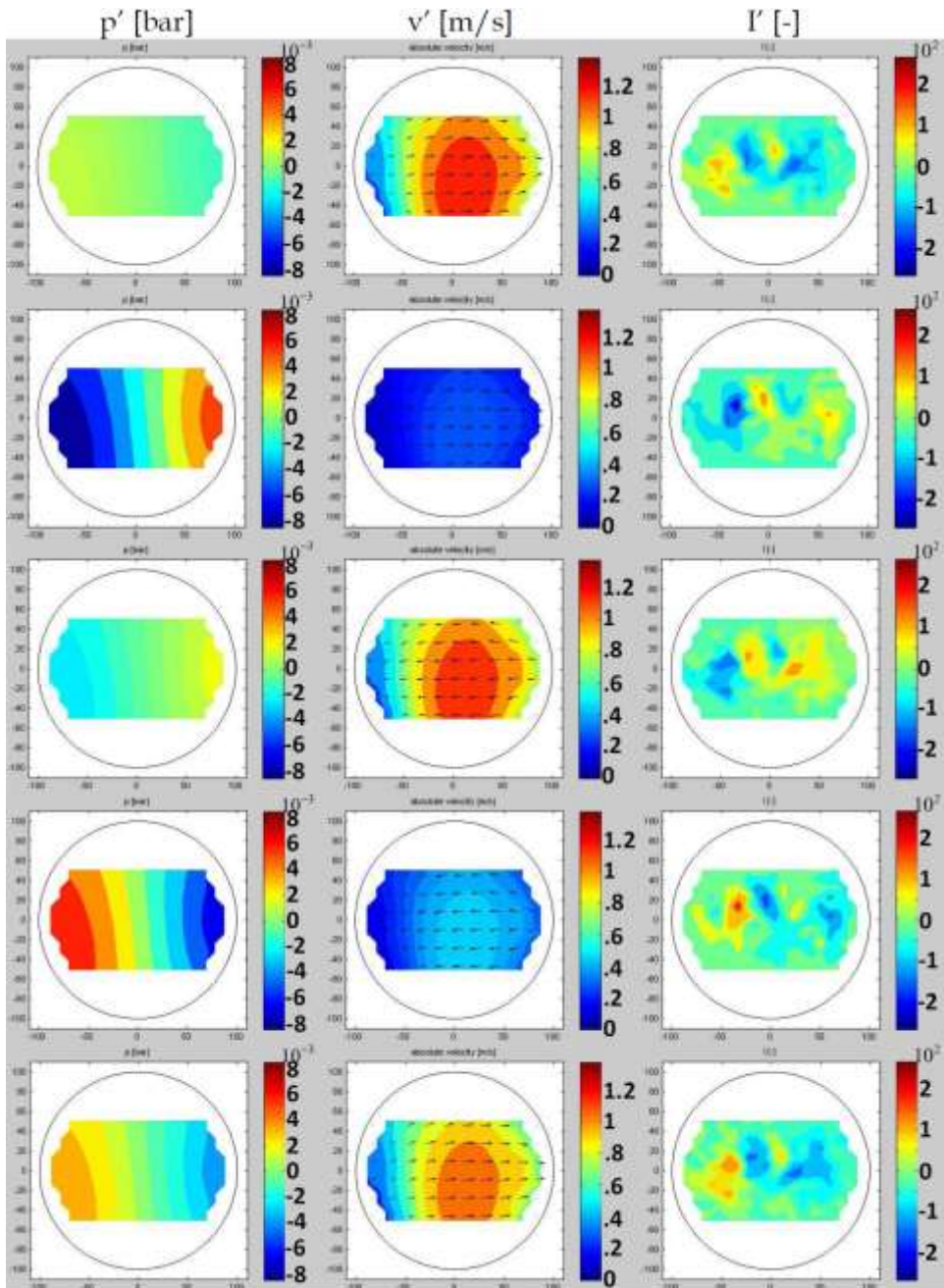


Figure 7.4: Acoustic field vs. Intensity field for $\theta = 180^\circ$ ($\Delta t \approx 0.1$ ms)

This is relevant for the calculation of the response factor because it causes a phase shift between pressure and intensity, and will be discussed in more detail in section 7.2.

Comparing the orientation of the pressure and velocity field with the intensity field that basically defines the combustion zone, it is clear that the pressure node, and consequently the velocity anti-node, lies directly in the combustion zone for $\theta = 90^\circ$ and moves further away from the combustion zone for excitation for $\theta = 135^\circ$ and $\theta = 180^\circ$. The highest amplitudes of the acoustic and intensity fields, hence the strongest interaction between acoustics and combustion, occur for $\theta = 90^\circ$, so this is again substantiating evidence for what was found in earlier discussions that velocity is the dominant candidate for the coupling mechanism. An additional argument for velocity coupling was found, at least conclusively for $\theta = 90^\circ$, when analyzing the amplitude of the fluctuations itself. The amplitudes are normalized with appropriate quantities as they are used in the response factor, see section 7.2.4. In Figure 7.5, Figure 7.6 and Figure 7.7 (see Video 7, Video 8 and Video 9) the sequences show the evolution of the amplitude of the pressure, velocity and intensity oscillations for the three angular positions of the SN respectively. This amplitude, the maximum deviation from the average, was determined for every half period and by definition always positive. The temporal dependence of the fluctuation is now lost, but therefore the temporal evolution of the amplitude (larger timescale) can now be investigated more clearly. Figure 7.5 to Figure 7.7 show a time interval representative for 20 periods of oscillation (5 periods per time step, $\Delta t \approx 2$ ms, with again pressure, velocity and intensity in the left, middle and right columns), and one can see the dynamics of the local intensity when it moves through the combustion chamber. This behavior could be explained by a-periodic emerging of large ligaments that move downstream of the injector while burning intensely. These so-called flame balls have been observed for LOx/H₂ spray flames in the CRC by Knapp [37].

The most important aspect of these image sequences is the location of the highest intensity amplitude, which for all 3 angular positions of the SN could be explained with velocity coupling when superficially looking at the images, but looking more carefully, one should include pressure driven mechanisms as well. At $\theta = 90^\circ$, the highest concentration is directly on top of the pressure nodal line or in the velocity anti-node. There is no question what mechanism is most dominantly present here, it is velocity coupling. For $\theta = 135^\circ$ the highest intensity fluctuations might not be at the velocity anti-node but at the injector, but that could be due to the lower concentration of combustible mixture (larger distance from the injector) at the velocity anti-node. Nevertheless, one can see very clearly the presence of higher amplitudes around the velocity anti-node. The region in the upper right corner of the image can, on the other hand, not conclusively be explained with velocity coupling. The velocity in this region is decreasing, so why would there be an increase in response all of a sudden, especially because in this region there is hardly any combustible mixture left. The pressure amplitudes though have sharply increased here, and could be the cause of this phenomenon, which would indicate that a pressure driven mechanism is at work here. The intensity for $\theta = 180^\circ$ shows a fairly unclear picture because the spatial structure is relatively weak and not very consistent over time.

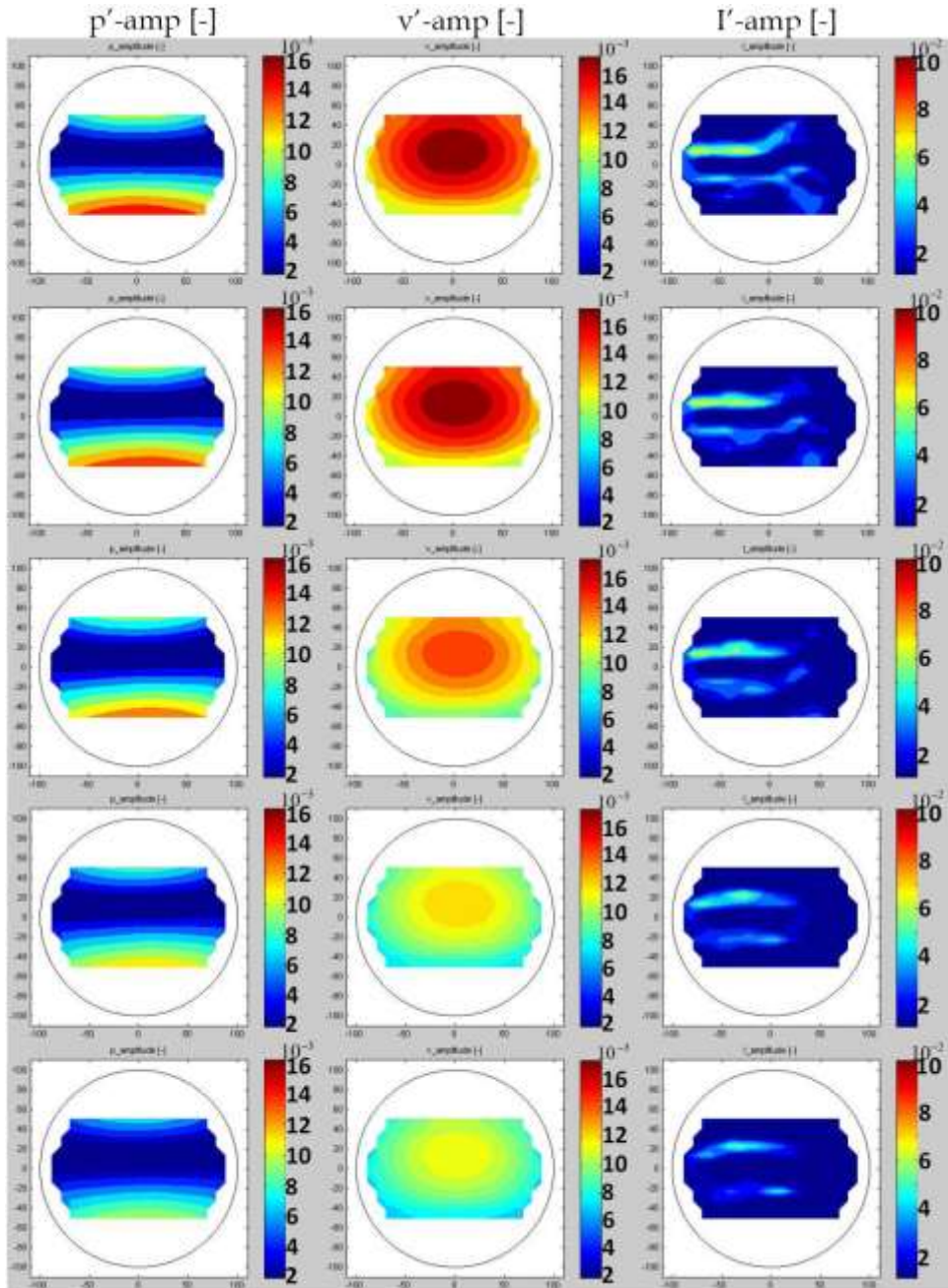


Figure 7.5: Temporal development of the amplitude of the fluctuation for $\theta = 90^\circ$ ($\Delta t \approx 2$ ms)

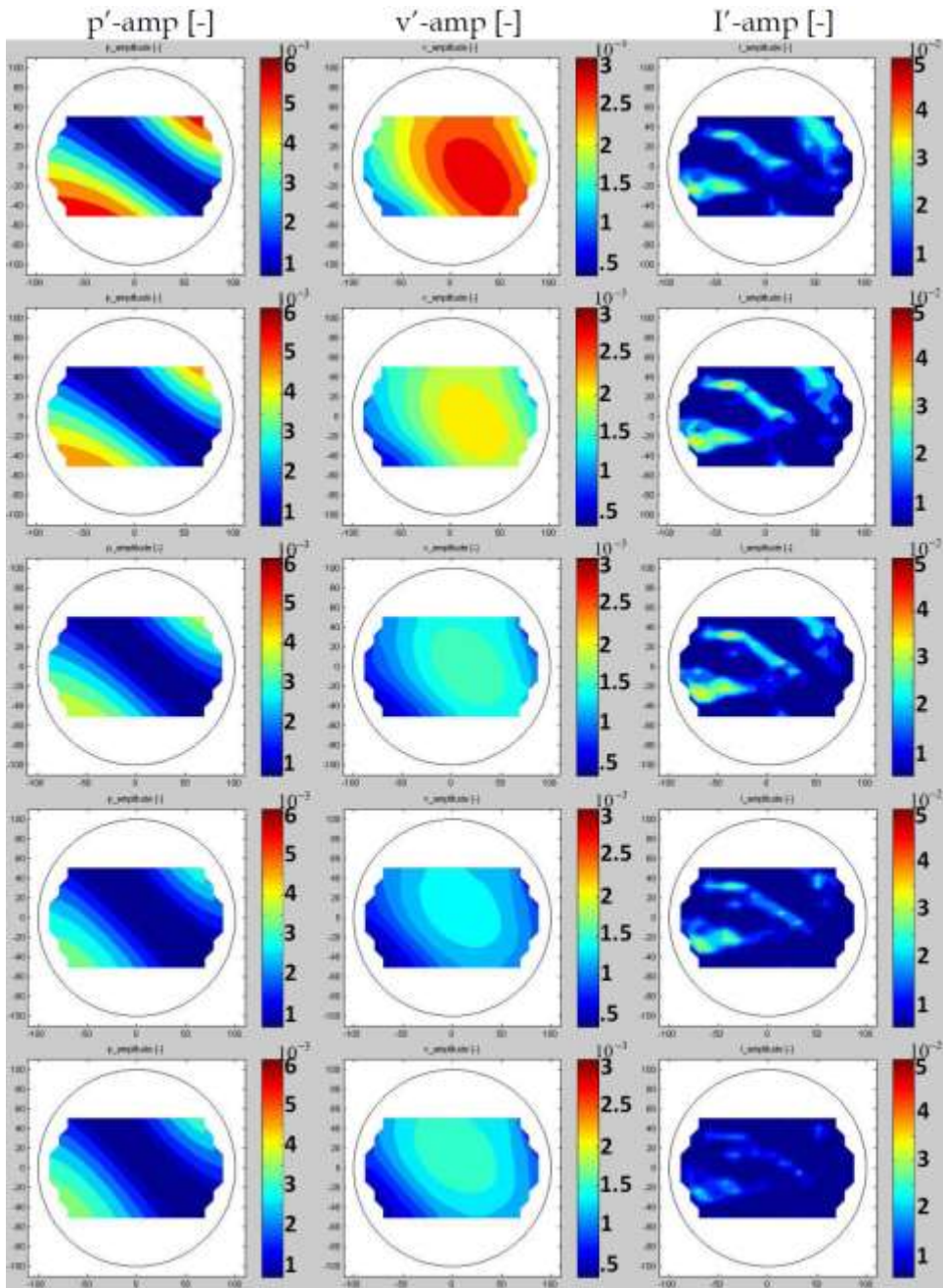


Figure 7.6: Temporal development of the amplitude of the fluctuation for $\theta = 135^\circ$ ($\Delta t \approx 2$ ms)

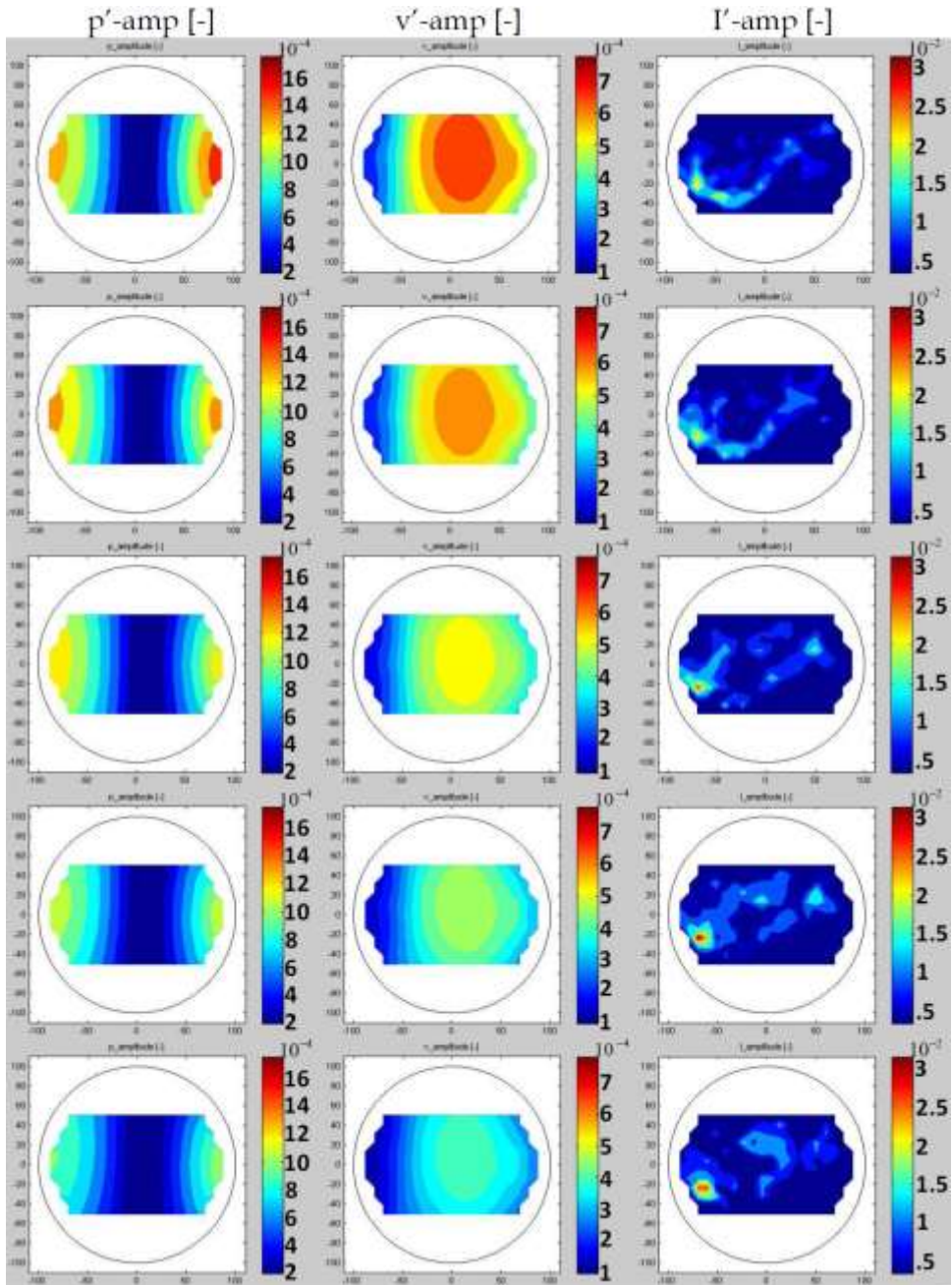


Figure 7.7: Temporal development of the amplitude of the fluctuation for $\theta = 180^\circ$ ($\Delta t \approx 2$ ms)

The intensity shows a high concentration directly at the injector, which can be expected since there is much combustion going on here, and islands of high concentration emerge on the spray axis, in the middle of the combustion chamber, and located on top of the velocity anti-node. So far, it might still be velocity coupling being active. But on the right, where the concentration of combustible mixture has become low, a region emerges where the intensity has higher amplitudes even though the velocity amplitude is rapidly decreasing. The region in the vicinity of the injector could also be explained by the presence of the pressure anti-node. So, for $\theta = 180^\circ$, the arguments for pressure coupling outweigh those for velocity.

An additional point to be made with these sequences of the evolution of the amplitude, is that it can be beautifully seen that the amplitude of the intensity fluctuations goes down with decreasing acoustic amplitudes, for all three cases.

The maxima of the amplitudes of pressure (velocity is omitted because it scales linearly with the pressure) and intensity, as a function of the angular position of the SN, are summarized in Table 7.1, and illustrated in Figure 7.8 (note that the signals are narrowly filtered, hence the very low amplitudes).

Table 7.1: Maxima of amplitudes of acoustic pressure and intensity

$p_c = 5$ [bar]	$\theta = 90^\circ$	$\theta = 135^\circ$	$\theta = 180^\circ$
$\Delta p'$ [mbar]	60	25	8
$\Delta p'/p_c$ [%]	1.28	0.53	0.19
$\Delta I/I$ [%]	10	5	2.5

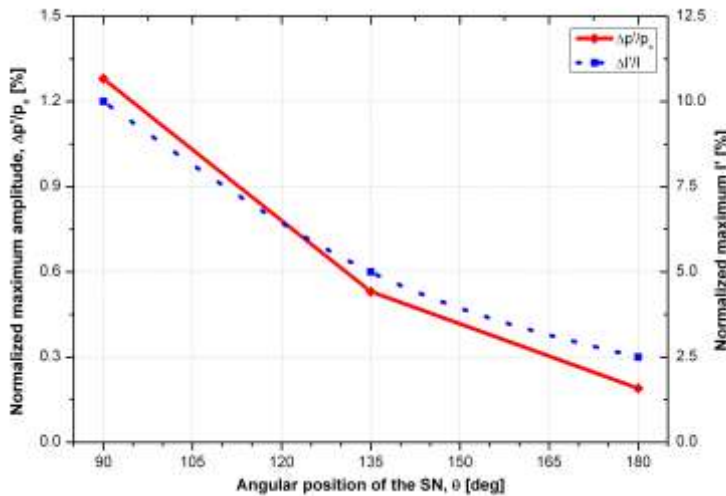


Figure 7.8: Maximum normalized amplitude of acoustic pressure and intensity as a function of θ

7.2 Combustion response

This section presents the more in-depth analysis of the relation between the acoustic pressure and velocity fields and the flame intensity field. Especially the phase between either of the acoustic components' signals and the intensity signal is of interest, because of the Rayleigh criterion and the response factors derived from it. The Rayleigh criterion (7-2) and response factors for pressure (7-3) and velocity (7-4), as defined by Sliphorst [142], [143] are repeated here for convenience.

$$\iiint_V \int_T p' \dot{q}' dt dV > 0 \quad (7-2)$$

$$N_p = \frac{I'_{max}}{p'_{max}} \cos \phi_p \quad (7-3)$$

$$N_v = \frac{I'_{max}}{v'_{max}} \cos \phi_p \quad (7-4)$$

In the comparison in the following sections, the analysis with respect to pressure (section 7.2.1 and 7.2.2) is presented independently from velocity (section 7.2.3) due to the complexity of the matter, after the discussion of the case without external excitation. This sub-chapter concludes with the analysis of the temporal structure and spatial distribution of combustion response (section 7.2.4), plus a quantification of the time delay (7.2.5) between the maximum of the acoustic fluctuation and the intensity fluctuation.

7.2.1 Phase relation between acoustic pressure and flame intensity, without external excitation

The acoustic field without external excitation shows a clear structure, for pressure as well as velocity. But the eigenmode is a general rotating wave as opposed to the standing wave for the cases with secondary nozzle, which could also be seen in Figure 7.1 to Figure 7.4. The flame intensity did not possess any well-defined, stable spatial structure, so, consequently, one would not expect a coherent phase relation between either of the acoustic signals and the intensity signal. This is supported by the phase-field shown in Figure 7.9. The development of the amplitudes of the oscillations, as in the previous section, is omitted here because it is irrelevant for the phase relation. Also, only the pressure oscillation is shown because the acoustic velocity component is only 90° phase shifted relative to the pressure and would not influence the stochastic distribution of the intensity field which causes the absence of structure in phase-field.

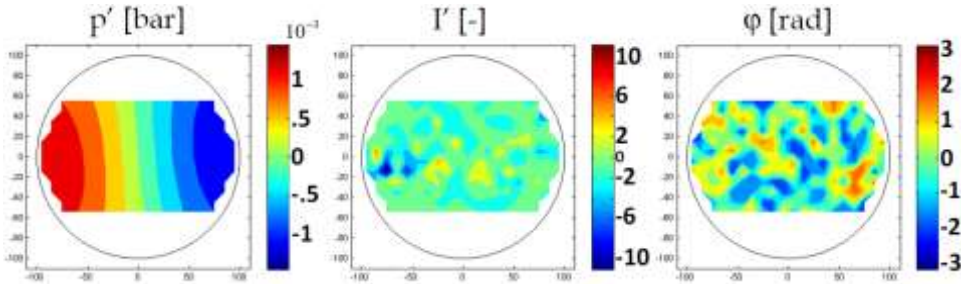


Figure 7.9: Phase relation (right) between acoustic pressure field (left) and intensity field (middle), Video 10

As mentioned, the phase-relation has a stochastic distribution, and it must be concluded that without external excitation, there is no acoustic field present of which the fluctuations contain enough energy to significantly (measurably) modulate the combustion processes for any kind of coupling to occur, let alone to trigger and sustain instability. So, calculating a response factor for a test without external excitation for either pressure or velocity is therefore as well omitted.

7.2.2 Phase relation between acoustic pressure and flame intensity, with external excitation

In the discussion on the relation between the acoustic field and flame intensity field (section 7.1.2) it became clear that not only the acoustic fields have a clear, stable spatial structure, but the intensity field possessed an obvious and constant structure as well. In the following, the phase analysis is elaborated by discussion of the phase-field. The phase-field resulting from the comparison between intensity and acoustic pressure signals is the most important in the Rayleigh criterion and the response factor, and will therefore be discussed first.

The acoustic pressure field contains a nodal line, which implicitly means that there exist two regions in the pressure field with different phases. Above the nodal line, the phase is always 180° (half of an acoustic period) phase shifted with respect to the region below the nodal line. This is illustrated in Figure 7.10, where for simplicity the phase above the nodal line is set to zero, and N denotes the position of phase transition (Nodal line). Similarly, the intensity field contains a symmetry line around which it fluctuates, which could be interpreted as the intensity nodal line. Analogue to the pressure, the phase of the intensity above its 'nodal' line is 180° phase shifted with respect to below the nodal line, as illustrated in Figure 7.11 with S denoting this symmetry line. The geometry of the pressure field in the CRC with secondary nozzle is not symmetric across the nodal line anymore (see section 2.2.2), which is confirmed by the asymmetrical nodal line position in the pressure field. Now comparing Figure 7.10 and Figure 7.11, and especially the position of the lines N and S, there exists a region where the phase of the pressure has jumped 180° , and the intensity has not yet, causing a small region in the phase-field with a large phase shift with respect to the surrounding regions, which is also illustrated in Figure 7.12.

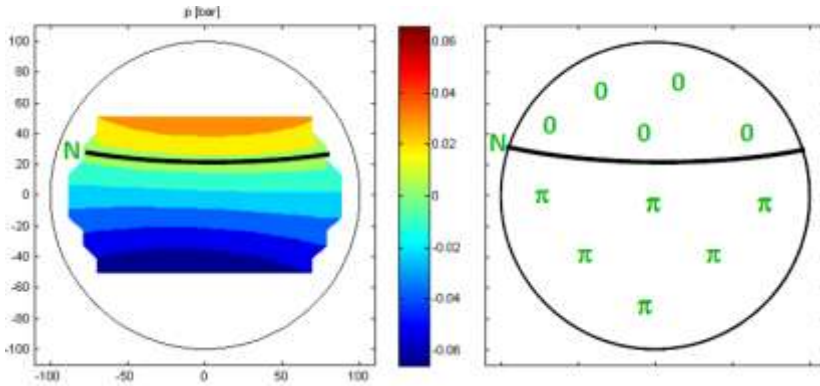


Figure 7.10: Pressure signal and nodal line

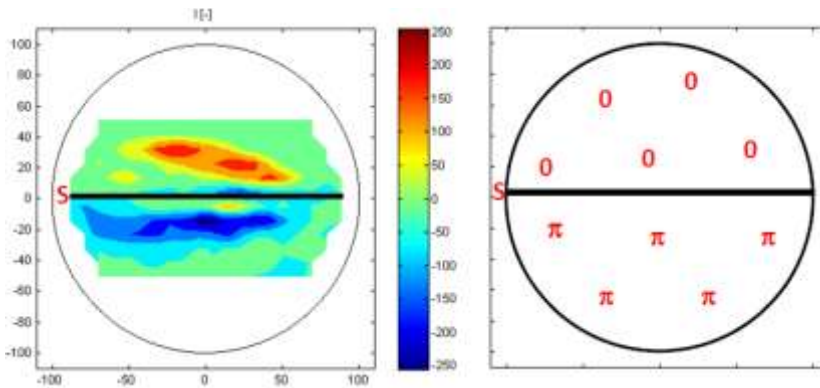


Figure 7.11: Intensity signal and symmetry line

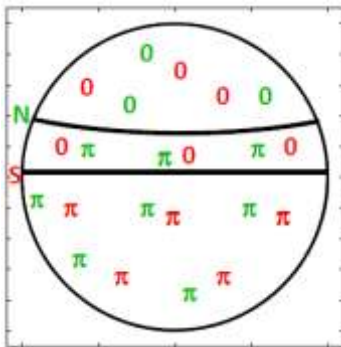


Figure 7.12: Phase relation due to nodal line of pressure field not coinciding with symmetry line of intensity field

The phase-field for three angular positions of the SN with the pressure and intensity fields it was derived from is shown in Figure 7.13 to Figure 7.15. The phase shift behavior just described is clearly shown, for all 3 angular positions. For clarity, the nodal and symmetry line for pressure (N) and intensity (S) respec-

tively are shown as well. It is again obvious that the intensity field's structure does not completely rotate towards the secondary nozzle for the 135° excitation, even though it seems to do just that for 180°. But all positions show the remarkable phase shift region due to the pressure nodal line and intensity symmetry line not coinciding. If pressure were to be the dominant coupling mechanism, one would at least expect the nodal lines of the intensity field and the pressure field to occupy the same space and follow the same direction, especially in those regions of large intensity amplitudes. Since they do not, velocity coupling is more likely.

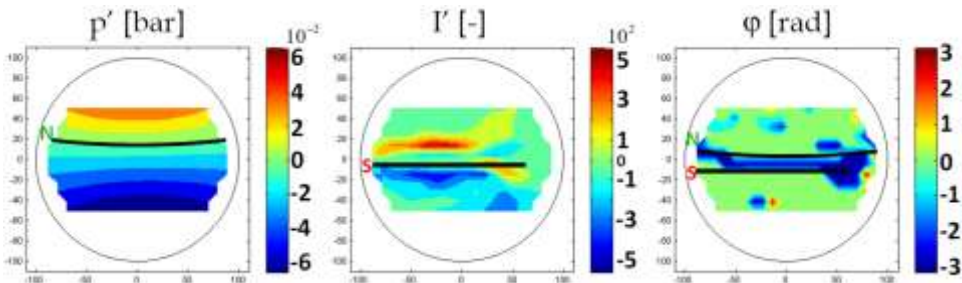


Figure 7.13: Phase relation (right) between pressure field (left) and intensity field (middle) for $\theta = 90^\circ$, Video 11

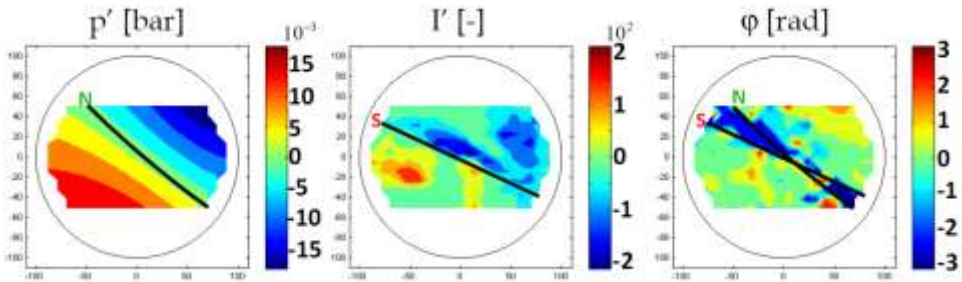


Figure 7.14: Phase relation (right) between pressure field (left) and intensity field (middle) for $\theta = 135^\circ$, Video 12

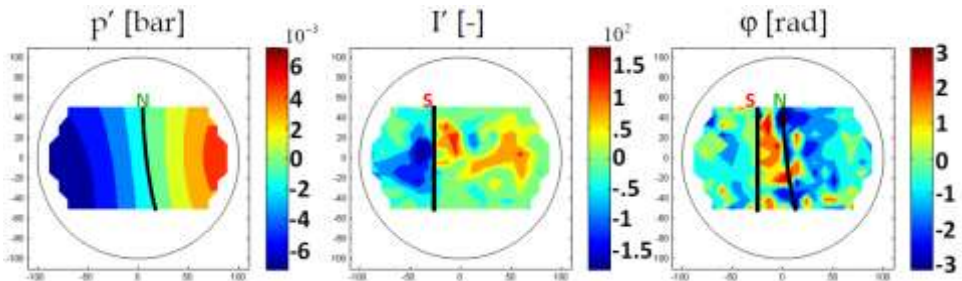


Figure 7.15: Phase relation (right) between pressure field (left) and intensity field (middle) for $\theta = 180^\circ$, Video 13

7.2.3 Phase relation between acoustic velocity and flame intensity, with external excitation

Based on the findings in the previous chapters that velocity is the more likely candidate for driving the coupling mechanism, the phase between acoustic velocity and intensity is also very important, because it quantifies the time delay [143] between the mechanism being active, and combustion responding to it. As opposed to the pressure, the velocity field does not have a nodal line. Hence, there cannot possibly exist such a double phase jump region as for the pressure. Figure 7.16 to Figure 7.18, which show the phase field and the velocity and intensity fields it was derived from, confirm this.

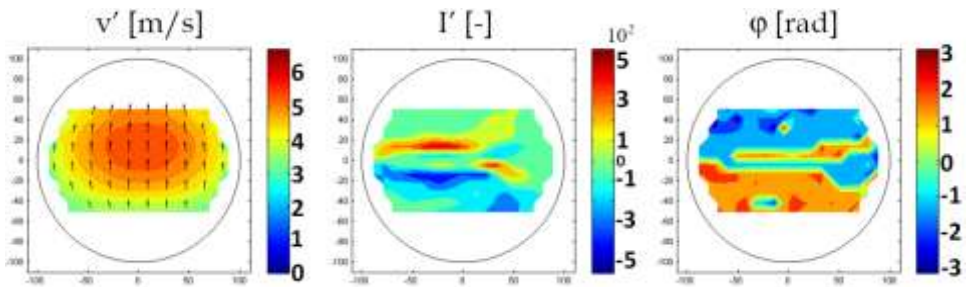


Figure 7.16: Phase relation between velocity field and intensity field for $\theta = 90^\circ$, Video 14

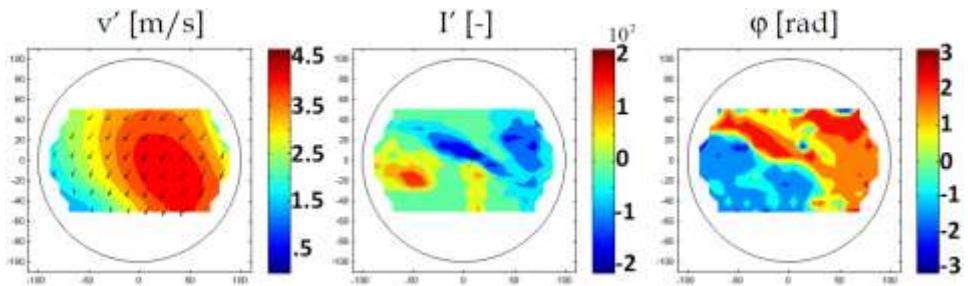


Figure 7.17: Phase relation between velocity field and intensity field for $\theta = 135^\circ$, Video 15

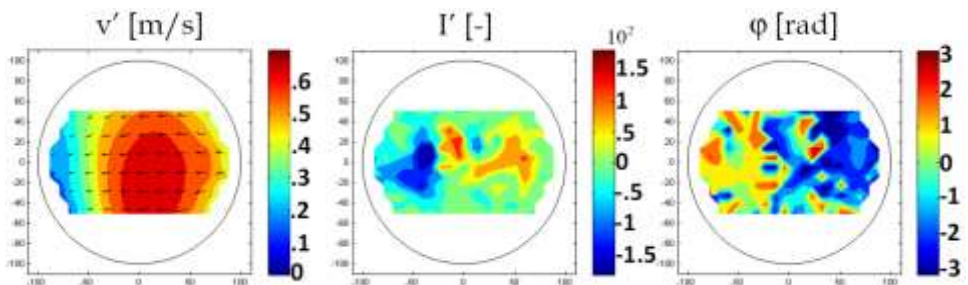


Figure 7.18: Phase relation between velocity field and intensity field for $\theta = 180^\circ$, Video 16

And even though the spatial structure of the intensity field becomes weaker and the amplitudes becomes smaller when increasing θ from 90° to 135° and 180° , the phase field for all cases show the same character. The phase jumps 180° when passing across the intensity symmetry line. That behavior can be explained, before going into the physical meaning of the phase field, by how the phase is determined. By calculating the cross-correlation between the velocity and intensity signal, it is determined how ‘similar’ the two signals are. The cross-correlation finds how much the intensity signal must be shifted to best match the velocity signal, and the result is the phase shift between the two. Since the velocity field has the same phase in the entire field (absence of nodal line), and the intensity field contains a symmetry line, and therefore the signals from above and below this line, for $\theta = 90^\circ$ (or right and left, for $\theta = 180^\circ$), are in anti-phase, it is inherent to the operation that the cross-correlation finds that the phase between the velocity and intensity on one side of the symmetry line is 180° phase shifted with respect to the phase on the other side of the symmetry line. This is illustrated in Figure 7.19, where three signals are plotted from a test with $\theta = 90^\circ$.

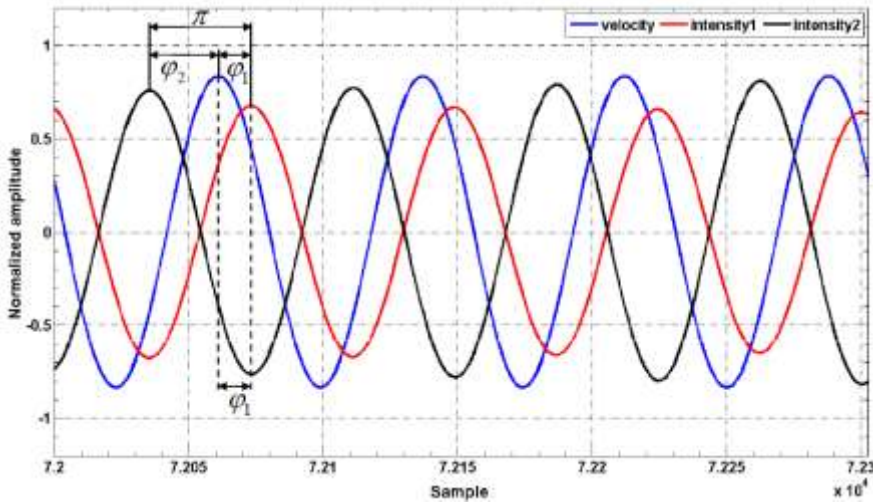


Figure 7.19: Comparison phase determination on both sides of the intensity symmetry line for $\theta = 90^\circ$

One velocity signal (entire field has the same phase, in blue), and two intensity signals, from above (in red) and below (in black) the intensity symmetry line are shown. With respect to the response factor this phase shift is irrelevant, but in determining the time delay (see section 7.2.5), the phase found by the cross-correlation must be taken with caution. Physically the phase denotes the time delay (or lag) between the response of the flame and the mechanism being active. Since it is a time delay denoting how much later the response comes after the mechanism, it is physically impossible to be positive because that would imply the response comes before the mechanism. The response of the flame in the bottom half of the combustion chamber to the upward direction of velocity (positive) is the decreasing intensity. Hence, in the bottom half of the combustion chamber, it is the phase between positive velocity and negative intensity that must be used

for physical interpretation with respect to the time delay. This phase can be found by subtracting the phase found by the cross-correlation, φ_2 , from π , or just by taking the phase in the upper half of the combustion chamber, φ_1 , which is identical ($\varphi_1 \equiv \pi - \varphi_2$).

According to the previous consistent argumentation for $\theta = 90^\circ$, with respect to the phase determination and modification, the phase should be negative and constant on both sides of the intensity symmetry line, for all θ . But after closer analysis of all fields, one must at least doubt that the same coupling mechanism is active in all three cases. For $\theta = 90^\circ$, the convective motion imposed by the velocity field transports combustible gas into the combustion zone above the intensity symmetry line yielding an increase in intensity, and at the same time taking gas away from the combustion zone below the intensity symmetry line yielding a decrease in intensity. But for $\theta = 180^\circ$ this argument cannot be valid, because the convective motion transports the gas parallel to the combustion zone in the entire combustion chamber. Such physics cannot possibly cause a phase jump as found by the cross correlation because the response to the mechanism should be the same in the entire field. But when considering the phase relation between the acoustic pressure and intensity (see Figure 7.15), but especially the similarities between the geometry of the pressure and intensity fields, one must conclude that, even though the pressure nodal line and intensity symmetry line do not exactly coincide, a pressure driven coupling mechanism is the more likely candidate for $\theta = 180^\circ$. For $\theta = 135^\circ$ it seems that both arguments could hold up because there is definitely a vertical convective motion that transports gas in and out of the combustion zone, where the vertical component of the velocity is much smaller as for $\theta = 90^\circ$, hence the smaller amplitudes, but also the pressure driven mechanism could be more dominantly active here when considering the higher response region in the upper right corner of the intensity field.

7.2.4 Response factor

Originally, Heidmann [66] based the response factor on the Rayleigh criterion, containing the integral of the product of pressure and heat release fluctuations over the volume of the combustion chamber. If using a response factor to quantify the stability of a combustion chamber, one must then of course calculate the response factor in the entire combustion volume. On the other hand, the response of the flame can also be studied locally to learn more about what regions are the most sensitive, hence what combustion chamber processes are dominantly responsible for driving instability. The response factors (7-3) and (7-4) are therefore analyzed locally before determining the global stability by integrating over the volume to find the global response factor R_F , through equation (7-5).

$$R_F = \int_V N dV \quad (7-5)$$

In (7-5) N denotes the local response factor of either pressure, N_p (7-3), or velocity, N_v (7-4). Since the experiment only allows line-of-sight-measuring of the OH-emission of the flame, it is assumed that the OH-intensity occurs in the same

plane as the pressure sensors are in, reducing (7-5) to an integral over a surface (or a plane).

$$R_F = \int_S NdS \quad (7-6)$$

The response factor roughly consists of a scaling factor describing the coupling mechanism and a phase relation describing the temporal dependence between heat release and acoustic pressure of the Rayleigh integral. The scaling factor is the ratio between the normalized amplitudes of the flame intensity (heat release) and pressure or velocity. The signal of normalized amplitudes has one value per cycle and is not continuous, even though the variations from cycle to cycle are minimal. To generate a more 'continuous' signal, it is necessary to interpolate for all time steps between two values of normalized amplitudes. The phase relation was determined in the previous section and would not cause any issues. The scaling factor on the other hand does when the pressure response factor is targeted. The normalized pressure fluctuation becomes zero at the nodal line, and assuming pressure coupling, the intensity should too. Both should happen at the same physical position (nodal line) which makes the analysis of the pressure response factor difficult. Considering the turbulent nature of the flow, the response to external excitation may become zero at the nodal line, the intensity fluctuations will still be a finite quantity, and therefore force the scaling factor to diverge. Also, the intensity was analyzed with the small windows which averages in space. This cannot be avoided, even if every single pixel were to be analyzed because a pixel as well has a finite width and is not an infinitesimally thin line as the nodal line is. The result is therefore that for coordinates in the vicinity of the nodal line where the pressure is very small, the intensity could still be significantly high to cause the response factor to become very large. This is true even if the pressure nodal line and the intensity symmetry line perfectly align, and they do not. The phase analysis in the previous section showed that for all three angular positions of the SN, the pressure nodal line and intensity symmetry may share a certain space, but are definitely not at the same position. This fact causes the very large values for the pressure response factor shown in Figure 7.20 to Figure 7.23, and it must be concluded that, even though there are indications from the phase analysis for pressure coupling for the two angular positions other than $\theta = 90^\circ$, pressure coupling is definitely not the only mechanism at play. If it were, the pressure nodal line and intensity symmetry line should at least be coinciding within the analysis resolution (small windows defined coordinates, $1 \times 1 \text{ cm}^2$), even when considering the pressure field is extrapolated from wall measurements, but the discrepancy is too large to be disregarded. The figures show the amplitudes of the acoustic pressure on the left, flame intensity in the middle, and the pressure related response factor is shown on the right. Note that the scaling of the four figures is different.

The pressure response factor distributions in the 4 figures all contain a similar spatial structure. There are high absolute values where the pressure nodal line is, and the rest of the field is close to zero. This result is inconclusive whether pressure coupling can be confirmed or not.

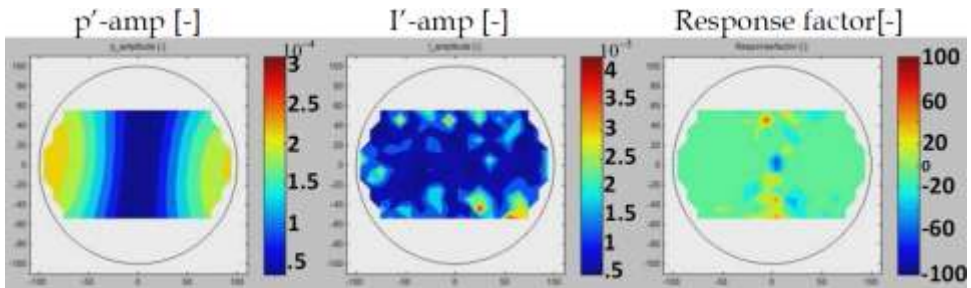
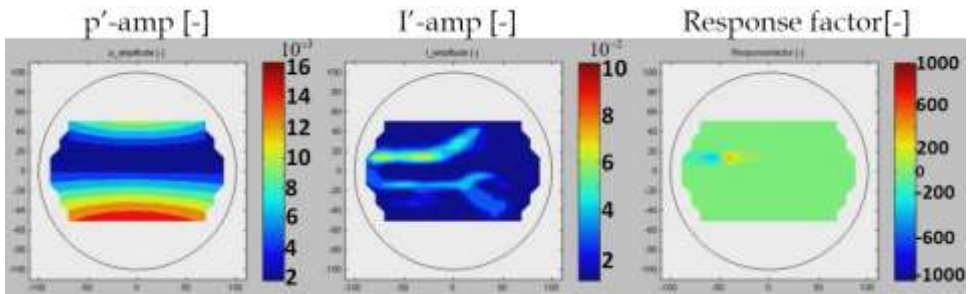
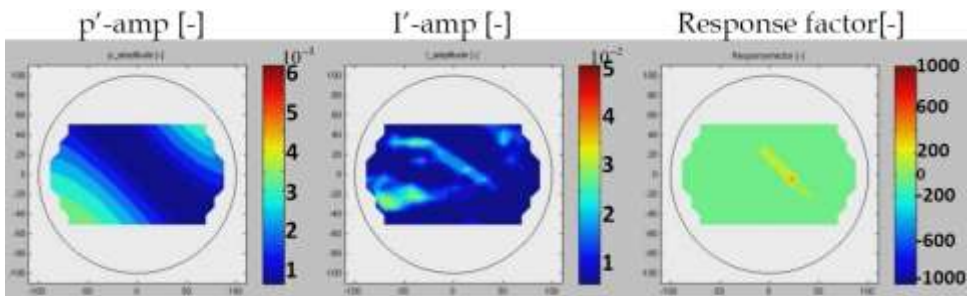
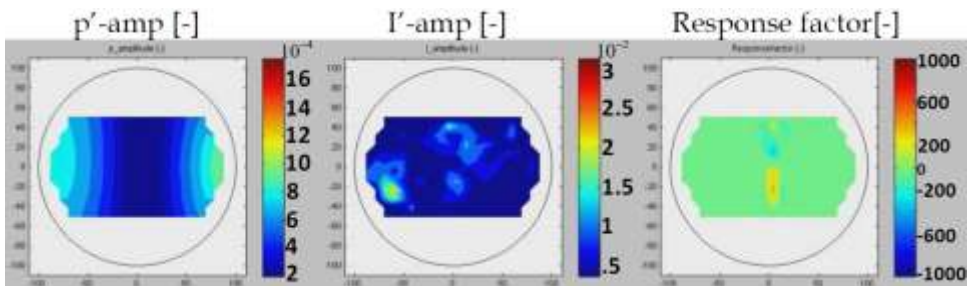


Figure 7.20: Pressure response factor without excitation, Video 17

Figure 7.21: Pressure response factor for $\theta = 90^\circ$, Video 18Figure 7.22: Pressure response factor for $\theta = 135^\circ$, Video 19Figure 7.23: Pressure response factor for $\theta = 180^\circ$, Video 20

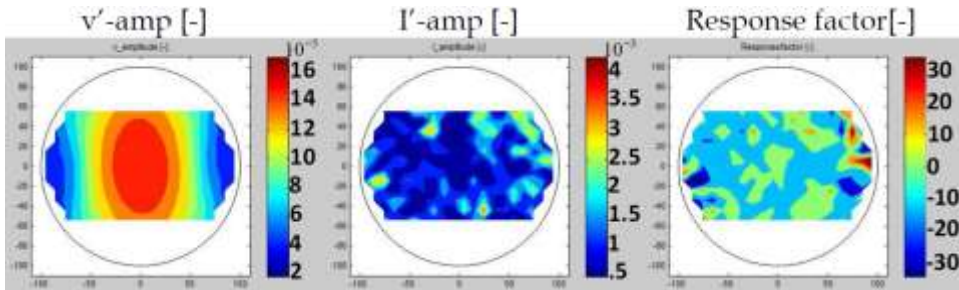


Figure 7.24: Velocity response factor without excitation, Video 21

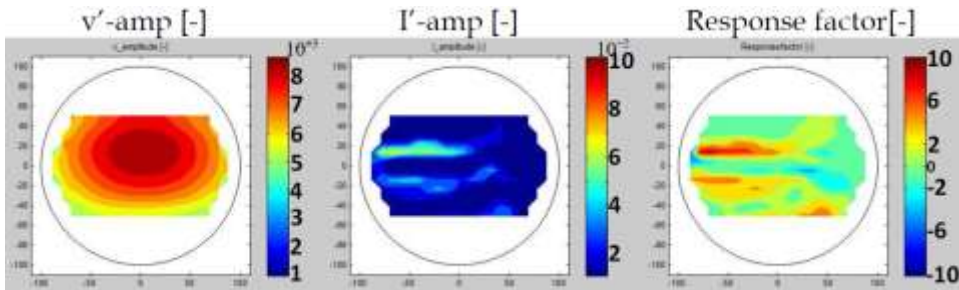


Figure 7.25: Velocity response factor for $\theta = 90^\circ$, Video 22

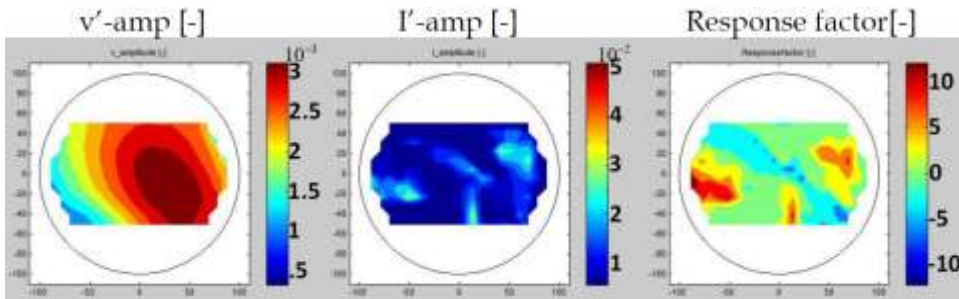


Figure 7.26: Velocity response factor for $\theta = 135^\circ$, Video 23

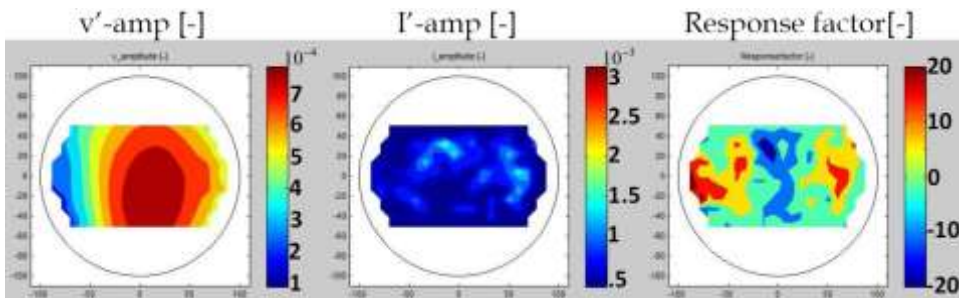


Figure 7.27: Velocity response factor for $\theta = 180^\circ$, Video 24

In Figure 7.24 to Figure 7.27 the normalized amplitudes of the velocity and intensity oscillations (left and middle) as well as the velocity response factor field (right) are shown [143].

For comparison, the videos showing the fluctuations (opposed to the amplitudes) and the response factor are included as well for all 8 cases discussed here, Video 17b to 24b.

Obviously, the range for the pressure response factor is unrealistically large. To illustrate a more sensible range, the value of the pressure response factor, for the case $\theta = 90^\circ$, for all coordinates is shown in Figure 7.28, at one single instant in time. The distribution is typical for all instants in time. The x-axis denotes the numerical identification of the coordinates, as illustrated in section 4.1. Ignoring the large values around the nodal line (the coordinates numbered roughly 20 to 50), the pressure response factor is in the order of unity.

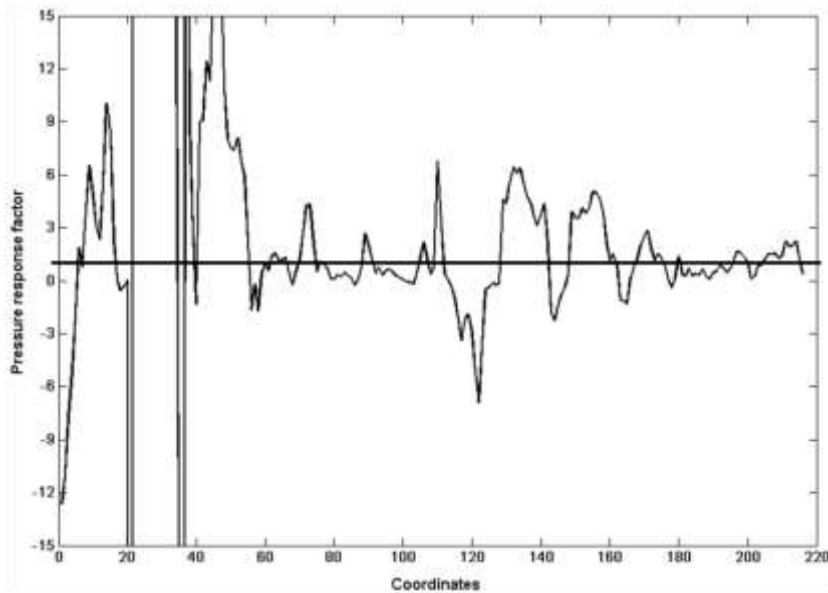


Figure 7.28: Instantaneous pressure response factor distribution

The response factor field without external excitation displays a similar stochastic distribution as the phase and intensity fields. The magnitude of the response factor seems to reach the highest local values compared to the cases with excitation, but this can be explained by the low acoustic amplitudes and the non-negligible intensity amplitudes. Integrated over the volume, the response factor seems negative due to the large area around or below zero, but the small areas with extreme values cause the response factor to still be positive, see Table 7.2.

For the three cases of external excitation, the response factor field becomes less structured when the angular position changes from $\theta = 90^\circ$ to $\theta = 135^\circ$ and $\theta = 180^\circ$. But, the magnitude of the response factor, at least locally, seems to increase. Also here, the same argument holds as for the case without excitation namely that the acoustic amplitude becomes smaller quicker than the intensity amplitude.

Table 7.2: Global velocity response factor

Response factor, R_F	No excitation	External excitation		
		$\theta = 90^\circ$	$\theta = 135^\circ$	$\theta = 180^\circ$
mean	4.48	1.61	1.96	-4.72
rms	6.5	1.7	70	1408
std	4.79	0.22	70.75	1408

The time averaged global response factor for all cases with relevant statistics (rms and standard deviation, std) with respect to the time averaging is summarized in Table 7.2. The typical ‘duration’ of resonance (during excitation) is about 100 ms. For comparison, such a time interval is selected for the case without excitation as well. The statistics are determined after the global response factor is calculated first, so integrated over the volume for every time step to calculate the time dependent global response factor (spatial mean), and then compute the mean, root mean squared and the standard deviation.

From Table 7.2 can be learnt that for $\theta = 90^\circ$, the magnitude of the time-averaged global response factor is the smallest, but the statistical scatter is also very small meaning that the value is stable and trustworthy. For the other cases, especially for $\theta = 135^\circ$ and $\theta = 180^\circ$, the statistics show that the data with respect to the response factor is fairly inconclusive and more work needs to be done to shed some light on what phenomena are responsible for this behavior.

7.2.5 Time delay

In determining the response factor, the phase between acoustic field and intensity field plays an important role. Since it was found that velocity coupling is the most likely, the analysis is taken a step further and the phase between acoustic velocity and the intensity is used to calculate how long combustion needs to respond to an acoustic wave. This time delay may yield a better idea what processes are important in sustaining combustion instability [143]. The time delay, τ_v , is found by combining the phase shift between velocity and intensity, φ_v , and the length of the acoustic period, T . So, that part of the acoustic period that the combustion response needs to reach its maximum multiplied with the length of the acoustic period gives the time delay.

$$\tau_v = \frac{\varphi_v}{2\pi} T \quad (7-7)$$

The time delay is calculated during resonance because if there is a coupling mechanism active, it is guaranteed to be present then. Also, it is physically sensible to look at the time delay in a small domain of the combustion chamber where the flame response is the highest, because here the coupling mechanism will be most dominant. To prevent local occurrences (in space and/or time) to strongly influence the result, 5 coordinates (local analysis, small window method, see section 4.1.3) with the largest normalized magnitude flame response (as used in the response factor), as shown in Figure 7.29, are selected to determine the time delay. But before the time delay is actually calculated, the phase itself is looked at more closely.

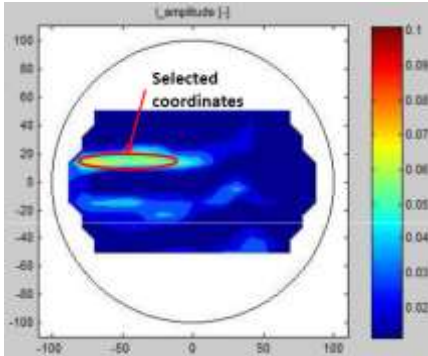


Figure 7.29: Selected region for analysis time delay

In Figure 7.30 a velocity and intensity signal of a test with external excitation with $\theta = 90^\circ$, as well as the phase between the velocity and intensity, φ_v , at one of the coordinates are plotted. It is well visible by the increasing amplitudes of velocity and intensity that the excitation frequency approaches the eigenfrequency and resonance starts to kick in shortly after $t = 4300$ ms. The evolution of the phase φ_v shows a slow increase over time combined with fairly large variations, but as soon as resonance hits, the phase remains constant and the variations are practically negligible, this is illustrated with the black trend lines in Figure 7.30. After about 100-150 ms, the excitation frequency 'leaves' the resonance domain and the phase starts slowly increasing again and also with slightly higher variations. It is likely that the increasing phase is caused by the ramp of the excitation frequency that the intensity follows, until resonance is reached and the acoustic and heat release fluctuations are locked in their feedback loop described by the Rayleigh criterion (Figure 2.10), with constant frequency and phase.

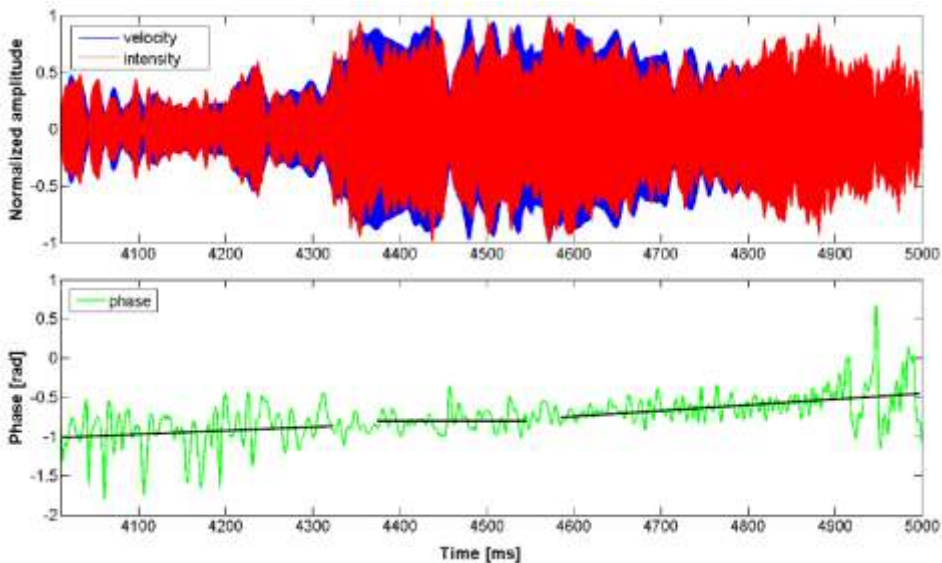


Figure 7.30: Temporal evolution velocity, intensity and phase

The feedback loop is broken when the excitation frequency diverts too far from the eigenfrequency and the phase starts following the excitation frequency again. Figure 7.31 shows the same temporal evolution of the signals and the phase, but in a small time interval, to illustrate how constant the phase is during several acoustic periods.

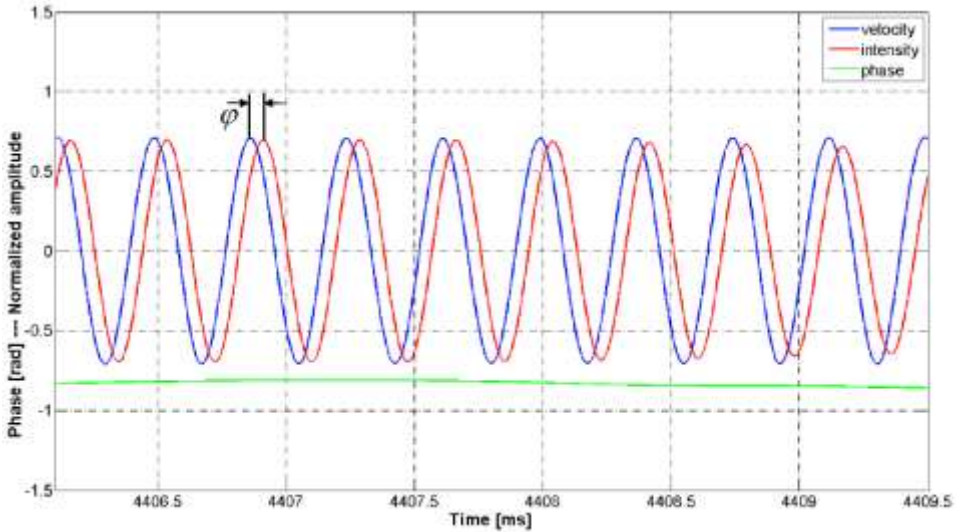


Figure 7.31: Short interval temporal evolution, velocity, intensity and phase

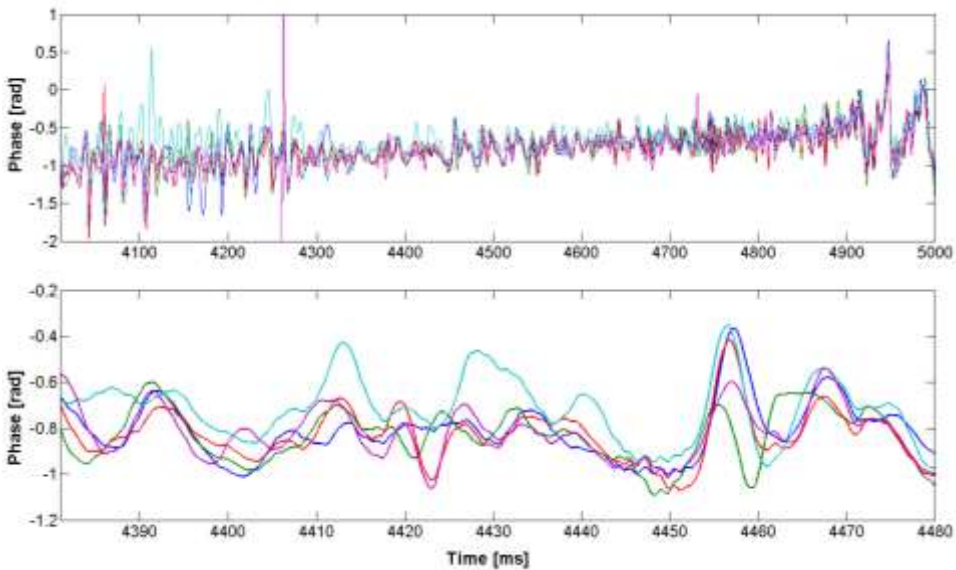


Figure 7.32: Temporal evolution of the phase at five selected coordinates

The temporal evolution of the phase at the selected coordinates is shown in Figure 7.32, for 1 second in the top part and a smaller time interval (100 ms) during resonance in the bottom part. Also here can be seen that the phase increases first, until resonance where phase remains constant, and afterwards again the increase. The bottom image shows the large agreement of the phase between the different coordinates.

As mentioned, to calculate the time delay, it is physically sensible to do so there where the flame response is strongest. And to guarantee the coupling mechanism being active, the short time interval in the bottom image of Figure 7.32 was selected during resonance. So, the phase in this time interval basically defines the time delay through equation (7-7). The time-average of the phase is calculated for all selected coordinates individually and used to determine the time delay. The result is summarized in Table 7.3, including all relevant statistics, where the last column is the spatial average over all selected coordinates.

Table 7.3: Time delay during resonance

Coordinate	1	2	3	4	5	average
Phase, φ_{p_2} [rad]	-0.813	-0.815	-0.822	-0.807	-0.816	-0.815
Time delay, τ_{p_2} [μ s]	-49.1	-49.2	-49.6	-48.7	-49.3	-49.2
rms, $\tau_{v,rms}$ [μ s]	49.8	50.1	50.4	50.3	49.8	50.1
std, $\tau_{v,std}$ [μ s]	8.32	9.67	8.8	12.5	6.39	9.25

The time delay roughly comes to 50 μ s, or about one eighth of an acoustic period. This is an order of magnitude smaller than the characteristic time scale for vaporization that Sirignano [139] described and which he classified as the most promising candidate for the driving mechanism. The magnitude found here is closer to the characteristic time scale of the mixing process. Sirignano argued that mixing, with a time scale of 10-1000 μ s, is not a likely candidate, but he was basing his findings on lower frequencies (that occur in larger engines). Considering the result found here using a relatively small combustor, one may have to conclude that mixing, at least for this combustor, is more dominantly present as a mechanism than vaporization. Especially because all aspects of this research has produced indicators that the coupling mechanism is velocity sensitive. There exist several theoretical discussions, such as by Sirignano [139], about what process is the likely driver of instability. The multiple experimental findings in this research do not unanimously point at one specific mechanism for the total combustor volume, but that does not render those discussions untrue. The vaporization rate is enhanced when the velocity fluctuations increase. Maybe the vaporization times are reduced by the imposed acoustic oscillations to the found order of magnitude, but that does not seem likely. This could very well be the reason why a self-sustained instability could never be observed in the CRC, and the observed flame response is merely caused by the enhanced mixing.

8 Concluding remarks

The main objective of the thesis was to contribute to the physical understanding of the driving and coupling mechanisms of the interaction between acoustics and combustion responsible for triggering and sustaining combustion instability. To reach this objective, several methods of analysis based on experimental measurements, such as dynamic pressure and optical diagnostics of spray and flame phenomenology, were to be used to quantify relations between the measured quantities.

Throughout the thesis, conclusions have been formulated with the relevant experimental and analytical results. These concrete conclusions and other general concluding statements will be summarized in section 8.1 and 8.2. In order to take the current status of the research a step further, a follow-up test program was designed to cover additional aspects that could answer some questions raised during the research. This test program and other perspectives for the near future with respect to the CRC are discussed in section 8.3.

8.1 Review of results

All important experimental findings will be recapitulated here and briefly reviewed, if necessary, before formulating the conclusion that consistently follows from the respective results.

Dynamic pressure

- The frequencies of the eigenmodes of the CRC are not where they are theoretically expected. It was shown that it is likely due to variations in speed of sound (temperature) throughout the combustion volume that were not considered in the initial theoretical analysis. For higher variations, the deviations of the experimental frequency distribution from the theoretical distribution, as shown with an FFT-analysis, are stronger. For a local high speed of sound around the spray, the tangential modes experience a shift to a lower and the

radial modes to a higher frequency, and vice versa. The frequency shifts, as observed, do not influence the spatial geometry of the acoustic field of the eigenmodes, but they must be considered when investigating for example higher modes to not confuse radial and tangential modes when looking at an FFT spectrum.

- The noise (rms) of the dynamic pressure signals without external excitation does not show any dependence on operating conditions such as the Weber number. It has to be concluded that when one wishes to learn something about physical phenomena from dynamic pressure signal noise in the CRC, the complete signal does not tell anything and this type of analysis can be omitted.
- The energy content of the dynamic pressure signals without external excitation filtered around the 1T-mode was correlated with several operating parameters. Only a few outliers were found which will be investigated further (see the perspectives in the next section). The quality of the fitted function to the experimental data was of high quality ($R^2 > 0.85$) in all cases. It was found that the energy content was higher for large Weber numbers (small droplets). It was also found that for higher velocity ratio, the energy content increased. Both correlations indicate that the energy content of the eigenmode is higher for a more homogeneous spatial distribution of droplets, hence more energy is transferred from combustion into the acoustic mode.
- Damping is an important aspect of the control of instabilities. No correlation was found between the damping (half width at half maximum) without external excitation and any operating conditions. The analysis was therefore omitted for tests with external excitation, also because the chosen ramp of the excitation makes the signal too instationary for which FFT operations are mathematically not well defined and physically pointless.
- The energy content of the dynamic pressure signals with external excitation filtered around the 1T-mode could not be correlated due to too large a scatter, even though the general trend was similar as for tests without external excitation. The scatter may have been caused by the insufficiently controlled distance between the siren wheel and the secondary nozzle exit. This will be verified in a follow-up test campaign (see the perspectives in the next section).
- Even though the scatter was somewhat large, the relation between angular position of the SN and the energy content was beyond a doubt. The energy content was clearly highest for $\theta = 90^\circ$, intermediate for $\theta = 135^\circ$ and lowest for $\theta = 180^\circ$. The position of the nodal line (lowest amplitudes of the acoustic pressure), fixed in space by the secondary nozzle, is right in the combustion zone for $\theta = 90^\circ$, and moving away from the combustion zone for $\theta = 135^\circ$ and $\theta = 180^\circ$. This strongly indicates that the coupling mechanism is velocity driven.
- The pressure field of the 1T-mode in the CRC without external excitation was found to be a superposition of two counter-flowing acoustic waves, as predicted by theory. The amplitude of both constantly rotating waves determined the non-constant rotational velocity of the nodal line of the pressure field. The rotational velocity of the nodal line could be determined and was both positive and negative, which respectively means rotation in clockwise and counter-clockwise direction, and depended on which of the counter-flowing acoustic waves was stronger (had a higher amplitude). A standing wave occurred only then when both counter-flowing waves have the same strength, and at such

an occurrence the rotation of the pressure field's nodal line changed direction. The position of the nodal line over time was found to have a preferred position in space. This position was confirmed by a numerical simulation that included several cavities such as the injector, igniter and purge module. For the CRC with SN, the pressure field was successfully determined as well.

Optical diagnostics, spray and flame high speed imagery

- The intact core length of the liquid spray was successfully determined and correlated with the momentum flux ratio. The general trend as found in literature was reproduced, albeit a factor of 2 smaller, which may have been caused by the geometry of the injector that was applied. External excitation did not seem to have any influence on the intact core length.
- The flame spreading angle was also successfully determined and correlated with several operating parameters. Most important are the correlations of the flame spreading angle with the Weber number and momentum flux ratio, both showing a negative relation. So, the flame spreading angle decreases for increasing Weber number and momentum flux ratio. Which is consistent, considering smaller droplets (higher Weber number) and droplets being carried further away from the injector (higher momentum flux ratio) both cause a more homogeneous spatial distribution of droplets. External excitation amplified these correlations which means that the flame spreading angle became smaller when external excitation was applied.
- The last two results combined, yielded the hypothesis that the injection and atomization processes were not affected by external excitation and therefore could not play a role in triggering or sustaining combustion instabilities. Also, it was concluded from the by the excitation amplified correlations for the flame angle that the processes after atomization are accelerated. Since the time scale of the chemical reaction is such that the acoustic oscillation seems stationary, it is concluded that chemical kinetics (next to injection and atomization) is not a likely candidate for driving instabilities. Therefore, it is theorized that the vaporization rate is increased and mixing is enforced due to the imposed high amplitude acoustic velocity field.
- The flame's intensity measured with its OH-emission does not show any response to acoustic fluctuations without external excitation, neither on a global nor on a local level. For hot flow with external excitation the amplitude of the OH-intensity fluctuations is dramatically increased, and the spatial distribution of these fluctuations becomes very structured as well. There exists a clear dependence of the amplitude of the intensity fluctuation as well as the structure of the intensity field on the angular position of the SN. Excitation from $\theta = 90^\circ$ yields the highest amplitude and the most pronounced spatial structure in the intensity field, both decreasing for $\theta = 135^\circ$ and even more for $\theta = 180^\circ$.
- The analysis of the amplitude of the intensity fluctuation yielded that the high amplitudes occur in the vicinity of the pressure nodal line, or the velocity anti-node. Based on this result, it was concluded that it is likely that the coupling mechanism is velocity, rather than pressure, driven, which substantiates the conclusion found with respect to dependence of the pressure fluctuations to the angular position of the SN.

Combustion response

- The phase relation between the acoustic pressure field and the flame intensity field is an important factor in whether the Rayleigh criterion is positive or not. It was determined for tests both with and without external excitation. Due to the absence of a spatial structure in the intensity field in the tests without external excitation, the phase field did not contain any spatial structure either, hence it was concluded that the acoustic field was too weak to modulate the heat release and therefore no coupling could be established. The phase for excited tests on the other hand did have a very pronounced structure, again strongest for an angular position of the SN of $\theta = 90^\circ$, and weakest for $\theta = 180^\circ$. This result again seems to corroborate velocity coupling, however, the convective motion caused by the velocity cannot explain the phase jump in the phase field for $\theta = 180^\circ$ because there is no transportation in and out of the combustion zone. So, if a velocity coupling exists, the phase between velocity and intensity should be constant in the entire domain, for $\theta = 180^\circ$. It is therefore concluded that for $\theta = 90^\circ$ velocity is definitely the driver of the coupling mechanism, whereas pressure is the most likely driver of the coupling mechanism for $\theta = 180^\circ$. For $\theta = 135^\circ$ both mechanisms are most likely to be active, but it is yet inconclusive to what extent.
- To quantify the local response of combustion to an acoustic disturbance, the local response factor was determined. Since the acoustic pressure fluctuations are zero at the nodal line, determining the pressure related local response factor poses an issue. Because of spatial averaging, extremely high values are obtained for the local pressure response factor in the vicinity of the nodal line which renders the result inconclusive.
- Because several analyses indicated velocity coupling to be the most promising candidate to trigger instability, also a velocity response factor was defined, which uses the acoustic velocity fluctuations instead of the pressure fluctuations as a parameter. The acoustic velocity field does not have a nodal line, and therefore the problem faced when considering the pressure does not exist. The velocity response factor was successfully calculated for three angular positions of the SN. The standard deviation for $\theta = 135^\circ$ and $\theta = 180^\circ$ was too high and as such the result was inconclusive, but for $\theta = 90^\circ$ the result was clear. It could be concluded that the global response factor for $\theta = 90^\circ$ was positive, which confirms the existence of a positive feedback between acoustic velocity and heat release.
- Since the result for the response factor for $\theta = 90^\circ$ was statistically sound, this data set was used to calculate the time delay between the coupling mechanism (acoustic velocity wave) being active and the response of the flame measured by the OH-intensity. The phase between the acoustic velocity and the intensity is the time delay expressed as part of an acoustic period (in rad). The time delay was readily determined and amounts to about 50 μs . This time-scale is typical for the mixing process.

8.2 Interpretation

Based on the experimental findings, the following description of the observed phenomena in the CRC is proposed.

- Due to the acoustic excitation (disturbance), an acoustic wave is imposed on the combustion zone. The liquid spray does not react to convective motion caused by the acoustic velocity due to too high inertia of the droplets, but the gas inside the combustion chamber does respond. The convective motion transports the gas, including newly formed gaseous oxygen surrounding the droplets, through the chamber. It depends on the location of the disturbance, or, more specifically, the direction of travel of the imposed acoustic wave, whether this convective motion enhances combustion. If the imposed acoustic wave travels perpendicular to the spray axis, combustible mixture is moved in and out of the combustion zone, amplifying the oscillation, but if the acoustic wave moves parallel to the spray axis the gas is moved within the combustion zone without resulting effect. Also, when the acoustic wave moves parallel to the spray axis, it forces a pressure gradient across the combustion zone in which case pressure sensitive processes become more prominent.
- Due to amplified transport of oxygen, the liquid droplets vaporize quicker (increased vaporization rate) to maintain the thermodynamic equilibrium with their surroundings. Therefore vaporization is enhanced, and more gaseous oxygen is produced. Also, because of the enforced convective motion and the additional gaseous oxygen, mixing is enhanced as well. The vaporization rate is enhanced no matter what direction the acoustic wave has, but mixing is most effectively enhanced when the wave moves perpendicular to the spray axis because the co-axial propellant jets are forced into each other that way by the convective motion instead of moved parallel to their own axis. Considering the effect of the position of the acoustic disturbance on the acoustics-flame interaction, and the corresponding time delay, mixing is concluded to be the process responsible for energy transfer in case of velocity coupling. Vaporization itself is a pressure sensitive process, and consistent with the same effect, vaporization is concluded to be the process responsible for energy transfer in case of pressure coupling.
- Extrapolating, in rocket combustors with 'common' dimensions (long in axial direction with respect to the diameter), the propellants are injected in axial direction. Waves parallel to the spray axis do not interact with combustion chamber processes through velocity driven coupling mechanisms, hence longitudinal modes are insensitive to velocity coupling. Also, due to the large number of injectors in 'common' rocket engines, situated closely together, a short distance downstream of the injector head there will be no more 'singular' jets. They will have formed one large combined spray, hence combustion zone. A convective movement, caused by an acoustic disturbance, perpendicular to the spray axis can only then move combustible mixture in and out of the combustion zone, when the jets of the individual injector elements and the corresponding flame fronts are still separated. This is only the case immediately at the injector exit and a short distance downstream (depending on injector geometry). So, velocity coupling through convective motion enhanced

mixing is only possible in this small region, and only then when the chamber's geometry yields a tangential mode (or a combined mode with tangential component) with a frequency coinciding with the typical timescale of the mixing process.

8.3 Perspectives

This section briefly presents an outlook on how to proceed given the experimental findings discussed in this thesis. Some notes describe an expansion on the current data set to improve or expand some of the conclusions found, others can be considered more advisory in nature to prevent some of the mistakes to be made again or generally improve methods or minimize errors.

8.3.1 Follow-up test campaigns

The test program executed for this thesis, with the objective to determine which variables have an influence on what process, is fairly extensive. There are some aspects where the test program could be expanded to learn more about stability relevant characteristics. The two campaigns carried out produced a large number of data points and many correlations and trends in behavior were found. The campaigns described in the following should each consist of only a small number of operating points and investigate a single parameter only. The selection of operating points should be based on a demonstrated high response and the results of the first two campaigns. This allows to guarantee a better signal and thus a clearer effect of the investigated variable. The operating points are selected such that they exclusively show what effect the investigated variable has. These campaigns are not expected to have a significant influence on the correlations and other results found in the first two campaigns, but could yield more insights in other not unimportant aspects of acoustics-combustion interaction that could not be pursued before.

Verification outliers

Some of the correlations found showed some outliers. It is strongly recommended to repeat these operating points as well as a set of the 'successful' operating points for benchmarking and comparison to the old test campaigns. The repetition of the outliers should verify whether these operating points were really outliers, and the benchmarking is then necessary to prevent comparing apples with pears and make sure the results are consistent with the older measurements. This should be done before any other, additional, test campaigns are executed.

Injector geometry

In literature (for example [59], [74]) the injector geometry plays a role in the stability margins of that specific engine. A co-axial injector can be modified to a large extent. It is advised to do a test campaign where the most important geometrical aspects of an injector, taper and recess length, are varied. Recess length describes how far the LOx-post exit is pulled back into the injector head with re-

spect to the face plate. Recess influences the position of the contact plane of the two propellants, hence the position of the flame and therefore its stability. Taper describes an expansion of the liquid oxygen towards the exit of the injector. The ratio of the actual exit and the post, and the length over which the expansion takes place (angle with respect to jet axis) is relevant. Taper controls the direction and magnitude of the LOx-injector exit velocity. These injector characteristics were illustrated in Figure 1.4.

Secondary nozzle diameter

Energy input was demonstrated to be another relevant variable defining stability margins [54], [79]. In the second campaign the secondary nozzle diameter was kept constant with respect to the main nozzle. It is recommended that in a new test series exactly the opposite is done to investigate the influence of the energy contents of the generated pressure wave. The operating points should be selected with 1 main nozzle, and carried out with three different secondary nozzles. With increasing diameter of the secondary nozzle, the pressure wave contains more energy when entering the combustion chamber. It is possible that this way a threshold of energy input is reached at which a self sustained instability occurs.

Damping

Another important aspect of acoustics is the inherent damping in the combustion chamber. When quantifying the effects of any variable on (in)stability it is important to be able to quantify the damping. Strictly speaking, damping can be investigated only when no disturbing external signal, such as external excitation, is present. But, investigating damping on a strong signal yields clearer results. Since damping could be influenced by any of the previously investigated variables, a substantial part of the test matrix of the second campaign should be repeated. But, for this campaign, the siren wheel has two sections of 90° where it excites the flame, and two other sections where the secondary nozzle is not closed off periodically, see Figure 8.1. In this way, the flame does experience excitation and will show high amplitude fluctuations, but at the same time, allows investigating damping characteristics of a very pronounced signal.



Figure 8.1: Siren wheel for 90 degree excitation

Multiple element injector

In reality, rocket engine combustion chambers have injector heads much more complex than the single element injector applied in the executed campaigns. Some injector heads have over 500 co-axial elements, see Figure 8.2 (cut-away of the Vulcain2 combustor showing the face plate).

A triple element injector for the CRC to investigate jet interaction under externally excited conditions is available. The three elements are aligned, injecting three parallel jets, allowing studying jet interaction through the optical access facility of the CRC, see Figure 8.3. Both spray and OH-intensity analysis should be carried out. Surely, to generate a frame of reference, all tests are to be executed without external excitation first. The first operating point is selected such that the mass flow through 1 injector element coincides with the single element operating point. The others must be defined to allow identifying any effects due to mass flow, chamber pressure and variation of injector conditions, and to compare to previous campaigns with the single injector.



Figure 8.2: Multi-element injector head of Vulcain2 [42]



Figure 8.3: Triple element injector for the CRC

Fuel comparison

The last recommended test series should be executed to compare different kinds of fuel. Currently it is possible to supply the CRC, besides methane (CH_4), with hydrogen (H_2) and ethanol ($\text{C}_2\text{H}_5\text{O}$). Especially the comparison with H_2 is interesting because it is not a hydro-carbon and expected to behave significantly different. This campaign should be designed to expand the current experimental data sets available such that the combustion response of the different fuels can be compared for similar injector conditions (Weber number, momentum flux ratio, injection velocities) as well as for similar operating conditions (mass flow, chamber pressure and mixture ratio). Obviously, combustion response is a very important aspect for the fuel comparison, so optical diagnostics for spray as well as OH-intensity must be applied and the data processing carried out very accurately.

8.3.2 General recommendations

- In the error analysis, a setting of the dynamic pressure amplifiers was found to play too large a role in the statistical error of the measurement. This setting controls the measurement range of the amplifier and it is strongly recommended to lower this setting one order of magnitude for any test without external excitation. This would lower the statistical error of the measurement chain by a factor of ten.
- The phase analysis module of the analysis program can be manually controlled to a certain extent to prevent erroneous results (e.g. in analysis of low amplitude signals), and must be edited for different angular positions of the SN. This module should be modified and extended for running calculations for several tests of different characteristics without any user interaction as well as to systematically ensure finding the correct phase in order to calculate time delays more accurately.
- From literature [18] it is known that a lifted flame might cause higher pressure amplitudes because the flame is then more sensitive to oscillations. With the current high speed camera, it was not possible to record the flame with such a spatial resolution that a lifted flame could be observed and keep the temporal resolution to be able to measure the first eigenmode at the same time. With a new model of the high speed camera, the spatial resolution could be significantly increased while still recording with a significantly high frame rate.
- The velocity related response factor was defined with the speed of sound as a normalizing factor for the velocity, which may seem somewhat unsatisfactory. It might be useful to consider other normalizing factors for the velocity that represent more physics.

Appendices

A. Chemical mechanism oxidation of methane

The very simplified reaction is illustrated in Figure A.1. A complex mechanism, suggested by Hughes [70] is given in Table A.1.

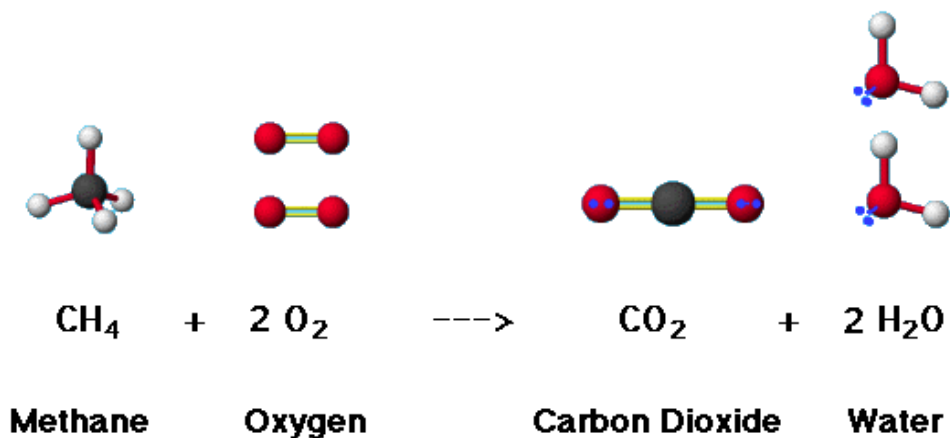


Figure A.1: Simplified reaction for methane oxygen combustion

Table A.1: Chemical reaction mechanism for methane oxidation [70]

	Reaction	A	n	E_a/kJmol^{-1}	Category	Reference
R1	$\text{H}_2 + \text{OH} \longrightarrow \text{H}_2\text{O} + \text{H}$	1.02×10^8	1.6	13.8	A	15
R2	$\text{O}_2 + \text{H} \longrightarrow \text{OH} + \text{O}$	9.76×10^{13}	0	62.11	A	15
R3	$\text{H}_2 + \text{O} \longrightarrow \text{OH} + \text{H}$	5.12×10^4	2.67	26.27	A	15
R4	$\text{OH} + \text{O} \longrightarrow \text{O}_2 + \text{H}$	1.45×10^{13}	0	2.94	A	15
R5	$\text{H} + \text{HO}_2 \longrightarrow 2\text{OH}$	1.69×10^{14}	0	3.66	A	15
R6	$\text{O}_2 + \text{H} + \text{M} \longrightarrow \text{HO}_2 + \text{M}$	2.10×10^{18}	-0.8	0.0	B	15
R7	$\text{H} + \text{HO}_2 \longrightarrow \text{H}_2 + \text{O}_2$	4.28×10^{13}	0	5.9	A	15
R8	$\text{CO} + \text{OH} \longrightarrow \text{CO}_2 + \text{H}$	1.66×10^7	-1.3	-3.2	A	32 ¹
R9	$\text{O} + \text{H}_2\text{O} \longrightarrow 2\text{OH}$	1.49×10^{11}	0.87	74.56	A	15
R10	$2\text{OH} \longrightarrow \text{O} + \text{H}_2\text{O}$	1.51×10^9	1.14	0.42	A	15
R11	$\text{CO}_2 + \text{H} \longrightarrow \text{CO} + \text{OH}$	8.70×10^{13}	0.01	105.97	A	15
R12	$\text{H} + \text{CO} + \text{M} \longrightarrow \text{HCO} + \text{M}$	5.49×10^{14}	0	3.08	A	15
R13	$\text{H} + \text{HCO} \longrightarrow \text{H}_2 + \text{CO}$	9.03×10^{13}	0	0.0	A	15
R14	$\text{HCO} + \text{M} \longrightarrow \text{H} + \text{CO} + \text{M}$	4.49×10^{14}	0	65.93	A	15
R15	$\text{CH}_3 + \text{OH} \longrightarrow {}^1\text{CH}_2 + \text{H}_2\text{O}$	7.23×10^{13}	0.0	11.64	B	15 ²
R16	$\text{H} + \text{CH}_3 + \text{M} \longrightarrow \text{CH}_4 + \text{M}$	1.69×10^{14}	0	0.0	B	15 ³
	Reaction 16, low pressure:	1.41×10^{24}	-1.8	0.0	B	
R17	$2\text{CH}_3 + \text{M} \longrightarrow \text{C}_2\text{H}_6 + \text{M}$	3.61×10^{13}	0	0.0	A	15
	Reaction 17, low pressure:	3.63×10^{241}	-7.0	11.56	A	
R18	$\text{CH}_3 + \text{O} \longrightarrow \text{CH}_2\text{O} + \text{H}$	8.43×10^{13}	0	0.0	A	15
R19	$\text{CH}_4 + \text{H} \longrightarrow \text{CH}_3 + \text{H}_2$	1.32×10^4	3.0	33.63	A	15
R20	$\text{CH}_3 + \text{H}_2 \longrightarrow \text{CH}_4 + \text{H}$	6.87×10^3	2.74	39.41	A	15
R21	$2\text{CH}_3 + \text{M} \longrightarrow \text{C}_2\text{H}_6 + \text{H} + \text{M}$	3.01×10^{13}	0	56.54	B	15
R22	$\text{CH}_4 + \text{M} \longrightarrow \text{CH}_3 + \text{H} + \text{M}$	2.40×10^{16}	0	439.01	B	15
	Reaction 22, low pressure:	1.29×10^{18}	0	379.97		
R23	$\text{O}_2 + \text{CH}_3 \longrightarrow \text{CH}_3\text{O} + \text{O}$	4.40×10^{13}	0	131.37	B	15 ⁴
R24	$\text{CH}_4 + \text{O} \longrightarrow \text{CH}_3 + \text{OH}$	7.23×10^8	1.56	35.50	A	15
R25	$\text{O}_2 + \text{CH}_3 \longrightarrow \text{CH}_2\text{O} + \text{OH}$	3.31×10^{11}	0	37.42	B	15
R26	$\text{CH}_4 + \text{OH} \longrightarrow \text{CH}_3 + \text{H}_2\text{O}$	1.57×10^7	1.83	11.64	A	15
R27	$\text{CH}_3 + \text{HO}_2 \longrightarrow \text{CH}_3\text{O} + \text{OH}$	1.80×10^{13}	0	0	B	15
R28	$\text{CH}_2\text{O} + \text{OH} \longrightarrow \text{HCO} + \text{H}_2\text{O}$	3.43×10^9	1.18	-1.87	A	15
R29	$\text{CH}_2\text{O} + \text{CH}_3 \longrightarrow \text{CH}_4 + \text{HCO}$	7.83×10^{-8}	6.1	8.23	A	15
R30	$\text{C}_2\text{H}_6 + \text{M} \longrightarrow 2\text{CH}_3 + \text{M}$	1.80×10^{21}	-1.24	379.97	A	15
	Reaction 30, low pressure:	1.89×10^{49}	-8.24	391.53		
R31	$\text{C}_2\text{H}_4 + \text{O} \longrightarrow \text{H} + \text{CH}_2\text{HCO}$	4.74×10^6	1.88	0.75	A/B	15
R32	$\text{C}_2\text{H}_4 + \text{O} \longrightarrow \text{CH}_3 + \text{HCO}$	8.13×10^6	1.88	0.75	A/B	15
R33	$\text{C}_2\text{H}_4 + \text{OH} \longrightarrow \text{C}_2\text{H}_3 + \text{H}_2\text{O}$	2.05×10^{13}	0	24.86	B	15
R34	$\text{C}_2\text{H}_2 + \text{O} \longrightarrow {}^3\text{CH}_2 + \text{CO}$	2.17×10^6	2.1	6.57	A/A	15
R35	$\text{C}_2\text{H}_2 + \text{O} \longrightarrow \text{HCCO} + \text{H}$	5.06×10^6	2.1	6.57	A/A	15
R36	$\text{CH}_2\text{CO} + \text{H} \longrightarrow \text{CH}_3 + \text{CO}$	1.81×10^{13}	0	14.13	B/U	15
R37	$\text{C}_2\text{H}_4 + \text{H} \longrightarrow \text{C}_2\text{H}_3 + \text{H}_2$	5.42×10^{14}	0	62.36	A	15
R38	$\text{C}_2\text{H}_6 + \text{H} \longrightarrow \text{C}_2\text{H}_5 + \text{H}_2$	1.45×10^9	1.5	31.01	A	15
R39	$\text{OH} + \text{HO}_2 \longrightarrow \text{H}_2\text{O} + \text{O}_2$	2.89×10^{13}	0	-2.08	A	15
R40	$\text{C}_2\text{H}_3 + \text{M} \longrightarrow \text{C}_2\text{H}_2 + \text{H} + \text{M}$	2.00×10^{14}	0	166.29	B	15
	Reaction 40, low pressure:	1.19×10^{22}	-7.5	190.4	B	
R41	$\text{OH} + \text{H} \longrightarrow \text{H}_2 + \text{O}$	3.53×10^4	2.62	18.95	A	15
R42	$\text{H}_2 + \text{H} \longrightarrow \text{H}_2 + \text{OH}$	4.52×10^8	1.6	77.08	A	15
R43	$\text{CH}_3 + \text{HCO} \longrightarrow \text{CH}_4 + \text{CO}$	1.20×10^{14}	0	0	B	21
R44	$\text{H} + {}^3\text{CH}_2 \longrightarrow \text{CH} + \text{H}_2$	6.02×10^{12}	0	-7.48	B	15

1, Increased by 10% above reference value; 2, Corrected a factor of ten error in the CEC evaluation summary page; 3, Modified to 80% of the CEC recommendation; 4, Reduced by a factor of three from the CEC evaluation.

B. Gain profile high speed camera

The digital high speed camera (Photron APX I²) has a setting to electronically amplify the signal. Of course, this has to be taken with caution because it also increases the noise of the signal, and in addition if one needs to compare different recordings that have different settings, the recordings need to be corrected for this setting. This can be done with the gain profile that is provided by the manufacturer of the camera, and is given in Figure B.1 [109]. The horizontal axis denotes the voltage that is set in the control software, and the vertical axis denotes the amplification factor. Two relations are shown to illustrate the performance loss of the camera over its lifetime. The duration of operation in this thesis was so short, the performance losses are considered negligible.

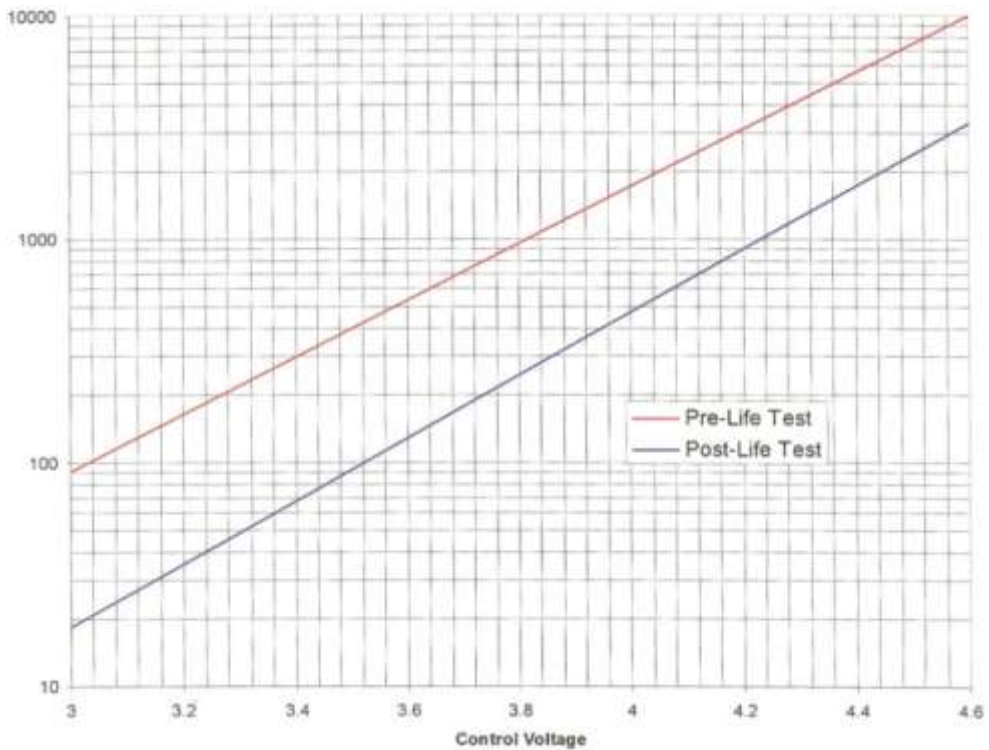


Figure B.1: Gain profile digital high speed camera

C. Bessel functions

The general solution to the three dimensional wave equation was derived in section 2.1.1, and is repeated here for convenience.

$$p(r, \theta, z, t) = \sum_{l,m,n} \left[J_n \left(\alpha_{nm} \frac{r}{R} \right) \cos \left(l\pi \frac{z}{L} \right) \right] \cdot \quad (\text{C-1})$$

$$[A \cos(n\theta) \cos(\omega t) + B \cos(n\theta) \sin(\omega t) + C \sin(n\theta) \cos(\omega t) + D \sin(n\theta) \sin(\omega t)]$$

with

- J_n = Bessel function of the first kind, of order n
- α_{nm} = $(m+1)^{\text{th}}$ root of the derivative of J_n : $\partial J_n(\alpha_{nm})/\partial r = 0$
- l, m, n = Mode number ($l, m, n = 0, 1, 2, \dots$)
- r, θ, z = coordinates in cylindrical coordinate system
- ω = angular frequency
- t = time

The Bessel functions of the first kind, of order n , largely determine the shape of the pressure field described by C-1. The important part is at which value of the independent variable the Bessel functions reach a local extremum. The frequency of an eigenmode depends on the respective root of the Bessel function. The order of the Bessel function (n) denotes which tangential mode is at hand. The number of the root (m) then determines the radial mode $(m+1)$. So, for example the root α_{nm} for the 4th tangential mode requires the 0th root of the 4th order Bessel function, α_{40} . The combined mode of the second tangential and first radial mode will have $n = 2$ and $m = 1$, α_{21} . The first 7 Bessel functions and a few of their roots are plotted in Figure C.1. The order and root number and the respective value of α_{nm} are summarized in Table C.1.

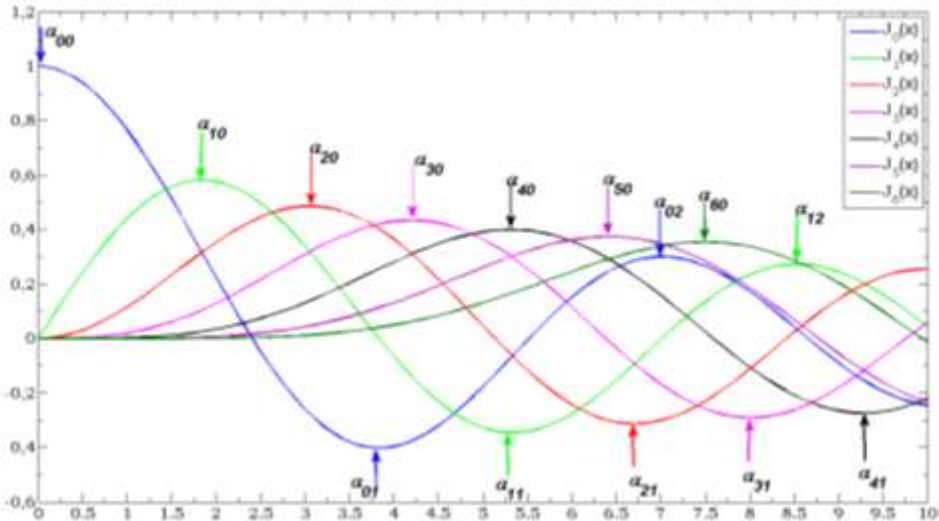


Figure C.1: Bessel functions

Table C.1: Eigenmodes and corresponding mode number and Bessel coefficient

Eigenmode	m	n	α_{nm}
1T	0	1	1.841
2T	0	2	3.054
1R	1	0	3.832
3T	0	3	4.201
4T	0	4	5.318
1R1T	1	1	5.331
5T	0	5	6.416
1R2T	1	2	6.706
2R	2	0	7.016
6T	0	6	7.501
1R3T	1	3	8.014
2R1T	2	1	8.536

D. Numerical simulations

In this section some numerical simulations are reproduced for illustration. The first section shows numerical solutions to equation C-1, which describes the acoustic pressure field in the CRC without secondary nozzle. The second section deals with how the length of the secondary nozzle affects the acoustic pressure field in the CRC.

D.1 CRC without secondary nozzle

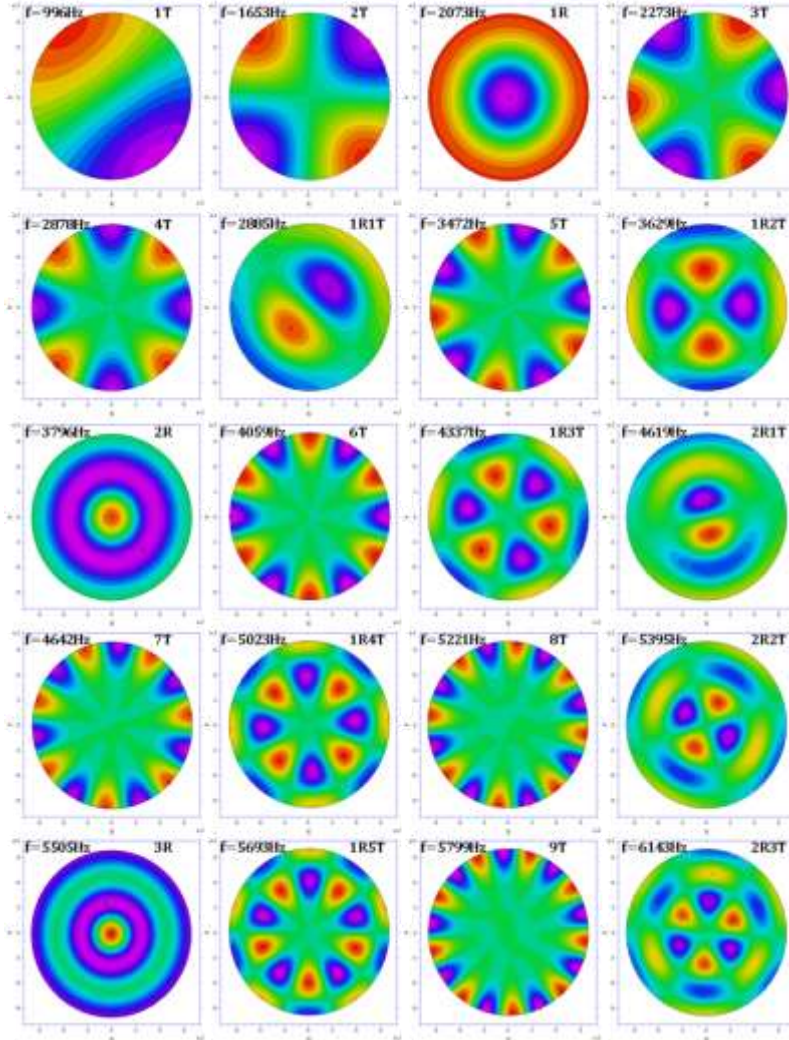


Figure D.1: First 20 eigenmodes in CRC without secondary nozzle

The first 20 individual eigenmodes are presented in Figure D.1. These are all part of the general solution to the wave equation, see equation C-1. As was discussed in section 2.2, in the numerical calculation all tangential modes result from double valued eigenvalues. Hence, tangential or combined radial-tangential modes will have, at least numerically, 2 solutions. They are mathematically equivalent, but experimentally only 1 will occur. The frequencies given in Figure D.1, valid for ambient temperature, can also be derived from the values for α_{nm} , given in Table C.1, through the following relation.

$$f_{nm} = \frac{\alpha_{nm}a}{2\pi R} \quad (\text{D-1})$$

With

- f_{nm} = the frequency of the respective eigenmode
- α_{nm} = $(m+1)^{\text{th}}$ root of the derivative of the Bessel function, as discussed in Appendix C.
- a = the (average) speed of sound in the CRC
- R = the radius of the CRC

From the geometry of the mode as shown in Figure D-1, the mode type is readily derived. The number of circular nodal lines denote the radial part of the mode, and the number of diagonal (straight) nodal lines denote the tangential part of the mode. So, for example, the left most mode in the middle row has two circular nodal lines, hence it's the 2R-mode. And the mode to its right has 6 diagonal nodal lines, hence it's the 6T-mode. This works for combined modes as well. The right bottom mode has 2 circular and 3 diagonal nodal lines, hence it's the 2R3T-mode.

D.2 CRC with secondary nozzle

The secondary nozzle (also: cavity or resonator) breaks the symmetry of the CRC. This causes the double-valued eigenvalues to split up in two single-valued eigenvalues with corresponding frequencies. One eigenfrequency remains virtually unchanged, and the other significantly drops, depending on the length of the secondary nozzle. The mode with unchanged frequency is called the π -mode referring to the parallel orientation of the mode's nodal line with respect to the cavity's axis and the mode with lower frequency is called the σ -mode referring to the perpendicular orientation of the nodal line to the cavity's axis. The π -modes' frequency and geometry are unaffected by the cavity.

An important number in this context is the quarter-wave ($\lambda/4$) length. For in-depth discussions on quarter-wave resonators is referred to Farago [44], [45]. The double-valued (tangential) eigenmode will start to show its double characteristic when the cavity length approaches the quarter-wave length and the one eigenfrequency will start falling. The same behavior is shown at every uneven number of quarter-wave lengths, so at $(n + 1) \cdot \lambda/4$, for uneven n . The principle of this behavior is illustrated in Figure D.2. The frequencies in Figure D.2 are based on hot flow conditions in the CRC (average speed of sound $a = 890$ m/s), as well as cold flow (ambient) conditions. The length of the SN used for the CRC is also shown,

as well as the quarter wave length for the 1T-mode. Figure D.2 also shows this principle for higher modes that have dropped at shorter lengths of the cavity. The second tangential (2T-) mode for example starts lowering its frequency earlier than the 1T-mode and keeps doing so until it reaches the original 1T-frequency, which happens to be the $1T\pi$ -frequency, or, to avoid confusion, the frequency of the undisturbed geometry of the CRC, $1T_{CRC}$. Basically, every time the cavity's length reaches a uneven multiple of the quarter-wave length, the frequency of any T σ - or R-mode drops down to frequency of the mode below. So, the frequency of 3T σ becomes the frequency of 1R $_{CRC}$ at $L = \lambda/4$, 2T $_{CRC}$ at $L = 3\lambda/4$, and eventually 1T $_{CRC}$ at $L = 5\lambda/4$. The evolution of the 1R-mode and the 3T-mode are shown in Figure D.3 and Figure D.4 respectively. In these Figures cold flow conditions ($a = 340$ m/s) are simulated. The frequency for the 1T-mode in the CRC with undisturbed geometry can be calculated with equation D-1, and comes to 996 Hz. Note that not only the frequency, but also the geometry of the pressure field shown, changes during the evolution. The last image in both series displays a geometry within the CRC very similar to the undisturbed 1T $_{CRC}$, and the frequency is very similar as well.

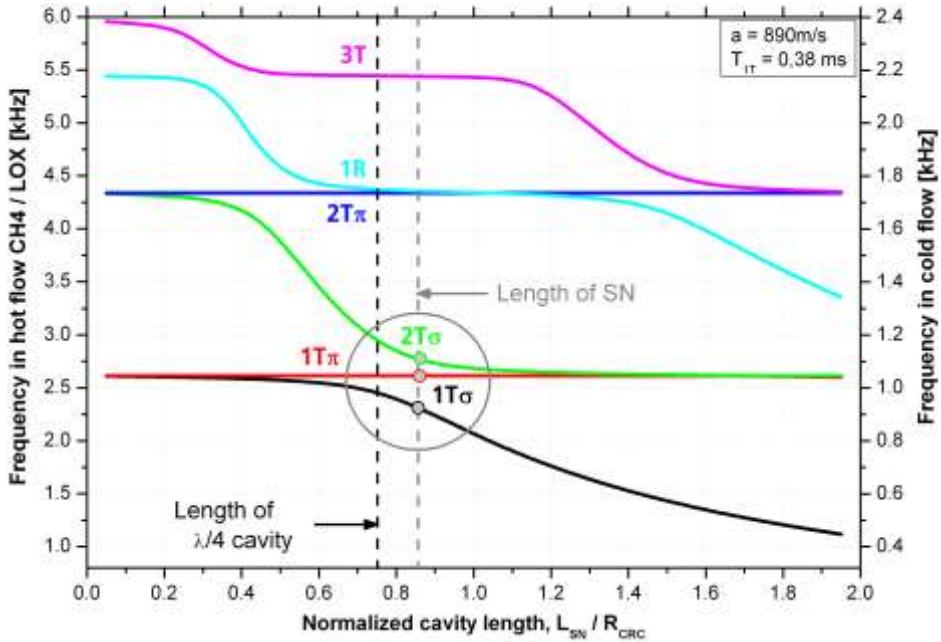


Figure D.2: Frequency vs. Cavity length

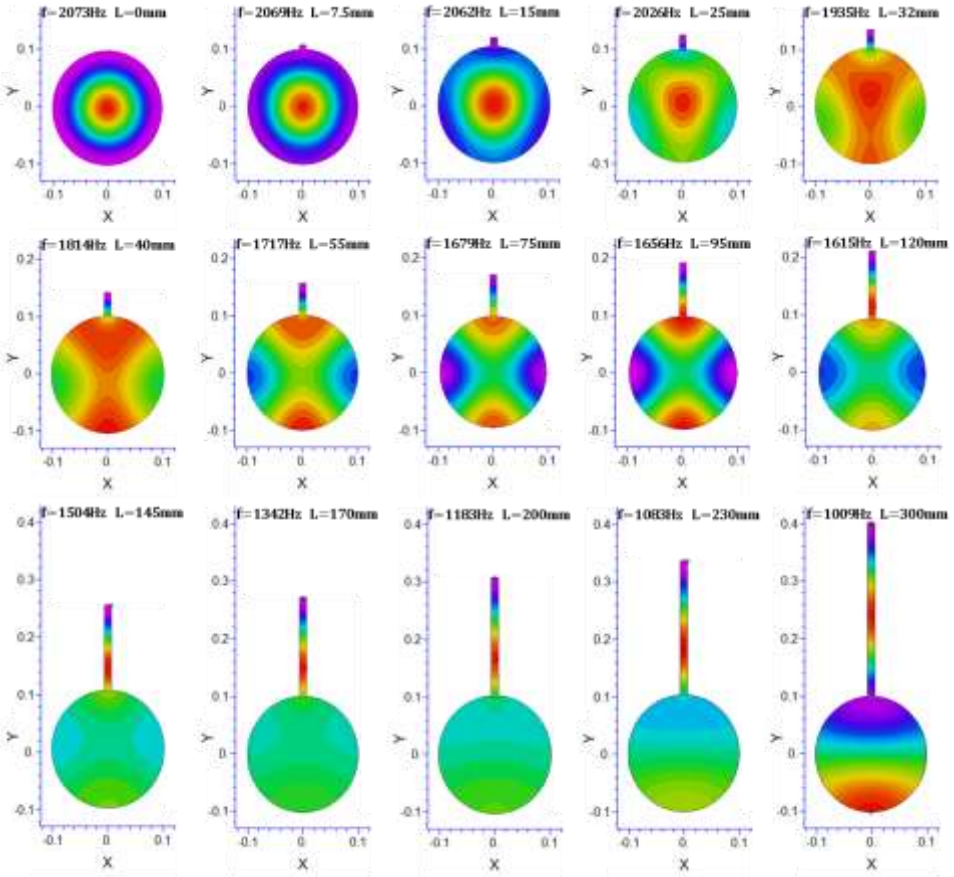


Figure D.3: Evolution of the 1R-mode for increasing cavity length

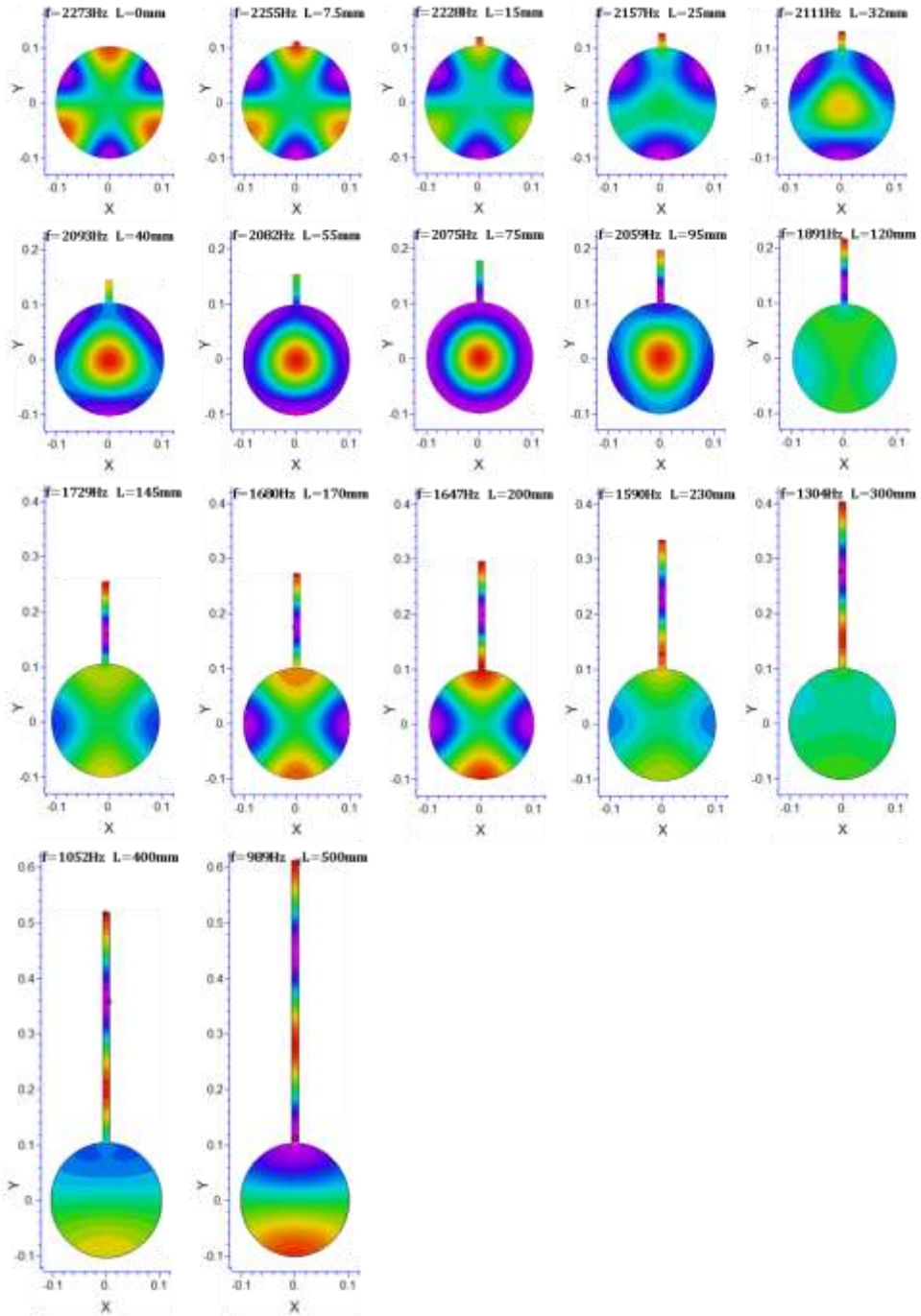


Figure D.4: Evolution of the 3T-mode for increasing cavity length

Bibliography

- [1] Adams, R.A., "Calculus: a complete course", 4th edition, Addison Wesley Longman Ltd., Canada, 1999.
- [2] Anderson, W.E., et al., "Effects of Periodic Atomization on Combustion Instability in Liquid-Fueled Propulsion Systems". In: Journal of Propulsion and Power, vol. 14, no. 5, pp 818-825, 1998.
- [3] Althen GmbH Meß- und Sensortechnik, "Lucas Schaevitz pressure sensor Datasheet", 1996.
- [4] Ariespace, "http://www.arianespace.com/news-images_library/ariane5.asp", 2010.
- [5] Ariespace, "Der Untersuchungsausschuss legt seinen Bericht vor". In: e.space, nr. 168, September 2001.
- [6] Bazarov, V.G., "Dynamics of liquid rocket injectors". In: International Symposium on Liquid Space Propulsion, 1995.
- [7] Bazarov, V.G., "Influence of propellant injector dynamic characteristics on combustion stability and efficiency", IAF-92-0645. In: 43rd Congress of the international astronautical federation, Washington, D.C., USA, 1992.
- [8] Bazarov, V.G., Yang, V., "Liquid-Propellant Rocket Engine Injector Dynamics". In: Journal of Propulsion and Power, vol. 14, no. 5, pp 797-806, 1998.
- [9] Bazarov, V.G., "Liquid Flow Pulsations Damping in Feed Lines and Injectors of Liquid Propellant Rocket Engines", IAF-93-S.2.468. In: 44th Congress of the international astronautical federation, Graz, Austria, 1993.
- [10] Bendat, J.S., Piersol, A.G., "Engineering applications of correlation and spectral analysis", second edition. John Wiley & Sons, Inc. Canada, 1993.
- [11] Benedictis, M. de, Ordonneau, G., "High Frequency Injection Coupled Combustion Instabilities – Study of Combustion Chamber/Feed System Coupling", AIAA 2006-4721. In: 42nd AIAA/ASME/SAE/ASEE Joint Propulsion Conference & Exhibit, Sacramento, CA, USA, 2006.

- [12] Bernier, D., et al., "Transfer function measurements in a model combustor: application to adaptive instability control". In: *Combust. Sci. and Tech.* 175, pp 993-1013, 2003.
- [13] Branam, R., et al., "Injection Characteristics on the Surface of a Coaxial Jet", AIAA 2002-3695. In: 38th AIAA/ASME/ASEE Joint Propulsion Conference and Exhibit, Indianapolis, IN, USA, 2002.
- [14] Breisacher, K.J., Priem, R.J., "Analysis of 5 kHz combustion instabilities in 40K methane/LOx combustion chambers", NASA TM-101368, Lewis Research Center, Cleveland, OH, USA, 1988.
- [15] Burkhardt, H., et al., "Comparative Study of Kerosene and Methane Propellants for Reusable Liquid Booster Stages". In: 4th International Conference on Launcher Technology "Space Launcher Liquid Propulsion", Liège, Belgium, 2002.
- [16] Burkhardt, H., et al., "Kerosene vs Methane: A Propellant Tradeoff for Reusable Liquid Booster Stages". In: *Journal of Spacecraft and Rockets*, vol. 41, no. 5, pp 762-769, 2004.
- [17] Candel, S., "Combustion dynamics and control: Progress and challenges". In: *Proceedings of the Combustion Institute*, vol. 29, pp 1-28, 2002.
- [18] Cheuret, F. "Instabilités thermo-acoustique de haute-fréquence dans les moteurs fusées", Ph.D. Thesis. l'Université de Provence, Aix Marseille I, 2005.
- [19] Clayton, R.M., Rogero, R.S., Sotter, J.G., "An Experimental Description of Destructive Liquid Rocket Resonant Combustion". In: *AIAA Journal*, vol. 6, no. 7, pp 1252-1259, 1968.
- [20] Clayton, R.M., Rogero, R.S., "Experimental Measurements on a Rotating Detonation-Like Wave Observed During Liquid Rocket Resonant Combustion", NASA Technical Report No. 32-788, Jet Propulsion Laboratory, California Institute of Technology, Pasadena, CA, USA, 1965.
- [21] CNES, "R&T program on high frequency combustion instabilities in liquid rocket engines", proposal research program cooperation DLR - CNES - ONERA - CNRS, 1999.
- [22] Conn, A.R., Gould, N. I. M., Toint, Ph. L., "Trust-region methods", Society for Industrial and Applied Mathematics, Philadelphia, PA, USA, 2000.
- [23] Conrad, E. William, et al., "Interim summary of liquid rocket acoustic-mode-instability studies at a nominal thrust of 20000 pounds", NASA TN D-4968, Lewis Research Center, Cleveland, OH, USA, 1968.

- [24] Crocco, L., Cheng, S.-I., "Theory of combustion instability in liquid propellant rocket motors", Butterworths Scientific Publications, London, 1956.
- [25] Crocco, L., Harrje, D.T., "Combustion instability in liquid propellant rocket motors". In: Experimental methods in combustion research, section 3.4, 1964.
- [26] Crocco, L., "Theoretical studies on liquid-propellant rocket instability", In: Tenth Symposium (International) on Combustion, pp 1101-1128, The Combustion Institute, 1965.
- [27] Crocco, L., Grey, J., Harrje, D.T., "Theory of liquid propellant rocket combustion instability and its experimental verification". In: ARS Journal, 1960.
- [28] CSTM, "Excitateur HF Calcul mécanique transitoire sur une lame de la roue", Note technique. Réf. 7023-NT-S262-ed 1, Toulouse/Paris, 2001.
- [29] CSTM, "Conception excitateur HF", Dossier de conception. Réf. 7023-NT-S256-ed 2, Toulouse/Paris, 2001.
- [30] Culick, F.E.C., "Non-Linear Growth and Limiting Amplitude of Acoustic Oscillations in Combustion Chambers". In: Combustion Science and Technology, vol. 3: 1, pp 1-16, 1971.
- [31] Culick, F.E.C., "Combustion Instabilities in Liquid Rocket Engines: Fundamentals and Control". Lecture course California Institute of Technology, 2002.
- [32] Culick, F.E.C., "Overview of Combustion Instabilities in Liquid-Propellant Rocket Engines". In: Progress in Astronautics and Aeronautics, vol. 169, pp 3-37, AIAA, 1995.
- [33] Cuoco, F., Yang, B., Oswald, M., "Experimental Investigation of LOx/H₂ and LOx/CH₄ Sprays and Flames", ISTS 2004-a-04. In: 24th International Symposium on Space Technology and Science, Miyazaki, Japan, 2004.
- [34] Cuoco, F., et al., "Experimental Investigation on LOx/CH₄ Ignition", AIAA 2004-4005. In: 40th AIAA/ASME/SAE/ASEE Joint Propulsion Conference and Exhibit, Fort Lauderdale, FL, USA, 2004.
- [35] Davis, D.W., Chehroudi, B., "Measurements in an Acoustically Driven Coaxial Jet under Sub-, Near-, and Supercritical Conditions". In: Journal of Propulsion and Power, vol. 23, no. 2, pp 364-374, 2007.
- [36] Delaunay, B.N., "Sur la sphère vide". Bulletin of Academy Sciences of the USSR, vol. 6, pp 793-800, 1934.

- [37] DLR, Departmental/private communications HF-research group, 2005-2010.
- [38] Dranovsky, M.L., "Combustion Instabilities in Liquid Rocket Engines, Testing and Development Practices in Russia". Progress in Astronautics and Aeronautics, vol. 221, AIAA, 2007.
- [39] Ducruix, S., Candel, S., "External Flow Modulation in Computational Fluid Dynamics". In: AIAA Journal, vol. 42, no. 8, 2004.
- [40] Ducruix, S., et al., "Combustion Dynamics and Instabilities: Elementary Coupling and Driving Mechanisms". In: Journal of Propulsion and Power, vol. 19, no. 5, pp 722-734, 2003.
- [41] Duthheil, J.Ph., Langel, G., "Ariane 5 upper-stage ignition conditions improvement, and return to operation with "Envisat" payload". In: Acta Astronautica, no. 53, pp 585-595, 2003.
- [42] EADS Astrium, "<http://cs.astrium.eads.net/sp/LauncherPropulsion/Vulcain-2-Rocket-Engine.html>", 2010.
- [43] Emerson Process Management, "Coriolis Micro Motion ELITE Massdurchfluss- und Dichtesensoren Datasheet", PS-0047, Rev. B, 2004.
- [44] Farago, Z., Anders, S., Oswald, M., "Investigation of the Acoustic Characteristics of the CRC". DLR-LA-HF-RP-001, intermediate progress report, DLR 2003.
- [45] Farago, Z., Oswald, M., "Resonance Frequencies and Damping in Combustion Chambers with Quarter Wave Cavities". DLR-LA-HF-RP-015, DLR 2005. Also published in: 6th International Symposium on Launcher Technologies, Munich.
- [46] Feiler, C.E., Heidmann, M.F., "Dynamic response of gaseous-hydrogen flow system and its application to high-frequency combustion instability", NASA TN D-4040, Lewis Research Center, Cleveland, OH, USA, 1967.
- [47] Flandro, G.A., Majdalani, J., "Aeroacoustic Instability in Rockets". In: AIAA Journal, vol. 41, no. 3, pp 485-497, 2003.
- [48] FlexPDE, "A Flexible Solution System for Partial Differential Equations". PDE Solutions Inc., 2002.
- [49] Friel, N., Molchanov, I.S., "A new thresholding technique based on random sets". In: Pattern Recognition 32, pp 1507-1517, 1998.

- [50] Gautam, V., Gupta, A.K., "Cryogenic Flow and Mixing from a Single Element Coaxial Rocket Injector", AIAA 2006-4529. In: 42nd AIAA/ASME/SAE/ASEE Joint Propulsion Conference & Exhibit, Sacramento, CA, USA, 2006.
- [51] Ghosh, A., Diao, Q., Yu, K.H., "Flame-Acoustic Interaction in GOX/GH₂ Shear-Coaxial Injector Flow-field", AIAA 2006-762. In: 44th AIAA Aerospace Sciences Meeting and Exhibit, Reno, NV, USA, 2006.
- [52] Ghosh, A., et al., "Effect on Density Ratio on Shear-Coaxial Injector Flame-Acoustic Interaction", AIAA 2006-4528. In: 42nd AIAA/ASME/SAE/ASEE Joint Propulsion Conference & Exhibit, Sacramento, CA, USA, 2006.
- [53] Gröning, S., "Berechnung eines Response Faktors in einer Raketenbrennkammer durch Bestimmung des dynamischen Druckfeldes und einem anschließenden Vergleich mit Flammenemissionsmessungen", Diplomarbeit, RWTH Aachen, Aachen, Germany, 2010.
- [54] Gordon, S., McBride, B.J., "Computer Program for Calculation of Complex Chemical Equilibrium Compositions and Applications", NASA Reference Publication 1311, 1994.
- [55] Götz, A, et al., "Application of Non-Toxic Propellants for Future Advanced Launcher Vehicles", AIAA 2001-3546. In: 37th AIAA/ASME/SAE/ASEE Joint Propulsion Conference and Exhibit, Salt Lake City, UT, USA, 2001.
- [56] Gurliat, O., et al., "Ignition of cryogenic H₂/LOX sprays". In: Aerospace Science and Technology 7, pp 517-531, 2003.
- [57] Habiballah, M., et al., "Experimental studies of high-pressure cryogenic flames on the mascotte facility". In: Combustion Science and Technology 178, pp 101-128, 2006.
- [58] Habiballah, M., et al., "High Frequency Combustion Instability in Liquid Propellant Rocket Engines – A Review of Studies Carried Out at ONERA for the Ariane Launcher", AIAA-92-0774. In: 30th Aerospace Sciences Meeting & Exhibit, Reno, NV, USA, 1992.
- [59] Harrje, D.T., Reardon, F., "Liquid propellant rocket combustion instability", NASA SP-194, 1972.
- [60] Harrje, D.T., Sirignano, W.A., "Combustion instability in liquid propellant rocket motors", AMS Report no. 1203, Princeton University, dept. of Aerospace and Mechanical Engineering, Princeton, NJ, USA, 1974.
- [61] Heidmann, M.F., "Effect of steady velocities on the dynamic response of liquid jet atomization", NASA TN D-5565, Lewis Research Center, Cleveland, OH, USA, 1969.

- [62] Heidmann, M.F., "Oscillatory combustion of a liquid-oxygen jet with gaseous hydrogen", NASA TN D-2753, Lewis Research Center, Cleveland, OH, USA, 1965.
- [63] Heidmann, M.F., "Oxygen-jet behavior during combustion instability in a two-dimensional combustor", NASA TN D-2725, Lewis Research Center, Cleveland, OH, USA, 1965.
- [64] Heidmann, M.F., Feiler, C.E., "Evaluation of tangential velocity effects on spinning transverse combustion instability", NASA TN D-3406, Lewis Research Center, Cleveland, OH, USA, 1966.
- [65] Heidmann, M.F., Groeneweg, J.F., "Analysis of the dynamic response of liquid jet atomization to acoustic oscillations", NASA TN D-5339, Lewis Research Center, Cleveland, OH, USA, 1969.
- [66] Heidmann, M.F., Wieber, P.R., "Analysis of Frequency Response Characteristics of Propellant Vaporization", NASA TN D-3749, Lewis Research Center, Cleveland, OH, USA, 1966.
- [67] Heidmann, M.F., Wieber, P.R., "Analysis of Frequency Response Characteristics of Propellant Vaporization", NASA TM X-52195. In: Second Propulsion Joint Specialist Conference, AIAA, Colorado Springs, CO, USA, 1966.
- [68] Heidmann, M.F., Wieber, P.R., "Analysis of n-Heptane vaporization in unstable combustor with traveling transverse oscillations", NASA TN D-3424, Lewis Research Center, Cleveland, OH, USA, 1966.
- [69] Heister, S.D., Rutz, M.W., Hilbing, J.H., "Effect of Acoustic Perturbations on Liquid Jet Atomization". In: *Journal of Propulsion and Power*, vol. 13, no. 1, pp 82-88, 1997.
- [70] Hughes, K.J., et al., "Development and Testing of a Comprehensive Chemical mechanism for the Oxidation of Methane". In: *International Journal of Chemical Kinetics*, vol. 33, issue 9, pp 513-538, 2001.
- [71] Hutt, J.J., Rucker, M., "High-Frequency Injection-Coupled Combustion Instability". In: *Progress in Astronautics and Aeronautics*, vol. 169, pp 345-355, AIAA, 1995.
- [72] Ibrahim E.A., Kenny R.J., Walker, N.B., "A Computational and Experimental Investigation of Shear Coaxial Jet Atomization", AIAA 2006-5049. In: 42nd AIAA/ASME/SAE/ASEE Joint Propulsion Conference & Exhibit, Sacramento, CA, USA, 2006.
- [73] Jacob, E.J., "A Study of Nonlinear Combustion Instability". Dissertation, University of Tennessee, Knoxville, TN, USA, 2009.

- [74] Jensen, R.J., Dodson, H.C., Claflin, S.E., "LOX/Hydrocarbon Combustion Instability Investigation", NASA CR-182249, Lewis Research Center, 1989.
- [75] Jones, W.P., Sheen, D.-H., "A Probability Density Function Method for Modelling Liquid Fuel Sprays". In: *Flow, Turbulence and Combustion* 63, pp 379-394, 1999.
- [76] Kelsall, G., Troger, C., "Prediction and control of combustion instabilities in industrial gas turbines". In: *Applied Thermal Engineering* 24, pp 1571-1582, 2004.
- [77] Keppeler, J., Edouard, B., Fassl, F., "Startup Simulation of Upper Stage Propulsion System of ARIANE 5". In: 4th International Conference on Launcher Technology "Space Launcher Liquid Propulsion", Liege, Belgium, 2002.
- [78] Kistler, "ThermoCOMP-Quarz-Drucksensor TYP6125". Operation Manual, Datasheet and Calibration protocol, 2005.
- [79] Kistler, "Charge Amplifier". Operation Manual, Datasheet and Calibration Protocol, 2005.
- [80] Knapp, B., Farago Z., Oswald, M., "Interaction of LOX/GH₂ Spray-Combustion with Acoustics", AIAA 2007-0572. In: 45th AIAA Aerospace Sciences Meeting and Exhibit, Reno, NV, USA, 2007.
- [81] Knapp, B., Oswald, M., "High speed visualization of flame response in a LOx/H₂ combustion chamber during external excitation". In: 12th International symposium on flow visualization, DLR, Göttingen, Germany, 2006.
- [82] Knapp, B., Oswald, M., Anders, S., "Untersuchung der tangentialen moden von hochfrequenten verbrennungsinstabilitaeten in raketenbrennkammern", DGLR-JT2005-189, Germany, 2005.
- [83] Lartigue, G., Meier, U., Bérat, C., "Experimental and numerical investigation of self-excited combustion oscillations in a scaled gas turbine combustor". In: *Applied Thermal Engineering* 24, pp 1583-1592, 2004.
- [84] Lasheras, J.C., Hopfinger, E.J., "Liquid jet Instability and Atomization in a Coaxial Gas Stream". In: *Annu. Rev. Fluid Mech.* 32, pp 275-308, 2000.
- [85] Lasheras, J.C., Villermaux, E., Hopfinger, E.J., "Break-up and atomization of a round water jet by a high-speed annular jet". In: *J. Fluid Mech.* vol. 357, pp 351-379, 1998.

- [86] Legrand, B., Albano, G., Vuillermoz, P., "Start up transient modeling of pressurised tank engine: AESTUS application". In: 4th International Conference on Launcher Technology "Space Launcher Liquid Propulsion", Liege, Belgium, 2002.
- [87] Lee, J.G., Santavicca, D.A., "Experimental Diagnostics for the Study of Combustion Instabilities in Lean Premixed Combustors". In: Journal of Propulsion and Power, vol. 19, no. 5, pp 735-750, 2003.
- [88] Lee, J.-Y., et al., "The Dependence of Combustion Instability upon Liquid Fuel Spray Properties", AIAA 2002-4176. In: 38th AIAA/ASME/SAE/ASEE Joint Propulsion Conference & Exhibit, Indianapolis, IN, USA, 2002.
- [89] Litchford, R.J., Weiwei L., "On Destructive Liquid Rocket Resonant Combustion", AIAA 2008-5115. In: 44th AIAA/ASME/SAE/ASEE Joint Propulsion Conference & Exhibit, Hartford, CT, USA, 2008.
- [90] Maeding, C., Preklik, D., Haeseler, D., "Recent Investigations on Hydrocarbon Based Fuels for Future Propulsion Systems". In: European Conference for Aerospace Sciences (EUCASS), Moscow, Russia, 2005.
- [91] Marmottant, P., Villermaux, E., "On spray formation". In: Journal of Fluid Mechanics, vol. 498, pp 73-111, 2004.
- [92] Marshall, W.M., et al., "Combustion Instability Studies Using Gaseous Methane and Liquid Oxygen", AIAA 2006-4526. In: 42nd AIAA/ASME/SAE/ASEE Joint Propulsion Conference & Exhibit, Sacramento, CA, USA, 2006.
- [93] Marshall, W., et al., "Experimental and Computational Investigation of Combustor Acoustics and Instabilities, Part II: Transverse Modes", AIAA 2006-538. In: 44th AIAA Aerospace Sciences Meeting and Exhibit, Reno, NV, USA, 2006.
- [94] MatLAB®, "The Language of Technical Computing". The Mathworks™, 2009.
- [95] Mayer, W., Tamura, H., "Propellant Injection in a Liquid Oxygen/Gaseous Hydrogen Rocket Engine". In: Journal of Propulsion and Power, vol. 12, no. 6, pp 1137-1147, 1996.
- [96] Méry, Y., et al., "Injection coupling with high amplitude transverse modes: experimentation and simulation", 2nd Colloque INCA, 2008.
- [97] Méry, Y., et al., "Experimentation, modeling and simulation of high frequency acoustic coupling in rocket engines", Ecole Centrale Paris, E.M2.C, 2007.

- [98] Mickelsen, W.R., "Effect of standing transverse acoustic oscillations on fuel-oxidant mixing in cylindrical chambers", NACA TN 3983, Lewis Flight Propulsion Laboratory, Cleveland, OH, USA, 1957.
- [99] Moore, J.D., et al., "Stability of Methane/Oxygen Coaxial Diffusion Flame", AIAA 2003-4636. In: 39th AIAA/ASME/SAE/ASEE Joint Propulsion Conference and Exhibit, Huntsville, AL, USA, 2003.
- [100] Natanzon, M.S., "Combustion Instability". Progress in Astronautics and Aeronautics, vol. 222, AIAA, 1999.
- [101] Nelder, J.A., Mead, R., "A simplex method for function minimization". The Computer Journal, vol. 7, pp 308-313, 1965.
- [102] Nicole, A., Habiballah, M., "Investigations of some generic coupling mechanisms in high frequency combustion instability phenomenon – Theory and Numerical simulations", AIAA 2006-750. In: 44th AIAA Aerospace Sciences Meeting and Exhibit, Reno, NV, USA, 2006.
- [103] Nicole, A., Habiballah, M., "Numerical analysis of acoustic instability". In: 4th International Conference on Launcher Technology "Space Launcher Liquid Propulsion", Liège, Belgium, 2002.
- [104] Oefelein, J.C., Yang, V., "Comprehensive Review of Liquid-Propellant Combustion Instabilities in F-1 Engines". In: Journal of Propulsion and Power, vol. 9, no. 5, pp 657-677, 1993.
- [105] Oppenheim, A.V., Schaffer, R.W., Buck, J.R., "Discrete-time signal processing", 2nd ed. Prentice Hall, Inc., 1999.
- [106] Oswald, M., et al., "Combustion Chamber Acoustics and its Interaction with LOX/H₂- and LOX/CH₄-Spray Flames". In: 26th International Symposium on Space Technology and Space, Hamamatsu, Japan, 2008.
- [107] Oswald, M., et al., "Resonance Frequencies and Damping of a Combustor Acoustically Coupled to an Absorber". In: Journal of Propulsion and Power, vol. 24, no. 3, pp 524-533, 2008.
- [108] Pempie, P., Frohlich, T., Vernin, H., "LOx/Methane and LOx/Kerosene high thrust engine trade-off", AIAA 2001-3542. In: 37th AIAA/ASME/SAE/ASEE Joint Propulsion Conference, Salt Lake City, UT, USA, 2001.
- [109] Photron, "FASTCAM-ultima APX-i2 Hardware Manual", Rev. 1.01, Photron Limited, 2005.
- [110] Photron, "Photron FASTCAM Viewer Operational Manual", Rev. 2.431, English version, Photron Limited, 2005.

- [111] Photron, "FASTCAM-1024PCI Hardware Manual", Rev. 1.01, International version, Photron Limited, 2005.
- [112] Philippart, K.D., Moser, M.D., "Stability Analyses of Liquid Oxygen/Methane Injectors Using Currently Available Analytical Tools", AIAA-88-2851. In: 24th AIAA/ASME/SAE/ASEE Joint Propulsion Conference, Boston, MS, USA, 1988.
- [113] Popp, M., Stanke, J., "Experimental Investigation of the HM7B Thrust Chamber Start-Up Transient", AIAA-88-2931. In: : 24th AIAA/ASME/SAE/ASEE Joint Propulsion Conference, Boston, MS, USA, 1988.
- [114] Portillo, J.E., Sisco, J.C., "Generalized Combustion Instability Model", AIAA 2006-4889. In: 42nd AIAA/ASME/SAE/ASEE Joint Propulsion Conference & Exhibit, Sacramento, CA, USA, 2006.
- [115] Press, W.H., et al., "Numerical recipes in C". Cambridge University Press, 2nd Edition, Cambridge, 1992.
- [116] Priem, R.J., Breisacher, K.J., "Combustion instability coupling with feed system acoustics", N90-28629, Lewis Research Center, 1988.
- [117] Priem, R.J., Pierro, R., "Trends in HF-Instability studies nonlinear considerations". In: 4th International Conference on Launcher Technology "Space Launcher Liquid Propulsion", Liege, Belgium, 2002.
- [118] Putnam, A.A., "Combustion-Driven Oscillations in Industry", American Elsevier Publishing Company, Inc., New York, pp 3-4, 1971.
- [119] Rayleigh, J.W.S., "The explanation of certain acoustical phenomena". In: Nature, pp 319-321, 1878.
- [120] Rayleigh, J.W.S., "The theory of sound", volume I and II, Dover Publications, New York 1894.
- [121] Raynal, L., et al., "Primary instability in liquid-gas shear layers". In: Proc. Symp. On turbulent shear flows 11, vol. 3, pp 27.1-27.5, 1997.
- [122] Reardon, F.H., Crocco, L., Harrje, D.T., "Velocity Effects in Transverse Mode Liquid Propellant Rocket Combustion Instability". In: AIAA Journal, vol. 2, no. 9, pp 1631-1641, 1964.
- [123] Rehab, H., Villermaux, E., Hopfinger, E.J., "Flow regimes of large-velocity-ratio coaxial jets". In: J. Fluid Mech, vol. 345, pp 357-381, 1997.
- [124] Richecoeur, F., Ducruix, S., Candel, S., "A Velocity Coupling Model for High Frequency Instabilities". In: 2nd European Conference for Aerospace Sciences (EUCASS), 2007.

- [125] Richecoeur, F., et al., "Effect of temperature fluctuations on high frequency acoustic coupling". In: Proc. Combust. Inst., vol. 32, issue 2, pp 1663-1670, 2009.
- [126] Richecoeur, F., et al., "Interactions between propellant jets and acoustic modes in liquid rocket engines: experiments and simulations", AIAA 2006-4397. In: 42nd AIAA/ASME/SAE/ASEE Joint Propulsion Conference & Exhibit, Sacramento, CA, USA, 2006.
- [127] Richecoeur, F., et al., "High-Frequency Transverse Acoustic Coupling in a Multiple-Injector Cryogenic Combustor". In: Journal of Propulsion and Power, vol. 22, no. 4, pp 790-799, 2006.
- [128] Rossing, T.D., "Springer Handbook of Acoustics", Springer Science + Business Media, LLC, New York, NY, USA, 2007.
- [129] Rupe, J.H., Jaivin, G.I., "The Effects of Injection Mass Flux Distributions And Resonant Combustion on Local heat Transfer in a Liquid-Propellant Rocket Engine", NASA Technical Report No. 32-648, Jet Propulsion Laboratory, California Institute of Technology, Pasadena, CA, USA, 1964.
- [130] Sahoo, P., et al., "Threshold selection using Renyi's entropy". Pattern Recognition 30, no. 1, pp 71-84, 1997.
- [131] Salmi, R.J., Wanhainen, J.P., Hannum, N.P., "Effect of thrust per element on combustion stability characteristics of hydrogen-oxygen rocket engines", NASA TN D-4851, Lewis Research Center, Cleveland, Ohio, USA 1968.
- [132] Santoro, R.J., "Swirl Effects on Coaxial Injector Atomization". Final Technical Report for Air Force Office of Scientific Research. PSU, Dept. of Mechanical Engineering, 1996.
- [133] Schmehl, R., Steelant, J., "Influence of injection temperature on the pre-flow phase during start-up of an upper-stage rocket engine". In: 40th AIAA/ASME/SAE/ASEE Joint Propulsion Conference, Fort Lauderdale, FL, USA, 2004.
- [134] Schuller, T., Durox, D., Candel, S., "A unified model for the prediction of laminar flame transfer functions: comparisons between conical and V-flame dynamics". In: Combustion and Flame 134, pp 21-34, 2003.
- [135] Schuller, T., et al., "Modeling tools for the prediction of premixed flame transfer functions". In: Proceedings of the Combustion Institute, vol. 20, pp 107-113, 2002.
- [136] Schuller, T., Durox, D., Candel, S., "Self-induced combustion oscillations of laminar premixed flames stabilized on annular burners". In: Combustion and Flame 135, pp 525-537, 2003.

- [137] Sezgin, M., Sankur, B., "Survey over image thresholding techniques and quantitative performance evaluation". In: *Journal of Electronic Imaging* 13, vol. 1, pp 146-165, 2004.
- [138] Sirignano, W.A., Crocco, L., Harrje, D.T., "A theoretical study of non-linear combustion instability: longitudinal mode", NASA TN-677, Princeton University, dept. of aerospace and mechanical sciences, 1964.
- [139] Sirignano, W.A., et al., "Liquid-Propellant Droplet Vaporization: A Rate-Controlling Process for Combustion Instability". In: *Progress in Astronautics and Aeronautics*, vol. 169, pp 307-343, AIAA, 1995.
- [140] Sisco, J.C. et al., "Examination of Mode Shapes in an Unstable Rocket Combustor", AIAA 2006-4525. In: 42nd AIAA/ASME/SAE/ASEE Joint Propulsion Conference & Exhibit, Sacramento, CA, USA, 2006.
- [141] Sliphorst, M., Gröning, S., Oschwald, M., "Theoretical and experimental identification of an acoustic spinning mode in a cylindrical combustor". In: *Journal of Propulsion and Power*, vol. 27, no. 1, pp 182-189, 2011.
- [142] Sliphorst, M., et al., "Combustion instability coupling mechanisms between acoustics and LOx/CH₄ spray flames", AIAA-2011-0327. In: 47th Aerospace Sciences Meeting, Orlando, USA, 2011.
- [143] Sliphorst, M., et al., "Combustion instability coupling mechanisms between cryogenic LOx/CH₄ spray flames and acoustics". In: *Journal of Propulsion and Power*, SUBMITTED.
- [144] Sliphorst, M., Knapp, B., Oschwald, M., "Hochfrequente Verbrennungsinstabilitäten in Raketenbrennkammern mit LOx/CH₄ Sprayverbrennung", DLRK 2009-1317, Aachen, Germany, 2009.
- [145] Souchier, A., Lemoine, J.C., Dorville, G., "Resolution du problem des instabilités sur le moteur Viking". In: 33^{eme} Congres International Astronautical Federation, Paris, France, 1982.
- [146] Stearns, S.D., "Digital Signal Analysis", Hayden Book Company, Inc. Rochelle Park, New Jersey, USA.
- [147] Steelant, J., "Fluid Dynamic Effects during Priming of Aestus' Fuel Dome". In: 4th International Conference on Launcher Technology "Space Launcher Liquid Propulsion", Liege, Belgium, 2002.
- [148] Sutton, G.P., Biblarz, O., "Rocket Propulsion Elements", seventh edition. John Wiley & Sons, Inc., Canada, 2001.

- [149] Tamura, H., et al., "An experimental study on the stability characteristics of the LOx/Methane rocket combustor", AIAA 95-2359. In: 31st AIAA/ASME/SAE/ASEE Joint Propulsion Conference, San Diego, CA, USA, 1995.
- [150] TC Ltd., "Guide to thermocouple and resistance thermometry", Issue 6.1, 2007.
- [151] Villiermaux, E., Rehab, H., "Mixing in coaxial jets". In: Journal of Fluid Mechanics, vol. 425, pp 161-185, Cambridge University Press, 2000.
- [152] Villiermaux, E., "Mixing and Spray Formation in Coaxial Jets". In: Journal of Propulsion and Power, vol. 14, no. 5, pp 807-817, 1998.
- [153] Vingert, L., Habiballah, M., Vuillermoz, P., "Upgrading of the Mascotte cryogenic test bench to the LOX/Methane combustion studies". In: 4th International Conference on Launcher Technology "Space Launcher Liquid Propulsion", Liège, Belgium, 2002.
- [154] Wanhainen, J.P., Feiler, C.E., Morgan, C.J., "Effect of chamber pressure, flow per element, and contraction ratio on acoustic-mode instability in hydrogen-oxygen rockets", NASA TN D-4733, Lewis Research Center, Cleveland, Ohio, USA, 1968.
- [155] Wanhainen, J.P., Morgan, C.J., "Effect of injection element radial distribution and chamber geometry on acoustic-mode instability in a hydrogen oxygen rocket", NASA TN D-5375, Lewis Research Center, Cleveland, Ohio, USA 1969.
- [156] Wanhainen, J.P., Parish, H.C., Conrad, E.W., "Effect of propellant injection velocity on screech in 20000-pound hydrogen-oxygen rocket engine", NASA TN D-3373, Lewis Research Center, Cleveland, Ohio, USA, 1966.
- [157] Wieber, P.R., Mickelsen, W.R., "Effect of transverse acoustic oscillations on the vaporization of a liquid-fuel droplet", NASA TN D-287, Lewis Research Center, Cleveland, OH, USA, 1960.
- [158] Yang, B., Cuoco, F., Oswald, M., "Atomization and Flames in LOX/H₂- and LOX/CH₄-Spray Combustion". In: Journal of Propulsion and Power, vol. 23, no. 4, pp 763-771, 2007.
- [159] Yang, V. and Anderson, W., editors, "Liquid Rocket Engine Combustion Instability". Progress in Astronautics and Aeronautics, vol. 169, AIAA, 1995.
- [160] Yang, V., Culick, F.E.C., "On the Existence and Stability of Limit Cycles for Transverse Acoustic Oscillations in a Cylindrical Combustion Chamber. 1: Standing Modes". In: Combustion Science and Technology, vol. 72: 1, pp 37-65, 1990.

- [161] Younglove, B.A., Ely, J.F., "Thermophysical Properties of Fluids. I. Argon, ethylene, parahydrogen, nitrogen, nitrogen trifluoride, and oxygen". In: Journal of Physical and Chemical Reference Data, vol. 11, suppl. 1, 1982.
- [162] Younglove, B.A., Ely, J.F., "Thermophysical Properties of Fluids. II. Methane, Ethane, Propane, Isobutane and Normal Butane". In: Journal of Physical and Chemical Reference Data, vol. 16, no. 4, 1987.
- [163] Zähringer, K., Durox, D., Lacas, F., "Helmholtz behavior and transfer function of an industrial fuel swirl burner used in heating systems". In: International Journal of heat and mass transfer 46, pp 3539-3548, 2003.
- [164] Zilwa, de, S.R.N., Sivasegaram, S., Whitelaw, J.H., "Control of Combustion Oscillations Close to Stoichiometry". In: Flow, Turbulence and Combustion 63, pp 395-414, 1999.
- [165] Zinn, B.T., Crocco, L., Sirignano, W.A., "A theoretical study of nonlinear transverse combustion instability in liquid propellant rocket motors", NASA TN 732, Princeton University, dept. of Aerospace and Mechanical sciences, 1966.
- [166] Zucrow, M.J., Hoffmann, J.D., "Gas Dynamics" volume II, 2nd edition, Robert E. Krieger Publishing Company, 1985.

Curriculum Vitae

Personal Data

Family name: Sliphorst
First name: Mark
Date of birth: January 21st, 1978
Place of birth: Amsterdam

Education

03/2007 – 03/2011 Delft University of Technology, Delft (Netherlands)
Applied Physics, Degree: Ph.D. (Dr.)
09/1997 – 08/2004 Delft University of Technology, Delft (Netherlands)
Aerospace Engineering, Degree: M.Sc. (Ir.)
08/1996 – 05/1997 Elizabethtown College, Elizabethtown, PA (USA)
09/1990 – 06/1996 Secondary education (VWO)
Montessori Lyceum Amsterdam (Netherlands)

Work experience

05/2007 – present Test engineer / Research scientist, DLR Lampoldshausen
(Germany)
09/2005 – 05/2007 Ph.D.-candidate, DLR Lampoldshausen (Germany)
08/2003 – 05/2004 Master's thesis work, EADS-Astrium, Ottobrunn,
near Munich (Germany)